First principles molecular dynamics study of the influence of acid strength on MTO conversion in H-SAPO-5 and H-SSZ-24

Margot Matton

Supervisors: Prof. dr. ir. Veronique Van Speybroeck, Prof. dr. ir. Karen Hemelsoet
Counsellors: Kristof De Wispelaere, Jeroen Van der Mynsbrugge

Master's dissertation submitted in order to obtain the academic degree of
Master of Science in Chemical Engineering

Department of Applied Physics
Chairman: Prof. dr. ir. Christophe Leys
Faculty of Engineering and Architecture
Academic year 2014-2015

UNIVERSITEIT
GENT

This research was conducted at the Center for Molecular Modeling.

The author gives permission to make this master dissertation available for consultation and to copy parts of this master dissertation for personal use. In the case of any other use, the limitations of the copyright have to be respected, in particular with regard to the obligation to state expressly the source when quoting results from this master dissertation.

Margot Matton
Ghent, August 7 2015

Preface

During the past year in research, I got help and support from many people. I would like to thank a few of them in particular.

First of all, I would like to thank professor Van Speybroeck, professor Hemelsoet, Kristof and Jeroen for their helpful input during the progress meetings and for granting me the opportunity to finish my thesis at my own pace. Their patience is much appreciated. They also gave me the chance to partake in a scientific conference. Kristof must be thanked in particular for the time and effort he put into reading of all chapters multiple times and helping me with the day to day problems.

I will never forget the kindness and support from the people of the CMM, especially the last two months. I would like to thank professor Waroquier for his interest in my thesis and for organizing and inviting me at the annual reception and the CMM lunch. I must thank Dietmar and Pieter for keeping me posted on the most unusual trivia. Thanks to them and Simon, our office was always a fun place to work at.

I must thank all other thesis students at the CMM as well as at the LCT. The lunches together always formed a pleasant distraction in between the daily thesis routine. Thank you to my girl friends from high school for entertaining me with the usual girly gossip. I should also mention Julie Ottoy and Laurens Tembuyser, because they always make me laugh and look at the bright side of life.

Special thanks go to my mom and grandma, who had to bear with my bad mood sometimes and who excused me from many home chores, often to the annoyance of my sister Lisa. Sorry Lisa, I will make it up to you! Furthermore, every evening after working at the CMM, a lovely diner awaited me at home thanks to my wonderful mom and grandma.

Last but not least, I must thank my boyfriend Matthias for helping me whenever I messed up with my LaTeX file. Believe me, I managed to mess up a lot! I appreciate the effort you put in fixing my python scripts more than once. I apologize for all times I canceled on our dates due to my thesis and I thank you for all times you cheered me up when I was down. With the words of Tina Turner: "You're simply the best"!

First principles molecular dynamics study of the influence of acid strength on MTO conversion in H-SAPO-5 and H-SSZ-24

Margot Matton

Master's dissertation submitted in order to obtain the academic degree of
Master of Science in Chemical Engineering
Academic year 2014–2015
Supervisors: prof. dr. ir. Veronique Van Speybroeck, prof. dr. ir. Karen Hemelsoet
Counsellors: dr. ir. Kristof De Wispelaere, dr. ir. Jeroen Van der Mynsbrugge

Faculty of Engineering and Architecture – Ghent University

Center for Molecular Modeling

Abstract

The methanol-to-olefin (MTO) process has gained a lot of attention as promising alternative for crude oil as olefin feedstock. The zeolitic acid strength is an important factor to regulate the product selectivities within this process, since the MTO process proceeds over a zeolite or zeotype acid catalyst. In this master thesis, the influence of the zeolitic acid strength was investigated in the AFI structured materials, H-SAPO-5 and H-SSZ-24 by focusing on the crucial methylation of aromatics by methanol, dimethyl ether (DME) and framework-bound methoxides. In a molecular dynamics (MD) study of the co-adsorption complexes, two reactivity indices were defined in terms of probabilities. The probability of pre-reactive complex formation suggests that DME is more reactive than methanol towards methylation. The protonation probabilities for both methanol and DME were the highest in the most acidic catalyst, H-SSZ-24. The probability of pre-reactive complex formation with a framework-bound methoxide as the methylating agent generally increased with the number of methyl groups on the aromatics. Furthermore, this probability was found to be also higher in H-SSZ-24. Metadynamics (MTD) simulations revealed lower free energy barriers for the methylation reaction of toluene at relevant MTO conditions in the more acidic H-SSZ-24 compared to H-SAPO-5. During these MTD simulations, only the concerted methylation mechanism was sampled for methanol in both catalysts, whereas for DME the first step of the stepwise methylation mechanism was also sampled in H-SSZ-24. Thus, next to the acid strength, the involved methylating agent was also found to influence the methylation mechanism.

Keywords: MTO, methylation reactions, Brønsted acid strength, zeolites, DFT, molecular dynamics, metadynamics

First principles molecular dynamics study of the influence of acid strength on the MTO conversion in H-SAPO-5 and H-SSZ-24

Margot Matton

Supervisor(s): prof. dr. ir. Veronique Van Speybroeck and prof. dr. ir. Karen Hemelsoet
Counsellor(s): dr. ir. Kristof De Wispelaere and dr. ir. Jeroen Van der Mynsbrugge

Abstract— **The influence of the zeolitic acid strength on the methanol-to-olefin (MTO) conversion is investigated in two AFI materials: H-SAPO-5 and H-SSZ-24. The MTO process over a Brønsted acid zeolite or zeotype catalyst is typically co-catalyzed by hydrocarbon pool (HP) species. This master thesis focuses on the methylation reactions of aromatics by methanol, dimethyl ether (DME) and framework-bound methoxides, since these reactions play a crucial role in the HP mechanism. A molecular dynamics (MD) study of the co-adsorption complexes revealed that the methylating agents are preferentially located on the acid site. However, for o-xylene and methanol competition for the acid site is observed. The probability of pre-reactive complex formation for methanol and DME indicates that DME appears to be more reactive towards methylation. Furthermore, the protonation probability of methanol and DME is higher in H-SSZ-24 than in H-SAPO-5. During the MD simulations, the probability of the pre-reactive complex formation with a framework-bound methoxide as the methylating agent generally increases with the number of methyl groups on the aromatics. Lower free energy barriers were retrieved from the metadynamics (MTD) simulation of the methylation reaction of toluene at relevant MTO conditions for the more acidic H-SSZ-24 compared to H-SAPO-5. During these MTD simulations, the first step of the stepwise methylation mechanism, the formation of a framework-bound methoxide, was sampled when using DME as the methylating agent in H-SSZ-24, while only the concerted mechanism was observed for methanol in H-SSZ-24 and H-SAPO-5. Thus, not only the acid strength can influence the methylation mechanism, but also the involved methylating agent.**

Keywords— **MTO, methylation reactions, Brønsted acid strength, zeolites, DFT, molecular dynamics, metadynamics**

I. Introduction

RECENTLY, the methanol-to-olefin (MTO) process gained a lot of attention as result of the upcoming depletion of crude oil resources, while the world population keeps expanding and the need for consumer goods, primarily made from polymers, increases as well. Olefins lie at the basis of this polymer production and form the building blocks of the chemical industry. Therefore, the demand for olefins such as ethylene and propylene keeps rising and the crude oil feedstock will no longer be able to meet that demand in the near future [1]. Nowadays, olefins are mainly obtained from naphta, but the MTO process provides a promising alternative route starting from methanol.

M. Matton is with the Center of Molecular Modeling, Ghent University (UGent), Gent, Belgium. E-mail: Margot.Matton@UGent.be .

MTO conversion proceeds over zeolite or zeotype catalysts. Their ability to catalyze the MTO reactions is attributed to the presence of Brønsted acid sites. Several mechanisms have been proposed in the past [2]. First, it was believed that olefins were produced through direct coupling of intermediate C_1 species [3]. However, it soon became clear that not only the Brønsted acid sites are needed to catalyze MTO conversion: the reactions were found to be co-catalyzed by hydrocarbon pool (HP) species [4], [5]. The HP mechanism became generally excepted.

Two types of HP species can be distinguished: aromatic and aliphatic HP species. This has led to the proposal of the dual cycle mechanism containing an arene and alkene cycle as seen in Figure 1. However, the arene and alkene cycle do not always operate simultaneously inside the zeolitic material. In H-SSZ-24 the aromatic HP species are dominant, while in H-SAPO-5 the aliphatic HP species are the most active HP species [6]. Both H-SSZ-24 and H-SAPO-5 have an AFI topology, meaning that they consist of 12-ring 1D channels, but the Brønsted acid sites in H-SSZ-24 possess a higher acid strength than in H-SAPO-5. Thus, the comparison of these two isostructural zeolitic catalysts reveals that the acid strength regulates the HP species' reactivity and can shift the equilibrium to the arene or alkene cycle. H-SAPO-5 and H-SSZ-24 are ideal catalysts to elucidate the influence of acid strength in the MTO process. Although they both lack of industrial MTO applications, they are excellent for experimental tests, since their topology with large 1D channels allows feeding of bulky aromatic species. During an MTO experiment, the product contained much more paraffinic and aromatic products in H-SSZ-24 due to higher acid strength compared to H-SAPO-5 [6]. Moreover, methylation reactions proceeded faster in H-SSZ-24 than in H-SAPO-5. The methylation rate for benzene appeared to be higher than the rate for propylene in H-SSZ-24, while in H-SAPO-5 these rates were similar [7].

In both the arene and alkene cycle, methylation reactions are

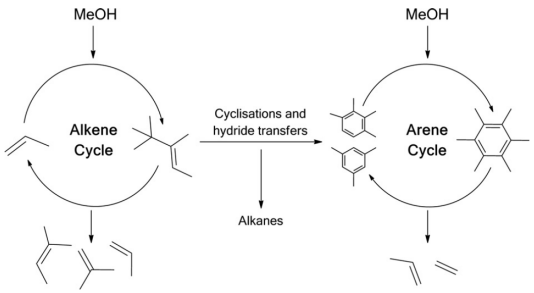

Fig. 1: Dual cycle mechanism. Taken from [8].

of utmost importance. For these methylation reactions a concerted and a stepwise mechanism have been proposed. During the stepwise route methanol or DME, the so-called methylating agent, is converted into a framework-bound methoxide, hereby releasing water or methanol respectively and subsequently this methoxide will methylate the HP species. During the concerted mechanism methanol or DME get protonated by the acid site and directly methylate the HP species and simultaneously release water or methanol respectively. Depending on the operating conditions, one of the two mechanisms is dominant [9], [10]. At high temperatures and low pressures the stepwise route becomes the most active, since this route exhibits smaller transition states with higher enthalpy and entropy [9]. Furthermore, the intermediate release of water or methanol results in a smaller enthalpy loss for this stepwise route [10].

To get insight in the effect of acid strength, theoretical modeling is used in this thesis. In contrast to experiments, first principles calculations can provide information on individual reaction steps of the MTO mechanism. In this master thesis, the first steps of the arene cycle are modeled in two AFI catalysts (H-SAPO-5 and H-SSZ-24): the methylation reactions of benzene, toluene and o-xylene by several methylating agents (methanol, DME and framework-bound methoxides) as shown in Figure 2.

II. Theoretical methods

Both H-SAPO-5 and H-SSZ-24 are represented by a periodic model with a 1x1x2 supercell. In both models, the acid site density is the same: the (Al+P)/Si ratio in H-SAPO-5 and the Si/Al ratio in H-SSZ-24 equal 47. In all simulations, the revPBE functional is used and D3 corrections are applied to include long-range Van der Waals interactions. The DZVP-GTH basisset and GTH pseudopotentials are used. All calculations are performed with the CP2K package [11].

To characterize the zeolitic acid site strength of the periodic models, static calculations were performed at 0 K. To model the adsorption and co-adsorption behavior of all species from Figure 2, MD simulations were performed in the NPT ensemble at

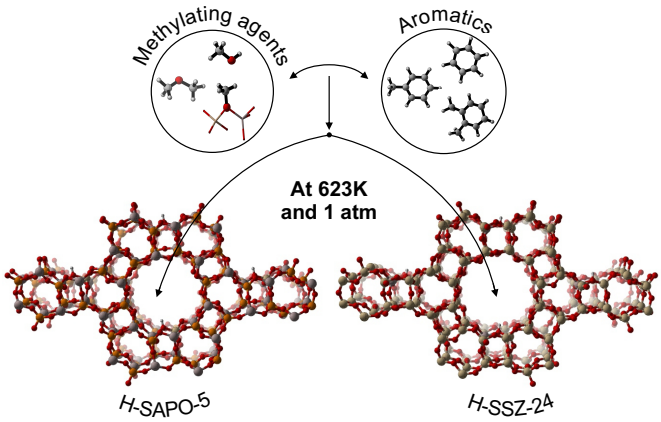

Fig. 2: Several MD simulations of aromatics (benzene, toluene and o-xylene) and methylating agents (methanol, DME and a framework-bound methoxide) are performed in both H-SAPO-5 and H-SSZ-24 at 623 K and 1 atm.

623 K and 1 atm. Subsequently, MTD simulations were executed in the NVT ensemble at 623 K and with the average volume and cell parameters taken from the NPT MD simulations to retrieve free energy barriers for the stepwise and concerted methylation reactions. Three collective variables (CVs) were used as described in ref. [12]: one CV to describe the coordination number for the CO bond(s) in the methylating agents, one CV for the coordination number from the C atom(s) of the methylating agent to the 6 C atoms of the aromatic ring of toluene and finally one CV for the coordination number from the C atom(s) of the methylating agent to the 4 framework O atoms surrounding the substitutional defect. This last CV tracks the formation of a framework-bound methoxide.

III. Results and Discussion

A. Acid strength characterization in H-SAPO-5 and H-SSZ-24

Static calculations were performed to characterize the zeolitic acid strength from the OH frequency shift upon CO adsorption in H-SAPO-5 and H-SSZ-24. The experimental shifts are equal to -265 cm^{-1} and -317 cm^{-1} in H-SAPO-5 and H-SSZ-24 respectively [6]. Via normal mode analysis (NMA) based on the static calculations, the frequency shifts upon CO adsorption are obtained which may be compared to the infrared (IR) data. A shift of -358 cm^{-1} was found in H-SAPO-5 and a shift of -406 cm^{-1} in H-SSZ-24. The obtained shifts in the OH stretching frequencies indicate that the model for H-SSZ-24 is indeed more acidic than the model for H-SAPO-5. However, the theoretical shifts differ from the experimental IR frequencies by approximately 100 cm^{-1}, which may be due to the lack of anharmonic effects, temperature effects and level of theory approximations.

It is important to emphasize that solid acid strength characterization is not straightforward and no uniform scale is yet available to describe the acid strength on a first principles basis. However, Arean et al. suggest that the enthalpy change upon CO adsorption is a good indicator for the zeolitic acid strength [13].

B. Adsorption and co-adsorption of aromatics and methylating agents in H-SAPO-5 and H-SSZ-24

The effect of co-adsorption on the behavior of the guest molecules in both H-SAPO-5 and H-SSZ-24 was studied. For methanol the addition of an aromatic, barely influenced its distance to the Brønsted acid site in the most acidic material, H-SSZ-24. However in H-SAPO-5, the methylating agent was pushed closer the acid site by the aromatics. Due to the lower acid strength of H-SAPO-5, the interaction between the methylating agent and Brønsted acid site was weaker and hence the distance to the acid site was also larger than for single adsorption of methanol in H-SSZ-24. Generally, the distance of the aromatics to the acid site increased upon adding the methylating agent, because the methylating agent would preferentially be located at the acid site with the aromatics co-adsorbed. This is the result of their capability of forming a hydrogen bond leading to a strong H bridge between the methanol's O atom and the acidic proton of the framework.

Although the methylating agent is preferentially located on the acid site, the study of the co-adsorption behavior of o-xylene and methanol, revealed competitive adsorption between o-xylene and methanol in both AFI materials. Thus, o-xylene may remain on the acid site in the presence of methanol. This competition may result in less favorable geometries for the methylation of o-xylene and therefore, o-xylene might posses a lower reactivity towards methylation reactions. However, this needs to be confirmed through MTD simulations (vide infra).

Next, a detailed analysis of the aromatic's orientation inside the large pores was performed. Overall, the aromatic's orientation can be divided into three cases, as indicated in Figure 3. The aromatic lies flat on the Brønsted acid site for case (1) and stands upright for cases (2) and (3). In the former, the aromatic faces the wall of the AFI channel (2) and in the latter, the aromatic is directed to the channel's end (3). Two effects of co-adsorption on the orientation of the aromatics inside the channel were observed. Firstly, addition of methanol and DME to the channel lowered the probability of case (1) for toluene and o-xylene compared to single adsorption of toluene and o-xylene. Secondly, occupying the acid site with a framework-bound methoxide resulted in a similar probability of case (1) as for single adsorption of toluene and o-xylene. These trend were observed in both materials. Thus, the acid strength had no substantial effect on the orientation of the aromatics. Furthermore, the upright position in which benzene is faced to the channel end, such as in case (3), appears to be preferred in both materials, while toluene and o-xylene seldom adopt this orientation and favor the flat orientation (case (1)).

Lastly, the probability of forming a pre-reactive complex and the protonation probability of the methylating agents was tracked throughout the MD simulations by defining two reactivity indices. The first index describes that a complex with a favorable orientation for methylation is obtained when methanol or DME are directed towards the aromatic ring with their C atom(s) instead of their O atom. The second reactivity index accounts for the fact that the methylating agent must be protonated to attack the aromatic during a methylation reaction.

Figure 4 shows that there is a clear clustering of the results for H-SAPO-5 and H-SSZ-24. The formation of properly oriented pre-reactive complexes is over two times higher for DME than for methanol in both H-SAPO-5 and H-SSZ-24, as indicated on Figure 4. Moreover, the protonation probabilities are higher for DME. Thus, DME is more reactive towards methylation of aromatics than methanol. Protonation probabilities are also higher in the more acidic material H-SSZ-24. Hence, the protonation probabilities are directly correlated with the acid strength of the catalyst. The type of aromatic has a subtle effect on both prob-

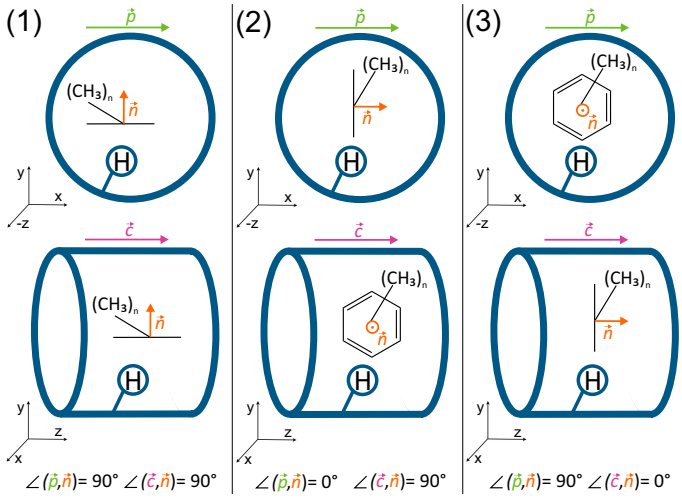

Fig. 3: Schematic representation of three orientations of an aromatic in the AFI channel (represented in blue): the aromatic lies flat with respect to the acid site (1), the aromatic stands upright with respect to the acid site while faced to the channel wall (2) and the aromatic stands upright with respect to the acid site while faced to the channel end (3). The orange vector $\vec{n}$ represents the normal to the aromatic plane. The green $\vec{p}$ and purple $\vec{c}$ vector are characteristics of the channel itself.

abilities in Figure 4, but the chosen reactivity indices were not able to discern a clear trend for the influence of the aromatics.

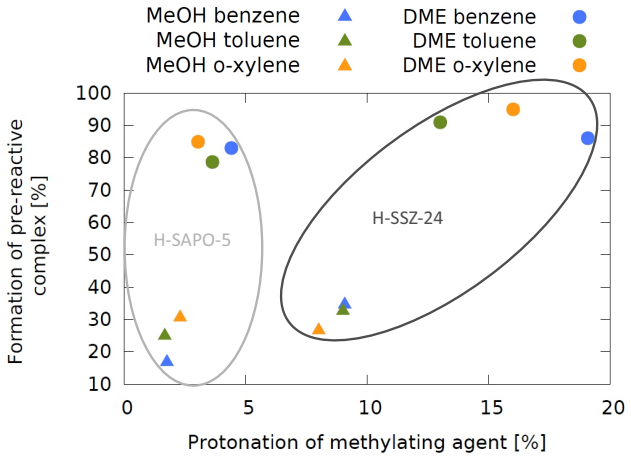

Fig. 4: Probability of forming a pre-reactive complex as function of the protonation probability of the methylating agent in H-SAPO-5 and H-SSZ-24.

When considering a framework-bound methoxide as the methylating agent, the probability of forming a pre-reactive complex was assessed based on the distance of the C atom of the methoxide to the C atoms of the aromatic ring. Figure 5 shows that the interaction between the methoxide and the HP species increases with the number of methyl substituents on the aromatic ring in both H-SAPO-5 and H-SSZ-24. However, the trend does not seem to apply to o-xylene in H-SSZ-24. Moreover, this increasing trend was not obtained for methanol and DME as methylating agent.

C. Reactivity towards methylation of aromatics in H-SAPO-5 and H-SSZ-24

To truly quantify the difference in reactivity between the three methylating agents and between H-SAPO-5 and H-SSZ-24, MTD simulations were performed focusing on the toluene methylation reaction as a case study. MTD can take into account a vast range of reaction paths between the reactant and product valley and thus account for the complexity of the free energy profiles. This is especially necessary for the considered AFI topology because the large channels allow high mobility of the guest molecules resulting in poorly defined reactant, transition state and product regions on the free energy surface.

During the simulations, the methylation barrier was crossed multiple times, but transition states were always geometrically different. Figure 6 shows two configurations around the transition state for the methylation at the ortho position on toluene in H-SAPO-5.

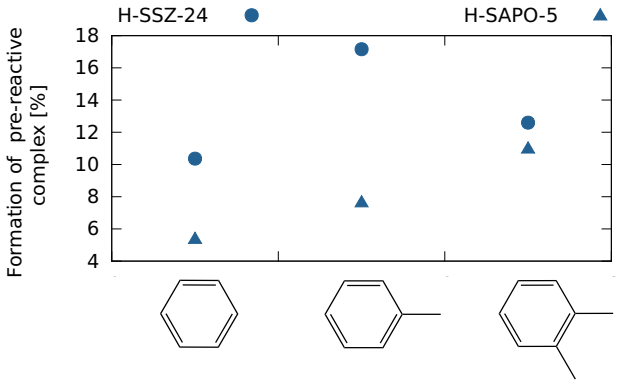

Fig. 5: Probability in H-SAPO-5 (triangles) and in H-SSZ-24 (circles) of finding geometries in which the shortest distance from the carbon atoms of the aromatic (benzene, toluene, o-xylene) to the C atom of the framework bound methoxide is lower than 3.5 Å.

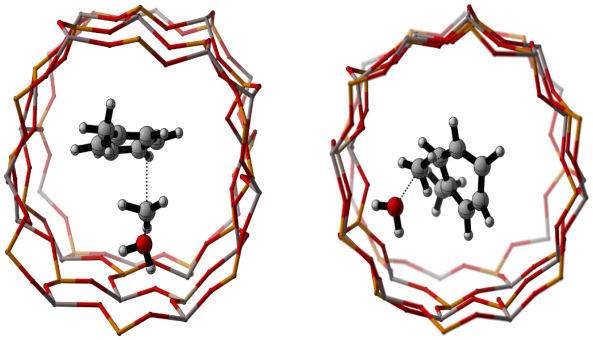

Fig. 6: Different configurations around the transition state for the methylation of toluene at the ortho position observed during the MTD simulation with methanol as methylating in H-SAPO-5 at 623 K.

Although the methyl group in toluene is an ortho/para director, transition states for the meta methylation were observed in both catalysts. In both catalysts the meta transition state corresponded to a geometry as shown by case (3) in Figure 3. This meta transition state benefits from the stabilizing interaction with the negatively charged framework, when standing upright. The meta product was even seen in H-SSZ-24 before any ortho or para product for an attack performed by DME as methylating agent. A configuration around the meta transition state is shown in Figure 7 along with a configuration close to the methylation transition state at the para position in H-SSZ-24. The ortho transition state was not observed for DME as methylating agent. This reaction probably suffers from steric hindrance. This might explain why a meta attack is observed, since it fol-

TABLE I: Free energy barrier $\Delta G^{\ddagger}$ for a methylation reaction via the converted pathway in H-SAPO-5 and H-SSZ-24 with methanol and DME as methylating agent for toluene at 623 K and 1 atm.

Methylating agent	Catalyst	$\Delta G^{\ddagger}_{\text{concerted}}$ [kJ/mol]
Methanol	H-SAPO-5	99
Methanol	H-SSZ-24	90
DME	H-SSZ-24	91

lows from a failed ortho attack.

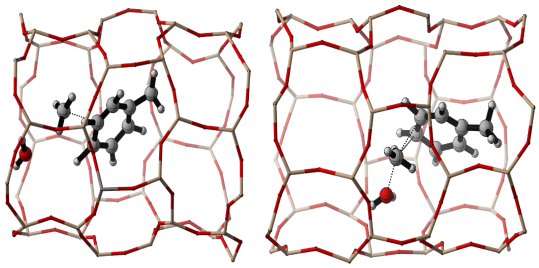

Fig. 7: Different configurations around the transition state for the methylation of toluene at the meta (left) and para (right) position observed during the MTD simulation with methanol as methylating in H-SSZ-24 at 623 K.

These simulations confirm the predictions made based on the MD simulations: the more acidic material, H-SSZ-24, shows a higher reactivity for methylation reactions during MTO conversion. The calculated free energy barriers for the methylation of toluene by methanol or DME indeed show that H-SSZ-24 is more reactive. The barriers are summed up in Table I for the concerted methylation reactions. De Wispelaere et al. reported the free energy barrier in H-SSZ-24 for the concerted methylation of benzene in the presence of two methanol molecules. A value of $138\,\mathrm{kJ\,mol^{-1}}$ was found there [12]. At first sight, toluene appears to be methylated much more easily than benzene. This was already reported for H-ZSM-5 [14] and CHA catalysts [15]. However, the barriers reported in Table I must be treated with caution, since they might not be fully converged due to the low number of recrossings of the methylation barrier.

Finally, only the first step of the stepwise methylation mechanism was observed during the MTD runs, namely the formation of a framework-bound methoxide. Furthermore, this is only observed for DME as methylating agent. The free energy barrier for the formation of a framework-bound methoxide from DME in H-SSZ-24 equals $92\,\mathrm{kJ\,mol^{-1}}$. The first step of the stepwise mechanism is believed to be the rate determining step. This means the concerted and stepwise mechanism are competitive under the studied MTO conditions, since the free energy barriers are similar.

IV. Conclusion and Outlook

In this master thesis the influence of zeolitic acid strength on the MTO conversion was investigated by comparing methylation reactions of benzene, toluene and o-xylene, in two isostructural catalysts with different acid strength, H-SAPO-5 and H-SSZ-224. The study of the adsorption and co-adsorption complexes via MD simulations revealed that the probability of finding pre-reactive complexes was substantially higher for DME as methylating agent than for methanol. The number of methyl groups on the aromatic ring did not seem to influence this probability for DME and methanol, whereas for a framework-bound methoxide this probability seemed to increase with the number of methyl groups. Furthermore protonation probabilities for methanol and DME were the highest in more acidic material, H-SSZ-24. The probability for pre-reactive complex formation with methoxide also increased due to the higher acid strength of H-SSZ-24. Through MTD simulations, free energy barriers were obtained for the methylation reaction of toluene inside H-SAPO-5 and H-SSZ-24. As expected, H-SSZ-24 shows a higher reactivity towards methylation than H-SAPO-5. Comparison of DME and methanol as methylating agents revealed that the stepwise methylation mechanism might become important for DME in H-SSZ-24 rather than for methanol.

Both MD and MTD can be considered valuable tools to attain insight into the MTO mechanism and the role of zeolitic acid strength. Further investigation of methylation reactions is recommended for other HP species, such as more bulky aromatics or aliphatic HP species. Moreover, MTD simulations of other types of reactions that occur during paring and side-chain mechanism and the alkene cracking reactions might be useful to obtain a thorough understanding of the influence of zeolitic acid strength on the MTO conversion.

Acknowledgments

The computational resources (Stevin Supercomputer Infrastructure) and services used in this work were provided by the VSC (Flemish Supercomputer Center), funded by Ghent University, the Hercules Foundation and the Flemish Government — department EWI.

References

[1] John Q. Chen, Andrea Bozzano, Bryan Glover, Terje Fuglerud, and Steinar Kvisle, "Recent advancements in ethylene and propylene production using the UOP/Hydro MTO process," *Catalysis Today*, vol. 106, no. 1–4, pp. 103–107, Oct. 2005.

[2] Karen Hemelsoet, Jeroen Van der Mynsbrugge, Kristof De Wispelaere, Michel Waroquier, and Veronique Van Speybroeck, "Unraveling the Re-

action Mechanisms Governing Methanol-to-Olefins Catalysis by Theory and Experiment," *ChemPhysChem*, vol. 14, no. 8, pp. 1526–1545, June 2013.

[3] Michael Stöcker, "Methanol-to-hydrocarbons: catalytic materials and their behavior," *Microporous and Mesoporous Materials*, vol. 29, no. 1–2, pp. 3–48, June 1999.

[4] Im Dahl and S. Kolboe, "On the Reaction-Mechanism for Propene Formation in the Mto Reaction Over Sapo-34," *Catal. Lett.*, vol. 20, no. 3-4, pp. 329–336, 1993, WOS:A1993LU35400017.

[5] I. M. Dahl and S. Kolboe, "On the Reaction Mechanism for Hydrocarbon Formation from Methanol over SAPO-34: I. Isotopic Labeling Studies of the Co-Reaction of Ethene and Methanol," *Journal of Catalysis*, vol. 149, no. 2, pp. 458–464, Oct. 1994.

[6] Marius Westgård Erichsen, Stian Svelle, and Unni Olsbye, "The influence of catalyst acid strength on the methanol to hydrocarbons (MTH) reaction," *Catalysis Today*, vol. 215, pp. 216–223, Oct. 2013.

[7] Marius Westgård Erichsen, Kristof De Wispelaere, Karen Hemelsoet, Samuel L. C. Moors, Thomas Deconinck, Michel Waroquier, Stian Svelle, Veronique Van Speybroeck, and Unni Olsbye, "How zeolitic acid strength and composition alter the reactivity of alkenes and aromatics towards methanol," *Journal of Catalysis*, vol. 328, pp. 186–196, Aug. 2015.

[8] Marius Westgård Erichsen, Stian Svelle, and Unni Olsbye, "H-SAPO-5 as methanol-to-olefins (MTO) model catalyst: Towards elucidating the effects of acid strength," *Journal of Catalysis*, vol. 298, pp. 94–101, Feb. 2013.

[9] Andrew J. Jones and Enrique Iglesia, "Kinetic, Spectroscopic, and Theoretical Assessment of Associative and Dissociative Methanol Dehydration Routes in Zeolites," *Angew. Chem. Int. Ed.*, vol. 53, no. 45, pp. 12177–12181, Nov. 2014.

[10] Rasmus Y. Brogaard, Reynald Henry, Yves Schuurman, Andrew J. Medford, Poul Georg Moses, Pablo Beato, Stian Svelle, Jens K. Nørskov, and Unni Olsbye, "Methanol-to-hydrocarbons conversion: The alkene methylation pathway," *Journal of Catalysis*, vol. 314, pp. 159–169, May 2014.

[11] S. Goedecker, M. Teter, and J. Hutter, "Separable dual-space Gaussian pseudopotentials," *Phys. Rev. B*, vol. 54, no. 3, pp. 1703–1710, July 1996.

[12] Kristof De Wispelaere, Bernd Ensing, An Ghysels, Evert Jan Meijer, and Veronique Van Speybroeck, "Complex Reaction Environments and Competing Reaction Mechanisms in Zeolite Catalysis: Insights from Advanced Molecular Dynamics," *Chem. Eur. J.*, vol. 21, no. 26, pp. 9385–9396, June 2015.

[13] Carlos O. Arean, Montserrat R. Delgado, Petr Nachtigall, Ho Viet Thang, Miroslav Rubeš, Roman Bulánek, and Pavla Chlubná-Eliášová, "Measuring the Brønsted acid strength of zeolites–does it correlate with the O-H frequency shift probed by a weak base?," *Phys Chem Chem Phys*, vol. 16, no. 21, pp. 10129–10141, June 2014.

[14] David Lesthaeghe, Veronique Van Speybroeck, and Michel Waroquier, "Theoretical evaluation of zeolite confinement effects on the reactivity of bulky intermediates," *Phys. Chem. Chem. Phys.*, vol. 11, no. 26, pp. 5222–5226, June 2009.

[15] Veronique Van Speybroeck, Karen Hemelsoet, Kristof De Wispelaere, Qingyun Qian, Jeroen Van der Mynsbrugge, Bart De Sterck, Bert M. Weckhuysen, and Michel Waroquier, "Mechanistic Studies on Chabazite-Type Methanol-to-Olefin Catalysts: Insights from Time-Resolved UV/Vis Microspectroscopy Combined with Theoretical Simulations," *ChemCatChem*, vol. 5, no. 1, pp. 173–184, Jan. 2013.

Contents

List of Abbreviations

AMBER	Assisted model building with energy refinement
AO	Atomic orbital
CC	Coupled cluster
CHA	Chabazite
CHARM	Chemistry at harvard macromolecular mechanics
CGF	Contrated Gaussian basis function
CN	Coordination number
CV	Collective variable
CSVR	Canonical sampling through velocity rescaling
DFT	Density functional theory
DME	Dimethyl ether
DZVP	Double-zeta valence polarized
BEEF-vdW	Bayesian error estimation functional with Van der Waals correlation
FCC	Fluid Catalytic Cracker
FES	Free energy surface
FT	Fischer-Tropsch
GGA	Generalized gradient approximation
GPW	Gaussian and plane wave
GTF	Gaussian type function
GTH	Goedecker Teter Hutter
GTO	Gaussian type orbital
GROMOS	Groningen molecular simulation
HF	Hartree-Fock
HMB	Hexamethylbenzene
HP	Hydrocarbon pool
H MAS NMR	Proton magic angle spinning nuclear magnetic resonance
IR	Infrared
IZA-SC	International zeolite association structure commission
KS	Köhn Sham
LDA	Local density approximation
LFEP	Lowest free energy path
LPG	Liquefied petroleum gas
LSD	Local spin density approximation
LYP	Lee Yang Parr

MD	Molecular dynamics
MM	Molecular mechanics
MTD	Metadynamics
MTG	Methanol-to-gasoline
MTH	Methanol-to-hydrocarbons
MTO	Methanol-to-olefins
MTP	Methanol-to-propylene
NG	Natural gas
NMA	Normal mode analysis
ONIOM	Our own n-layered integrated molecular orbital and molecular mechanics
PES	Potential energy surface
PMB	polymethylbenzene
PW	Perdew Wang
QM	Quantum mechanics
revPBE	revised Perdew Burke Ernzerhof
RPA	Random gas approximation
SAPO	Silicoaluminumphosphate
STO	Slater type orbital
syngas	Synthesis gas
TPD	Temperature programmed desorption
TS	Transition state
TST	Transition state theory
USD	United States dollar
vdW-DF	non-local Van der Waals functional
VPS	Velocity power spectrum

List of symbols

α, β, γ	$^\circ$	cell angles
δ_s		Width of the Gaussian hills
$\Delta \mathrm{E}_0^\ddagger$	kJ mol^{-1}	Forward reaction barrier
$\Delta \mathrm{E}_r$	kJ mol^{-1}	Reaction energy
$\Delta \mathrm{G}^\ddagger$	kJ mol^{-1}	Free energy barrier
$\Delta \mathrm{G}_{app}^\ddagger$	kJ mol^{-1}	Apparent free energy barrier
$\Delta \mathrm{G}_{int}^\ddagger$	kJ mol^{-1}	Intrinsic free energy barrier
$\Delta \mathrm{H}_{app}^\ddagger$	kJ mol^{-1}	Apparent enthalpy barrier
$\Delta \mathrm{H}_{int}^\ddagger$	kJ mol^{-1}	Intrinsic enthalpy barrier
$\Delta_r H$	kJ mol^{-1}	Reaction enthalpy
G	kJ mol^{-1}	Free energy
$\Delta\nu$	cm^{-1}	Stretching frequency shift
$\Delta\omega$	cm^{-1}	Error in the ω/r method
ϵ		Dielectric constant
ϵ_x	kJ mol^{-1}	Exact exchange energy
ω	kJ mol^{-1}	Height of the Gaussian hills
ρ		Energy density
ϕ_i		Unoccupied level i
Φ		wave function
ν	cm^{-1}	stretching frequency
ν_{CO}	cm^{-1}	CO stretching frequency upon CO adsorption
τ		non-interacting kinetic energy density
τ_G	s	Time interval between Gaussian hills
$a(i)$	m s^{-1}	Acceleration of atom i
$\vec{c}$		Vector aligned with the length of the AFI channel
C		Dispersion coefficient
d(CO)	Å	Average CO bond length
d(OH)	Å	Average OH bond length
E	J mol^{-1}	Energy
$E^{(2)}$	kJ mol^{-1}	Two-body contribution to the energy
$E^{(3)}$	kJ mol^{-1}	Three-body contribution to the energy
E_a	kJ mol^{-1}	Activeringsenergie
E_{DFT}	kJ mol^{-1}	Energy from DFT calculations

$E_{\text{DFT-D3}}$	kJ mol^{-1}	Energy after D3 Grimme corrections
E_{disp}	kJ mol^{-1}	Correction for the dispersion energy
$E_{xc}[\rho]$		Exchange-correlation functional
F	N	Force
$\hat{H}$	kJ mol^{-1}	Hamiltonian
h	J s	Planck constant
I_{VPS}		Intensity of VPS
k_app	s^{-1}	Apparent rate coefficient
k_B	J K^{-1}	Boltzmann constant
$\vec{n}$		Normal vector of the aromtic plane
nCV		Number of collective variables
N		Total number of atoms
$\vec{p}$		Vector aligned with the broadness of the AFI channel
p_i	bar	Partial pressure of species i
R	J mol^{-1} K^{-1}	Universal gas constant
r_0	Å	Reference distance
r_{ij}	Å	distance from atom i to atom j
s		coordinates along the lowest free energy path
$S(x(t))$		A function of the coordinates with trajectory x at time t
T	K	Temperature
$\hat{T}$	kJ mol^{-1}	Kinetic energy
$\hat{T}_e$	kJ mol^{-1}	Electron contribution to the kinetic energy
$\hat{T}_n$	kJ mol^{-1}	Nuclei contribution to the kinetic energy
$v_{i,\alpha}(t)$		Time dependent velocity of atom i in direction α
$\hat{V}$	kJ mol^{-1}	Potential energy
$\hat{V}_ee$	kJ mol^{-1}	Electron-electron contribution to the potential energy
$\hat{V}_ne$	kJ mol^{-1}	Nuclear-electron contribution to the potential energy
$\hat{V}_nn$	kJ mol^{-1}	Nuclear-nuclear contribution to the potential energy
V_G	kJ mol^{-1}	Sum of Gaussian Potential

Chapter 1

Introduction

The growing global demand for oil and more generally for energy has a significant influence on the availability and pricing of traditional feedstocks for light olefin production. Today, ethylene is mainly produced from naphtha, which is an important crude oil fraction. Starting from the two oil crises in 1973 and 1979, crude oil prices have gone up severely. In July 2008 the highest price was reached with 145 USD/barrel for crude oil as indicated in Figure 1.1.

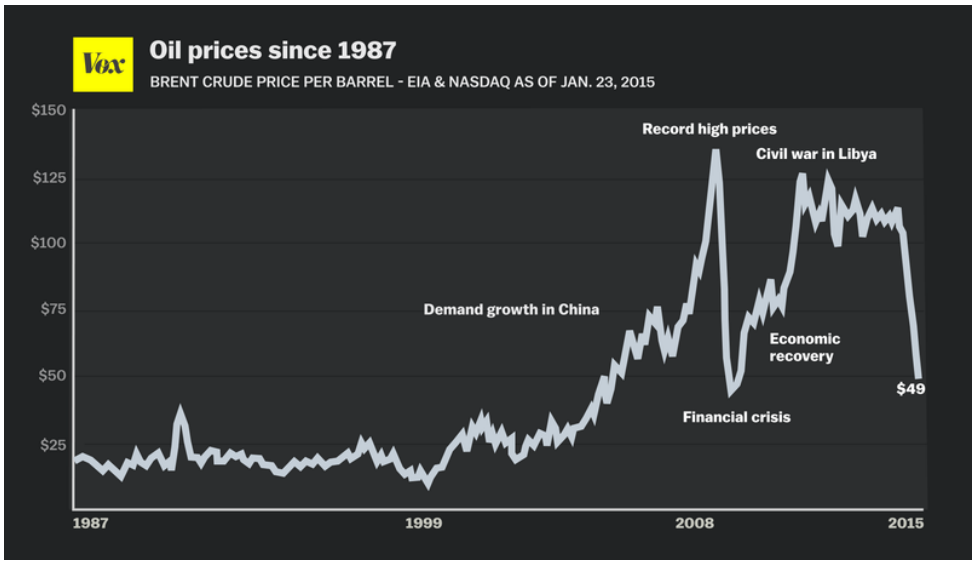

Figure 1.1: Crude oil price development until 2015 [1].

However, very recently the price of crude oil went into a free fall. This free fall is attributed to an excess capacity. Non-OPEC countries have been supplying the oil market, while the American economy is shifting towards cheaper shale gas and oil [2] as energy feedstock, decreasing the crude oil export to the United States [1], [3], [4]. Furthermore, the OPEC countries refuse to cut back their oil production, leading to a higher supply than demand as seen in Figure 1.2 [1].

On the other hand, the oil reserves are depleting and most of the remaining reserves are located in the Middle East and in other politically sensitive areas, which leads to an uncertain availability of crude oil [5]. This is a rising concern because the world population is growing and living

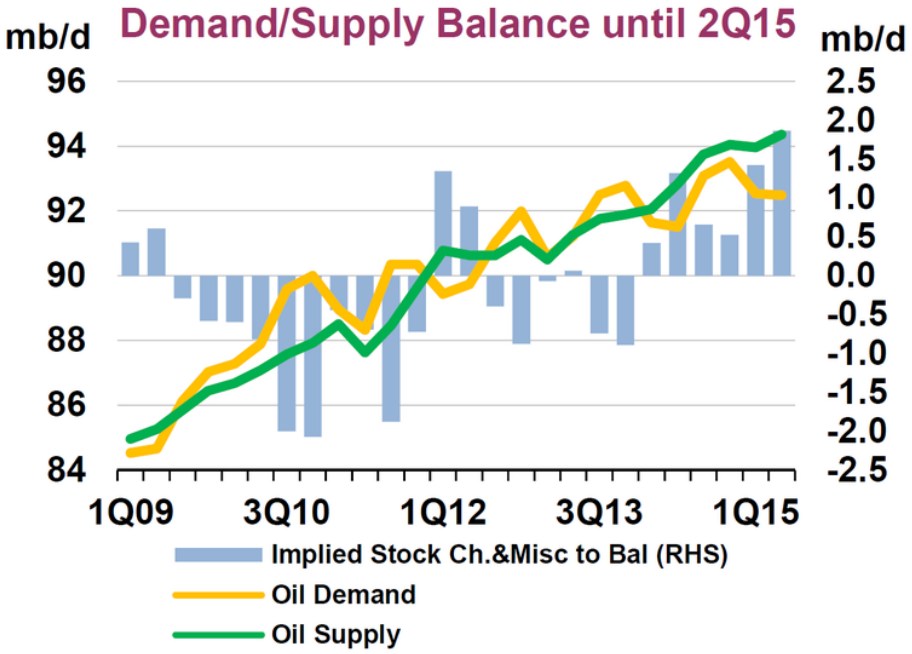

Figure 1.2: Crude oil supply and demand from the first quarter of 2009 to the first quarter of 2015 [1].

standards are increasing. This has led to the unset of the search for alternative feedstocks.

Specifically, the need for consumer goods increases and with it the worldwide demand for ethylene and propylene [6]. Polypropylene production is responsible for the consumption of 60 % of the propylene supply. The annual growth in the demand for polypropylene keeps increasing, among other things because polypropylene is increasingly used as a replacement for wood, steel, paper... This rise will be reflected in the demand for propylene as well. It is expected that for the next two decades the propylene demand will rise at least with 4.5 % each year [7]. Due to the rising demand for propylene, a growing gap is expected between its production and consumption as shown in Figure 1.3 [6]. Besides the disadvantageous dependence on crude oil, the production of ethylene and propylene from naphtha and gas oil crackers is also limited by a propylene-to-ethylene ratio ranging from 0.53 to 0.65 [8]. Therefore a growing need has developed for alternative feedstocks and technologies that favor higher ratios of propylene-to-ethylene production. Natural gas (NG), biomass and coal are seen as alternative feedstocks for the production of petrochemicals.

While a direct route to olefins from these alternative feedstocks is not yet feasible, technology for the production of olefins from methanol is available and practiced today. Methanol can be easily obtained from these alternative feedstock through an intermediate, called synthesis gas (syngas). The methanol-to-olefin process opens up new horizons for a segregated gas-to-olefins chain [6], since syngas, a mixture of CO and H_2 (*vide infra*), can be used to produce methanol. Technology for the production of methanol from syngas is readily available and can be coupled to an MTO plant. This syngas can be produced from just about any gasifiable hydrocarbon material, such as NG, coal, biomass, heavy residues... Therefore, it can provide an indirect route from alternative feedstocks like NG and biomass towards olefins. This contributes in a positive way to the less crude oil dependent chemical industry of tomorrow.

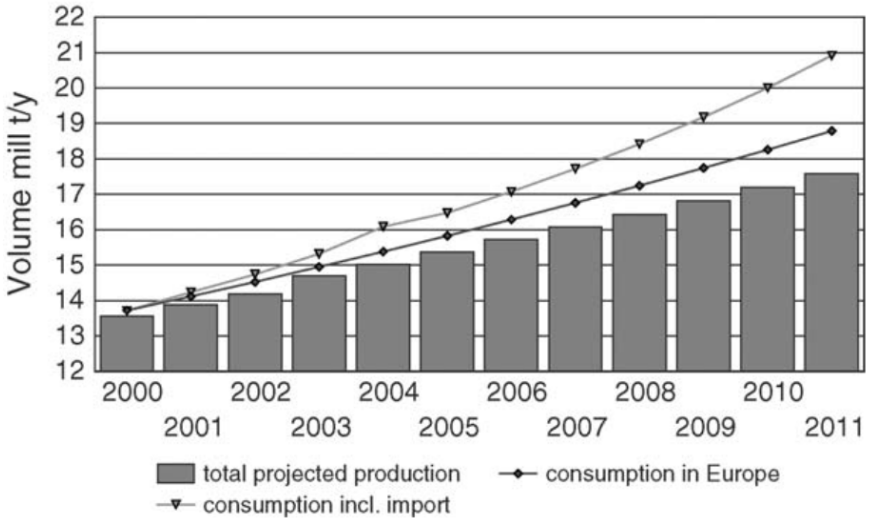

Figure 1.3: Increasing gap between propylene consumption and production in Europe [6].

Since the MTO process is such a promising technology, it forms the topic of this master thesis. During the oil crisis researchers at Mobil discovered that with the help of an acid solid catalyst methanol could be used for the production of gasoline [9]. Based on this knowlegde, they invented a process called MTG (methanol-to-gasoline). With their catalyst, H-ZSM-5, the yield towards olefins was rather low. However, with the invention of the H-SAPO-34 catalyst in the 1980s by researchers at Union Carbide, the route from methanol towards olefins became possible. A detailed discussion of these catalyst materials is provided in chapter 3. After the discovery of H-SAPO-34, the methanol-to-olefins (MTO) process was developed in the 1990s by UOP and Norsk Hydro.

In most regions of the world coal or methanol are available at a price that makes MTO more viable than a naphtha cracker to obtain light olefins. A first advantage lies in the required capital investments: the naphtha plant's capital investments are twice as high as for an MTO plant [10]. However, to obtain 1 metric ton of light olefins, 2 metric ton of naphtha are needed for a cracker compared to 2.6 metric ton of methanol in MTO. Nevertheless, MTO still has a feedstock advantage over naphtha crackers ranging from 530 to 820 USD/metric ton when considering an average naphtha feedstock cost of about 800 USD/metric ton and a methanol feedstock cost ranging from 300 to 400 USD/metric ton. Moreover, MTO has the advantage to allow greater control over the propylene-to-ethylene ratio than a naphtha cracker, which means it could resolve the increasing gap between the propylene supply and demand [6]. All these factors make of an MTO plant a profitable alternative for the production of light olefins in regions where methanol or coal are cheap. The MTO technology has the potential to play an important role in the olefin industry.

The following sections provide an outlook on the way to produce olefins from methanol starting from syngas production. In addition, also some renewable routes to methanol are given. Afterwards, the MTG process is briefly discussed. As final part, the introduction focuses on the MTO process.

1.1 Syngas production

Syngas is a mixture of CO and H_2 with CO-to-H_2 ratios ranging from 1:1 to 1:3. It can be produced from NG, biomass, waste, coal up to heavy residues. From syngas a wide range of products can be obtained such as hydrogen, methanol, ethanol, liquid fuels...

Syngas is used as feed for methanol production and can be coupled to an MTO plant. This can be referred to as a segregated gas-to-olefin chain. The first step in the segregated gas-to-olefin chain is the production of syngas itself. Ideally, the syngas must have a CO-to-H_2 ratio equal to 1:2 for the methanol production.

When starting from NG (methane), the most common technologies for the production of syngas are the steam reforming and partial oxidation of methane [11]. The former process is based on an exothermic reaction, while during steam reforming an endothermic reaction occurs. Therefore it is possible to combine these two technologies in so-called autothermal reformers [12]. In this setup, gases from the partial oxidation burner are combined with steam and sent to the steam reformer hereby also providing the required heat for the reforming reaction. Another used technology for the production of syngas is dry reforming, which is also discussed in this section. The final part of this section is devoted to the gasification process, which is used to process solid feedstocks like biomass or coal into syngas.

1.1.1 Steam reforming

In steam reforming, methane is mixed with steam over a heated platinum or rhodium catalyst at a temperature of 850 °C to 940 °C and a pressure of 15 bar to 30 bar. As seen from the stoichiometry of the reaction below a fixed CO-to-H_2 ratio of the syngas is obtained through steam reforming, equal to 1:3. In reality this ratio can deviated from 1:3 due to the occurrence of side-reactions. The reaction is highly endothermic with a reaction enthalpy $\Delta_r H$ of $206\,\mathrm{kJ\,mol^{-1}}$).

$$CH_4 + H_2O \longrightarrow CO + 3H_2$$

To obtain the desired CO-to-H_2 ratio of 1:2 for methanol production, an excess of steam can be added to promote the exothermic water-gas shift reaction ($\Delta_r H = -41\,\mathrm{kJ\,mol^{-1}}$) represented below. Therefore, to produce the required syngas, two reactors are necessary: a steam reformer and a shifter.

$$CO + H_2O \rightleftharpoons CO_2 + H_2$$

The most important advantage of steam reforming compared to other syngas producing routes is that there is no need for oxygen. A disadvantage is the formation of carbon due to the high temperatures [13] and the problems with steam corrosion.

1.1.2 Catalytic partial oxidation of methane

During partial oxidation of methane, air from which the nitrogen is removed, is used as oxygen source. In this oxygen-based atmosphere methane is converted into CO and H_2 over a supported

nickel or platinum catalyst at a temperature between 800 °C and 900 °C.

The obtained syngas has a CO-to-H_2 ratio of 1:2 resulting from the main reaction given below. This reaction is only slightly exothermic with a reaction enthalpy Δ_rH of $-38\,\mathrm{kJ\,mol^{-1}}$ [13]. Due to this small exothermicity the reactor can be operated adiabatically.

$$CH_4 + \tfrac{1}{2}O_2 \longrightarrow CO + 2H_2$$

The major disadvantage of this technique is the carbon deposition inside the reactor and the catalyst bed [14]. Furthermore during the reaction loss of the active catalyst particles is reported, especially for Fe-based catalyst. The use of noble metals could reduce this activity loss significantly, however at the expense of catalyst cost.

1.1.3 Dry reforming

In the dry reforming process steam is replaced by CO_2, resulting in syngas with a 1:1 ratio of CO-to-H_2. The fact that via dry reforming two greenhouse gases are consumed, makes this technology very interesting. The following reaction ($\Delta_r H = 247\,\mathrm{kJ\,mol^{-1}}$) occurs during dry reforming [13]:

$$CH_4 + CO_2 \longrightarrow 2\,CO + 2H_2$$

Cokes formation is one of the major drawbacks of this technology. However, testing of several types of catalyst revealed that the use of a sulfur-poisoned nickel catalyst can block the carbon formation sites on the catalyst, while still having enough sites for reforming [15].

One must also take into account that the reaction above is in competition with the water-gas shift reaction which has a lower activation energy. This means that hydrogen tends to react with carbon dioxide, creating water and carbon monoxide [16].

1.1.4 Gasification

Gasifiers can be used to convert coal, biomass and oil into syngas. To obtain the syngas, steam and oxygen must be injected into the gasifier [17]. Oxygen is needed to partially burn the feedstock, providing the required heat for the endothermic reaction between steam and the hydrocarbons from the feedstock. The gaseous product coming out of the gasifier does not only contain H_2 and CO, but also CO_2, some light hydrocarbons and soot.

The steam injection also controls the temperature. Inside the gasifiers, the temperature can go easily above 700 °C. Both high pressure and low pressure gasifiers are available. For the gasification of biomass, the low pressure set up is recommended [18]. For coal, gasifiers at atmospheric as well as elevated pressure are available.

There is a wide variety of gasifiers on the market. They can be divided into three main categories: fixed bed, fluidized bed and entrained bed gasifiers. Almost 90 % of the coal gasifiers uses a fixed bed configuration. The coal or fuel is continuously fed at the top of the fixed bed to preserve a constant height of the bed. As it is moving down due to gravity the feedstock is first preheated

and subsequently dried, then pyrolysed/devolatilized, gasified and combusted. This implies that a vertical temperature profile is present in the bed. In a fluidized bed gasifier steam and oxygen or air are injected at the bottom just like in a fixed bed. In this configuration the syngas is removed from the remaining feedstock and carbon by a cyclone and the fine solid particles are being recycled to the combustion area. This ensures a high level of back mixing which creates a uniform temperature in the gasifier. The category of the entrained bed gasifiers is the type of gasifier that is mostly used to obtain syngas for methanol production purposes. The feedstock together with steam and oxygen or air enter the gasifier at the top and react with each other in a suspended fluid flow. Of all three gasifier types, the entrained bed gasifier is operated at the highest temperature (>1500 °C).

1.2 Methanol production from syngas

For decades, methanol production has been based on fossil fuels such as oil, natural gas and coal. More recently also biomass and waste are used. From these feedstocks, methanol is obtained by converting conventional syngas. The most used techniques to obtain this syngas were discussed in section 1.1. In the current section, the technique to produce methanol from syngas will be explained.

The formation of methanol from syngas over a $Cu{-}ZnO{-}Al_2O_3$ based catalyst follows from these two equilibrium reactions [19]:

$$CO + 2H_2 \rightleftharpoons CH_3OH \qquad \Delta_r H = -91\,\mathrm{kJ\,mol^{-1}}$$

$$CO_2 + 3H_2 \rightleftharpoons CH_3OH + H_2O \qquad \Delta_r H = -49\,\mathrm{kJ\,mol^{-1}}$$

The equilibrium of both reactions can be driven towards methanol by increasing the pressure and decreasing the temperature because of the exothermic nature of the reactions and the resulting volume decrease. On the other hand, one must also consider the occurrence of the reverse water-gas shift reaction, which is endothermic.

The mechanism through which the syngas conversion proceeds is still uncertain [20]–[22]. The effect of the CO_2 content of the syngas also remains up for debate, although several studies agree that CO_2 hydrogenation is intrinsically faster than CO hydrogenation, as long as the right oxidation state is available on the catalyst surface [23], [24].

1.3 Renewable methanol production

Following methods to produce methanol are seen as renewable technology, since they do not start from syngas, but directly use CO_2 as methanol feedstock. These technologies are more sustainable since they consume one of the most abundant greenhouse gases, which lie at the basis of global warming.

A wide range of CO_2 sources can be considered for the methanol chemistry including exhausts from the combustion of natural (shale) gas, high-concentration exhausts of varied chemical

plants, cement plants, breweries and power plants. Moreover, natural sources such as CO_2 in natural gas, in geothermal wells or in the air can also be used as feedstock [5]. The technology to capture and purify CO_2 is a key aspect towards producing methanol from carbon dioxide [25].

Widely studied is the catalytic hydrogenative conversion of CO_2 into methanol over a combined zinc- and copperoxide based catalyst via the reaction given below:

$$CO_2 + 3H_2 \rightleftharpoons CH_3OH + H_2O$$

This process proceeds at a temperature between 220 °C and 250 °C and a pressure of 10 bar to 30 bar. The drawback of this technology is that one third of the hydrogen gas ends up in the production of water.

Another possible route for reducing the amount of carbon dioxide in the atmosphere is the electrochemical CO_2 recycling route in which CO_2 is selectively reduced to formic acid molecule. Subsequently the formic acid with methanol is converted to methyl formate, which is later catalytically reduced with hydrogen. This results in the formation of two methanol molecules per formic acid. The reaction scheme is represented below [5]. Several electrodes have been tested in the past. Molybdenum [26] and Ruthenium-modified electrodes [27] resulted both in the production of methanol in a very energy efficient way.

$$CO_2 + 2H^+ + 2e^- \longrightarrow HCOOH$$

$$HCOOH \xrightarrow{CH_3OH} HCOOCH_3 + H_2O \xrightarrow{2\,H_2} 2\,CH_3OH$$

Methanol may also be produced from methane or natural gas, CO_2 and steam via metgas in a single-step process called bireforming [5]. Metgas is a special form of syngas that is exclusively suitable for methanol production due to its CO_2 to H_2 ratio of 1:2. Bireforming proceeds via the following reaction over a nickel-based catalyst.

$$3CH_4 + CO_2 + 2H_2O \longrightarrow 4CO + 8H_2 \longrightarrow 4CH_3OH$$

This process operates at a temperature of 800 °C to 1000 °C and a pressure between 5 bar and 40 bar. This technique has the advantage that removal of CO_2 present in the natural gas is not required prior to the bireforming. By simply adjusting the steam to CO_2 ratio the correct composition of the metgas can be obtained.

By recycling CO_2 and converting it into methanol via the aforementioned technologies, chemical plants become one step closer to being carbon neutral.

1.4 Methanol as feedstock for hydrocarbon production

There is a wide range of technologies to convert methanol into more valuable products. Methanol-to-hydrocarbons (MTH) processes are among these technologies and gain more and more popularity. In the 1970s Mobil developed the methanol-to-gasoline (MTG) process to produce

gasoline at a reasonable cost during the oil crisis. This process provided at that time an alternative route to gasoline from coal [9], [28]. In Mobil's design a ZSM-5 catalyst (cf. section 3.2) formed the key to producing a good gasoline blend.

Over the years the demand for light olefins increased and especially the supply of propylene could no longer meet the demand. Therefore, from the MTG process the methanol-to-olefin route (MTO) was derived. By altering the operating conditions during MTG, the product distribution shifted somewhat towards light olefins such as ethylene and propylene. However the light olefin yield was not high enough and the MTO route became only viable after the discovery of the H-SAPO-34 catalyst. Not long after the invention of the MTG process, the first MTO process was commercialized by UOP and Norsk hydro. In this section these two methanol converting processes will be discussed.

1.4.1 MTG

The MTG process is represented in Figure 1.4 [29]. In a dimethyl ether (DME) reactor methanol is transformed into an equilibrium mixture of methanol, DME and water, which is subsequently sent over the ZSM-5 catalyst in a fixed bed reactor to obtain the gasoline. The reactor effluent is cooled to about 25 °C and water is removed, while the light ends are recycled to the reactor. A small gas purge is necessary to avoid build up of inerts.

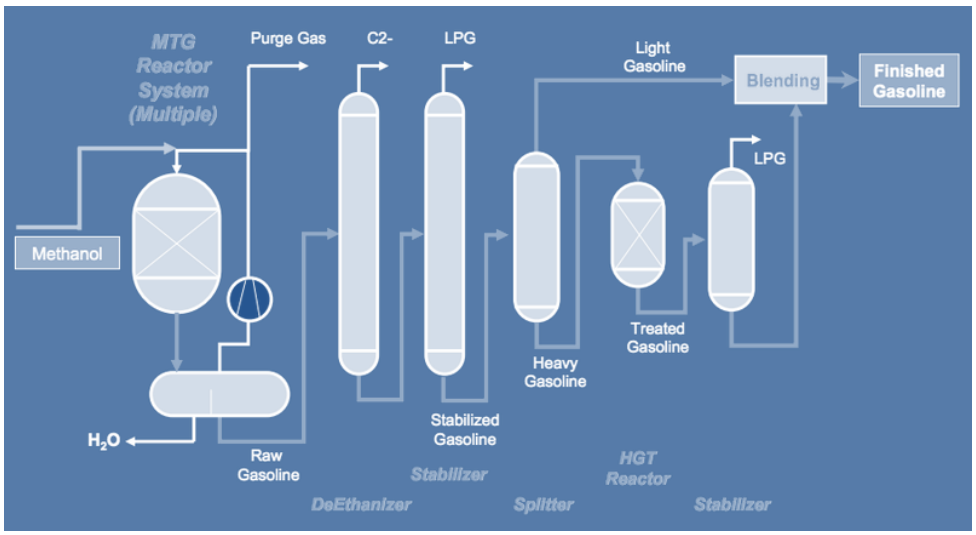

Figure 1.4: Mobil's MTG plant [29].

The liquid hydrocarbons are further processed in the separation train. To meet the required volatility specifications of the gasoline, the non-hydrocarbon together with the $C_{1\text{-}2}$ fraction and some propane are removed in a de-ethanizer and afterwards the remaining propane and some butane are removed via a stabilizer column. The top fraction of this column can be used as liquefied petroleum gas (LPG), while the liquid bottom is further separated into light and heavy gasoline. To achieve good drivability of the gasoline, the amount of durene in the heavy gasoline must be reduced. This is done in a finishing reactor, followed by another stabilizer column to remove light ends. As a final step, both the light and the treated heavy gasoline go to a blending

unit in which the finished gasoline is obtained.

The first MTG plant in New Zealand started up in 1985 [30], [31] and has known great success. The aforementioned fixed bed configuration makes it easy to scale up. This is an advantage over the Fischer-Tropsch (FT) process, another alternative route from syngas to liquid fuels that was considered at the time of the oil crisis. In FT a slurry-bed reactor is used, making the scale up very difficult. Furthermore FT has the disadvantage that the resulting straight-chain paraffinic hydrocarbon stream must be upgraded before it is useful as a liquid fuel. The product stream coming from MTG can be directly used or blended with other fuels, since it contains only a limited amount of benzene and virtually no sulfur [29].

1.4.2 MTO

The MTO process became viable after the discovery of H-SAPO-34. H-SAPO-34 appeared to provide a high selectivity towards ethylene and propylene H-SAPO-34. Although higher hydrocarbons are also produced, their contribution to the end product is drastically lower in comparison with the product distribution obtained with Mobil's ZSM-5. The higher selectivity towards light olefins in SAPO-34 is attributed to the small windows (3.8 Å compared to 5.5 Å in H-ZSM-5) through which the products need to exit the catalyst, as seen in Figure 1.5. These small windows prevent diffusion of heavy and highly branched hydrocarbons.

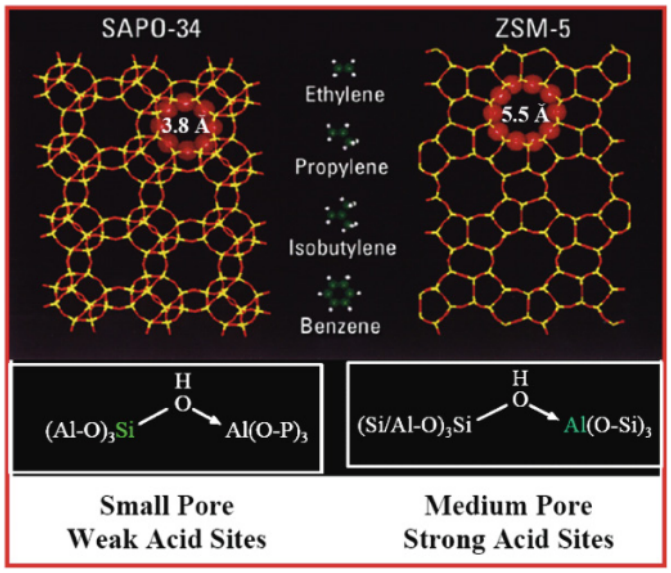

Figure 1.5: Comparison between SAPO-34 and ZSM-5 [32].

Furthermore, SAPO-34 possesses a lower acid strength than ZSM-5 which drastically reduces the production of paraffinic byproducts [32]. The zeolitic acid strength forms an important aspect in the MTO process and can influence the conversion and selectivities. Therefore this master thesis focuses on elucidating the effect of this acid strength on the MTO process. During this master thesis, H-SAPO-5 and H-SSZ-24 will be compared. They both have the AFI topology, which only contains 12-ring 1D channels. Furthermore, H-SAPO-5 has a comparable acid strength as H-SAPO-34, while H-SSZ-24 contains stronger acid sites. For more detailed information about

the catalyst types and their acid strength, the reader is referred to chapter 3.

The exploration of SAPO-34 has led to the development of the first MTO plant by UOP in collaboration with Norsk Hydro in the early 1990s. By dehydrating methanol over a solid acid catalyst such as H-SAPO-34, a high selectivity towards olefins such as ethylene and propylene can be obtained. The UOP/Hydro MTO process is very similar to a Fluid Catalytic Cracker (FCC) unit. This is based on the fact that SAPO-34 must be frequently regenerated due to the rapid cokes formation and the high exothermicity of the reactions occurring in MTO. The required fast regeneration and the need for heat removal have led to the design of the plant as seen in Figure 1.6. This combines a fluidized-bed reactor with a regenerator system, in which the cokes are burned off. Water is generated in the process, therefore the product stream from the reactor is first sent to a flash to remove water. Afterwards, CO_2 is removed followed by a drying step. Further downstream, a de-ethanizer is installed. As seen in Figure 1.6 the separation section of the reactor is based on the one for a cracking unit, because the product composition is very similar. This is a classical example of a de-ethanizer-first separation train in which the desired products, ethylene and propylene are recovered at the top of respectively the C_2-splitter and the C_3-splitter.

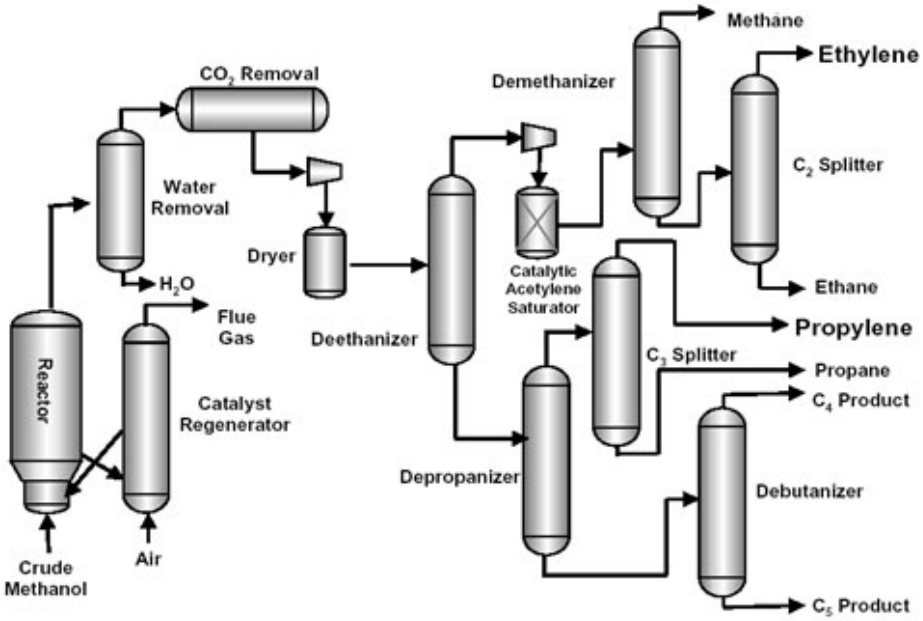

Figure 1.6: UOP/Hydro MTO plant [33].

Through a collaboration between Total and UOP in 2000, the MTO process was further improved, resulting in the advanced MTO plant [32]. Nowadays, state-of-the-art MTO plants include the Total Petrochemical/UOP olefin cracking process (OCP) as shown in Figure 1.7. This limits the C_{4+} fraction drastically and increases the yield of propylene.

The conditions inside fluidized bed reactor in the advanced MTO plant range from 340 °C to 540 °C at a pressure from 1 bar to 3 bar. High activity of the catalyst is obtained by frequent regeneration, leading to very high methanol conversion in the reactor. After exiting the reactor of the advanced MTO plant, the product gas stream is quenched upon water removal. Subsequently,

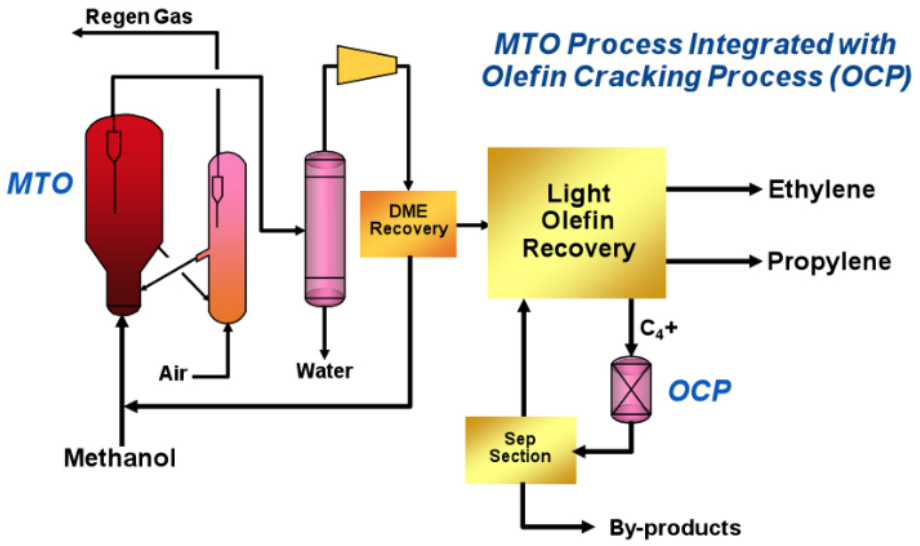

Figure 1.7: Advantanced MTO plant [32].

the remaining oxygenates, such as DME, are removed from the gas and recycled to the reactor. Only a minor recycle stream is required, since high conversion is already obtained after a single pas through the reactor. The rest of the gas stream is sent to the separation train to remove contaminants and obtain the desired product fractions. The achieved ethylene and propylene fraction are of polymer grade. The $C_{4\text{-}6}$ fraction enters the OCP in which it is selectively converted to light olefins with a reactor effluent ratio of 4 propylene molecules per ethylene molecule [32]. The $C_{3\text{-}}$ fraction from the OCP is sent to the MTO separation train and the remaining C_{4+} fraction can be used as a fuel.

One of the main reasons for the succes of MTO is its wider range of achievable propylene-to-ethylene ratios compared to the traditional naphtha and gas oil crackers. This is particularly interesting since new ethane crackers produce even less propylene than classic naphtha crackers, while the demand for propylene is rising more rapidly than for ethylene, leading to an increasing gap between the propylene demand and supply as mentioned before. The propylene-to-ethylene ratio in gas oil and naphtha crackers ranges from 0.53 to 0.65 [8]. Whereas Figure 1.8 indicates that the advanced MTO process reaches propylene-to-ethylene ratios between 1.2 and 1.8 at a conversion higher than 85 %. As seen in Figure 1.9 the advanced MTO process achieves even higher yields of ethylene and propylene compared to the classical MTO process. Furthermore, the propylene yield in advanced MTO is in stark contrast to the more or less 15 % yield in a naphtha cracker. As seen on Figure 1.9, a methanol-to-propylene (MTP) process also exists. As the name suggests, this process yields mostly propylene and only limited amount of ethylene. It was invented by Lurgi and has already been proven in various plants [34]. This higher propylene-to-ethylene ratio is one of the main reasons for the succes of advanced MTO and MTP.

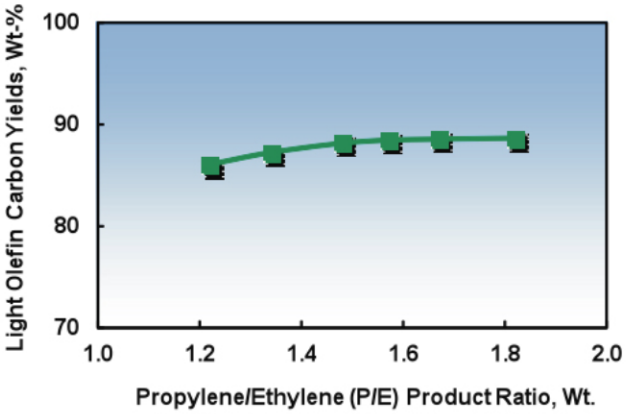

Figure 1.8: Propylene-to-ethylene ratio in UOP's advanced MTO process [32].

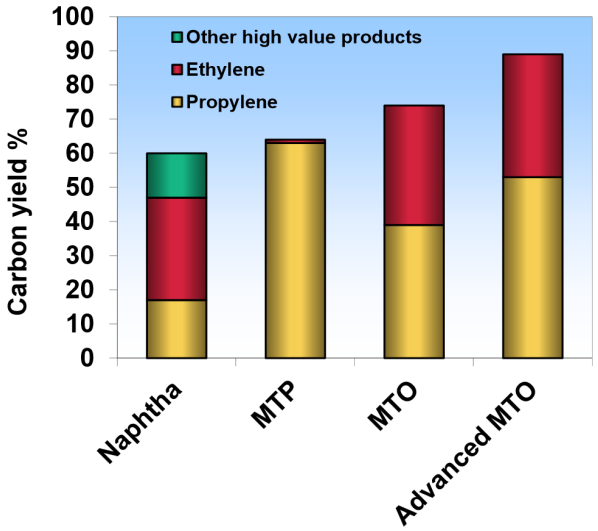

Figure 1.9: Product yield obtained by naphtha cracking, MTP (methanol-to-propylene), MTO and advanced MTO.

Chapter 2

The MTO mechanism

During the MTO process methanol is converted into light olefins over a solid Brønsted acid catalyst. Depending on the type of catalyst, different product distributions are obtained. The most well known MTO catalysts are H-SAPO-34 and H-ZSM-5. By using H-SAPO-34 a product mixture with ethylene and propylene as most abundant species is made, while over H-ZSM-5 a more alkane-like product mixture is obtained with a high C_{4+} fraction. Mechanistic insights into the MTO reaction mechanism are necessary to optimize the process and catalyst design to tune the product selectivities towards the desired blend.

Several stages occur during the MTO process [35]. As indicated in Figure 2.1, the first stage of MTO converts methanol into an equilibrium mixture of DME, water and some remaining methanol. Afterwards, this mixture will be converted into light olefins e.g. ethylene and propylene. During the third stage, secondary reactions will result in the production of higher olefins, alkanes and aromatics. Eventually, coke is formed and the catalyst is deactivated.

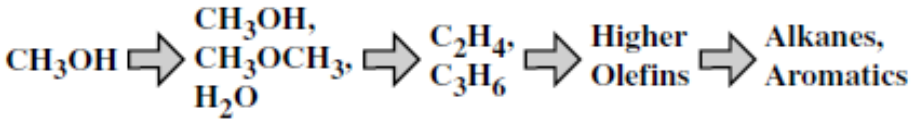

Figure 2.1: General scheme of the conversion of methanol to hydrocarbons [36].

The mechanism behind this process is still a controversial topic. Several mechanisms have been proposed. They can be classified into two groups, namely direct mechanisms and parallel mechanisms [37]. The latter is formally known as the hydrocarbon pool (HP) mechanism.

2.1 Direct Coupling

Originally, a direct coupling of C_1 species derived from methanol or dimethyl ether was proposed for the MTO mechanism. First two C atoms from two methanol molecules form a new C-C bond.

The next step in the mechanism is the attachment of other methanol molecules to this newly formed C-C bond. These type of mechanisms are thus based on chain growth. Each proposed direct mechanism uses a different type of intermediate, such as carbocations, carbenium ions, oxonium ylides, free radicals and surface-bound alkoxy species [37].

The problem with these mechanisms is that not one of them can really explain the formation of the first C-C bond. Several studies have proven that these direct routes fail. For instance the reactions involved have too high activation energies and the intermediates are too unstable [38]. Apart from this, experiments have also shown that there are two different reaction stages during MTO: an induction period reaction stage and a steady-state reaction stage [39]. During the induction period there is virtually no production of light olefins. It is expected that during this period other type of hydrocarbons are building up inside the catalyst. Once the amount of these hydrocarbons inside the catalyst reaches a certain threshold, the formation of light olefins kicks off. Once a stable olefin production is achieved, the induction period is finished and the steady-state regime begins. This induction period could not be explained by the direct mechanisms [40]. Isotopic labeling experiments with ^{13}C methanol and unlabeled ethylene showed that the resulting labeling pattern in the product mixture is also not consistent with the direct mechanisms [41]. 90 % of the ^{12}C ethylene had not reacted and the isotopic distribution of propylene and butene are nearly random. This shows that the direct mechanism in which ethylene would be subsequently methylated by methanol is fails, since ethylene appears to be inert. These isotopic product distributions are however consistent with the HP mechanism, which will be explained in the next section.

2.2 Hydrocarbon pool mechanism

Several proposals have been published for indirect mechanisms. They suggest that hydrocarbons present in the catalyst pores act as a co-catalyst. These species are called HP species and are formed during the induction period. This was confirmed by Mole et al., who performed co-feeding experiments of methanol and cyclic species [42]. This indicated that aromatic species are able to increase the rate of the MTO process and hence co-catalyze the MTO process. Some examples of these HP species are methylated benzenes from toluene up to heptamethylbenzene cations, but also alkenes can act as HP species. Linear alkenes species were reported in H-ZSM-5 as HP species by Dessau [43] and Svelle et al.[44], while in H-SAPO-34 mostly aromatic species are found as HP species [36]. This suggests the catalyst properties e.g. topology, pore size and acid strength affect the presence or absence of certain HP species and their reactivity.

Dahl and Kolboe proposed a mechanism based on these HP species [41], [45]. They suggested that the reactions are catalyzed by an acid site belonging to the zeolite framework and by an active HP species. The desired olefins are thus not produced by a direct coupling mechanism but result from the reactions between the HP species and methanol or DME. Without the presence of this HP intermediate, the catalyst cannot be active and hence cannot produce enough olefins. Only if there is a sufficient amount of HP species present in the zeolite, the olefin production can truly kick off and a stable methanol conversion is reached.

The origin of these HP species remains unclear. Although the direct coupling mechanism seems to fail during steady state MTO operations, it is possible that this mechanism plays a role during the induction period and results in the formation of the first C-C bond. Song and co-workers suggest that feed and zeolite impurities lie at the basis of the formation of the HP species [36], [46]. Often ethanol is present in the methanol feed and also the carrier gas and the calcinated catalyst may contain contaminants. Indeed, experiments have proven that the induction period is prolonged and the catalyst is almost unreactive when extremely pure methanol, carrier gas and catalyst are used [47]. However other studies suggest that the impurities have only a minor effect on the formation of hydrocarbons [48].

The growth of the HP may be explained by a ship-in-a-bottle mechanism in which small hydrocarbon molecules and methanol react multiple times to create an HP species [49]. Once a sufficient amount of HP species is present in the zeolite, a steady state olefin production is established. The production of the small hydrocarbons e.g ethylene and propylene will result in the formation of even more HP intermediates via secondary reactions. Quantum mechanical calculations show that this route for the HP growth is plausible [49]. Only recently, the presence of HP species during the induction period in H-SAPO-34 was observed experimentally by the group of Hunger [50]. Some examples of these HP species are three-ring compounds, dienes, polymethylcyclopentenyl and even polymethylcyclohexenyl cations. It must be stressed that the aromatic HP species are not only the active species during the MTO process. They are also the precursors for coke formation, which will eventually lead to deactivation of the catalyst. This is schematically represented in Figure 2.2.

The formed HP species are often very bulky and often cationic, since bulkier molecules have a higher proton affinity. These bulky molecules can be stabilized by the zeolite or zeotype framework. As mentioned before the type of zeolite, along with the operating condition during MTO, highly influences the reactivity and the nature of the present HP species. Two major types of HP species are distinguished: the aromatic and aliphatic HP species. Different HP species will be preferentially present in a certain catalyst topology and will have a different reactivity in each catalyst type. The competition between the aromatic and aliphatic HP species is further discussed in section 2.4.

The nature and reactivity a certain HP species is also reflected in the product distribution, because each type of HP species results in the formation of different products. For instance, when co-feeding methanol and benzene in H-SAPO-5 (see section 3.3 for more information on this catalyst) and hereby increasing the amount of aromatic HP species and their reactivity, a shift was seen in the product spectra in Figure 2.3 towards a higher production of $C_2$and C_3 species at the expense of the C_{4+} product fraction [51]. Furthermore, in H-SAPO-34 less substituted methylbenzenes merely produce ethylene, while polymethylbenzenes (PMBs) with 4 to 6 methyl groups are more selective towards propylene [46]. This was also reported by Haw and Marcus who saw a decrease in theoretically modeled reaction barriers for ethylene and propylene formation with increasing methyl substitutions on the aromatic ring [36]. This effect was more pronounced for propylene than for ethylene, explaining the difference in selectivity. These experiments and theoretical calculations all show the large effect of the type of HP species on the product distribution.

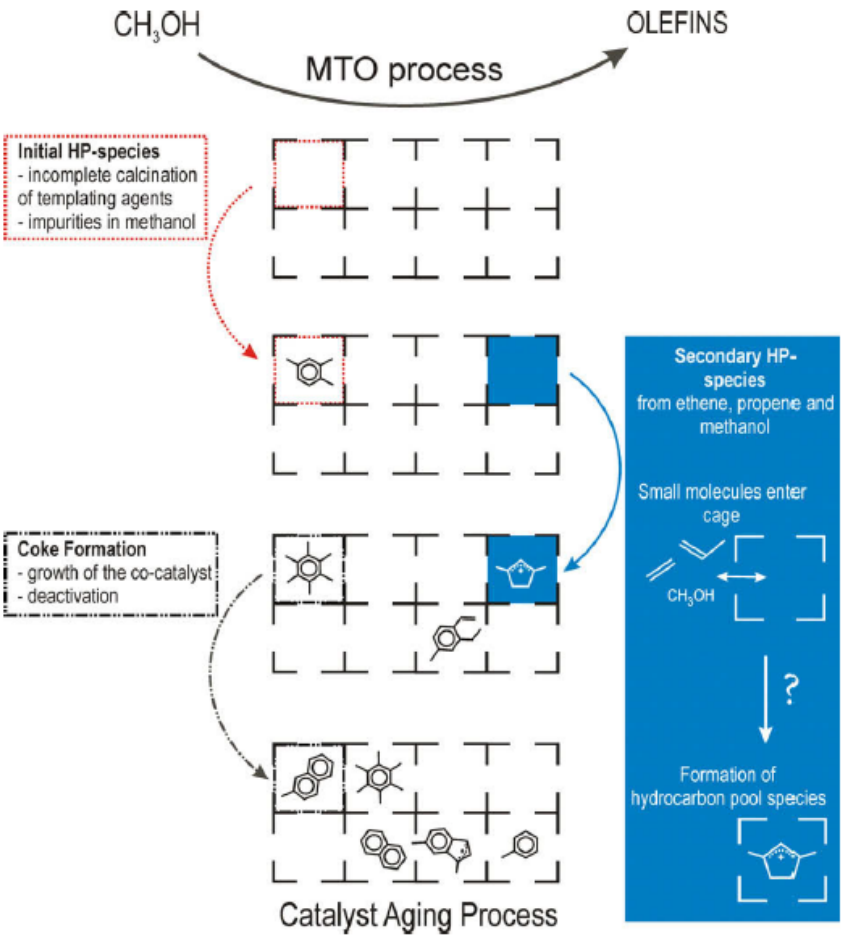

Figure 2.2: The evolution of the HP species during the catalyst's lifetime [36], [49].

2.3 Paring vs. side chain cycle

As mentioned before, the aromatic HP species play an important role in the steady-state regime of MTO. Therefore this section is devoted to the mechanism through which olefins are produced from aromatics. Several experimental techniques, such as isotopic labeling experiments, are used to obtain clues about the underlying mechanism. However obtaining reaction rates of individual reaction step is very difficult experimentally as many reactions take place simultaneously. Therefore a big part of the MTO research relies on first-principles calculations of the elementary reactions to obtain reliable kinetic data. The combination of both experimental and first-principles techniques helped form a consensus about the importance of the aromatic HP species and the presence of a paring and side chain cycle in the MTO mechanism.

Starting from an aromatic HP compound, two possible cycles are proposed: the paring and side chain cycle, which are shown in Figure 2.4. Both cycles start with subsequent methylations of benzene, until a gem-methylated species is obtained. In Figure 2.4 the gem-methylated carbocation is a heptamethylated benzenium cation. Although at first sight this species seems unstable, this gem-methylated species is very well stabilized by the CHA structure of H-SAPO-34 [52]. In chapter 3, the CHA topology is explained into detail.

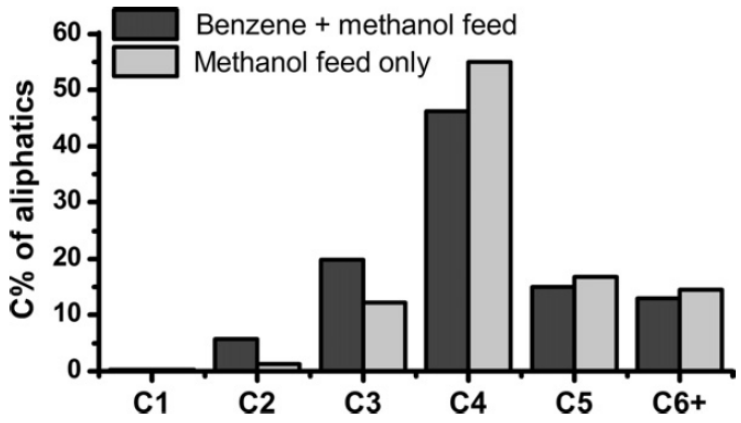

Figure 2.3: Comparison of the product spectra in H-SAPO-5 for a methanol feed with (black) and without (light gray) benzene [51].

After the formation of this species, a ring contraction and ring expansion take place in the paring cycle, hereby releasing an alkene. This cycle was proposed by Sullivan et al. [53]. This mechanism has proven to be consistent with isotopic labelling experiments. During these experiments a feed of ^{13}C labeled methanol and unlabeled benzene was used and incorporation of ^{13}C in benzene was observed [51]. This can only be the result of the ring contraction and subsequent expansion.

Another mechanism was proposed by Mole and co-workers [54]. For the side chain cycle, an exocyclic double bond must be formed, which can then be methylated, followed by a side chain elimination. This elimination can either occur by directly expelling the side chain and creating ethylene or by generating a new double bond at the side chain and subsequently methylating it. In this last case eventually a propylene species is produced as can be seen on the top right part of Figure 2.4.

In H-SAPO-34, the reactivity of PMBs and the selectivity towards propylene increases with the number of methyl substituents [55]. Furthermore, hexamethylbenzene (HBM) appears to have a crucial part in the mechanism as it contains the highest activity of all HP species in H-SAPO-34 [55]–[59].By performing extended cluster first principles calculations (see chapter 4), De Wispelaere et al. found a full low-barrier side chain cycle for the production of ethylene and propylene starting from HMB as HP species [60]. Based on DFT-cluster calculations (see section 4.2), Hemelsoet et al. reported that the side chain cycle using naphtalenic HP species, instead of polymethylated benzenes, cannot be regarded as an active ethylene producing mechanism [61]. Wang and co-workers concluded, based on their first principles calculations of the paring cycle, that this cycle is only of minor importance in H-SAPO-34 due to higher barriers and difficult regeneration of PMBs from the 5-ring cations [62].

However, the production of propylene over a H-ZSM-5 catalyst can not be explained by this side chain cycle. Lesthaeghe et al. report too high activation energies, calculated using DFT (see chapter 4), for the ethylene production from the side chain cycle. The paring cycle is preferred over the side chain cycle in H-ZSM-5, since H-ZSM-5 is more confined [63].

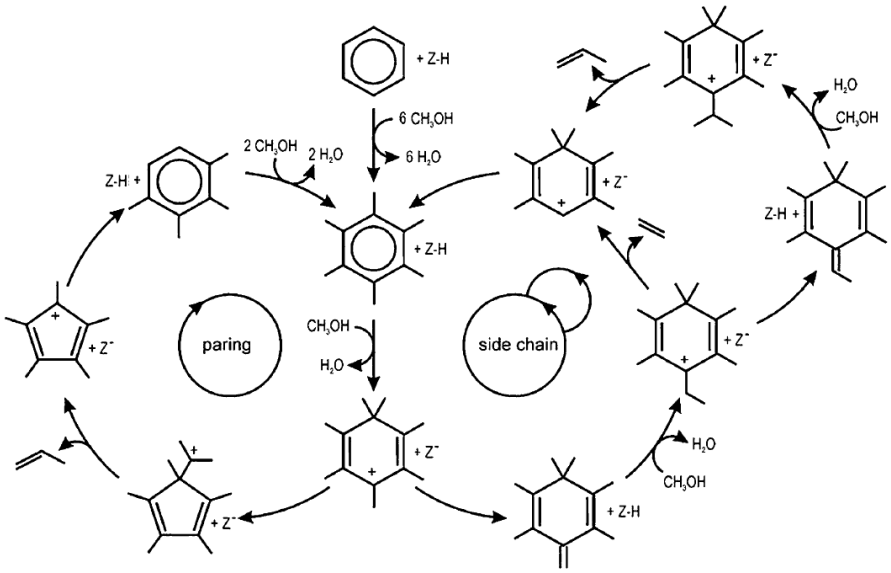

Figure 2.4: Scheme of the proposed mechanism based on aromatic HP species.

Although, Svelle et al. conclude that ethylene is formed via the PMB HP species with a low degree of methylation in H-ZSM-5, an important role goes to the alkene-like HP species [64]. Svelle and co-workers report that propene and higher alkenes are formed via an autocatalytic alkene cycle [44], [65]–[68]. This mechanism using aromatic and alkene-like HP species is referred to as the dual-cycle mechanism, which is discussed in the next section.

2.4 Dual cycle mechanism

The dual cycle mechanism claims that there are two different types of HP species responsible for the MTO process [68]. The dual cycle mechanism contains two different cycles, one based on arene like HP species and the other based on alkene like HP species, as shown in Figure 2.5. For H-ZSM-5 it was reported that branched alkenes are methylated more easily than PMB with an exocyclic double bond, which is used in the side chain cycle. To produce ethylene and propylene from the alkene cycle, branched and methylated olefinic carbocations have to be cracked. Higher alkenes, which have not been cracked, can also undergo a cyclisation reaction hereby creating an aromatic HP species, which can be used to produce olefins in the arene cycle.

In H-ZSM-5 the formation of ethylene has been shown to be mechanistically different from the formation of higher alkenes [44]. This difference is explained by the occurence of both the arene and alkene cycle in H-ZSM-5. Whereas ethylene is attributed to the arene cycle, C_{3+} alkenes are mainly produced via alkene methylation reactions.

The reason for the higher activity of the small HP species can be found in the smaller available spaces in H-ZSM-5 than in H-SAPO-34. This dual cycle is not seen in H-SAPO-34 since the aliphatic HP species will have lower activity because they are less stabilized by the CHA cages.

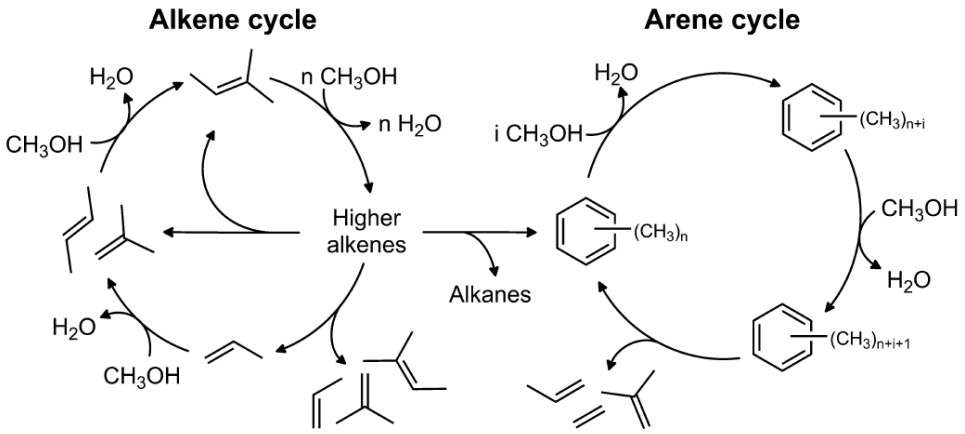

Figure 2.5: Dual cycle mechanism in MTO. Reprinted from [51].

The occurence of the dual cycle has been validated by Lesthaeghe et al. in H-ZSM-5. It appears that isomerization and de-protonation reactions occur extremely fast due to the stabilization of the intermediate carbenium ions by the host framework [69].

Other catalyst types are also prone to the dual cycle mechanism. For instance a study has been executed to compare H-ZSM-5 and H-beta [64]. Under identical reaction conditions, the ethylene to propylene product selectivity in H-ZSM-5 is seven times higher than in H-beta. In both catalysts, the arene and alkene cycle are active. The difference in product selectivities can be explained by the higher amount of lower PMBs in H-ZSM-5. Since these PMB with low degree of methylation are held responsible for the ethylene production in the arene cycle. Another example is the H-ZSM-22 catalyst in which the arene cycle is suppressed and the olefin methylation and cracking route is preferred due to its narrow one-dimensional straight channels (cf. section 3.4) [70]. This shows that whether or not a certain cycle (paring vs. side chain, arene vs. alkene) takes place depends strongly on the catalyst topology.

Another parameter that influences the occurence of the alkene cycle is the Brønsted acid strength. Comparison of wide pore catalysts H-SAPO-5 and H-beta, showed that lower acid strength in H-SAPO-5 leads to an alkene-based mechanism [51]. This was further confirmed by comparing two isostructural solid acid catalysts, H-SAPO-5 and H-SSZ-24. It appears that the alkene cycle is dominant in the catalyst with the moderate acid strength, whereas the arene cycle is the most active cycle in the catalyst with the high acid strength [71]. This effect will be further discussed along with the aforementioned catalyst materials in chapter 3 .

2.5 Methylation reactions

Methylation reactions are an essential part of the MTO mechanism. First-principles calculations of these methylation reactions are crucial to get insights into the MTO mechanism. The methylation reactions described in section 2.3 are catalyzed by Brønsted acid zeolites. The mechanism behind these methylations can either be concerted or stepwise. In the former, a physisorbed methanol or dimethyl ether acts as methylating agent and the methylation occurs in a single

step, as depicted in the top row of Figure 2.6. In the latter mechanism, a framework-bound methoxy needs to be formed prior to methylation [72], [73]. The stepwise mechanism is shown for the methylation of benzene in the middle and bottom row of Figure 2.6. To form a methoxide species on the zeolite, a methanol or DME molecule must be protonated by the Brønsted acid site, subsequently transferring a methyl group to the framework oxygen, hereby releasing a water or methanol molecule.

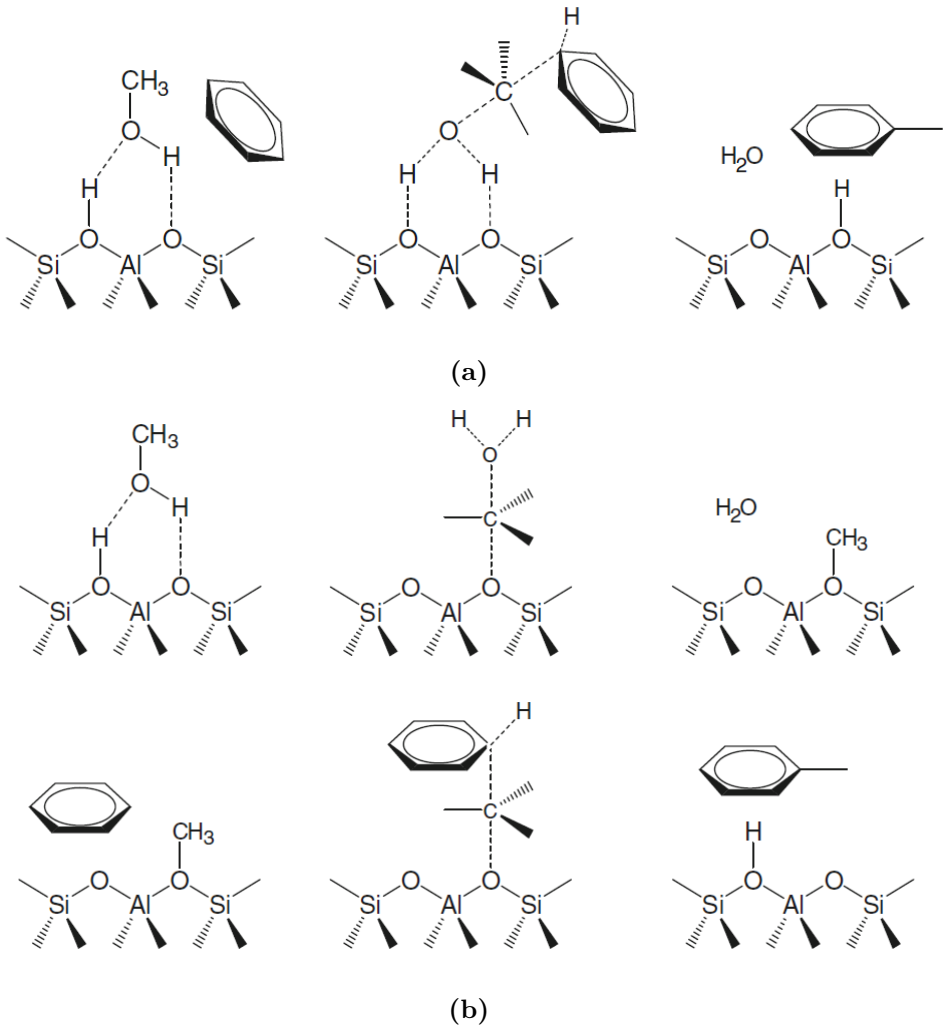

Figure 2.6: Proposed mechanisms for the methylation of benzene. The concerted methylation (a) of benzene with methanol acting as methylating agent is given in the top row. Stepwise methylation (b) of benzene with the formation of framework-bound methoxide species is given in the middle row and the subsequent methylation is represented in the bottom row [72].

Through in-situ infrared (IR) spectroscopy Saepurahman et al. followed the methylation reaction of benzene with methanol [74]. The rate of this reaction normalized to the density of acid sites is significantly lower in H-beta than in H-ZSM-5. Furthermore, the corresponding IR spectra reveal the presence of methoxy species on silanol groups in the first minutes on stream. However, the methoxy species are not seen on the Brønsted acid sites. Still this does not mean that the stepwise mechanism for methylation fails, since it is likely that reactive intermediates, such

as a methoxy species on an acid site, are present in very low concentration due to their high reactivity.

The stepwise and concerted mechanisms are competitive paths for methylation reactions. The operating conditions decide which of these mechanism is dominant. Jones et al. state that for the DME formation from methanol at higher temperatures and lower pressures the stepwise route becomes the most active. Although this route corresponds to a higher enthalpy barrier than the concerted mechanism, at high temperatures it may become dominant due to its higher entropy barrier as result of the favorable intermediate release of water. The more complex transition states attributed to the concerted mechanism are preferred at lower temperatures and higher pressures. The dominant pathway for the methylation of alkenes during MTO is also controlled by temperature and pressure. Through a micro-kinetic model, Brogaard et al. proved that the stepwise mechanism for the alkene methylation reactions in H-ZSM-22 prevails at typical MTO temperatures (above 600 K) and pressures (around 1 bar) [75].

Based on theoretical modeling, Vos et al. report a higher barrier for methoxide formation than for the subsequent methylation step [76]. This would imply that the methoxide formation is the rate-determining step in case the methylation would proceed via the stepwise mechanism. Lesthaeghe et al. report that an additional water or methanol molecule, physisorbed on the neighboring Brønsted acid site, stabilizes the transition state of the formation of a framework-bound methoxide, resulting in a significant decrease in the reaction barrier [38]. These calculations were only performed on small clusters (see subsection 4.1.1).

Via a more accurate method, called metdadynamics (see Figure 4.3.5) Van der Mynsbrugge et al. found that the barrier for the formation of a methoxy species is slightly higher than for the methylation reaction itself in H-ZSM-5, but overall the kinetics seem to be very alike [77]. Furthermore, it appears that once a framework-bound methoxide is formed, this species is very reactive towards methylation reactions. As seen in the middle drawing at the top of Figure 2.6 a methoxide formation proceeds via an S_n2-type mechanism: while breaking the C-O bound and forming the new C-O bound, the methyl group experiences an umbrella inversion. Similar intrinsic barriers in terms of enthalpy and free-energy are found for methanol and dimethyl for the formation of methoxide. Moreover, the formation proceeds in both cases via the proposed S_n2-type mechanism.

Moses and Nørskov saw that the formation of a framework-bound methoxy species also takes place in H-ZSM-22. They modeled the formation of DME from methanol over H-ZSM-22 via the use of a methoxy intermediate and via a concerted pathway. They concluded that the stepwise route is always dominant in H-ZSM-22 even if different acid strength are modeled. The effect of the acid strength is explained in chapter 3.

Apart from the first-principles calculations to investigate the formation of the methoxy species prior to the methylation reactions, apparent and intrinsic kinetic data for the methylation reactions of methanol or DME with alkenes and aromatics have been reported. Figure 2.7 clearly shows the difference between the term "apparent" and "intrinsic". During an experimental kinetic study, the apparent kinetics are measured. This means that the difference in enthalpy and free energy for the reaction is measured with respect to the reactants in the gas phase. However

theoretical calculation of reaction kinetics always result in intrinsic data, meaning that the kinetics are expressed with respect to the reactants adsorbed on the zeolite as shown in Figure 2.7. Therefore, to compare apparent kinetic data with intrinsic kinetic data, the adsorption enthalpy and free energy must be known as well.

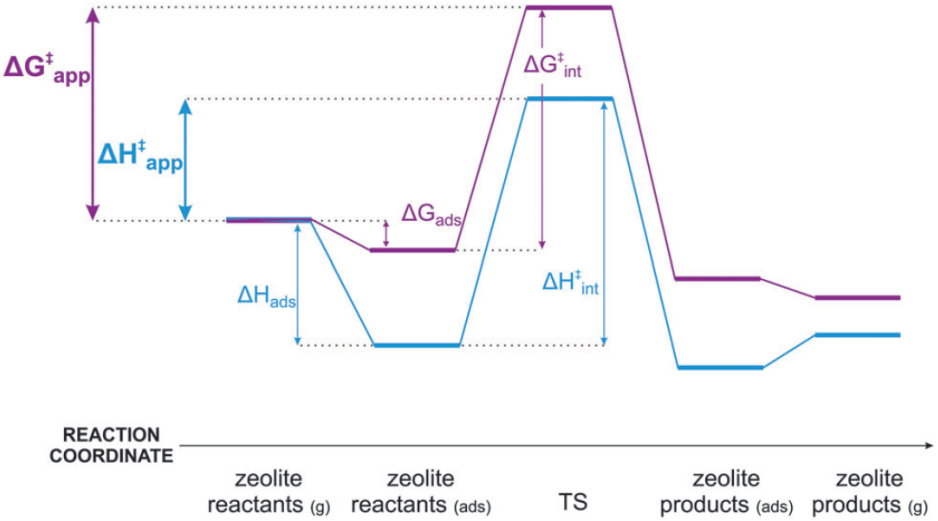

Figure 2.7: Schematic representation of the free energy and enthalpy profile for a reaction inside a zeolite. $\Delta G^{\ddagger}_{app}$ and $\Delta H^{\ddagger}_{app}$ are the apparent free energy and apparent enthalpy barrier respectively, while $\Delta G^{\ddagger}_{int}$ and $\Delta H^{\ddagger}_{int}$ stand for the intrinsic free energy and intrinsic enthalpy barrier respectively [78].

From experiments in H-ZSM-5, the intrinsic activation energies were derived for the methylation reaction of ethylene, propylene and n-butene with methanol [65], [66]. A decrease in reaction barrier was found with increasing amount of carbon atoms. This trend was also confirmed by first-principle calculations performed by Svelle et al. [79]. Svelle and co-workers also reported that the forward reaction rate for a methylation reaction shows a zero-order behavior in the methanol pressure and a first-order behavior in the alkene pressure as given by Equation 2.1 [66]. The same zero-order behavior was also seen for DME as methylating agent over H-FER, H-MFI, H-BEA and H-MOR zeolites [73]. The measured apparent rate coefficients k_{app} exhibits the following relationship: $k_{\text{ethylene}} : k_{\text{propylene}} : k_{\text{n-butene}} = 1 : 17 : 52$ in H-ZSM-5 [66]. Hill et al. also reported an increase in rate coefficient and decrease in barrier from ethylene to propylene, suggesting that with increasing olefin substitution reactive intermediates and activated complexes are better stabilized. Van Speybroeck and co-workers used the experimentally obtained kinetic data of the methylation reaction with methanol as a bench mark. They found that first-principle calculations can provide kinetic data with near chemical accuracy[1] [78].

$$r = k_{app} p^{0}_{\text{methanol}} p^{1}_{\text{alkene}} \tag{2.1}$$

As for the alkene methylation, benzene and toluene methylation also proceed via a first-order

[1] Chemical accuracy is reached when the ratio of the rate coefficients obtained from the theoretical calculation and the experiment fulfills: $10^{-1} < k_{\text{theory}} : k_{\text{experiment}} < 10$.

behavior in the aromatics partial pressure and a zero-order behavior in the DME partial pressure [80]. However for the methylation reaction of p-xylene over H-ZSM-5 a saturation in the reaction rate was observed as shown in Figure 2.8. This saturation is not linked to diffusional limitations but is attributed to a change in the predominant surface species. Whereas at low xylene partial pressures framework-bound methoxide is the predominant surface species, at high xylene partial pressures a co-adsorption complex of xylene onto the methoxy species is abundantly observed. The latter complex blocks DME from reacting with xylene and therefore leads to a saturation in the methylation rate. This shows that the concerted and stepwise mechanism are in competition and can be controlled adjusting the xylene partial pressure.

An experimental study revealed that the methylation of benzene with methanol occurs faster in H-ZSM-5 than in H-beta (cf. section 3.4). This was also reported after performing a first principles study of the two catalyst with benzene and methanol as guest molecules [81]. This study not only confirms the previously reported trend, it also gives an explanation for the difference in reactivity. As H-ZSM-5 is a medium pore size catalyst, it provides the optimal confinement for the reactive species. The increased rate is therefore linked to the stabilization host-guest interaction in H-ZSM-5, which outweighs the loss in entropy upon benzene adsorption.

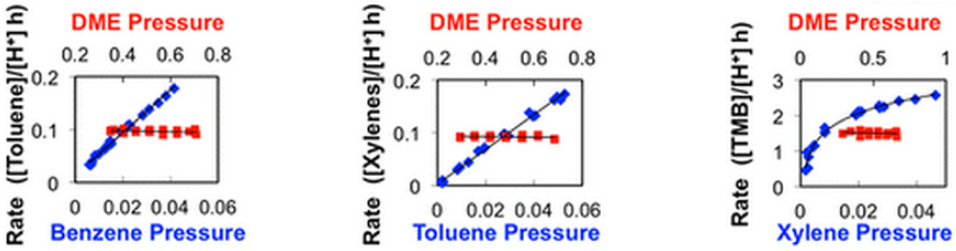

Figure 2.8: Rates for the methylation reaction of benzene (left), toluene (middle) and p-xylene (right) as function of the partial pressure of the aromatic and DME [80].

2.6 Deactivation

As catalyst deactivation is the last stage of the MTO process and highly undesired, this final section of the MTO mechanism chapter will briefly discuss it. Growth of aromatic species and their methylation frequently occur inside the MTO catalyst. However the aromatic intermediates can eventually grow into a larger coke species, hereby blocking the pores of the catalyst or poisoning it. In general coke formation is the deposition of carbonaceous residues, leading to aging and modifications of a catalyst [82]. The HP species are precursors of coke and the coke species leading to deactivation depend on the type of catalyst. The smaller the catalyst pore, the more prone it is to deactivation. Coke formation is undesired and industrial MTO catalysts need to be frequently regenerated by burning off the coke at high temperature [83].

Moreover, this coke can also lead to a shift in the product spectrum, since they modify the available space inside the catalyst pore and the acidic properties of the zeotype of zeolite catalysts by blocking active sites and pores [82]. This way the catalyst selectivity is altered. In H-ZSM-5, coke is mainly deposited on the outer surface of the catalyst in form of a graphite like structure

[82], [84]. Because the interior of the catalyst crystals is less blocked by coke H-ZSM-5 posesses a superior life-time and coking has only a minor effect on its product selectivity. On the other hand, in H-SAPO-5 coke species are trapped in the catalyst cages [85]. Chen et al. reported that this increased the transition-state shape selectivity, hereby promoting the yield of ethylene [86].

Not only the catalyst pore size affects the coke formation, but also the acid strength and acid site density highly influences the rate of deactivation. By comparing the isostructural catalysts, H-SAPO-34 and H-SSZ-13, Bleken et al. revealed that higher acidity results in higher coking rates besides higher olefin production rates [87]. Because the acid strength has numerous effects on the MTO mechanism, this will be separately discussed in the next chapter.

In attempts to prevent coke formation, Cr or Ni can be incorporated in the MTO catalyst [88], [89]. These transition metals will decrease the acid strength, hereby decreasing coking rates and increasing the catalyst life time. Alternatively, the feed composition may be altered and water may be added to the catalyst to slow down the coking process. Water will adsorb to the acid site and decrease the possibility of secondary reactions [90]. If coking does occur and the catalyst is deactivated, the only solution is to burn the coke. However these high temperatures can harm the catalyst structure.

In conclusion, the hydrocarbon pool mechanism is nowadays widely accepted in the MTO research field. These HP species can be of the aromatic or aliphatic type. The production of olefins through an aromatic species can be described by the paring and side chain cycle. Depending on which type of catalyst is used during MTO, different HP species and different cycles will dominate. Once a lot of large HP species are formed the catalyst channels get blocked resulting in deactivation of the catalyst. By burning off coke the catalyst can be reactivated and the olefin production can continue [83]. On all levels of the MTO mechanism, the Brønsted acid strength has an effect. It influences the nature and reactivity of the HP compounds, partially determines the dominant routes and cycles and eventually also plays a role in the catalyst resistance to deactivation. Therefore the next chapter is devoted to the influence of acid strength on the MTO process for each zeolite and zeotype topology separately.

Chapter 3

Influence of zeolitic acid strength on MTO chemistry

The MTO mechanism has been discussed in the previous chapter. Herein a closer look is given to the zeolite and zeotype catalysts that are used in this process. Their ability to catalyze these MTO reactions is attributed to the presence of Brønsted acid sites. Therefore this chapter is devoted to the role of the zeolitic acid strength on the MTO process.

Zeolites are crystalline solids that form a framework with channels and cavities in which cations, water and/or other molecules may reside [91]. The word zeolite means "boiling stone", since water can be retained in the zeolite pores, this water can boil upon heating of the zeolite and steam will leave the solid material. A zeolite consists of silicon, aluminum and oxygen forming an open 3D framework structures built of SiO4 and AlO4 tetrahedra linked together by sharing all the oxygen atoms. This way a wide variety of structures is obtained. The elements from the tetrahedra aside from O are known as T-atoms.

Zeotype materials also exist. Just like zeolites, they consist of microporous frameworks. They differ from zeolites by using different type of T-atoms besides silicon, aluminum such as phosphorous, gallium, germanium, boron... Due to their microporous structure, zeolite and zeotype materials are often referred to as molecular sieves. A vast range of zeolite and zeotype catalyst exists. In general zeolite and zeotype materials are microporous frameworks consisting of T-atoms linked together with oxygen atoms. There are about 40 natural zeolites in the form of minerals and more than 150 synthetic zeolite and zeotype materials. They can be found in the atlas of zeolite structure types published by the international zeolite association structure commision (IZA-SC) [92]. Every known framework topology irrespective of its chemical composition is referred to by a three letter code which was assigned by the IZA-SC. In this chapter the CHA, MFI, AFI, BEA and TON topology will be discussed in more detail.

A lot of zeotype materials exhibit acid properties. They can possess Lewis and Brønsted acid sites. A Lewis acid site can accept an electron pair from a Lewis base (=electron pair donor), while a Brønsted acid can donate a proton to a Brønsted base (=proton acceptor). These acid

properties are introduced by substitution of T-atoms in the framework resulting in a negatively charged framework, which can be neutralized by a positive counter-ion. This master thesis focuses on the Brønsted acid sites.

A Brønsted acid site in a zeolite or zeotype material is typically an OH group where the proton acts as counter-ion compensating the negative charge introduced by substitution of a silicon atom with an aluminum atom, as represented in Figure 3.1. The hydroxyl group is located on one of the nearest neighbor oxygen atoms of the substitutional aluminum atom. A well-known class of zeotype materials is the silicoaluminumphosphate (SAPO) framework. Starting from a neutral aluminophosphate (AlPO) framework consisting of aluminum and phosphorous atoms linked with oxygen bridges, a Brønsted acid site is obtained by substituting an aluminum atom with a silicon atom as shown in Figure 3.1.

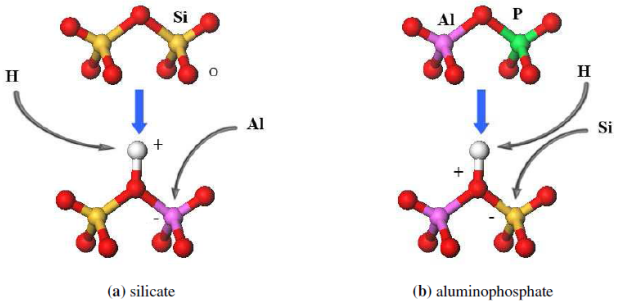

Figure 3.1: Creating brønsted acid sites by substituting a silicon atom by an aluminum atom in silicate (left), while a substitution of an aluminum atom with a silicon is needed to create an acid site in aluminumphosphate (right).

Depending on the chemical composition of the zeolite or zeotype material and the location of the Brønsted acid site, different acid strength is achieved in the framework. The stronger the Brønsted acid site, the more easily the proton of the acid site is donated and the faster they will protonate other species.

Another property is the acid site density, this is defined as the number of acid sites per surface unit. In zeolites the Si-to-Al ratio is linearly dependent with the acid site density, since the incorporation of each Al atom results in the creation of one Brønsted acid site. However in SAPO materials, the incorporated Si atoms tend to cluster [93], which leads to a lower acid site density than expected on the basis of the Si-to-(Al+P) ratio. It is expected that at high acid site density, the acid strength is lowered. For instance in the USY zeolite, it was proven that for a Si-to-Al ratio below 7 (for high acid site densities) the acid strength per site starts to decrease, whereas above 7 the acid site strength is more or less constant.

Furthermore, it must be stressed that a zeolite or zeotype molecular sieve can possess multiple types of acid sites, each with their own acid strength. Therefore, not only the total acid site density is important but also the number of sites of each acid strength available in the catalyst. This results in an acid site distribution. Chapter 5 describes how these acid properties can be determined experimentally and theoretically.

These acid properties also affect the conversion, selectivities and reaction rates in the MTO

process. Generally speaking, a higher Brønsted acid strength will result in a higher catalytic activity and thus a faster conversion, but with a sooner onset of coke formation. The acid site density also affects this coke formation, because a higher acid site density means that acid sites are closer to one another, enhancing the probability of secondary reactions. In the following sections, several topologies will be discussed, along with some experimental findings and theoretical insights into the effect of their acid strength on product selectivities, active pathways and catalyst life time in MTO. Finally, the goal of this master thesis is outlined.

3.1 CHA

The CHA topology is based on a 3-dimensional cage system represented in Figure 3.2. Its framework features cages with windows of 8, 6 and 4 T-atoms as seen on the left figure in Figure 3.2. The biggest sphere that can fit into the cages has a diameter of 7.37 Å. Due to the relatively small windows only spheres with a maximum diameter of 3.72 Å can diffuse through the framework along the a-, b- and c-axis. This means species such as isobutane (smallest diameter = 4.15 Å) are already too big to diffuse through the cages [37].

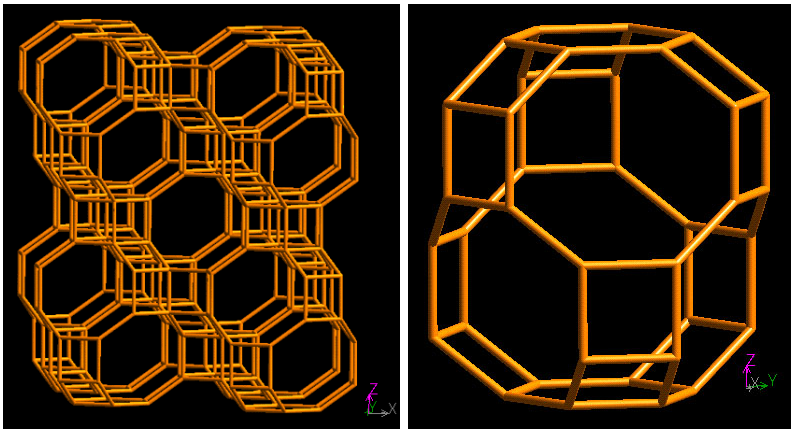

Figure 3.2: Chabazite (CHA) topology viewed along the [010] direction (left) and CHA cage viewed normal to the [001] direction (right) [94].

The most well-known zeotype material with CHA topology is H-SAPO-34. H-SAPO-34 is a typical example of a silicoaluminumphosphate. The CHA topology is also available in a more acidic form, namely in the zeolite H-SSZ-13. When trying to elucidate the role of zeolitic acid strength in MTO these two materials are often compared, since they have the same topology but contain different Brønsted acid strengths due to their different chemical composition.

Early studies showed that the acid strength affects the product selectivities in MTO to a lesser extent than the catalyst topology [95]. Yuen et al. fed methanol to CHA catalysts using different T-atoms, such as B, Ge, Al, to compare Brønsted acid sites with different acid strengths. They reported that the product over the CHA topology mostly contains C_2 to C_4 species and some C_{5+} species but no aromatics. This results from the small CHA cage windows that prevent aromatics from diffusing out of the cages. When comparing H-SAPO-34 with its more acidic

Table 3.1: Product selectivities in wt% for methanol conversion of H-SSZ-13 and H-SAPO-34 [95].

Component (wt%)	H-SSZ-13	H-SAPO-5
CH_4	3.86	1.40
C_2H_6	5.38	0.27
C_2H_4	27.81	53.80
C_3H_8	18.85	0.85
C_3H_6	32.40	35.15
n-butane	0.51	1.00
isobutane	0.00	0.00
1-butene	2.55	2.02
2-butene (*trans*)	1.55	2.80
2-butene (*cis*)	1.25	1.93
isobutene	0.00	0.00
C_{5+}	3.70	0.70
aromatics	0.00	0.00

equivalent H-SSZ-13, a higher amount of alkane species are observed in H-SSZ-13, as indicated in Table 3.1.

In 1999, Dahl et al. also compared several CHA type catalysts, two silicoaluminum samples with an Si-to-Al ratio of 7 and 25 and two H-SAPO-34 samples with an (Al+ P)-to-Si ratio of 10 and 30 [96] by streaming methanol over the catalysts for about two hours and analyzing the amount of hydrocarbons in the product stream with gas chromatography. Although no significant differences in the initial selectivities were observed between the catalysts, the deactivation rate was remarkably higher with increasing acid site density and acid strength, indicating that the catalyst's life time depends on its acid strength. Yuen et al. reported the longest time-on-stream for the mildly acidic H-SAPO-34, meaning that lower acidity leads to slower deactivation [95]. The acid site density also affects the catalyst life time. To achieve the maximum life time, an optimal acid site density must be found, which will depend on the operating conditions.

Bleken et al. also performed experiments on H-SSZ-13 and H-SAPO-34 and concluded like Yuen et al. and Dahl et al. that H-SAPO-34 reaches higher conversion than H-SSZ-13 at 400 °C. Bleken et al. measured the amount of methanol converted at different temperatures for the two materials, as shown in Figure 3.3 [87], [97]. This revealed that the optimum operating temperature for H-SSZ-13 is 350 °C instead of 400 °C, which is the optimum operating temperature for H-SAPO-34. This means that H-SSZ-13 exhibits a higher activity, which is consistent with its higher acid strength. However, at their optimum temperatures the maximum achievable methanol conversion is higher for H-SAPO-34 than for H-SSZ-13. This agrees with the findings of Yuen et al. and Dahl et al. who claimed that H-SAPO-34 is better suited for the MTO process.

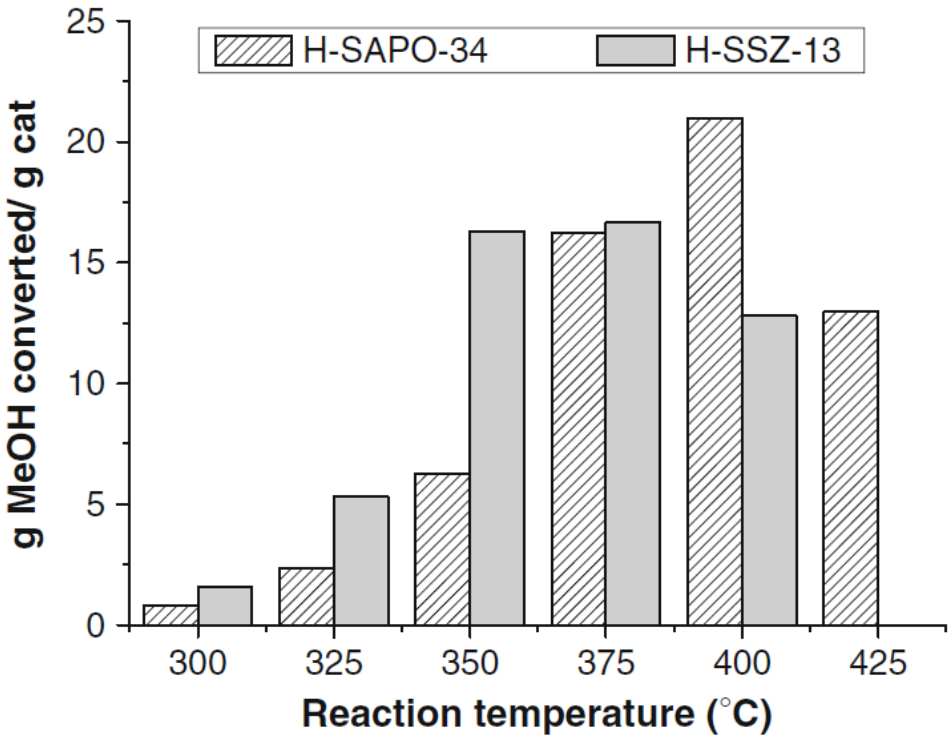

Figure 3.3: The total amount of methanol converted over 1 gram of H-SAPO-34 (striped bars) and H-SSZ-13 (fully colored bars) catalyst for increasing temperatures by the time the catalyst was deactivated to 20 % conversion [87].

The active HP species inside the CHA topology are considered to be aromatics. In both H-SAPO-34 and H-SSZ-13 polymethylated benzenes are active HP species, as well as some naphthalenic species [59]. Van Speybroeck et al. modeled several methylation reactions of these HP species via first-principle calculations in both materials. From these calculations, it was concluded that polymethylated benzenes do not experience transition state selectivity and that activation barriers towards methylation decrease with increasing number of methyl groups, which leads to increased rate of the methylation reaction. However, transition state selectivity was observed for polymethylated naphthalenes and aromatics containing even more rings. This means that the topology mostly defines the activity of the HP species. The effect of the acid strength difference between H-SAPO-34 and H-SSZ-13 was, however, reflected in the activation energies and consequently also in the reaction rates of the methylation reactions. The more acidic H-SSZ-13 catalyst showed methylation rates about three orders of magnitude larger than H-SAPO-34.

Qian et al. followed the MTO reactions through in situ UV–VIS micro-spectroscopy by tracking the HP species as a function of reaction time and temperature [98]. By using optical micro-photographs, they could also visualize the active area of the catalyst. Several effects of the acid strength and acid strength density are observed in their study. First, an effect was observed on the activation energies E_a for the formation of the PMB's, which is much lower in H-SSZ-13 due to its stronger acidity. Second, Qian et al. claim that the active zone in H-SSZ-13 during MTO is much wider due to the lower acid site density, since the formed HP species are more spread throughout the material, making it easier for methanol to access the active sites deeper in the

crystals. Whereas for H-SAPO-34 only a small outer rim of the crystal is used, the active rim for H-SSZ-13 is broader. Lastly, a faster deactivation of H-SSZ-13 also results from the higher acid site strength, as was already observed in multiple studies.

Wu and Hensen further investigated the effect of acid site density on the conversion and deactivation during MTO. They synthesized mesoporous H-SSZ-13 with an increased Si-to-Al ratio of 50 instead of 20. This lower acid site density has a positive influence on the catalyst lifetime and lowers the deactivation rate [99]. By increasing the mesoporosity even more, an even better time-on-stream was achieved for H-SSZ-13. However, a decrease in catalyst life time is observed for mesoporous H-SAPO-34 catalyst when compared to the regular H-SAPO-34. This might be explained by the better use of the microporous spaces in regular H-SAPO-34. Due to the lower acid strength, the rate of coke formation is lower and the micropores get blocked much more slowly by carbonaceous species. This means that there is no advantage in creating mesopores, since the use of the micropores is already very efficient.

This section highlights the effects for the zeolitic acid site density and strength in CHA type materials. However, this effect has been investigated for several other catalyst topologies as well such as MFI and AFI which will be discussed in the next sections.

3.2 MFI

The MFI topology consists of a network of sinusoidal and straight channels. The topology is represented in Figure 3.4 along with its typical 10 ring straight channels. Next to these 10 rings, MFI also contains windows of 6, 5 and 4 T-atoms. The biggest sphere that can fit into the topology has a diameter of 6.36 Å. Spheres with a maximum diameter of 4.72 Å can diffuse along the a-axis while only maximum diameters of 4.42 Å are suitable to diffuse in the b and c directions.

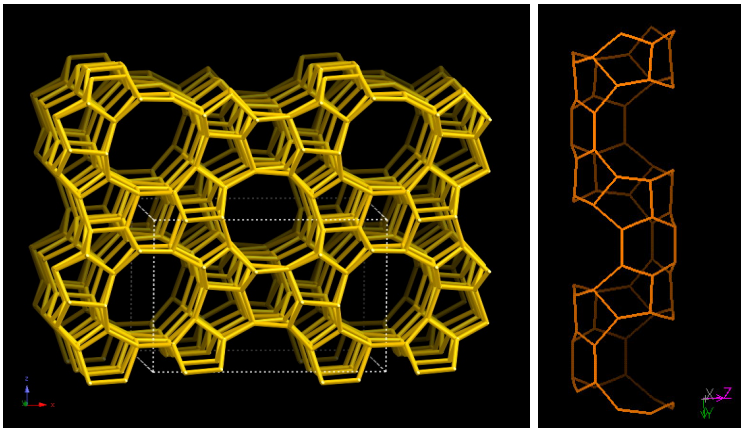

Figure 3.4: MFI topology viewed along the [010] direction (left) and a typical MFI 10 ring straight channel (right) [94].

The most well-known zeolite from the MFI family is H-ZSM-5. This is one of the archetypal MTO catalysts. As mentioned in the previous chapter, the dual cycle mechanism plays an

important role in H-ZSM-5 and contains both aliphatic and aromatic HP species. The ethylene production is attributed to the lower methylbenzenic HP species, while the C_{3+} is formed from subsequent methylation and cracking of alkenic HP species. Typical product distribution after methanol conversion over H-ZSM-5 contains much more propylene than ethylene and a broad range of higher hydrocarbon species. These higher hydrocarbon species are the result of the high acid strength of H-ZSM-5, which facilitates secondary reactions.

To maximize the propylene selectivity over H-ZSM-5 the acid strength could play a key role. This effect was studied by Lee et al [100]. They controlled the acid strength of H-ZSM-5 by incorporation of Fe^{3+} and/or Al^{3+} and kept the acid site concentration equal in all samples. As a result, the H-[Al]-ZSM-5 had the highest acid strength and H-[Fe]-ZSM-5 the lowest, whereas the sample with both Fe^{3+} and Al^{3+} had an acid strength in between the two other samples. The best catalytic performance is obtained with the moderate sample, H-[Fe,Al]-ZSM-5. It achieved the highest propylene selectivity of all three samples and was most active at a temperature of 500 °C. This article showed that incorporation of Fe^{3+} and Al^{3+} formed the key towards controlling the MFI acid strength and optimizing the propylene selectivities.

Next to Fe^{3+} and Al^{3+} incorporation, Valle et al. studied the influence of Ni incorporation in H-ZSM-5 and concluded that Ni helps decreasing the acid strength of each site and also the total amount of acid sites [101]. When looking at the catalytic activity, a reduction was reported for the Ni containing samples as the normal maximum conversion over H-ZSM-5 could not even be reached. Beside the lower conversion, a higher selectivity towards light olefins is obtained by Ni incorporation. This results in similar conclusion as for Fe, namely the incorporation of these metals results in a reduction of the acid strength and an increase in the olefin selectivity. On the downside the Ni containing samples suffer from higher deactivation rates than the standard H-ZSM-5 catalyst. On the other hand, applying successive regeneration cycles reveals that Ni has a positive effect on the catalyst performance, since after each cycle the original catalyst activity is achieved, while for standard H-ZSM-5 the conversion after each cycle deteriorates due to dealumination.

Another factor influencing the MFI acid strength is the type of binder used for industrial catalysts. Industrial zeolite catalysts are prepared by embedding the zeolite crystals in a matrix by using a binder material such as alumina, silica or natural clay. These binders are needed to obtain the desired pellet shape and the required mechanical strength for industrial applications. They are not fully chemically inert and tend to alter physiological properties of the catalyst, such as the Brønsted acid strength. Different binders were tested and the resulting acid strength was measured using ammonia temperature programmed desorption (TPD) (for more information on this technique see subsection 5.1.4) [102]. After investigation of silica, alumina and aluminum phosphate solution binders (APS), it appears that the use of 10 wt% APS results in a significant increase in propylene selectivity by decreasing the amount of strong acid sites. However the mechanical strength was not optimal. Therefore, binary binder systems using 10 wt% APS and either silica or alumina are recommended. These binders result in comparable propylene selectivities as for the single binder system but have an increased mechanical strength.

It is interesting to also compare the two archetypal MTO catalysts, since H-SAPO-34 contains

smaller pores and is also less acidic than H-ZSM-5. The latter was confirmed by comparing their shift in the OH stretching frequency upon CO adsorption at -196 °C (this technique is explained in chapter 5). For H-SAPO-34 a shift of 270 cm^{-1} [103] was found whereas a shift of 300 cm^{-1} was reported for H-ZSM-5 [104]. This higher shift means that there is substantially more interaction between the adsorbed CO and the acid site, resulting from a higher acid strength.

In Figure 3.5 the product selectivity of H-ZSM-5 is compared with that of H-SAPO-34 [6]. This clearly shows that the overall light olefin production is highest over H-SAPO-34. This can be explained by the smaller pore sizes of the CHA topology favoring smaller products, whereas the moderate acid strength of H-SAPO-34 reduces the occurrence of secondary reactions, such as hydride transfer reactions, which result in undesired paraffinic species. H-SAPO-34 has a lower acid strength than H-ZSM-5. These two effects yield a higher light olefin production for H-SAPO-34. On the downside, H-SAPO-34 is much more prone to deactivation than H-ZSM-5, among others due to its smaller pore size. While the inside of the H-SAPO-34 crystals coke very easily, the coke in H-ZSM-5 grows only at the outside of the crystals (cf. section 2.6), resulting in a superior catalyst life time for H-ZSM-5 [68]. This means that in an industrial setting H-SAPO-34 must be much more frequently regenerated than H-ZSM-5.

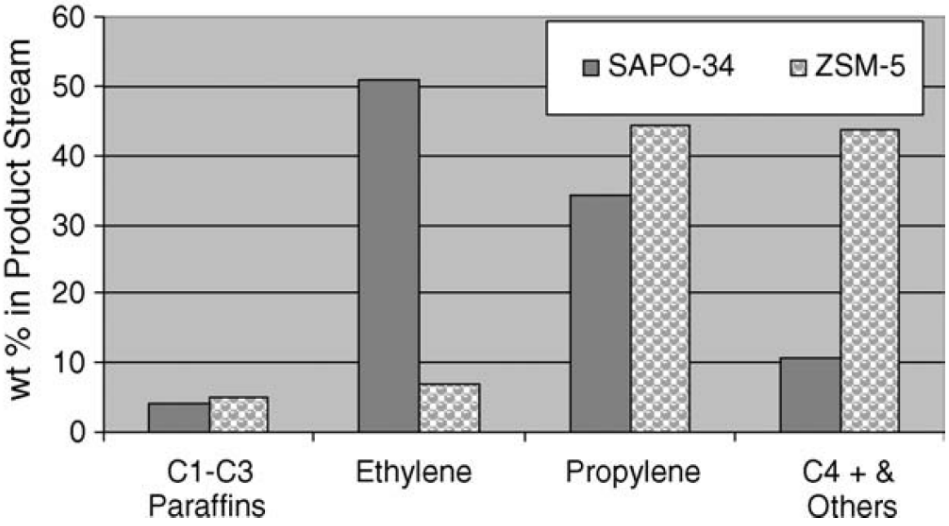

Figure 3.5: Product distribution over H-SAPO-34 (dark grey) and H-ZSM-5 (light grey) after methanol conversion at maximum ethylene mode [6].

3.3 AFI

The pore system of the AFI topology consists of one-dimensional 12-ring channels being open to the exterior, as shown on Figure 3.6. With its 12, 6 and 4 rings, AFI has similar diameters of cavities as in CHA. However due to the one-dimenional channels diffusion of bulkier species, such as benzene and toluene, in and out of the structure is possible, whereas in CHA these species are subject to higher diffusional constraints. The maximum sphere that fits in the AFI framework has a diameter of 8.30 Å and species with a maximum diameter of 7.42 Å can diffuse

along the c-axis.

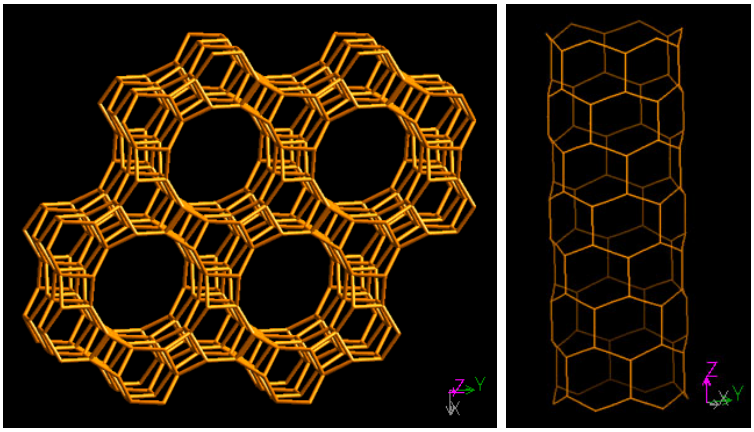

Figure 3.6: AFI topology viewed along the [001] direction (left) and a typical AFI 12 ring straight channel (right) [94].

A typical AFI topology is found in H-SAPO-5. This catalyst, with a OH stretching frequency shift of -268 cm^{-1} upon CO adsorption at -196 °C, possesses comparable acid strength as H-SAPO-34 [51]. However its structure allows feeding of larger molecules, implying that this catalyst can be used as a model for H-SAPO-34 for mechanistic studies as it allows co-feeding of several bulky aromatic reaction intermediates. To elucidate the effect of zeolitic acid strength on the MTO process, H-SAPO-5 is compared with H-SSZ-24, which is the more acidic zeolite equivalent of H-SAPO-5 with its OH stretching frequency shift of -317 cm^{-1} upon CO adsorption at -196 °C [71]. Both H-SAPO-5 and H-SSZ-24 are only used in research and do not have any industrial applications with the field of MTO.

Detailed experimental studies on H-SAPO-5 and H-SSZ-24 have been performed by Westgård Erichsen, Svelle, and Olsbye [51], [71], [105]. Firstly their co-feeding experiments of methanol and benzene over H-SAPO-5 showed a shift in product selectivities towards light olefins in comparison with pure methanol feed. This means that if aromatic species are present in sufficient amounts, the arene cycle can contribute to the production of ethylene and propylene. On the other hand heavier alkenes are more likely to be formed by the alkene cycle, since their selectivities did not significantly shift. Secondly, they performed isotopic labeling experiments in H-SAPO-5, hereby co-feeding ^{13}C-methanol and ^{12}C benzene. This revealed that for the largest ethylene fraction contained one labeled C atom and most propylene molecules contained 2 ^{13}C atoms, while for isobutene and isopentene the largest fractions contained only labeled C atoms. As shown in Figure 3.7, this can be explained by the presence of 2 types of mechanisms arising from the arene cycle: either the paring cycle is preferred or the exocyclic cycle. The former will lead to incorporation of all but one labeled C atom and the latter will lead to species fully built out of ^{13}C atoms. The labeling pattern in ethylene and propylene are consistent with the paring cycle. For C_{4+} alkenes the labeling pattern is dominated by the exocyclic mechanism. This article is the first to find proof of the contributing paring cycle in the ethylene formation from polymethylated benzene intermediates [51]. Furthermore, in comparison to the wide pore H-beta zeolite (see section 3.4), the C^{13} incorporation in the alkene species was higher than in the retained polymethylated benzenes over H-SAPO-5. Since they are both wide pore catalysts, the

shift from arene-based mechanism to a predominantly alkene-based mechanism in H-SAPO-5 is attributed to its lower acid strength.

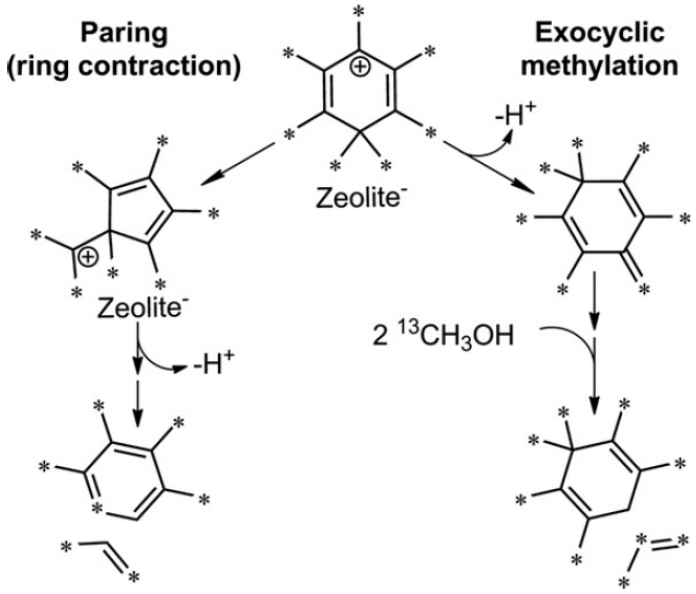

Figure 3.7: Methylation in H-SAPO-5 mostly proceeds via paring (a.k.a. ring contraction) for light olefins resulting in all but one C^{13} atoms (left), while heavier olefins are produced via an exocyclic mechanism incorporating only C^{13} atoms (rigth) [51].

After this thorough study of the product selectivities over H-SAPO-5, a comparison was made with H-SSZ-24 [71]. The results for a methanol conversion of 20 % and 60 % at 350 °C are shown in Figure 3.8. Over H-SSZ-24 significantly higher amounts of aromatics are produced and a higher conversion towards C_1 - C_3 products is obtained than over H-SAPO-5. H-SAPO-5 clearly produces much higher amount of C_{4+} fractions. In both catalysts the C_4 fraction was dominated by isobutyl species. The non-aromatic fraction in H-SSZ-24 contained mostly paraffinic species, whereas in H-SAPO-5 only limited amounts of parafins were observed. These findings are in contrast with the product selectivities reported by Yuen et al., who claimed there are no differences between H-SAPO-5 and H-SSZ-24 in selectivities. However their experiments were conducted at full conversion, resulting in the thermodynamic most stable products.

When performing isotopic labeling experiments by co-feeding ^{13}C methanol and ^{12}C benzene, the C_2 - C_4 alkene formation over H-SSZ-24 at 250 °C proceeds mostly via polymethylated benzene intermediates and at 300 °C this mechanism also partly contributes to the products. In H-SAPO-5, only ethylene and propylene formation can be attributed to the polymethylated benzene species. The more random incorporation of labeled ^{13}C in isobutene suggest that these species are formed through successive methylation and cracking of alkenes rather than only through polymethylated benzenes.

When looking at the methylation rates in the two isostructural materials, methylation reactions were found to proceed more rapidly in the more acidic H-SSZ-24 material [106]. During co-feeding experiments of methanol and benzene, the methanol feeding rate was varied. These experiments showed that when increasing the methanol partial pressure with respect to a constant

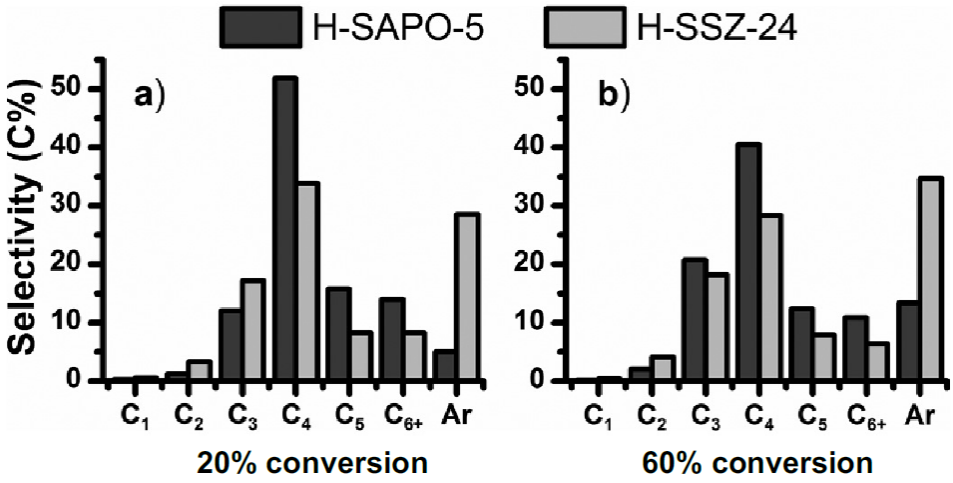

Figure 3.8: Product selectivities for H-SAPO-5 (dark gray) and H-SSZ-13 (light gray) at a methanol conversion of 20 % (left)and 60 % (rigth) at 350 °C [71].

benzene partial pressure, the toluene formation rate decreases simultaneously with an increasing net production rate of other aromatics in H-SSZ-24, whereas in H-SAPO-5 this decrease is coupled to an increase in the net production rate of aliphatic compounds, as shown in Figure 3.9. A comparison was made between the rates during co-feeding experiments of methanol and benzene and co-feeding experiments of methanol and propylene. A significantly higher methylation rate of benzene compared to propylene was observed in H-SSZ-24. However in H-SAPO-5, the rates of benzene and propylene methylation appeared to be similar. These experiments show that there is a significant influence of the acid strength on the reaction rates in MTO hereby determining the dominant HP species. To fully understand this influence, the next step is to perform theoretical calculations to obtain further mechanistic insight into MTO. Molecular dynamics simulations were performed of the co-adsorbed complexes of methanol with benzene and with propylene. As expected, the probability to form protonated methanol was higher in the more acidic H-SSZ-24. As consistent with the experiments the probability for methanol protonation increased when co-adsorbed with benzene compared to co-adsorption with propylene. This increasing trend was not observed in H-SAPO-5. Additionally, the probability to find pre-reactive complexes of methanol and benzene was also higher than for methanol and propylene in H-SAPO-5. In contrast, in H-SAPO-5 the formation of a pre-reactive complex with propylene appeared to be more likely. This work shows the importance of molecular dynamics simulations to unravel the adsorption behavior of guest molecules in large pore AFI materials and reveal the effect of acid strength on the MTO conversion.

3.4 Other catalyst topologies

For completeness, two other type of catalyst topologies used in the MTO research field are briefly discussed in this section. The BEA and TON topology are used in the MTO process for academic purposes only.

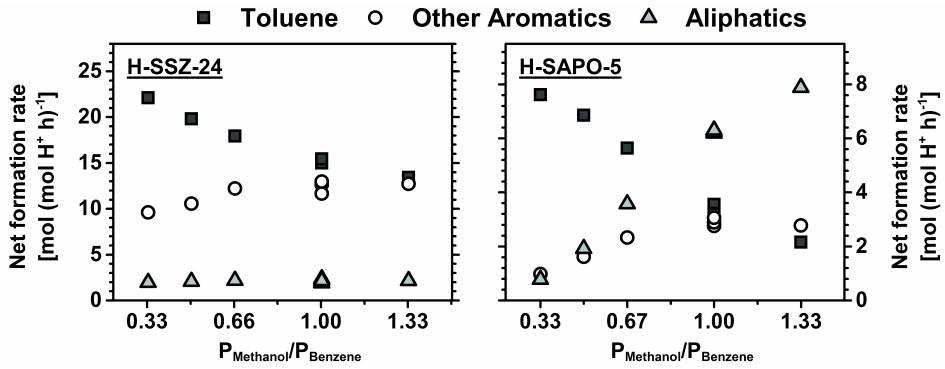

Figure 3.9: Net rates of formation of the main product groups during co-feeding of benzene and methanol as a function of the methanol to benzene molar feed ratio over H-SSZ-24 (left) and H-SAPO-5 (right) at 250 °C [106].

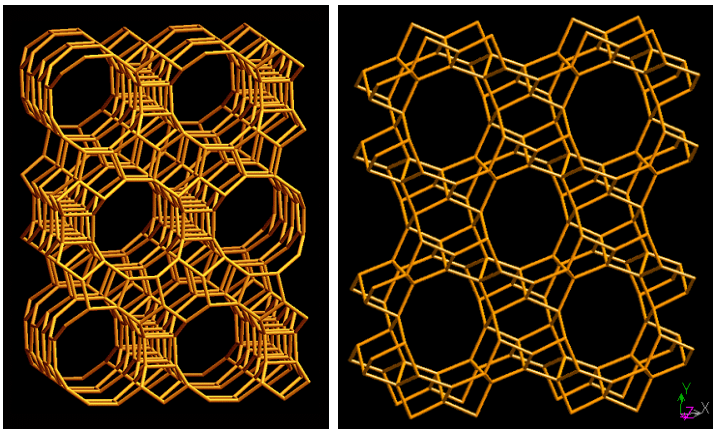

Figure 3.10: BEA topology viewed along the [100] direction (left) and TON topology viewed along the [001] direction (right) [94].

The BEA type catalysts are three-dimensional wide pore catalysts, as shown on the left side of Figure 3.10. They consist of large 12-ring channels perpendicular to one another. Next to these large channels, they also contain windows with 6, 5 and 4 T-atoms. Just like in AFI, these large channels allow co-feeding experiments of methanol and larger hydrocarbon species, which can help get insight into the reaction mechanism. A downside of these large channels is that bicyclic molecules are easily formed from PMBs and act as coke precursors [107]. Therefore, this catalyst is very sensitive to deactivation. That is one of the reasons why BEA type catalyst are industrially irrelevant.

A typical BEA catalyst is H-beta. The product mixture over this catalyst during methanol conversion meanly consists of propylene and higher alkenes. The preferred HP species are penta- and hexamethyl benzene and heptamethylbenzenium cation, however the alkene cycle also contributes to the product distribution [64], [67].

In the study of Aguayo et al. several beta type catalysts are compared with H-SAPO-11, H-SAPO-18 and H-SAPO-34 to elucidate the effect of the acid strength and acid site density [108]. The initial conversion is clearly affected by the total number of acid sites: samples with the

same catalyst structures but lower number of acid sites exhibited very low initial conversions. This was also reported by Dai et al., who did a profound study on the effect of acid strength and topology by comparing different silicoaluminumphosphate molecular sieves [109].

Furthermore Aguayo et al. claim that the selectivity to olefins is not determined by the acid strength and acid site density, but by the pore sizes [108]. H-beta yields very little olefins since its pore size allows the growth of larger paraffinic species. This is also partly the result of its low acid strength. Bortnovsky and co-workers state that to have a high cracking capacity, very high acid strength must be present in the catalyst at a low acid site density [110].

The effect of acid strength and acid site density on the deactivation rate during MTO has been reported many times [68], [87], [96], [99], [103]. In the aforementioned study of Aguayo et al., they report that the deactivation is the result of an interplay between topology and acid properties [108]. When decreasing the pore size, the production of heavy hydrocarbons that are retained on the porous structure is also lowered. Moreover, the production of these heavy hydrocarbons and more precisely the evolution towards polyaromatic species can be further reduced by decreasing the acid site density and acid strength.

The TON type catalysts feature one-dimensional 10-ring channels that are slightly smaller than the MFI channels. The TON topology also possesses windows of 6 and 5 T-atoms. Due to these small channels the arene cycle is suppressed and the alkene cycle is favored [70], [111]. The most well-known catalyst with the TON topology is H-ZSM-22. The product distribution for methanol conversion over H-ZSM-22 consists solely of branched alkenes and no aromatics.

Although the TON topology is often used in research, not much is reported on its acid strength. The acidic properties of H-ZSM-22 were investicated by Borade et al. These authors reported that the Brønsted acid site possess a higher acid strength in H-ZSM-22 than in H-ZSM-5 when both acid sites are induced by Al [112]. The effect of this acid strength on the stepwise and concerted pathway from methanol to DME in H-ZSM-22 was modeled by Moses and Nørskov [113], as explained in section 2.5. To elucidate the effect of the acid strength on these competitive pathways, they introduced different metals (Al, Ga, In) to obtain different Brønsted acid strengths. For all samples, they found that the stepwise pathway was dominant. Therefore, they concluded that the dominant pathway is independent of the acid strength in H-ZSM-22.

3.5 Objectives of this master thesis

This master thesis focuses on the MTO process. Next to the Brønsted acid site, arene and alkene-like HP species co-catalyze the reactions during the MTO conversion. In the mechanism, methylation reactions play a crucial role. Therefore, this master thesis selected the methylation of aromatics as a key reaction to get insights into the acid strength effects on the MTO conversion. The methylation of aromatics with a different number of methyl groups (benzene, toluene and o-xylene) will be compared inside H-SAPO-5 and H-SSZ-24. Both methanol and dimethyl ether are used as methylating agent, since DME is typically formed as first step in the MTO mechanism and is therefore abundantly available in the MTO catalyst.

It is opted to work with the AFI topology instead of the architypal H-SAPO-34 catalyst, since these AFI catalysts allow feeding of larger molecules and are often studied experimentally. Moreover, AFI catalysts have similar dimensions as CHA, but only contain one-dimensional channels instead of the complex three-dimensional CHA cages. With a similar Brønsted acid strength and similar dimensions, H-SAPO-5 can be considered as a model for H-SAPO-34. Furthermore, to elucidate the influence of acid strength H-SAPO-5 and H-SSZ-24 may be compared, since they only differ in chemical composition, which results in stronger Brønsted acid sites for the H-SSZ-24 molecular sieve.

With the use of molecular dynamics and a periodic catalyst model, the adsorption of a single reactant for the methylation reaction onto the Brønsted acid site is studied in both catalysts and for each methylating agent and aromatic. These simulations are performed at a typical MTO temperature (623 K) and pressure (1 atm), while also taking into account the interaction with the catalyst framework.

Furthermore, the co-adsorption complexes preceding the methylation reactions are studied in the AFI materials. During these molecular dynamics simulations, the adsorption behavior of the methylating agent, accompanied by an aromatic, is studied at the aforementioned temperatures and pressure.

As final step, the methylation reaction itself is modeled by using metadynamics. As a test case, the reaction of toluene and methanol is considered in the two AFI materials. A comparison between methanol and DME as methylating agents will also be made by performing a metadynamics simulation in H-SSZ-24 of the methylation reaction of toluene with DME.

In conclusion, the final goal of this master thesis is to get insights into the effect of the zeolitic acid strength on the MTO conversion in the AFI materials H-SAPO-5 and H-SSZ-24. This is achieved by performing dynamic simulations of the adsorption and co-adsorption complexes of all reactants involved in a methylation reaction and by performing metadynamics simulations to get insight in the difference in reactivity of a methylation reaction.

Chapter 4

Modeling zeolite-catalyzed reactions

As stated in the objectives of this thesis, it is desired to perform quantum mechanical (QM) calculations on the methylation reactions inside H-SAPO-5 and H-SSZ-24 to reveal the influence of acid strength on the reactivity towards these very important MTO reactions. Before starting with the modeling of reactions in the MTO process, an adequate model must be selected to describe the catalyst topology. The catalyst in the MTO process inherently possesses a supramolecular nature, as discussed in chapter 3, which imposes challenges to theoretical modeling. The selection of the catalyst is discussed in section 4.1.

Next to picking out a catalyst model, the level of theory must also be selected (cf. section 4.2). As a final step the type of methods required to obtain the desired data are discussed in section 4.3.

4.1 Zeolite models

It has been proven that taking into account the zeolite topology, in which the modeled reactions take place, is of utmost importance to obtain accurate results. Commonly used zeolite models consist either of a cluster of zeolite atoms or contain the zeolite unit cell which is extended infinitely by applying periodic boundary conditions. Thus, the catalyst models can be divided in two categories: finite cluster models and periodic models. In reality zeolites possess irregularities i.e. defects. However, during theoretical studies the catalyst is simplified by an ideal model.

4.1.1 Finite cluster model

As a first attempt, catalysts were described by a finite cluster model. In this cluster model, part of the catalyst topology is cut out of the catalyst structure and bonds at the edge are broken. These broken bonds are resaturated by forming new bonds at the edge with auxiliary atoms, such as hydrogen. To keep the boundary of the cropped cluster fixed in space and mimic the rigidity of the zeolite, an infinite mass is attributed to the auxiliary atoms[78]. The major drawback of the saturation with infinitely heavy atoms is that breathing of the zeolite framework is no longer

allowed. Breathing is important, since it allows the framework to expand or contract, hereby facilitating diffusion or reactions occurring inside of the catalyst [63].

The finite clusters are categorized by the number of T atoms contained in the cluster. T atoms (Si, Al or P) are connected by oxygen atoms in the zeolite framework. The first studies reporting the use of finite clusters, applied very small clusters. Blaszwoski and van Santen used clusters containing only one T-atom as shown in Figure 4.1a [114]. Later on they also used clusters containing three to four T-atoms [115]. These very small clusters only contained the T-atoms of the active site as shown in Figure 4.1b. With such small clusters the catalyst active site could be incorporated in the QM calculations, but the interactions between the zeolite walls and the reactive species were not modeled [115]. For small species this is not a problem. However, for bulky species neglecting the topology will lead to inaccurate results. The effects of topology on the reaction barriers may be very pronounced and the deviation on the barriers resulting from the very small cluster models ranges from 70 to 140 kJ mol^{-1} [79].

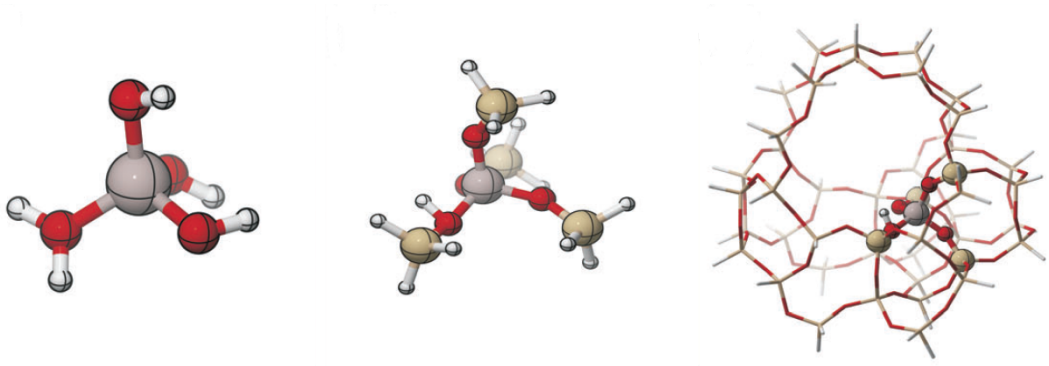

(a) **(b)** **(c)**

Figure 4.1: A 1T (a), 5T (b) and 46T (c) finite cluster model representing H-ZSM-5 with one acid site. Taken from ref. [78].

Once more computational power became available, extended finite clusters could be used and it became possible to properly account for the catalyst topology. Figure 4.1c shows a 46 T cluster of H-ZSM-5, which gives a good representation of the catalyst cage surrounding the active site. Selecting the size of the finite cluster involves a trade-off between the obtained accuracy and the required computational effort. The larger the cluster, the more computationally demanding it gets.

To reduce the computational effort, a lower level of theory can be used. Therefore often multiple methods are combined in one simulation: the atoms taking part in the reaction are computed at a high level of theory, while the surroundings are calculated at a lower level of theory. One typical example is an ONIOM (Our Own n-layered Integrated molecular Orbital and molecular Mechanics) calculation [116]. The modeled system in the ONIOM simulation is divided in layers and a different level of theory is assigned to each layer. Here, a QM method can be combined with a less computational demanding QM method or with a molecular mechanics (MM) method. Another possibility is to combine a Hartree-Fock (HF) method with a post-HF method or with density functional theory (DFT) (for more information concerning these methods see section 4.2).

Dapprich et al. compared the ONIOM(MP2:HF) method with ONIOM(CCSD(T):HF) and ONIOM(CCSD(T):MP2), herein the first methods are post-HF methods used for the crucial atoms, while the last method is used for the remaining atoms [117]. Svennson et al. even divided their molecular system into three layers, one active, semi-active and non-active layer [116]. Their method is referred to as ONIOM3(CCSD(T):MP2:MM3): the active part is modeled with the coupled cluster method CCSD(T), the semi-active part with the perturbation method MP2 and the last part with the use of the MM3 forcefield. MM methods can only optimize atom positions but not calculate chemical reactions or alter the topology, since the electronic structure problem is not solved and charges are kept fixed. Some other examples of forcefields are AMBER (Assisted Model Building with Energy Refinement) [118], CHARMM (Chemistry at HARvard Macromolecular Mechanics) [119] and GROMOS (GROningen MOlecular Simulation) forcefields [120], [121]. These are frequently used for simulating biomolecules.

4.1.2 Periodic models

Another way to describe the catalyst's topology is a periodic model. Herein the unit cell is used as building block. The coordinates of the standard unit cells of most of the zeolite topologies can be found in the IZA database of zeolite structures [94]. When several unit cells are used, the building block is referred to as a supercell. Using the periodic boundary conditions, this building block is then periodically extended in all three dimensions to obtain an infinitely large catalyst crystal. This is shown in Figure 4.2, where the same clusters from Figure 4.1 are incorporated in the periodic model.

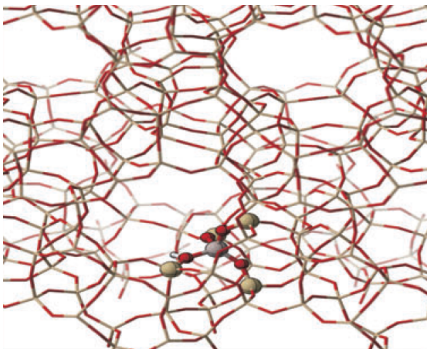

Figure 4.2: Representation of a H-ZSM-5 catalyst by using periodic boundary conditions in which each unit cell contains one acid site. Taken from ref. [78].

With this type of model, the true periodic nature of a catalyst is captured [122]. Many factors of the catalyst topology are included, for instance the shape of the channels and pores, the location of the acid site and the framework flexibility.

These periodic models require more computational effort and the search algorithms for transition states are less established. Extended cluster models can be used with a wider range of computational methods including the most recent functionals [122]. However, the use of periodic boundary conditions is well implemented in CP2K [123]. CP2K is the computer code used in this master thesis to perform the first-principles molecular dynamics calculations. In section 4.3

molecular dynamics will be explained. For a more detailed discussion of CP2K and the used methods in this thesis, the reader is referred to section 4.4.

Furthermore, real catalysts also contain defects in their framework [124]. These are either physical defects such as mesopores or chemical defects such as unexpected atom substitution [125]. This heterogeneous aspect of a zeolite framework can not yet be included in a fully periodic structure and remains challenging in the future.

In conclusion, both the extended cluster approach and the periodic approach have their own strengths and weaknesses [122]. A perfect catalyst model has not yet been found and computational constraints are still limiting the possibilities to describe a real catalyst.

4.2 Quantum mechanical methods

Quantum mechanical (QM) or ab initio methods for the determination of the electronic structure of a molecular system are based on first principles. They attempt to solve the Schrödinger equation to find the nuclei and electron positions of the system and their corresponding energy levels. The Schrödinger equation can be interpreted as an eigenvalue problem in which the eigenfunction is the system's wave function. The Schrödinger equation is shown in Equation 4.1, where $\hat{H}$ is the Hamiltonian, ψ the system's wave function and E the total energy of the system. The Hamiltonian is equal to the sum of the kinetic energy $\hat{T}$ and potential energy $\hat{V}$ of the system, as shown in Equation 4.2. The kinetic energy consist of a nuclei contribution $\hat{T}_n$ and an electron contribution $\hat{T}_e$, while the potential energy consists of three contributions namely, one for the nuclear-nuclear repulsion $\hat{V}_{nn}$, one for the nuclear-electron attraction $\hat{V}_{ne}$ and one for the electron-electron repulsion $\hat{V}_{ee}$.

$$\hat{H}\psi = E\psi \tag{4.1}$$

$$\hat{H} = \hat{T} + \hat{V} = \hat{T}_n + \hat{T}_e + \hat{V}_{nn} + \hat{V}_{ne} + \hat{V}_{ee} \tag{4.2}$$

4.2.1 Born-Oppenheimer Approximation

To solve the Schrödinger equation, the Born-Oppenheimer approximation is often applied [126]. This approximation assumes that the time scale for the motion of nuclei is much longer than that of electrons, since nuclei are much heavier than electrons. Working within the Born-Oppenheimer approximation allows solving the Schrödinger equation for the nuclei and for the electrons separately. However due to the nuclear-electron attraction term in the Hamiltonian, it remains a coupled problem.

To solve the electronic Schrödinger equation, the nuclei positions must be kept fixed. The result of this equation is a set of eigenfunctions and eigenvalues. The surfaces created by each electronic eigenvalue are known as Born-Oppenheimer surfaces. On each of these surfaces the nuclear Schrödinger equation will be solved and this will yield a set of energy levels corresponding

to rotations and vibrations of the nuclei. An example of Born-oppenheimer surfaces as function of the nuclear coordinates is giving in Figure 4.3 with the indication of the vibrational energy levels in red and the rotational in blue.

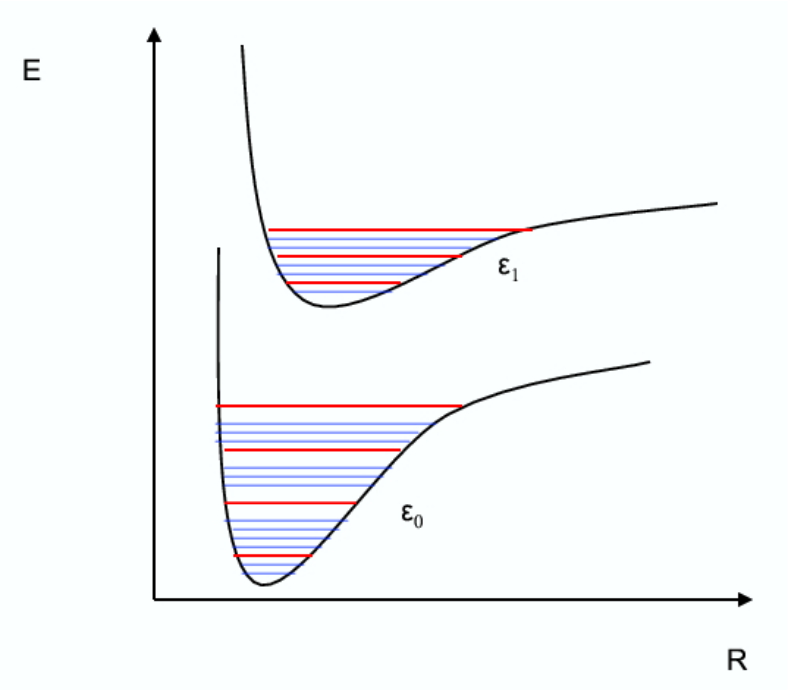

Figure 4.3: Born-Oppenheimer surface of the ground state ϵ_0 and of the first excited state ϵ_1 for a diatomic molecule with vibrational (red lines) and rotational (blue lines) energy level [127].

Finding the many electron wave function $\psi_{e,n}$ from the electron Schrödinger equation is very challenging and this problem is referred to as the electronic structure problem. Several methods are available to solve this electronic structure problem, such as (extended or post-) Hartree Fock (HF) methods, density functional theory (DFT) etc. After a brief discussion of the HF method, the DFT method is explained in more detail, since this method will be applied in this master thesis.

4.2.2 Hartree Fock

The HF method is a true ab initio method for solving the Schrödinger equation using the Born-Oppenheimer approximation. A true ab initio method starts from basic physical laws, without using any experimental input. As mentioned before, the electronic correlation term causes the most problems in solving the Schrödinger equation. Therefore during HF approach, the system is approximated by an independent particle model in which the interaction between the electrons is substituted by a mean-field [128]. This means that each electron moves in an mean-field induced by the other electrons. This field consists of a Coulomb potential operator and an exchange potential operator. The Coulomb operator accounts for the classical electrostatic repulsion between two electrons, while the exchange operator is the result of the Pauli exclusion principle and is purely quantum mechanical. This principle states that electron with the same

spin cannot be located on the same orbital.

Due to the use of the mean-field, the electron correlation energy is neglected. This results in an overestimation of the true energy of the system, because the HF energy is too high since stabilization due to electron correlation was not taken into account. When a complete basisset (see subsection 4.2.4) is used, meaning that all orbitals are accounted for, the lowest possible HF energy will be found by solving the HF equations. The difference between the true energy of the system and this HF limit is equal to the electron correlation energy.

4.2.3 Density Functional Theory

A way to include the electron correlation energy is by solving the Schrödinger equation with DFT. DFT is an alternative method for solving the electronic structure problem. It is computationally very attractive and has the possibility to include correlation, which is not possible with the HF method.

A state of a system is completely defined by its wave function, hence all the system's properties can be derived from its wave function. However a system in its ground state [1] is also unambiguously defined by its energy density ρ. Therefore as an alternative for the wave function the system's properties can also be described by a functional[2] of the energy density.

DFT describes the Hamiltonian from the Schrödinger equation as sum of a universal functional, which is purely electronic, and an external potential. By solving the Köhn Sham equations the exact electronic density could be calculated on the condition that the exchange-correlation potential is exactly known. However the true form of this potential is not known. As long as this potential needs to be approximated, DFT cannot be considered as an exact or ab initio method. DFT is considered somewhere in between ab initio and semi-empirical methods, since the exchange-correlation energy is often determined in a semi-empirical way. Due to this fact, the correlation energy is over- or underestimated and unlike the HF method, there is no way of knowing whether the exact energy is higher or lower than the energy from DFT.

In general, the DFT scheme for solving the electronic structure problem is exact. The DFT scheme and HF method are alike, since the Köhn Sham (KS) equations used in the DFT to solve the electronic structure problem look very similar to the HF equations. However, in comparison to the HF equations the KS equations account for correlation.

The success of DFT relies mainly on finding a good form for the universal functional. This search comes down to finding a correct expression for the exchange-correlation energy functional. The available functionals can be categorized on the basis of the accuracy. This pool of functionals is often represented through the Jacob's ladder of chemical accuracy, shown in Figure 4.4 [129]. Going up the ladder, each class of functionals gives rise to a more accurate approximation of the true exchange correlation energy functional. Often the exchange and correlation energy is described by two different functionals.

[1] The ground state is the lowest possible energy state of a system.

[2] A functional is a function of a function

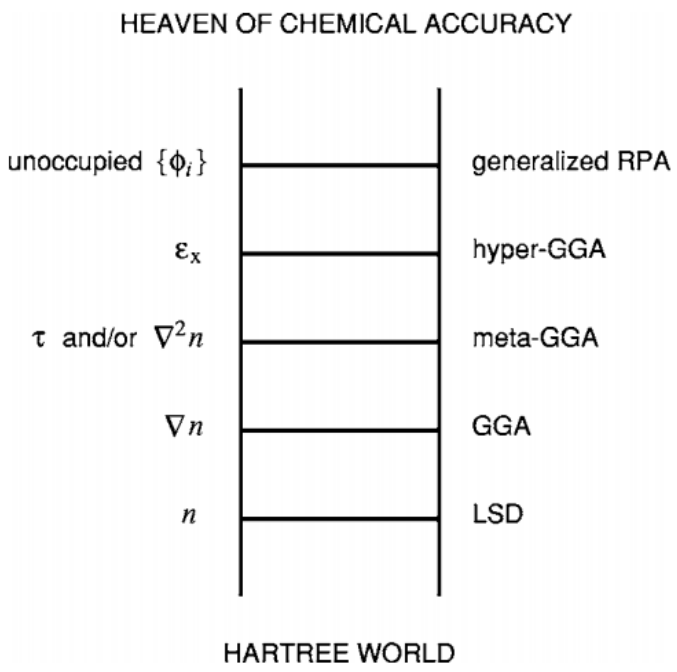

Figure 4.4: DFT functionals according to the Jacob's ladder of chemical accuracy . Here n represents the energy density, Δn the gradient of the energy density, ∇ non-interacting kinetic energy density, $\nabla^2 n$ the second gradient of the energy density, ϵ_x the exact exchange energy and $\{\phi_i\}$ a set of wave functions. Taken from ref. [129].

The first density functional model was proposed by Thomas Fermi and was based on a uniform electron gas and constant density. This functional was the first step towards density functionals which only depended on the local spin density (LSD). These functionals are referred to as the local functionals and are based on the local density approximation (LDA). However in the limit to infinity these functional showed the wrong exponential behavior of the density [130].

To further improve the accuracy of the functionals not only the local density but also the density gradient was included in the functional. These type of functionals are called semi-local functionals and are based on the generalized gradient approximation (GGA). To ensure the correct asymptotic behavior several exchange functionals were proposed. One of the most famous GGA functionals is that of Becke, invented in 1988 [131]. This B88 functional contains a parameter fitted to the HF energy of the noble gases. This means empirical input was used. Another well known exchange energy functional is that of Perdew which contains no empirical input and was constructed to obey as many properties as possible for the exchange functional [132]. Next to an expression for the exchange energy functional, a correlation energy functional must also be defined. Some examples are the P86 functional from Perdew [133] which is fitted to an accurate energy of Neon and the PW91 functional invented by Predew and Wang [134], which is parameter free. However, the most well known correlation functional is probably the LYP functional created by Lee, Yang and Parr which possesses a parameter based on the exact properties of Helium. Every exchange functional can be combined with every correlation functional. Another often used functional is the PBE functional and revPBE proposed by Perdew, Burke and Ernzerhof [135], [136], which try to limit the amount of parametrization.

These two functionals are similar to the LYP functional.

To increase the accuracy of the functionals, the HF exchange energy was included in the functionals. This class is called the hybrid functionals. This class is of course also computationally more expensive. Important hybrid functionals are B3LYP and B3PW91. In these examples the Becke exchange energy is augmented with an exchange energy from the LDA and the HF exchange energy with the KS integrals.

Furthermore, one could improve the accuracy by including the non-interacting kinetic energy density (τ in Figure 4.4), the exact exchange energy (ϵ_x in Figure 4.4) or the unoccupied levels (ϕ_i in Figure 4.4). This leads to respectively the class of the meta-GGA, the hyper-GGA and Generalized RPA (random phase approximation) functionals. Hyper-GGA functionals would lead to a full ab initio description of the exchange and correlation energy. However these type of functionals are not yet available.

One crucial disadvantage of DFT is that it does not take into account long-range dispersion interactions which arise from the fact that most functionals only describe the local density and the gradient of the density. These long-range interactions significantly influence the chemistry and physics of large systems. Therefore to obtain chemical accuracy, the inclusion of these interactions are indispensable. Several a posteriori corrections [137]–[141] and new highly parametrized density functionals, such as the non-local van der Waals functional (vdW-DF) [142]–[144], the M05 and M06 fuctionals [145] and the Bayesian error estimation functional with van der Waals correlation (BEEF-vdW) [146], have been developed to tackle this shortcoming of DFT.

Frequently used is the a posteriori correction proposed by Grimme [147]. There are many variants of this correction: DFT-D1, DFT-D2, DFT-D3. The correction applied in this master thesis is the DFT-D3 correction. This correction implies that an additional term, E_{disp}, must be added to the energy obtained with the DFT functional, E_{DFT}. This results in a new energy, $E_{\text{DFT-D3}}$, as shown in Equation 4.3. The dispersion correction represented in Equation 4.4 contains a two-body contribution, $E^{(2)}$ and a three-body contribution, $E^{(3)}$. The two body contribution is a sum over all possible atom pairs AB in the system. Furthermore it depends on a dispersion coefficient C^{AB} and is scaled to the reciprocal of the distance between the atoms of the considered pair, r_{AB}^{-1}, to the power 6, 8, 10.... The third body is a sum over all possible combinations of 3 atoms ABC from the system. It also depends on the dispersion coefficient of the considered atom trio C^{ABC} and next to the product of the distances $r_{AB}r_{AC}r_{BC}$, also the angles of the triangle formed by the atom trio θ_a, θ_b and θ_c must be taken into account. This method's popularity stems from its simplicity and low computational expense.

$$E_{\text{DFT-D3}} = E_{\text{DFT}} + E_{\text{disp}} \tag{4.3}$$

$$E_{\text{disp}} = E^{(2)} + E^{(3)} \tag{4.4}$$

4.2.4 Basissets

Before solving the many-body problem an initial basisset must be constructed. With this basisset one can describe the molecular orbitals, the wave functions of the system via linear combinations of the basisset functions. In theory, an infinite number of basisset functions are required to describe the molecular orbital. In practice, this is impossible and a finite basisset is selected, which contains enough basisfunction to ensure high accuracy.

These basisfunctions are often atomic orbitals and these atomic orbitals (AO) are approximated by linear combinations of Slater type orbitals (STO). However STOs are difficult to integrate and therefore it is recommended to use Gaussian Type Functions (GTF) instead. These GTFs have the disadvantage that they resemble less the AO then the STOs. Hence, it is better to use a linear combination of GTFs as basis functions. These combinations are called contracted Gaussian basis functions (CGF). Eventually each STOs is approximated by a linear combination of a number of CGFs which are in turn linear combinations of GTFs.

Most of the time a Split Valence basisset is used, which means the core orbitals are described by only one STO and the valence orbitals are described by a combination of multiple STOs. In this way computational cost is reduced for the core orbitals, but correct results are still obtained since the most essential orbitals, the valence orbitals, remain highly accurate. Commonly used basissets for the valence orbitals are double-ζ and triple-ζ sets. The former constructs orbitals using linear combinations of two STOs and the latter using three STOs. Often the valence basisset is extended with diffuse functions and polarization functions since long range interactions are not described by the STOs and polarization functions allow deformation of the orbitals, which is essential when a reaction occurs.

On the other hand, one can also use a plane wave (PW) basisset to describe the system's electron density. These plane waves are not localized and therefore the Hartree energy can be calculated via Fast Fourier transform, which makes this computational less expensive [148]. Plane waves are often used for systems with periodic boundary conditions.

Often these plane waves are combined with a pseudopotential, since using only plane waves to represent the rapidly varying electron density near the core would require an impracticably large number of PWs [149]. With the pseudo potential, the core electrons are integrated out of the electronic problem, while the valence orbitals are represented by orbitals and the density by the plane wave auxiliary basis [148]. In this way, smoothly varying densities are obtained. When the orbitals used are Gaussian type orbitals, the above described basisset is referred to as a Gaussian Plane Wave (GPW) basisset. These GPW basissets are also implemented in CP2K. For more detailed discussion of CP2K, the used basisset and the used DFT method, the reader is referred to section 4.4

4.3 Static vs. dynamic methods

When it comes to calculating kinetics and simulating chemical reactions with the use of first-principles, two approaches are available. Chemical reactions can be studied with static or dynamic methods. With the static approach only one transition state at a time can be investigated, while dynamic methods allow to sample large portions of the potential energy surface (PES) to look for multiple transition states and reaction paths. Dynamic methods have several advantages over the static method for the study of heterogeneous catalysis. After a short introduction to the static and dynamic methodology in this chapter, these advantages will be discussed into detail.

4.3.1 Transition State Theory

To determine chemical kinetics on a first-principle basis, transition state theory is without doubt one of the most used methods. It assumes that a transition state (TS) or activated complex exists and that every successful reaction path passes through this point of the PES, as shown in Figure 4.5. This TS can be determined by finding a first order saddle point on the PES. This means that for the TS a minimum in all degrees of freedom is found except for the reaction coordinate in which it reaches a maximum. From these assumptions it follows that only the information at the reactants, products and TS position on the energy surface need to be known. If for these three point, the electronic energy, molecular partition functions and frequencies are known, then the reaction rate coefficient can be obtained. These properties can be calculated by performing a geometry optimization and subsequent frequency calculation of the reactants, products and transition state. Transition state theory has the strength to obtain an insight in the chemical reaction and its rate in an easy manner.

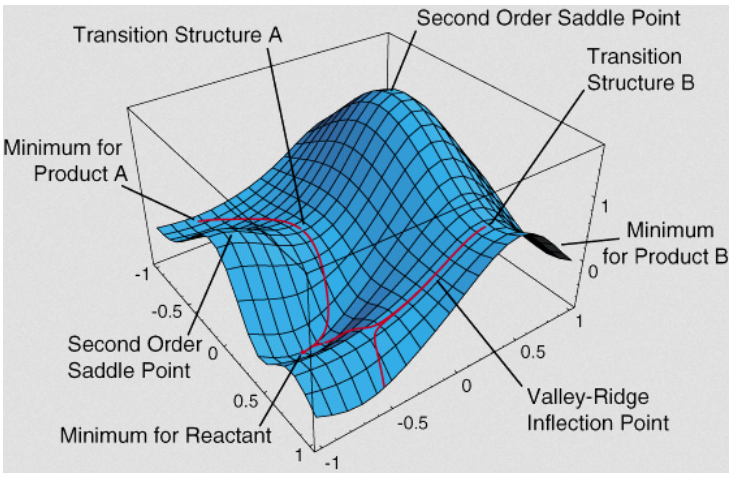

Figure 4.5: Potential energy surface with two reaction paths, which connect the reactant valley with a product valley. Taken from ref. [150].

4.3.2 Static Methods

With static QM calculations, a geometry on the PES is optimized at 0 K by solving the Schrödinger equations of the system. Once the atom coordinates at equilibrium position are known, a normal mode analysis (NMA) is performed. A normal mode is a concerted vibrational motion of multiple atoms in a system. Some examples of these vibrations are bond stretches or bends in a molecule. For non-linear molecules the number of normal modes is equal to $3N - 6$ (with N the number of nuclei). These normal modes are described within the harmonic oscillator approximation. In this approximation, each vibration is represented as a spring. This means that the displacements of the atoms can be described by a sinusoidal function with constant amplitude and frequency and that the potential energy is described by a quadratic function resulting in an energy well with infinitely high walls. This does not match reality, since these infinitely high walls do not allow the atoms to escape from the energy well and find a new equilibrium state. This is one of the shortcomings of the static QM methods. During the NMA, the partition function of the molecule and the resulting normal mode frequencies are calculated. From this frequencies all thermodynamic properties, such as the enthalpy and entropy, can be derived at a finite temperature by means of the partition function. This function forms the bridge between the thermodynamic properties and the molecular structure.

4.3.3 Ensemble

Before looking into the dynamic methods, the term ensemble must be explained. For both molecular dynamics (MD) and metadynamics (MTD) one needs to select an appropriate ensemble. A statistical ensemble is a collection of replicas of a system under identical conditions. It gives the probability distribution for the states of the system. In the NVT ensemble, the number of particles, the volume and the temperature of the system are kept fixed, while in the NPT ensemble the volume is variable but the pressure is constant. Furthermore, one can also consider the NVE ensemble, in which the number of particles, the volume and the energy of the system stay the same over the entire ensemble.

From the ensemble thermodynamic properties can be derived on the condition that the system is ergodic. Ergodicity implies that the time average of a property is equal to the ensemble average of that property. Therefore thermodynamic properties can be retrieved from MD if the simulated time is long enough so that the complete ensemble has been sampled.

When working with the NVT or NPT ensemble the temperature must be kept constant. This is done by implementing a thermostat. Popular thermostats are canonical sampling through velocity rescaling (CSVR) [151] and Nosé-Hoover [152]. With a CSVR thermostat the velocities calculated during MD or MTD will be rescaled based on the difference between the instantaneous temperature and the target temperature. CSVR is easy to implement and is moreover fit to handle big temperature differences and reach the target temperature in a very efficient way. Therefore, the CSVR thermostat is often used for equilibration of the temperature of the system before starting the actual production run. For the actual simulation, the Nose-Hoover thermostat is often employed, since it is more robust than the CSVR thermostat. It is based on the idea

that the total system is an NVE ensemble containing a heat bath and the real system described by an NVT ensemble. With the Nosé-Hoover thermostat a constant temperature for the NVT ensemble is maintained by exchanging energy with the NVE ensemble through the heat bath. For more information on the thermostats used in this thesis, the reader is referred to section 4.4.

4.3.4 Molecular Dynamics

Although a lot of theoretical studies in zeolites were performed using static methods, researchers become more convinced that dynamic effects cannot be ignored in heterogeneous catalysis [78], [153]–[156]. These dynamic effects are reflected in the complex PES of a zeolitic system. There are several methods to sample energy states on a PES, i.e., to walk on the PES and find equilibrium geometries. In this thesis, the MD method is considered. This methodology is deterministic, which means every geometry is uniquely determined by previous states and the model parameters. Consequently, MD allows to reveal the time evolution of a system. During classical MD, Newton's equations of motion need to be integrated to construct the trajectory of the atoms of a system. Hereby the following steps are pursued [157]:

1. Specify initial atom coordinates $r(t=0)$, initial velocities $v(t=0)$ and time step Δt.
2. Get the forces for each atom $F = -\nabla V(r(i))$, calculate the acceleration $a = F/m$ and subsequently the velocity for that atom $v(i) = v(i-1) + \frac{1}{2}(a(i-1) + a(i))\Delta t$ (here $V(r(i))$ is the potential energy at time step i and m is the mass of the system).
3. Move atoms according to $r(i+1) = r(i) + v(i)\Delta t + \frac{1}{2}a(i)\Delta t^2$.
4. Move time forward: $t = t + \Delta t$.
5. Go to step 2.

The selection of a good time step in step 1 is crucial for the outcome of the MD simulation. Overall, chemical reactions occur on a relatively long time scale. Depending on the type of reaction, the reaction can take place in the order of microseconds up to even full seconds in case of typical MTO reactions (see chapter 2). However, the time step of the MD simulation must be made small enough so that the fastest dynamics during a chemical reaction can still be observed. Therefore, the time step must be equal to the order of magnitude of the time scale of the fasted dynamics that one desires to study during the simulation. For instance, in solid acid catalysis, the Brønsted acid site plays a crucial role and exhibits a bond vibration with a frequency of about 10^14 s^{-1}. Thus, this bond vibration occurs a time scale of a femto second. For this reason the time step applied in this master thesis is 0.5 fs (see section 4.4 for more computational details). However the smaller the time step, the longer it takes to get a desired length of the MD run and the more computational resources are required. The MD runs must be sufficiently long to retrieve statistically relevant data. Only when simulating long enough, one can reach ergodicity and the time-average of the MD run can be assumed equal to the average over the ensemble. To sum up, the choice of the right time step involves a trade-off between computational effort and the loss of information of phenomena at a time scale smaller than the time step.

The equation of motion represented in step 2 is coupled to the many body problem, since the potential energy surface must be constructed to solve the equations of motion in case of ab initio MD. Furthermore the Born-Oppenheimer (BO) approximation is often applied. For MD simulations this means the nuclei move on the ground state electronic surface and their forces result from recalculating the electronic structure at each time step by solving the electronic Schrödinger equation at fixed nuclear coordinates. DFT methods are mostly used to solve the electronic problem in MD simulations. Once the electronic structure is known, a new set of nuclear coordinates is set for the next time step. Note that the nuclei are described classically.

In step 2 and 3 the velocity Verlet algorithm is used as integration method [158]. This is a very simple and efficient integration algorithm which does not require any higher order energy derivatives besides the forces from step 2. It also guarantees the time reversibility of the MD simulation, meaning that one can unambiguously reconstruct all earlier states starting from a state at step i. This velocity Verlet algorithm will be used in this master thesis. However other schemes are also available [159], [160], such as simple leapfrog algorithm [161].

4.3.5 Metadynamics

For zeolite catalysis, the computational power nowadays only delivers MD simulations of a couple of hundreds of ps within reasonable time. During this period, is it very unlikely to sample transition states and therefore to sample chemical reactions. Chemical reactions can be considered as rare events during MD, since this involves high energy states with low probability that scales with $exp(-E/kT)$, where E stands for the energy of the state. To speed up the sampling process, metadynamics (MTD) can be used. MTD provides a powerful algorithm to accelerate rare events and reconstruct the underlying free energy surface [162]. It will bias the potential of the system by adding Gaussian potentials with a predefined height w and width δ_s at regular time intervals τ_G. The reciprocal of the sum of the added Gaussian potentials after a sufficiently long simulation can then be used to reconstruct the free energy, as seen in Equation 4.5 where V_G is the sum of Gaussian potentials, G is the free energy, $S(x(t))$ is a function of the coordinates with trajectory x at time t and $s(t')$ is the value of the collective variables (CVs) (*vide infra*) at time t'. The system is able to escape a local minimum and pass through transition states to fall into a new local minimum by using a bias potential.

$$\lim_{t\to\infty} V_G(s,t) \sim -G(s) \tag{4.5}$$

$$\text{with } V_G(S(x),t) = w \sum_{\substack{t'=\tau_G,2\tau_G,\ldots \\ t'<t}} exp(-\frac{(S(x)-s(t'))^2}{2{\delta_s}^2})$$

In detail, during metadynamics an MD simulation is performed within a certain ensemble. The difference between normal MD and MTD is clarified by Figure 4.6. At a fixed time, the normal MD simulation is biased as a hill (or Gaussian potential) is placed on top of the free energy surface at the current position of the CVs (indicated by an orange dot referred to as the walker).

By doing this, the well is slowly filled, until the top is reached and the walker can escape the minimum and fall into a new energy minimum. As Gaussian hills are continued to be placed on regular time basis along the trajectory followed by the CVs, the walker will overcome the second high-energy region and reach the third energy minimum, as seen in Figure 4.6 (b). By keeping track of all positions and characteristics of the added hills, the free energy surface can be reconstructed based on the sum of the spawned Gaussians, see Figure 4.6 (c).

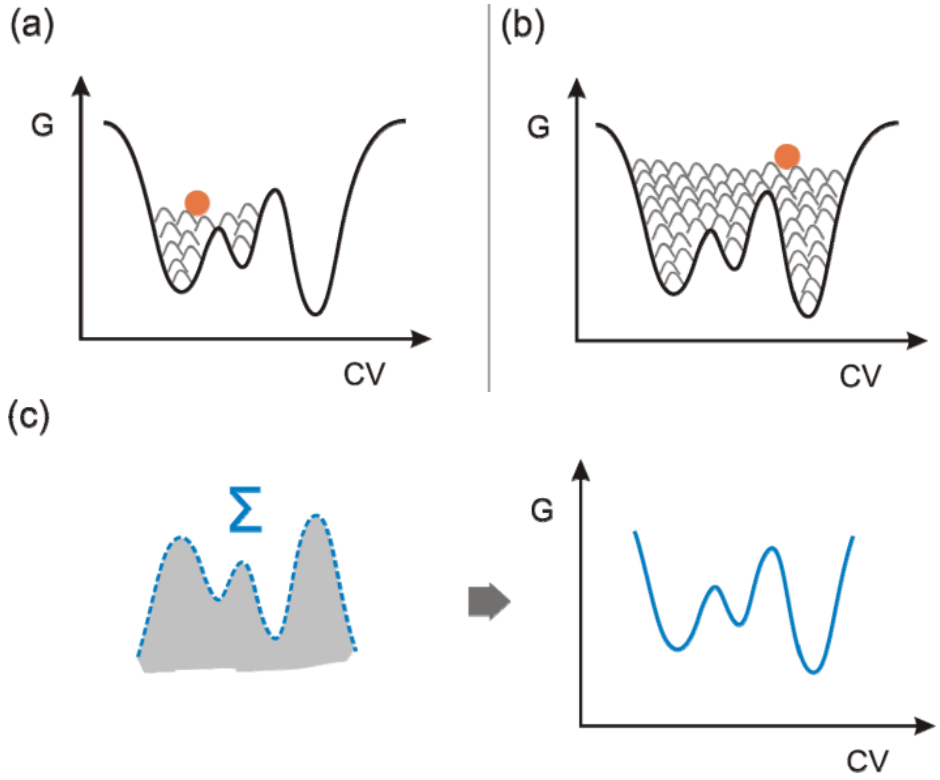

Figure 4.6: Schematic representation of the metadynamics algorithm: (a) adding of the Gaussian potential on the free energy surface (b) sampling a rare event by overcoming a high energy region (c) reconstruction of the free energy surface. Taken from ref. [78].

From the MTD simulation the free energy barrier is obtained by taking into account all sampled reaction routes. Unlike the transition state theory, the obtained free energy barrier will account for multiple sampled transition states. This will result in a more accurate approximation of the true barrier. First, the lowest free energy path (LFEP) between the reactant and product valley is selected from all sampled routes. For a MTD simulation using more than two CV's a one dimensional free energy profile is found with the LFEP method proposed by Ensing et al. and this method is implemented in the trace-irc program [163]. Two free energy minima, corresponding to the reactant and product valley, are searched and afterwards a path with the lowest free energies is constructed which connects the two minima. The first step in this construction exists of finding a coarse path that connects the two minima by taking large steps on the multidimensional energy surface. The second step is to refine the path by searching for lower free energies in between the large steps perpendicular to the coarse path. The free energy G along this refined path is now known. If desired, a smoothness factor can be used to lower the bumpiness of the refined path.

To obtain the free energy barrier, the unnormalized probability of the transition state, which is the highest energy state on the minimum energy path, is divided by the unnormalized probability of the reactants. Finally, the free energy barrier $\Delta G^{\ddagger}$ is obtained by taking the natural logarithm of this ratio and multiplying by the Boltzmann constant k_B and temperature T, as shown in Equation 4.6. Here s represents the coordinates along the LFEP.

$$\Delta G^{\ddagger} = -\frac{1}{\beta} \ln \frac{\exp(-\beta G(\mathrm{TS}))}{\int_{-\infty}^{\mathrm{TS}} \exp(-\beta G(s)) ds} \text{ with } \beta = \frac{1}{k_B T} \tag{4.6}$$

An important aspect of MTD is the upfront selection of a set of CVs which should allow to describe the process of interest. The sum of Gaussians will be centered around the trajectory followed by the set of CVs. These CVs should allow the distinction between the initial, intermediate and final states. It must be possible to describe the reaction coordinates with the chosen set of CVs. Finally, the efficiency of MTD scales exponentially with the number of used CVs. Therefore, the number of involved CVs is limited due to the increase of computational effort with increasing amount of CVs. Some examples of possible CVs are bond lengths, angles, dihedrals, potential energy and coordination numbers.

In this master thesis, the implemented CVs are coordination numbers (CN). The formula for these number is given in Equation 4.7, where r_{ij} is the distance between the atom i and atom j, r_0 is a reference distance, n and m are parameters to tune the smoothness of the f function and the corresponding asymptotic behavior since for large r the function limits to $\frac{1}{r^{m-n}}$. Most of the time n is equal to 6 and m is equal to 12. To calculate this CN, a set of atoms i and a set of atoms j is necessary. These sets allow to account for multiple possible new bonds when the two reacting species are not a priori known, for instance in a methylation reaction of benzene it is not known upfront which C atom of the ring will be methylated. From the coordination number, one can derive the number of bond between the two different set of atoms, since the $f(r_{ij})$ is approximately 1 for r_{ij} smaller than r_0, 0.5 for r_{ij} equal to r_0 and close to zero for r_{ij} much larger than r_0 as seen on Figure 4.7.

$$CN = \sum_{i,j} f(r_{ij}) = \sum_{i,j} \frac{(1 - \frac{r_{ij}}{r_0})^n}{(1 - \frac{r_{ij}}{r_0})^m} \tag{4.7}$$

The set of CVs must be a priori chosen, but there is no recipe for finding the right set and often trial and error is needed to come up with the right set of CVs. Forgetting a crucial CV is disastrous for the outcome of the simulation. When neglecting a CV, the studied process will not be accurately described since the minima will be overfilled with Gaussian potentials and hysteresis in the free energy profile can occur [164].

Other parameters that have a high influence on the accuracy and efficiency of the MTD simulations are the width, height and frequency of the placed Gaussian hills. The statistical error on the free energy difference calculated with MTD is approximately scaled with $\sqrt{\delta_s w / \tau_G}$. The higher the width of the hills, the coarser and less accurate the sampling will be. It will be also faster, since the time needed to escape an energy minimum is scaled with $(\frac{1}{\delta_s})^{nCV}$ with nCV the number of CVs. However, a limit is imposed on the width by the shape of the energy profile,

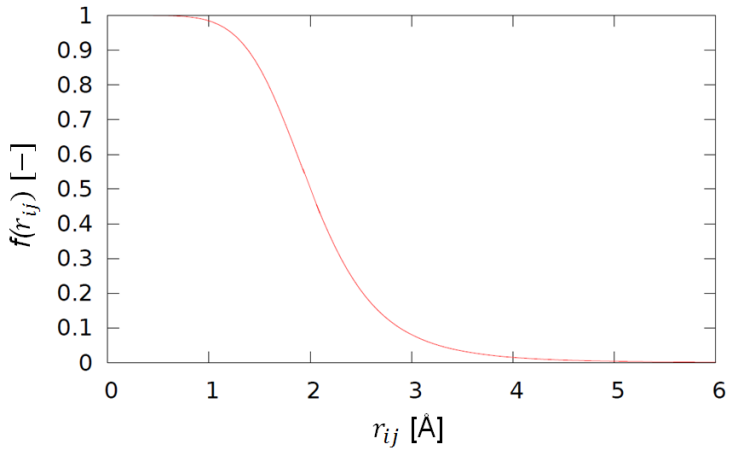

Figure 4.7: Representation of the f function with parameters n, m and r_0 equal to 6, 12 and 2 Å respectively.

since the width must be smaller than the energy well itself. Moreover, a good rule of thumb is to choose the width in such a way that the CVs range is subdivided in 50 to 100 intervals.

Furthermore, the error depends on the ratio of the height and frequency with which the hills are placed. The larger the height of the hills, the longer it will take for the walker to relax again and slide down the hill. If the time interval between the addition of new hills is smaller than the time needed to relax, a phenomenon called "hill surfing" will take place. This means that the CVs will ride the tail of the previous placed hill and that a new hill will be added on top of the tail of the previous hill. This leads to very inaccurate results. One must also make sure that no wells are overfilled. To ensure convergence of the FES, the height of the hills can be lowered on regular basis. For instance the height can be divided by two after each recrossing of an energy barrier or like in well-tempered MTD [165], the new height can follow an exponential decay ($w = \omega\tau_G exp(-V(s,t)/\Delta T)$) with ω the initial bias depositing rate and ΔT a temperature. Nevertheless, to reach a good efficiency of the MTD simulations the hills cannot be too small or the time between the addition of hills cannot be too long.

Some extended types of MTD were developed to solve some of the issue in normal MTD. In multiple walker MTD, multiple interacting MTD simulations can be performed in parallel by working with more than one walker for which the dynamics are simultaneously biased by the potential V_G. Parallel tempering MTD is a combination of the parallel tempering method and the MTD method [166]. In this technique multiple MTD runs are performed at different temperatures. At a certain time interval there will be an exchange between two replicas of the MTD simulation. This means that if the acceptance ratio allows for the occurrence of an exchange then the coordinates of the first replica become the coordinates of the second and vice versa. Furthermore, the impulses of the two replicas will be rescaled. This method helps to overcome the difficulty of the a priori determination of the set of CVs, since sampling over the degrees of freedom not explicitly included in the set of CVs is possible. Another method which involves replicas is the bias exchange MTD [167]. This allows the use of a much larger set of CVs than in normal MTD. Parallel MTD runs are used with one or two CVs out of the complete set. At certain intervals, an exchange between two replicas will take place by swapping their bias

potentials. This technique minimizes the problem with hysteresis under the condition that the set of CVs provided is complete. The reconnaissance MTD is a self-learning technique which also allows the use of a large number of CVs which don't have to be a priori known [168]. Thus, this resolves one of the major MTD bottlenecks. Furthermore, the underlying mechanism leading to reactions in the studied system does not need to be known beforehand. During reconnaissance, the local minima are searched and from there on the system is biased to explore regions away from these minima.

4.3.6 Advantages and disadvantages of a dynamical approach

As already mentioned, research in the field of zeolite catalysis is more and more relying on dynamics calculations. In 1998 Jeanvoine et al. used MD to investigate the proton transfer from a single water molecule to the Brønsted acid site in H-SAPO-34 [169]. Via MD with periodic boundary conditions, they managed to model proton transfer to a water dimer. Through MD simulations of alkane cracking reactions in H-ZSM-5, Zimmerman et al. found that not only the energy barriers but also the system's dynamics largely determine the catalytic selectivity [155]. MD can also be used to study the temperature effect on the adsorption of alkanes inside a zeolite such as H-SSZ-13 [170]. Now, the advantages of MD and MTD over static modeling are discussed together with the disadvantages.

Static calculations are always performed at 0 K. Therefore, the optimized geometries and normal modes obtained with static calculations are only accurate at 0 K. However, to get insight into industrial processes, the relevant reaction temperature must be considered hereby obtaining the correct enthalpy, entropy and free energy. With the use of the partition function these thermodynamic properties can be calculated at relevant temperatures. However, with MD and MTD it is possible to directly sample the PES at a finite temperature [78]. This results in geometries and normal modes calculated at a finite temperature, which is not possible with static calculations.

Furthermore, all frequencies are treated as harmonic oscillators during static calculations. This harmonic oscillator approximation is however incorrect. Some extension can be applied to the static calculations such as the hindered and free rotor approximation to limit the error for the anharmonicity of the system [171], [172]. However, during dynamics calculations the anharmonicity of the normal modes is fully taken into account, resulting in an even more accurate description of these modes.

The PES of a zeolitic system is very complex. First of all, the framework itself contains many degrees of freedom, since each bond length, angle and dihedral angle is adjustable. This results in a quite flat PES. For static calculations it is very challenging to find a true minimum on the PES. Furthermore, adsorbates in the zeolite add even more degrees of freedom. Especially for large channel zeolites, the mobility of the adsorbates is high, resulting a vast number of adsorption complexes. It is impractical to describe this many possible configurations through static calculations. By using MD the plethora of complexes formed between molecules present in the pore can be explored [78].

MTD has the advantage over static calculations, that it can take into account multiple transition states and reaction paths when determining the thermodynamics and kinetics of a certain reaction. This is a huge advantage, since kinetics based on static calculations only consider three points on the PES, namely one reactant state, one product state and one transition state when working within the TST.

The biggest disadvantage over static calculations is that MD and MTD generate many data, requiring a lot of storage and making the data analysis very complex. Long simulation runs, resulting in lots of data, are however needed to obtain equilibrated properties. Furthermore, when MD or MTD are combined with periodic boundary conditions, these simulations become computationally very demanding.

A dynamical approach shows a lot of advantages over static calculations for the study of (co-)adsorption and chemical reactions. Therefore, the use of dynamic first-principle calculations are preferred in this master thesis.

4.4 Methodology applied in this master thesis

This master thesis focuses on the methylation of aromatics during MTO inside H-SAPO-5 and H-SSZ-24. First the adsorption and co-adsorption complexes are studied on the catalyst surface with the use of MD simulations, since static calculations are unpractical due to the large amount of possible adsorption complexes that need to be sampled on the PES. Next, the reactions are modeled inside the two different catalyst by performing MTD simulations. All dynamic simulation are performed with CP2K. This is an open source package to execute atomistic and molecular simulations of solid state, liquid, molecular, and biological systems [123].

Both catalyst models are periodic and contain one acid site. The exact location of the substituted defect is irrelevant, since in AFI topology all 24 T positions in the unit cell are equivalent [94]. However, the O positions for the proton are not equivalent and vary in acid strength. In chapter 5, methods for the validation of the acid strength of these periodic models are considered. The periodic models for H-SAPO-5 and H-SSZ-24 were already used in the paper of Westgård Erichsen, De Wispelaere, Hemelsoet, *et al.* [106]. Both models are 1x1x2 supercells. This means that the H-SAPO-5 and H-SSZ-24 unit cells are duplicated in the c-direction, the axial direction of the 1D channel. The (Al+P)/Si ratio in H-SAPO-5 is 47 and the Si/Al in H-SSZ-24 is also 47. Figure 4.8 represents the periodic supercells used in the calculations.

The dynamic calculations are performed with DFT. This theory is implemented in CP2K as QUICKSTEP and uses a Gaussian and plane wave (GPW) basisset [173]. Since the use of hybrid-GGA functionals in CP2K is still computationally too expensive and not yet established, the revPBE functional is applied. DZVP-GTH is used as basisset and the GTH pseudopotential is also implemented in CP2K [174]. Furthermore, DFT-D3 or so-called Grimme corrections are applied to include long-range dispersion interactions.

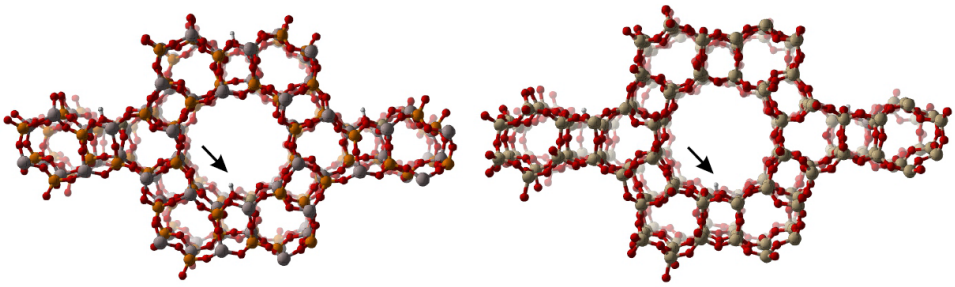

Figure 4.8: The 1x1x2 supercells used for H-SAPO-5 (left) and H-SSZ-24 (right) both containing one Brønsted acid site as indicated by the arrow.

4.4.1 MD calculations

The goal is to get insight into the adsorption behavior of methanol and DME in the presence of aromatics with different methylation degrees e.g. benzene, toluene, xylene etc. in both H-SAPO-5 and H-SSZ-24.

Before starting the dynamic calculations each geometry is optimized to ensure a good starting configuration. All MD simulations are done in the NPT ensemble. To ensure ergodicity of the ensemble, the modeled runs must be long enough. In this master thesis, runs of 50 ps are assumed to be sufficient to achieve an ergodic ensemble.

Each MD step, corresponding to 0.5 fs, is performed at 623 K and 1 atm. To obtain a constant temperature and pressure a thermostat and barostat are used. The first 2000 steps are done with a CSVR thermostat, to speed up the convergence to the desired temperature. Afterwards about 100 000 steps are performed with a chain of 5 Nose-Hoover thermostats.

4.4.2 MTD calculations

With MTD, the reaction between methanol and toluene will be modeled inside both catalysts to study the influence of the acid strength on the free energy barriers. While in H-SSZ-24 also a MTD simulation is performed for the methylation reaction between DME and toluene. This enables to compare the performance of two methylating agents towards toluene alkylation. These type of simulations are computationally very expensive due to the use of three CVs (*vide infra*). Therefore, the MTD run with DME as reactant is only performed in H-SSZ-24.

The temperature is the same as for the MD runs and is controlled by the Nosé-Hoover thermostat. Furthermore each time step is still 0.5 fs. In contrast to the MD simulations, the MTD runs are performed in an NVT ensemble. This requires fixed cell parameters. These are obtained from the MD simulations within the NPT ensemble by averaging the cell parameters out over the complete run. However, the resulting cell lengths slightly deviates from a unit cell with cell angles α and β equal to 90° and γ equal to 120°. To resolve this, a small correction is applied to the cell lengths. The new cell lengths only deviate from the original averages by less than 0.01 %. The used corrected cell lengths for the MTD simulations can be found in Appendix B along with the cell lengths retrieved from all the other MD simulation within the NPT ensemble.

As mentioned in section 2.5, two mechanisms are known for the methylation reaction. Therefore, a set of CVs is needed that can describe the concerted as well as the stepwise methylation mechanism. For the concerted route of the methylation of benzene in H-ZSM-5 a set of two CVs was used [175], however for in H-SSSZ-24 using only two CVs to describe the methylation of benzene, led to incomplete information [176]. This problem has already been tackled by De Wispelaere et al., who propose a 3D MTD simulation [176]. In their very recent paper, the methylation of benzene by methanol was explored via the competitive direct and stepwise pathway in H-SSZ-24. It is better to avoid the a priori selection of the concerted or stepwise mechanism by including an additional CV. As in the paper of De Wispelaere and co-workers, the first CV describes the CN for the methanol or DME CO bond cleavage. The second CV describes the CN for the formation of a CC bond between the methyl group of the methylating agent and aromatic ring in toluene. While the last CV describes the CN for the formation of an intermediate methoxide on the framework, thus for the bond between C atom of the methylating agent and one of the 4 possible framework O atoms. This last CV will provide information on the competition between the two paths in one single simulation. All three CVs are represented in Figure 4.9 for methanol (a)and DME (b). The implementation of the CVs in H-SAPO-5 and H-SSZ-24 is of course the same.

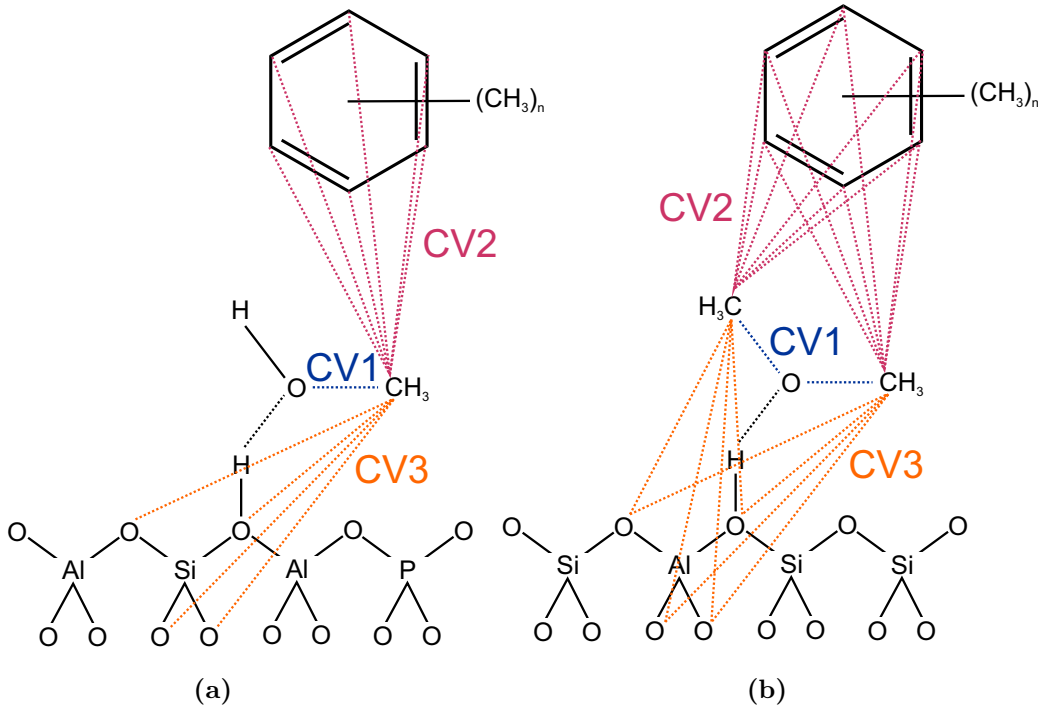

Figure 4.9: The representation of CV1, CV2 and CV3 in H-SAPO-5 (a) and H-SSZ-24 (b) in case of an aromatic co-adsorbed when methanol (a) or DME (b) are located on the acid site.

For the three considered CNs the parameters are the same: r_0 is equal to 2 Å, n is 6 and m is 12, see Equation 4.7. In the methanol case all CNs range between 0 and 1, whereas for DME the first CN ranges between 1 and 2, since one of the methyl groups will always be bonded at the O atom. After every 25 fs, a Gaussian hill is placed. For all CNs the Gaussian hill width is equal to 0.02 since this divides the CN ranges in 50 intervals. The Gaussian height will vary during

the MTD simulation. $5\,\mathrm{kJ\,mol^{-1}}$ is used as initial height, since this is close to the value for RT with R the gas constant and T the MTD temperature. Later on, this value will be halved each time a barrier is recrossed.

However, in a couple of cases walls are needed to further restrict the simulation to the region of interest of the CNs. This should increase the efficiency of the MTD simulation since undesired regions on the FES will be left unexplored. A first wall is needed to ensure that once the methyl group has left the previous methanol or DME molecule, the O atom will still remain close to the methyl group hereby enhancing the change of recrossing. Furthermore, the C atom from the methylating agent and from the aromatic ring must stay sufficiently close during the MD run to enhance changes of a methylation. Once a methylation reaction occurs, a carbocation is formed. This cation can easily undergo a hydride shift. This shift would of course hinder the recrossing to the reactants valley. Therefor, a third wall is implemented. Finally, one wall for DME and two walls for methanol are needed to secure that the methylating agent remains protonated.

Chapter 5

Characterizing zeolitic acid strength

The activity of zeolite or zeotype materials for the MTO-conversion is a result of their Brønsted acidic nature. Although zeolites can possess Lewis acid sites due to defects resulting from ion-exchange or steaming, this master thesis will solely focus on the Brønsted acid sites, which are most abundant in zeolite catalysts for the MTO process.

Next to the acid strength, the acid site density of the zeolite or zeotype material is an important property. In zeolites the Si-to-Al ratio is linearly dependent with the acid site density, since the incorporation of one Al atom results in the creation of one Brønsted acid site, as mentioned in chapter 3. However in SAPO materials, the incorporated Si atoms tend to form Si islands [93], which leads to a lower acid site density then expected on the basis of the Si-to-(Al+P) ratio. Furthermore, a zeolite or zeotype molecular sieve can possess multiple types of acid sites, each with their own acid strength. Therefore, not only the total acid site density is important but also the number of sites of each acid strength available in the catalyst.

5.1 Experimental approaches towards quantification of zeolitic acid strength

To date, there is no unambiguous technique or scale to describe the acid strength of solid materials. Whereas in liquids, one can express acidity in terms of pH, such scale system is not yet available for solids. Instead, several authors have tried numerous techniques to quantify the acid strength of solid catalysts [177], [178]. Next to experimental methods, also some theoretical approaches of the acid strength have been developed [179], [180], which will be discussed in section 5.2.

5.1.1 Titration

Titration of base molecules (in combination with a color indicator) is among the frequently used techniques for acid liquids to determine the acid strength. This test results in a value for the pH. To evaluate the acid strength of a solid acid a series of titrations must be performed, since the solid material may contain different acid site strengths [177]. By performing a series of titrations with different base molecules, the different acid site strengths are assessed and the corresponding number of acid sites are calculated resulting in an acid site strength distribution. However, performing such titrations with acid solids has proven to not adequately describe the acid strength. Especially for molecular sieves, the base molecules are not able to reach all cavities inside the catalyst and therefore are not able to determine the exact number of acid sites.

5.1.2 Infrared (IR) spectroscopy

With the use of IR spectroscopy phenomena occurring inside a zeolite can be probed with frequencies ranging from $10\,\mathrm{cm}^{-1}$ to $4000\,\mathrm{cm}^{-1}$. This allows to obtain crucial insights into the adsorption of small intermediates, but also in the zeolite formation and growth [156]. To characterize the zeolitic acid strength small base molecules, such as H_2, NH_3 and CO, are used as probe molecules. Upon adsorption at the acid site, the stretching frequency of these probe molecules will shift. This shift is an indication for the acid strength. Additionally, the shift of the OH stretching frequency of the Brønsted acid site itself is also used to determine the acidic properties of the solid catalyst.

CO is very often used as a probe molecule for the characterization of zeolitic acid strength. Due to its small size, this probe molecule can easily reach all acid sites in the porous material. Moreover, CO is a very weak base, which means it is very sensible to the local environment's acid strength. CO has three resonance structures as shown below in Figure 5.1. The negative charge is either located on the carbon atom or the oxygen atom, making both O- and C-end adsorptions on the acid site possible. However, in most cases the C-adduct occurs. When the C-end is adsorbed on a Brønsted acid site, a blueshift in the CO stretching frequency and a redshift in the OH stretching frequency is observed. A blueshift means that the frequency shifts towards higher values, while during a redshift the frequency shifts towards smaller values. The more acidic the material, the larger the shift will be. This technique provides a measure for the acid strength.

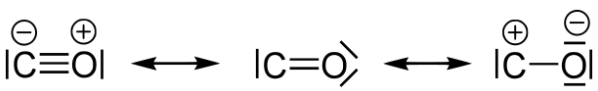

Figure 5.1: The three resonance structures of CO.

5.1.3 Proton magic angle spinning nuclear magnetic resonance (H MAS NMR)

Solid state NMR is a powerful tool for determining catalyst structure. NMR is an ideal technique to analyse zeolites and aluminophosphates, since ^{29}Si, ^{27}Al, ^{31}P and ^{17}O are NMR-active species. Next to structure determination, NMR has also been successfully used for the characterization of acid strength [181]. When considering proton MAS NMR the chemical shift of an H atom can be registered. Acid sites with higher acidity have more positively charged protons, meaning that these protons are less shielded and hence higher shifts are involved. Therefore the measured H shifts with H MAS NMR are a measure for the proton donor ability and acidity of the material.

5.1.4 Temperature programmed desorption (TPD)

During TPD, a temperature profile is used to gradually increase the temperature, leading to desorption of species with increasing adsorption energies. With the use of TPD, a distribution of the acid site strength is obtained, since at each temperature the amount of desorbing molecules will be followed and each temperature will correspond to a different adsorption energy and therefore a different acid site strength.

Pinto et al. have used ammonia temperature programmed desorption to obtain information on the acid sites in H-MFI and H-BEA materials [181]. In their experiments the samples were kept at 723 K for 8h under a continuous dry nitrogen flow to desorbe all traces of adsorbed water and other impurities. Afterwards the samples were cooled down to 423 K and ammonia was sent over the samples by pulsing a flow of ammonia into the dry nitrogen flow. After flowing pure nitrogen over the samples for 30 minutes, desorption was started by heating to 973 K at a rate of 10 K min^{-1}. The desorption of ammonia was then followed gravimetrically. This results in a desorption profile as function of the temperature, which can be deconvoluted in several peaks characterized by an acid strength and the number of acid sites with that strength. [103]

All the aforementioned techniques give away clues about the zeolitic acid strength, but are not inconclusive for the characterization and interpretation of a solid acid. Therefore, it remains crucial to combine these techniques to obtain a reliable quantification of the acid strength and its distribution.

5.2 Assessment of the acid strength of the H-SAPO-5 and H-SSZ-24 periodic model

Before starting with the study of the adsorption complexes inside the isostructural H-SAPO-5 and H-SSZ-24, the acidity of the periodic model must be evaluated to ensure that the used model for H-SSZ-24 is indeed a stronger acid over the H-SAPO-5 model in this master thesis. In literature several attempts towards the theoretical assessment of zeolitic acid strength have been described.

5.2.1 Tracking of the OH bond elongation

Sastre and co-workers have observed several linear relationships concerning the acid strength of CHA and AFI catalyst by using empirical and DFT derived forcefields (empFF and dftFF) [179]. They stress that the acidic properties of the catalyst model result from short-range as well as long-range interactions.

The elongation of the OH bond is a measure for the acid strength in general, since more acidic species will more easily donate their proton and thus the OH bond is stretched more easily. With this in mind, these authors found a linear relationship between the elongation of that bond and the square of the OH stretching frequency (ν(OH)), meaning that ν^2(OH) is also linearly dependent of the acid strength. Furthermore, a correlation between the second order derivative of the total energy and ν(OH) was discovered and finally ν(OH) could also be related to the square root of the gradient of the electric field.

To validate the acid strength of the periodic models used in this master thesis, the elongation of the OH bond is studied in both H-SAPO-5 and H-SSZ-24. First a static calculation is performed on both empty catalysts at 0 K. Form these optimized geometries, the length of the OH bonds is 0.98 Å in H-SAPO-5 and in H-SSZ-24 and suggests no difference in acidity between H-SAPO-5 and H-SSZ-24.

Therefore, in a new attempt to validate the difference in acid strength, temperature effects and anharmonicity are taken into account by comparing the bond elongation from two molecular dynamics simulation of the empty periodic catalyst models over an NPT ensemble of approximately 50 ps at 623 K and 1 atm. From these simulations an average bond length of 0.99 Å±0.02 Å is obtained for H-SAPO-5 and 0.99 Å±0.02 Å for H-SSZ-24 as well. Again this method is not conclusive to correlate the bond elongation lengths to the acid site strengths, since these two catalyst models result in very comparable bond lengths.

It is expected that the effect of acid strength on the bond length will be more visible when the acidic proton is interacting with a guest molecule for instance methanol or CO. MD simulation of methanol in both H-SAPO-5 and H-SSZ-24 are available and were performed by Kristof De Wispelaere at 623 K and 1 atm using the same level of theory used in this master thesis. When averaging out over all configurations were methanol was adsorbed at the acid site, a OH bond length of 1.05 Å±0.07 Å is found in H-SAPO-5 and 1.11 Å±0.19 Å in H-SSZ-24. Here, the bond length in H-SSZ-24 is slightly longer pointing out the higher acidity of the catalyst. However, by taking into account the standard deviation on the bond length, the difference between H-SAPO-5 and H-SSZ-24 remains insignificant. Therefore, in the next sections other measures are proposed to characterize the acidity of the Brønsted acid sites.

5.2.2 Intrinsic acid strength

Furthermore, the acid strength of the catalyst model could also be described by the intrinsic acid strength as defined by Soscun et al. [180]. This intrinsic acid strength is the ratio of the OH bond length and the OH stretching frequency as shown in Equation 5.1. The average bond

Table 5.1: Validation of the zeolitic acid strength of two AFI materials, H-SAPO-5 and H-SSZ-24, on the basis of the average OH bond length d(OH), the OH stretching frequency ν(OH), the intrinsic acid strength based on the NMA and the stretching frequencies $\nu(\mathrm{OH})_{\mathrm{CO}}$ and $\nu(\mathrm{CO})_{\mathrm{CO}}$ upon CO adsorption at 0 K.

	H-SAPO-5	H-SSZ-24
d(OH)	0.99 Å±0.02 Å	0.99 Å±0.02 Å
ν(OH)	3718 cm^{-1}	3718 cm^{-1}
intrinsic acid strength	2.65 10^{-12}	2.65 10^{-12}
$\nu(\mathrm{OH})_{\mathrm{CO}}$	3360 cm^{-1}	3312 cm^{-1}
$\nu(\mathrm{CO})_{\mathrm{CO}}$	2182 cm^{-1}	2146 cm^{-1}

length is obtained from the NPT ensemble MD simulation and the frequency is retrieved from a normal mode analysis (NMA) at 0 K. Unfortunately, there is no difference in the OH stretching frequencie obtained from the NMA in both catalysts. For both materials, a value of 3718 cm^{-1} is obtained. The results for the intrinsic acid strength are also given in Table 5.1. Both materials result in an intrinsic acid strength of 2.65 10^{-12}. It should be stressed that the frequencies are obtained at 0 K. It is recommended to take temperature effects and anharmonicity into account by obtaining the frequencies from an MD simulation.

$$\text{intrinsic acid strength} = \frac{d(\mathrm{OH})}{\nu(\mathrm{OH})} \tag{5.1}$$

The stretching frequency ν(OH) could also be taken from the corresponding velocity power spectrum (VPS). It has only recently been made possible to obtain accurate IR spectra from MD simulations, since it requires the calculation of the computationally demanding second order derivative of the total energy. Technically, the obtained vibrational spectrum from the MD simulations is not a true IR spectrum, but a VPS. This spectrum's intensity, I_{VPS}, results from the Fourier transformation of the auto-correlation function of the velocities $v_{i,\alpha}(t)$ of atom i ranging from 1 up to the total number of atoms N, as shown in Equation 5.2. It is recommended to retrieve the VPS from an MD simulation within the NVT ensemble. This might be something to try in future work.

$$I_{\mathrm{VPS}}(\omega) = \lim_{\tau\to\infty} \frac{1}{\tau} \sum_{i=1}^{N} \sum_{\alpha=x,y,z} \left| \int_0^{\tau} v_{i,\alpha}(t) e^{-i\omega t} dt \right|^2 \tag{5.2}$$

5.2.3 Shifts in the IR frequencies using CO as a probe molecule

Another possibility is to correlate the acid site strengths with the calculated shift of the OH stretching frequency and the CO stretching frequency as result from CO adsorption. Literature

reports for the CO blueshift in H-SAPO-5 and H-SSZ-24 values of +34 cm^{-1} and +38 cm^{-1} respectively and for the OH redshift values of −265 cm^{-1} and −317 cm^{-1} respectively [71].

These shifts were taken from the IR spectra at 77 K. As explained before, these type of spectra can be related to the VPS obtained from the MD simulations. However, CO will only adsorb on the solid acid catalyst at very low, cryogenic temperature. Such low temperature will result in very low velocities. The error on these low velocities is high and the VPS might lead to erroneous conclusions. Therefore the CO and OH stretching frequencies were obtained from a NMA. A NMA of the two catalyst models with CO adsorbed and a NMA of CO in the gas phase are needed. The NMA's of the empty zeolites and the zeolites with CO adsorbed all showed multiple negative frequencies. This means that the geometry optimization did not find a minimum on the PES and that the convergence criteria during the optimization were not strict enough. Applying more stricter criteria for convergence will make the time needed for optimization even longer and chances are that the geometry optimization will never converge, since it is very difficult to obtain the absolute minimum, especially when working with periodic boundary conditions, due to the very flat PES of the framework. This means that there are a lot of local minima on the surface which only differ from one another by e.g. a small adaptation in one of the bond lengths or angles of the framework. The energies related to these local minima are very similar and therefore it is extremely hard to find the true minimum of the framework.

However, the retrieved negative frequencies were in the order of a few hundred cm^{-1}, whereas the OH and CO stretching frequencies are located in the IR spectrum around 3600 cm^{-1} and 2200 cm^{-1} respectively. Therefore, it can be assumed that the motions given by the low negative frequencies are completely uncoupled from the high frequency motions of the OH and CO bond. Although, the values of the stretching frequency might not reach spectroscopic accuracy, they can be assumed to represent the correct trend. In Table 5.1, the obtained ν(OH) and ν(CO) for both H-SAPO-5 and H-SSZ-24 upon CO adsorption are also given. However, this assumption remains a hot topic for debate. When combining these frequencies with the other frequencies given Table 5.1 and the stretching frequency for CO in the gas phase (ν(CO) = 2114 cm^{-1}) the shifts can be determined. For H-SAPO-5, $\Delta\nu$(OH) and $\Delta\nu$(CO) are respectively equal to -358 cm^{-1} and +68 cm^{-1}. Whereas for H-SSZ-24, values of -406 cm^{-1} and 32 cm^{-1} were found for $\Delta\nu$(OH) and $\Delta\nu$(CO) respectively. The expected trend for the $\Delta\nu$(CO) is not respected, this could be due to the use of the poorly minimized geometries resulting in wrong frequencies from the NMA. Other errors might arise from the used functional and the lack of anharmonicity and temperature effects in the NMA. The trend for $\Delta\nu$(OH) is correct and shows that H-SSZ-24 is indeed more acidic. However, the deviation from the IR spectra is large.

Another method can be implemented that does not require the NMA. This method is called the ω/r method. It is a scaling method based on the correlation between the CO stretching frequency and the CO bond length [182]. It uses parameters which were developed, in such a way that an excellent agreement of the computational frequencies with the experimental values was obtained. The correlation is given in Equation 5.3 in which $d(CO)$ is the CO bond length, $\Delta\nu$ a correction of the anharmonicity and a, b and $\Delta\omega$ are parameters dependent on the basis set and the used functional. The anharmonicity is approximately -29 cm^{-1} and the error $\Delta\omega$ with respect to the exact frequency can be approximated by -5 cm^{-1}. However, there are no

parameters a and b available for the revPBE functional used in this master thesis. Therefore, this method can not supply reliable results here.

$$\nu(CO) = ad(CO) + b + \Delta\nu + \Delta\omega \tag{5.3}$$

Arean et al. state that the use of frequency shifts as a measure for the zeolitic acid strength should be handled with caution [183]. In many cases the enthalpy change involved in that hydrogen-bonding interaction and the frequency shifts are correlated. However, it is not always the case. Therefore, the enthalpy change is often a better indicator for the acid strength. In the future, these enthalpy changes upon CO adsorption could also be calculated for H-SAPO-5 and H-SSZ-24.

5.3 Conclusion

When theoretically modeling a solid acid catalyst, one must keep in mind that not only the topology but also the acid site density can influence the acid strength of a zeolite. This density can already be measured via experiments. However, no uniform scale is yet available to describe the acid strength on the basis of first-principles calculations. Almost all attempts to characterize the acid strength in this chapter led to inconclusive results. Only the shifts in the OH stretching frequency upon CO adsorption indicated that the used catalyst model for H-SSZ-24 contains indeed stronger acid sites than H-SAPO-5. However, the values of the shifts did not agree with experiments. The obtained IR spectra is temperature dependent, while the NMA values were taken at 0 kelvin. Furthermore, the calculated frequencies can also vary based on the chosen functional, basis set etc.

Chapter 6

Adsorption of methylating agents and aromatics in H-SAPO-5 and H-SSZ-24

The adsorption of the reactants for a methylation reaction is modeled inside H-SAPO-5 and H-SSZ-24 to elucidate the effect of zeolitic acid strength. As a consequence of the varying acid strength, the interaction between guest molecules and the framework is also different in both materials. This will be reflected in the adsorption behavior of the guest molecules. Therefore, the study of the adsorption behavior forms the first step towards revealing the differences in reactivity of H-SAPO-5 and H-SSZ-24.

As methylation reactions play a key role in the MTO mechanism (see chapter 2). These reactions will be addressed in this study. The focus will lie on the methylation of three aromatics: benzene, toluene and o-xylene, since the aromatics are considered to be important HP species during MTO (see chapter 2). As methylating agents methanol, DME and framework-bound methoxides will be compared. MD simulations at 623 K and 1 atm are performed for every combination of the methylating agents and aromatics, as represented in Figure 6.1.

First, the adsorption of the separate reactants is modeled for the methylation reaction inside H-SAPO-5 and H-SSZ-24. Once this single adsorption behavior is mapped, the effect of co-adsorption is investigated by adding the other reactant needed for methylation. This investigation can give insights into the catalyst reactivity towards methylation of aromatics.

The first section focuses on the difference in adsorption behavior between single and co-adsorption, while the second section investigates whether there is a competition for the acid site between the methylating agent and aromatic. This is examined, because certain configurations or adsorption complexes are more reactive towards methylation than others. As a final aspect, this chapter investigates the probability of the occurrence of pre-reactive complexes and the chances to protonate the methylating agent. With these two probabilities, a first step is taken towards

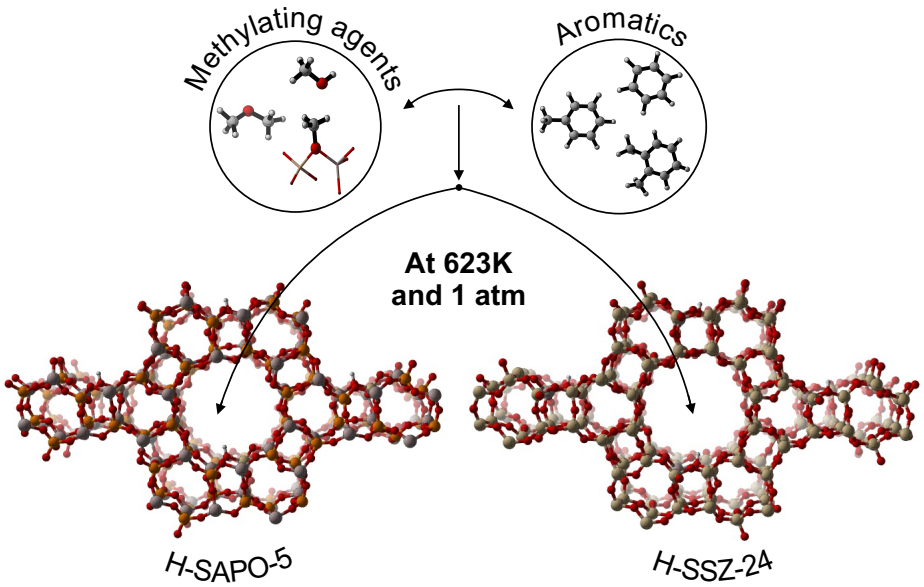

Figure 6.1: An MD simulation is performed at 623 K and 1 atm in H-SAPO-5 and H-SSZ-24 for each pair combining one methylating agent (methanol, DME and a framework-bound methoxide) and one aromatic (benzene [106], toluene, o-xylene).

a quantitative analysis of the reactivity towards methylation reactions in AFI.

6.1 Comparison between single and co-adsorption behavior in AFI

First the adsorption of a single molecule inside H-SAPO-5 and H-SSZ-24 is examined for the methylating agents (methanol and DME) and the aromatics (benzene,toluene and o-xylene) by performing separate MD simulations for each of the 5 species at 623 K and 1 atm. This adsorption behavior will be influenced once a second molecule enters the AFI channel. Therefore, the adsorption of a methylating agent together with an aromatic is also studied by means of MD simulations at 623 K and 1 atm in both H-SAPO-5 and H-SSZ-24. This section will focus on the differences in behavior of the methylating agents and aromatics for single adsorption and co-adsorption in the two catalytic materials.

First of all, the studied reactants all possess a different proton affinity, which will result in a different interaction strength with the acid site. This should lead to considerable differences in the adsorption behavior of all species. In 1998, Hunter and Lias studied the proton affinities of several molecules [184]. Table 6.1 represents the results of their experimental study for methanol, DME, benzene, toluene and o-xylene accompanied by the proton affinities obtained from static DFT calculations for the aromatics [122]. From the results of Hunter and Lias, methanol and benzene appear to have a comparable proton affinity and the proton affinity is found to increase with increasing methyl substitutions of the aromatic. This increase arises from the electron

Table 6.1: Proton affinities in the gas phase for methanol, DME, benzene, toluene and o-xylene in $kJ\,mol^{-1}$ from experiments by Hunter and Lias [184] and from DFT calculations by De Wispelaere [59], [185].

	Experiment [184]	DFT [59], [185]
Methanol	754	-
DME	792	-
Benzene	750	763
Toluene	784*	758**
O-xylene	794*	796**

*The proton is placed on the para position.

**The proton is placed on the geminal position.

donating nature of methyl groups. However, this increasing trend is not visible in the DFT based proton affinities, which can be due to the fact that proton affinities were considered for the protonation at the geminal position. A methyl group is known to be an ortho-para director, examining the ortho or para location of the proton with DFT would probably result in the desired trend.

6.1.1 Effect of co-adsorption on distance to acid site

The interaction of a species with the acid site will depend on the proton affinity of that species and the Brønsted acid strength of the acid site. A good measure for the interaction is the average distance between the proton of the acid site and the C atoms on the aromatic ring or the O atom on the methylating agent, since a shorter average distance is expected for species that adsorb more strongly and hence that might also be more susceptible to perform a reaction. Figure 6.2 and Figure 6.3 give this average distance respectively for the aromatics and for the methylating agents in both H-SAPO-5 and H-SSZ-24. Note that the data of the single adsorption of DME and benzene are not included, since they are not yet available. The data for benzene with methanol, DME and a framework-bound methoxide are retrieved from the MD simulations performed by De Wispelaere et al. [106].

Overall, the average distance of both methanol and DME to the acid site is the shortest in the H-SSZ-24 material, as seen in Figure 6.2. This arises from its higher acid strength. In H-SSZ-24, the average distance to the acid site is approximately 1.5 Å for both methanol and DME. In this case, the adsorption behavior of DME and methanol is not significantly different, although DME possesses a higher proton affinity. Unfortunately, data for the single adsorption of DME are still missing. Because of the higher proton affinity of DME compared to methanol, the average distance to the acid site for single adsorption of DME is expected to be substantially smaller in H-SAPO-5 than the average distance for methanol in H-SAPO-5, whereas the distance

in H-SSZ-24 would be similar for both methanol and DME. In that case, the graph would prove that once the acid strength is high enough, the effect of the difference in proton affinities is less visible.

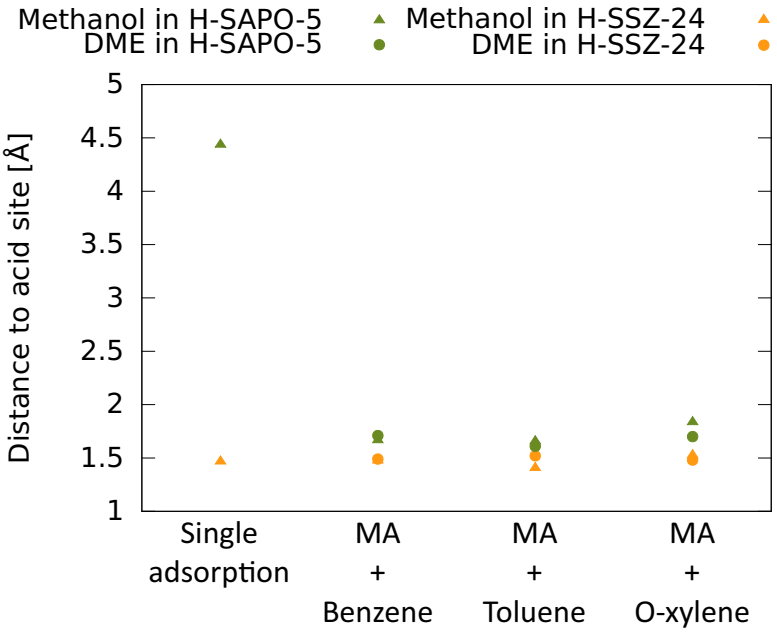

Figure 6.2: Average distance of the O atom of methanol (triangles) and DME (dots) to the acid site in H-SAPO-5 (green) and H-SSZ-24 (orange) in case of a single adsorption and adsorption on the acid site in the presence of benzene, toluene and o-xylene. MA is short for methylating agent. The data for benzene are taken from ref. [106].

Moreover, the difference between single adsorption of methanol in H-SAPO-5 and methanol co-adsorbed is striking. The average distance to the acid site for methanol was found to be equal to 4.4 Å. This is significantly higher than 1.7 Å, which is approximately the average OH distance for methanol during co-adsorption. Note that the value reported for single adsorption of methanol in H-SAPO-5 has a high standard deviation of 3.5 Å. Numeric data of Figure 6.2 and corresponding standard deviations are given in Appendix C. Apparently, the interaction between methanol and the mildly acidic site of H-SAPO-5 is limited at 623 K and methanol is allowed to move freely inside the AFI channel. However, once an aromatic enters the channel, methanol will be pushed to the acid site due to steric hindrance. This behavior is not seen in H-SSZ-24, since the interaction between methanol and the acidic proton is already stronger resulting from its higher acidity. In a follow-up study, it would be interesting to check whether the same trend is seen in H-SAPO-5 during the single adsorption of DME, which has a higher proton affinity than methanol.

The average distance from the aromatic ring to the acid site or a framework-bound methoxide is given in Figure 6.3 for single adsorption as well as for the MD simulations in which methanol or DME are already adsorbed on the acid site. Comparing single adsorption of toluene in H-SAPO-5 and H-SSZ-24 indicates that the interaction between the acid site and toluene is weaker for the mildly acidic material than for the strongly acidic one. Based on the average distance

from o-xylene to the acid site during single adsorption, the interaction inside H-SAPO-5 and H-SSZ-24 seems similar. Furthermore, it appears that in H-SSZ-24 o-xylene is adsorbed more strongly than toluene, whereas in H-SAPO-5 it is the other way around.

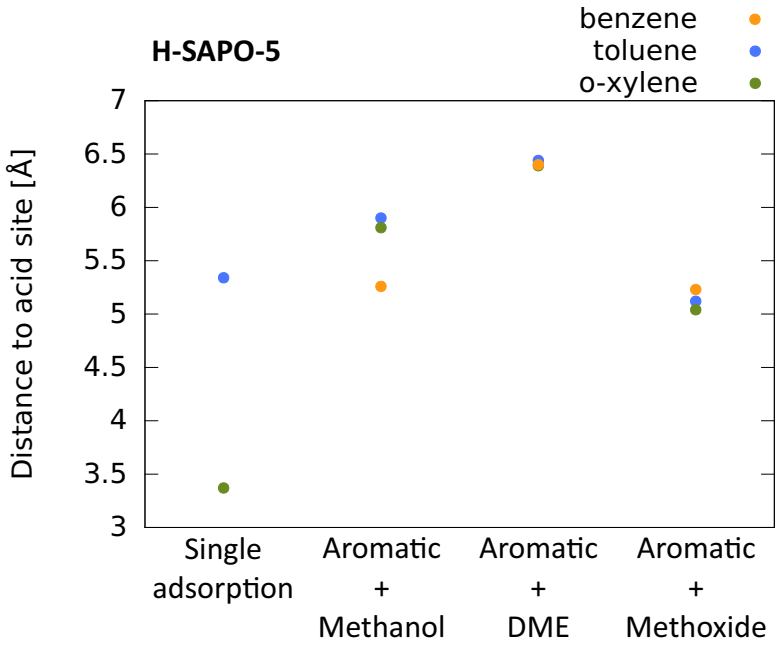

(a)

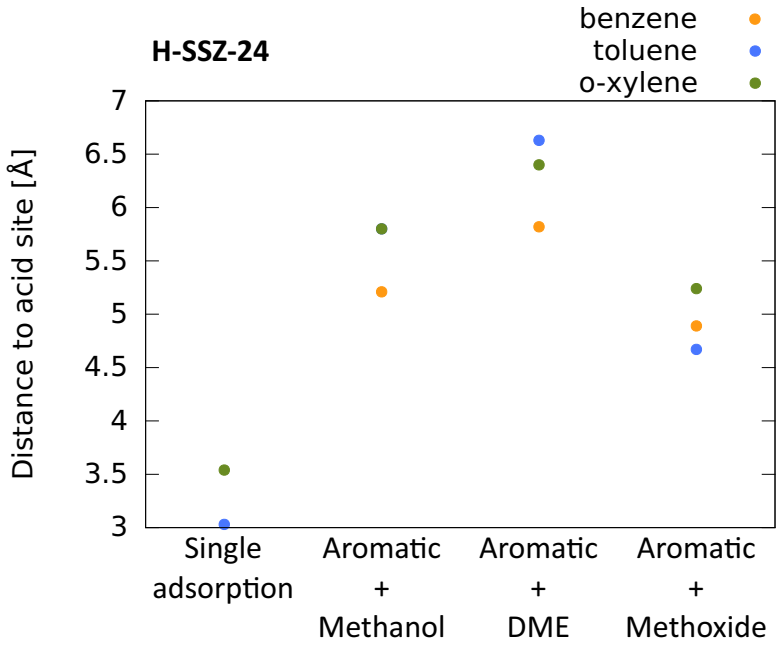

(b)

Figure 6.3: Average shortest distance of the C atoms of an aromatic ring to the acid site in H-SAPO-5 (a) and H-SSZ-24 (b) in case of a single aromatic adsorbed, an aromatic co-adsorbed when methanol or DME are located on the acid site and the average shortest distance of the aromatic ring to the C atom of a methoxide.The data for benzene are taken from ref. [106].

In case of co-adsorption no clear trends are discernible in Figure 6.3. When methanol is adsorbed

on the acid site, the average distance to the acid site for benzene is the smallest compared to toluene and o-xylene in both AFI materials. In H-SAPO-5, the average distances to the acid site are quite similar for all three aromatics when DME is co-adsorbed. This is also the case when the active site is a framework-bound methoxide in H-SAPO-5. However, in H-SSZ-24 the spread between the distances for each aromatic is larger. Nevertheless, there is no trend in the order of the distances for the aromatics. As expected, the difference in proton affinity of the aromatics does not affect the average distances to the acid site, since methanol and DME are blocking the access to those sites.

Depending on the mechanism (concerted or stepwise methylation), either the Brønsted acid site or the framework-bound methoxide will play the role of active site during the methylation reaction. When taking into account the standard deviations, the average distance for the aromatics to the framework-bound methoxide species lies between 3.73 Å and 6.53 Å in H-SAPO-5 and between 3.65 Å and 6.44 Å in H-SSZ-24. This is very similar to the average distance from the closest carbon atom of the aromatic to the carbon atom(s) of methanol and DME, which equals approximately 5 Å in all MD simulations. From these data, it might be concluded that a framework-bound methoxide species contains the same reactivity towards methylation as methanol and DME due to the similar CC distances. However, this can only be accurately checked by performing a metadynamics study to obtain activation barriers (see chapter 7).

6.1.2 Effect of co-adsorption on the orientation of aromatics in the AFI channels

During a previous adsorption study performed by Thomas Deconinck, the orientation of benzene inside the AFI channel seemed to dependent on the chemical composition and acid strength of the framework [186]. In H-SAPO-5, the benzene ring preferred to lie flat inside the channel on top of a methoxide, whereas in H-SSZ-24 the aromatic would stand upright above the methoxide. This upright position appeared to be stabilized by the interaction of the channel walls with the aromatic. These findings were based on static calculations and do not account for the finite temperature effect and conformational freedom of the guest molecules due to the large channels in the AFI materials. Analysis of the MD simulations of benzene with methanol, DME and a framework-bound methoxide, performed by De Wispelaere et al. [106], reveal that also other stable orientations are possible other than the ones optimized by static calculations. Therefore, it is better to examine the aromatic orientation during an MD study.

Figure 6.4 shows that the benzene molecule can stand up right in the channel while methanol is located on the acid site. This is either with the O atom or with the C atom of methanol pointed towards the aromatic. When benzene stands upright in the channel, two configurations are distinguishable: benzene faced to the channel walls and benzene faced to the channel end, as also shown in Figure 6.4 (b) and (c). For the simulation with DME as methylating agent, benzene seldom lies flat in the channel and preferentially stands upright faced to the channel end in both H-SAPO-5 and H-SSZ-24. Since the detected configurations for methanol and DME in both AFI materials are quite similar only snapshots of methanol in H-SAPO-5 are shown in

this chapter.

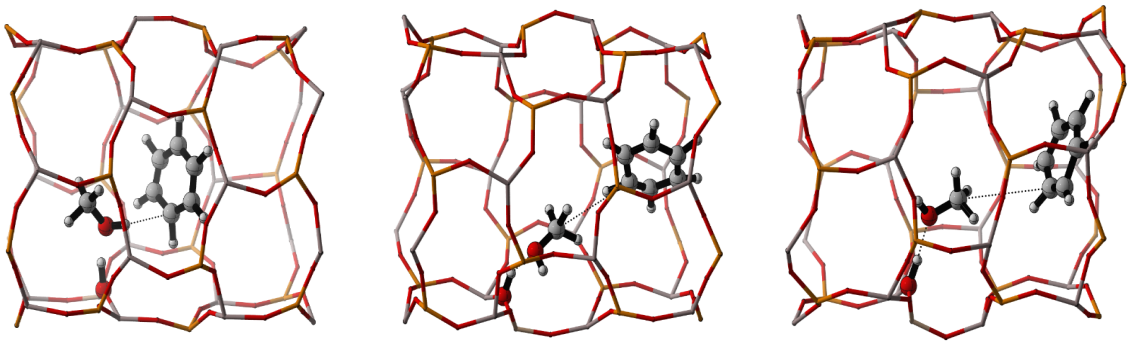

(a) **(b)** **(c)**

Figure 6.4: Three configuration observed in H-SAPO-5 at 623 K and 1 atm where methanol is located on the acid site with its O atom pointed towards benzene (a) and its C atom pointed towards benzene (b) and (c). In all configurations benzene stands upright, either to the wall of the channel (b) or faced to the channel end (c).

Also in case of a framework-bound methoxide, the conclusions from the static calculations are not completely correct. Although, the configurations obtained with the static calculations are present in the MD simulations, other configurations are also found. In H-SAPO-5, co-adsorption complexes are found in which benzene stands upright and in H-SSZ-24 benzene can also lie flat on top of the methoxide, as shown in Figure 6.5. So far no true differences were found in orientation behavior of benzene in the two AFI materials.

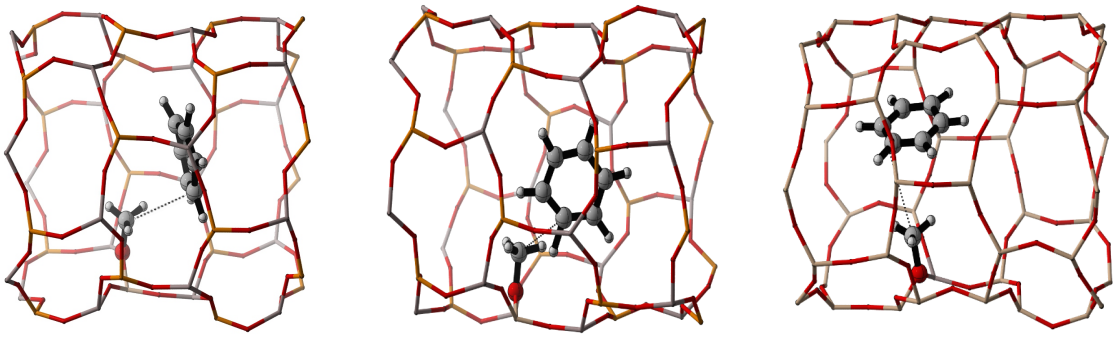

(a) **(b)** **(c)**

Figure 6.5: Co-adsorption complexes for benzene physisorbed at a framework-bound methoxide in H-SAPO-5 (a)(b) and H-SSZ-24 (c) at 623 K and 1 atm.

MD simulations were also carried out for toluene and o-xylene in both materials, in an attempt to describe the difference in orientation by defining probabilities of a number of possible orientations. The orientation of toluene and o-xylene is mapped in each material and for all methylating agents. Three orientations are considered: (1) the flat position above the active site, (2) the upright position with the aromatic faced to the catalyst wall and (3) the upright position in which the aromatic is stabilized by the surrounding framework. All of these positions are represented in Figure 6.6. Note that only position (1) and (3) were considered during the

static calculations [186].

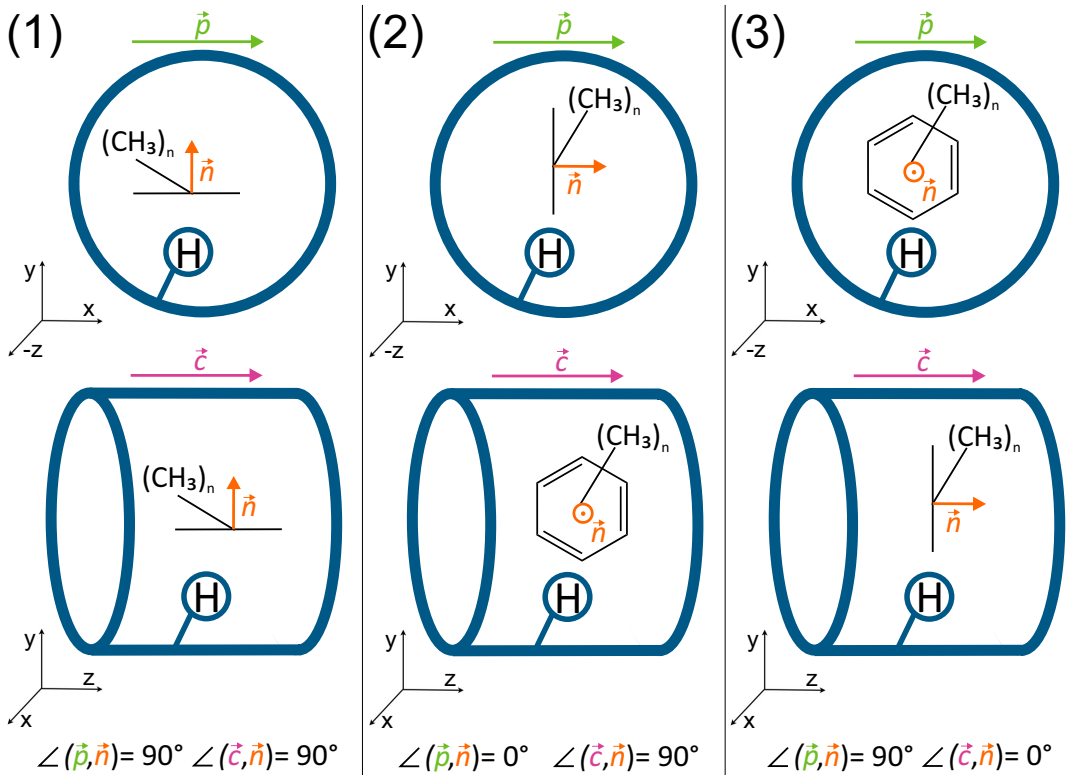

Figure 6.6: Schematic representation of three extreme cases for the orientation of an aromatic in the AFI channel (represented in blue): the aromatic lies flat with respect to the acid site (1), the aromatic stands upright with respect to the acid site while faced to the channel wall (2) and the aromatic stands upright with respect to the acid site while faced to the channel end (3). The orange vector $\vec{n}$ represents the normal to the aromatic plane. The green $\vec{p}$ and purple $\vec{c}$ vector are characteristics of the channel itself.

For each MD simulation, it is assessed for which percentage of the simulation the aromatic is positioned in a certain orientation. This was done by defining three vectors: the orange vector $\vec{n}$ in Figure 6.6 shows the normal vector perpendicular to the aromatic's plane, the green vector $\vec{p}$ is aligned with the channel width and approximately perpendicular to the acid site's OH bond and the yellow vector $\vec{c}$ is aligned with the channel itself. By considering these three vectors, each one of the aforementioned orientations can be uniquely described by two angles with respect to $\vec{n}$. These angles are also given at the bottom of Figure 6.6.

The percentage of the time that one of the three orientation cases occurs is given for toluene in Figure 6.7 and for o-xylene in Figure 6.8. At high temperatures, the guest molecules are very mobile, therefore a lot of deviation is allowed from the three ideal cases represented in Figure 6.6, namely 30° from the ideal angles. The main trend derived from these figures is that the aromatic will preferentially lie flat inside the cage and rarely stands upright faced to the channel end regardless of the type of adsorption (single or co-adsorption), type of methylating agent and acidity of the catalyst. Thus, for toluene and o-xylene, the order of the probability of the orientation is (almost) always: case (3) < case (2) < case (1).

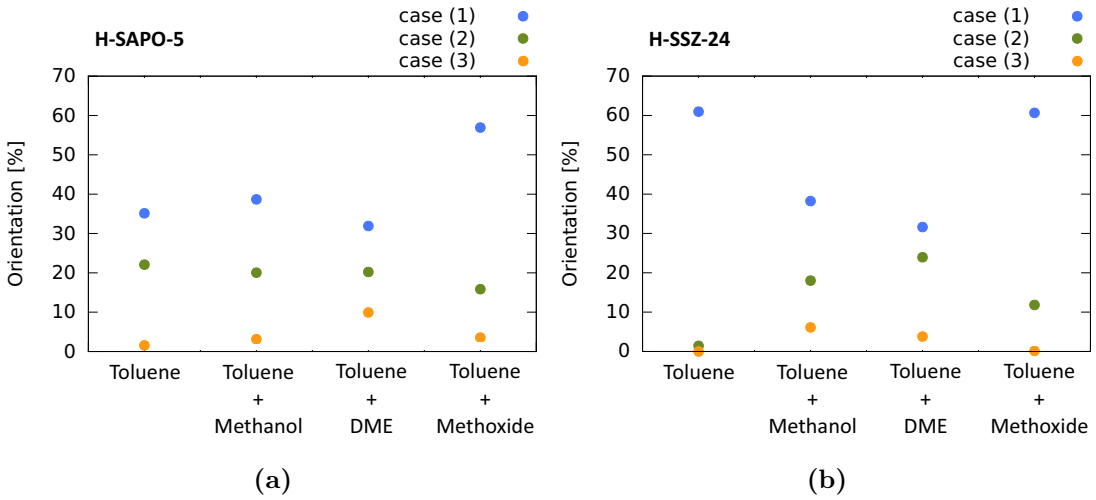

Figure 6.7: Probability for each of the three orientations (with an allowed deviation of 30° from the ideal cases) in H-SAPO-5 (a) and H-SSZ-24 (b) at 623 K and 1 atm for single adsorption of toluene and toluene in the presence of a methylating agent (methanol, DME or a framework-bound methoxide).

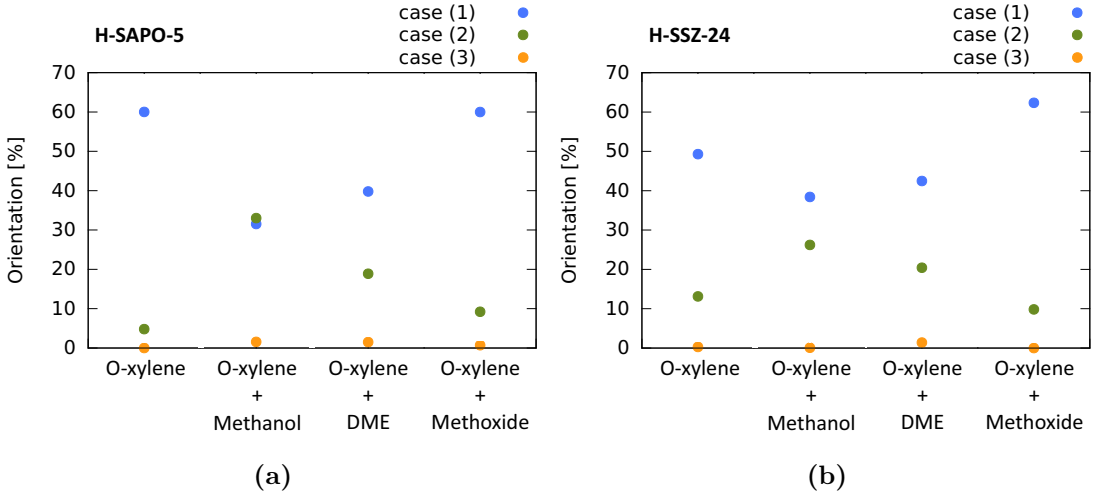

Figure 6.8: Probability for each of the three orientations (with an allowed deviation of 30° from the ideal cases) in H-SAPO-5 (a) and H-SSZ-24 (b) at 623 K and 1 atm for single adsorption of o-xylene and o-xylene in the presence of a methylating agent (methanol, DME or a framework-bound methoxide).

Due to a technical issue, the probabilities of benzene could not be obtained. However, by looking at the MD simulations a main trend was observed: case (3) is primarily present for benzene. Though, this third orientation case was frequently observed for benzene, this is not true for toluene and o-xylene. Evidentially, this is the result of the presence of the methyl groups at the aromatic ring which are preferentially not directed to the zeolite walls. The possibility of finding case (3) is therefore also the smallest for o-xylene.

When a framework-bound methoxide is present, the preference for the flat orientation is the highest (compared to methanol and DME) for toluene as well as for o-xylene in both AFI

catalysts. This might result from a stronger interaction between the methyl group from a framework-bound methoxide than from methanol or DME, which gives rise to less mobility of the aromatics. This stronger interaction can be derived from Figure 6.3, since the distance from the aromatics to the framework-bound methoxide is smaller than from the aromatics to methanol or DME.

Compared to single adsorption of the aromatic, the probability of the flat orientation slightly decreases mostly in favor of the upright orientation with the aromatic faced to the wall. This trend is absent in the MD simulation of toluene in H-SAPO-5. The lower probability of the flat orientation might be due to the weaker interaction between the acid site and toluene during single adsorption. This weaker interaction might result from the lower acid strength of H-SAPO-5 and lower proton affinity of toluene compared to o-xylene. However, no adsorption enthalpies were calculated during this master thesis, therefore it is not certain how strong or weak the interaction between the aforementioned species truly are.

Also, this investigation for toluene and o-xylene reveals no straightforward dependence of strength of the Brønsted acid site on the orientation of the aromatic. Thus, the acid strength controls the distance to the methylating agent, but not the distance to the aromatics and also not their orientation. The orientation of the aromatic is predominantly determined by its bulkiness. This is clearly shown by the difference between benzene and the methylated aromatics. While benzene almost always prefers the upright position faced to the channel end, toluene and o-xylene preferentially lie flat in the channel.

6.2 Competitive adsorption

In the previous section, only adsorption complexes were taken into account in which the methylating agent was present at the acid site and the aromatic was co-adsorbed. However, it is also possible for the aromatic to be adsorbed on the acid site and even get protonated. Therefore, the competition for adsorption on the acid site is investigated by performing two separate MD simulations. First, a MD simulation is started from a geometry in which the methylating agent is adsorbed on the acid site. Then, a simulation is started from a configuration with the aromatic directly adsorbed on the acid site. Both configurations are represented in Figure 6.9. This competitive behavior is of interest, since only the configuration on the left of Figure 6.9 can lead to the formation of a favorable pre-reactive complex for the methylation reaction.

In the mechanisms given in section 2.3 and section 2.4, Methanol and DME need to be protonated when executing a methylation reaction. To achieve this protonated state, the methylating agent must be a priori adsorbed on the acid site. When the aromatic is adsorbed on the acid site, thereby blocking methanol or DME from the acid proton, the methylation reaction cannot take place via the aforementioned mechanisms. Therefore, the configuration with the adsorbed aromatic is not preferred and to reach high methylation rates the configuration with methanol or DME on the acid site should be abundant in the zeolite framework. However, Svelle and Bjørgen suggested another methylation mechanism wherein polymethylbenzenes are protonated

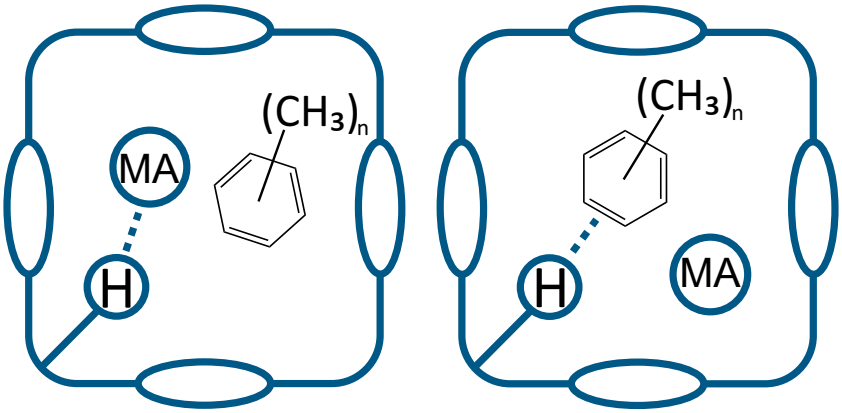

(a) **(b)**

Figure 6.9: Schematic representation of the initial configurations used during the MD simulation. Herein H represents the Brønsted acid site, MA the methylating agent (methanol or DME) and n the number of methyl substituents on the aromatic ring (0 for benzene, 1 for toluene and 2 for o-xylene). (a) shows the configuration in which the methylating agent is adsorbed on the acid site while (b) represents the adsorption of an aromatic compound on the acid site.

and react with a neutral methanol molecule [187]. This route seemed plausible based on the realistic energy barriers obtained from DFT calculations.

To have a good methylating agent its proton affinity must be high. Methanol and especially DME have a relatively hight affinity for the acid site, however since larger aromatics possess increasing proton affinities, the aromatic can start to compete with the methylating agent once it contains enough methyl groups [59], [122]. Whenever the fraction of the MD run in which the aromatic is located nearest to the acid site is very short, it can be assumed that no competitive adsorption takes place and that the methylating agent is located predominantly on the acid site. However, if the contribution of the aromatic on the acid site is significant, then competitive adsorption cannot be neglected.

From the MD simulations in H-SAPO-5 and H-SSZ-24 of benzene with methanol and with DME performed by De Wispelaere et al. [106], there is no sign of competitive adsorption. In the MD simulations starting from configuration (b) from Figure 6.9, the methylating agent starts pushing benzene away from the acid site. Already after a few ps the methylating agent will be physisorbed on the acid site and hence configuration (a) from Figure 6.9 is observed.

Appendix E represents the figures used to determine whether competitive adsorption takes place or not for methanol and DME as methylating agents and for toluene and o-xylene as aromatic compounds.

In both H-SAPO-5 and H-SSZ-24, no competitive adsorption is seen for methanol and toluene. Here, methanol is located preferably on the acid site. However, DME experiences more difficulty to get a grip on the acid site when toluene is physisorbed. This is demonstrated by Figure 6.10. Eventually after 25 ps, there is a clear switch from configuration (b) to (a) in H-SSZ-24 and

toluene does not try to push methanol away from the acid site. However in H-SAPO-5, the struggle for the acid site lives on even after 60 ps.

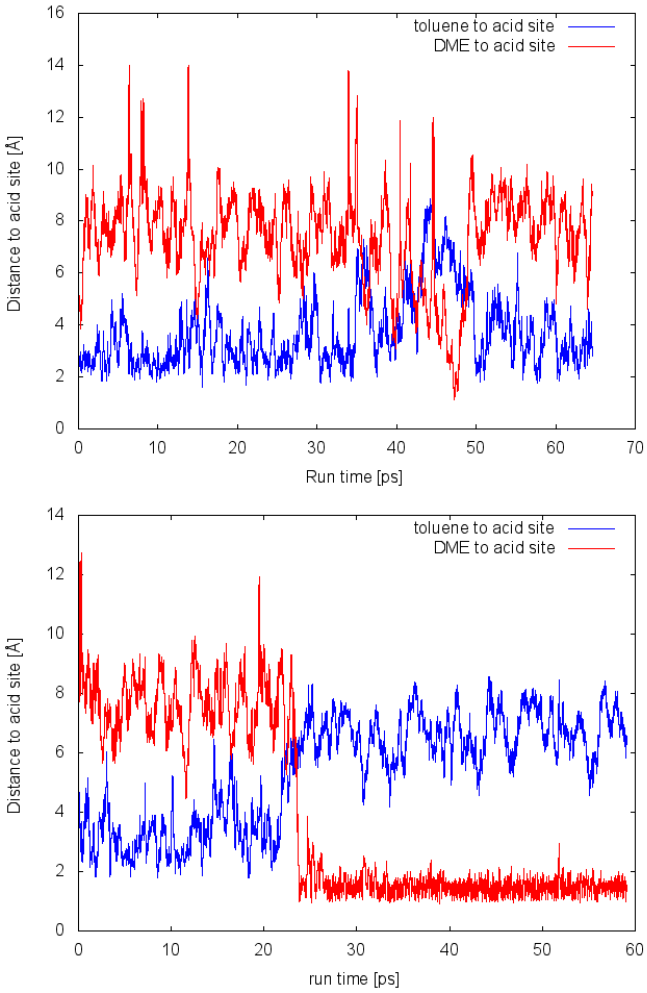

Figure 6.10: The distance in Å to the acid site for the closest C atom of the aromatic ring of toluene and for the O atom of DME as function of the run time in ps, when starting from a configuration where toluene is closest to the acid site in H-SAPO-5 (top) and H-SSZ-24 (bottom) at 623 K and 1 atm.

In an attempt to verify the results of the toluene simulation, the MD run in H-SAPO-5 with toluene on the acid site and in presence of DME was reproduced by starting from a slightly different initial geometry. The resulting distances, shown in Figure 6.11, are completely different from Figure 6.10 and there is no remaining sign of the competitive adsorption. The trajectory followed during MD was apparently dependent on the initial geometry, meaning that the ergodicity of the ensemble was not reached yet. The ergodicity can be improved by simulating over a very long time. However, the use of MD with DFT is still computationally very expensive. Nevertheless, it is expected that in the future very long MD runs will be achievable and even with the use of more accurate functionals. If there would be very accurate force fields available today, long MD runs would also be reachable.

For methanol and o-xylene, methanol is the most stable adsorbate in both catalysts. However,

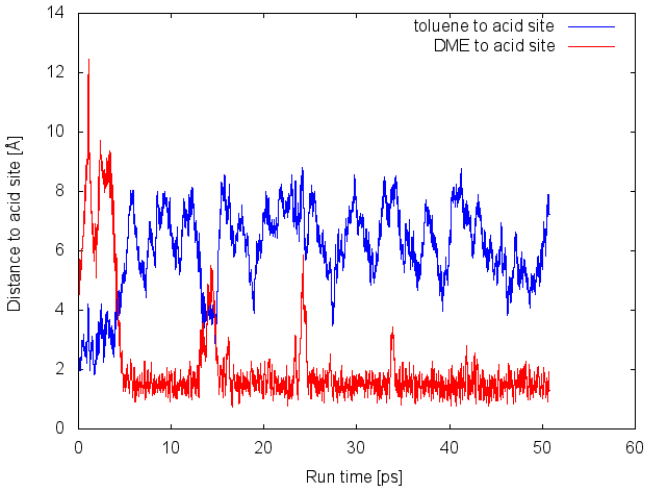

Figure 6.11: The distance in Å to the acid site for the closest C atom of the aromatic ring of toluene and for the O atom of DME as function of the run time in ps, when starting from a configuration where toluene is closest to the acid site in H-SAPO-5 (top) at 623 K and 1 atm from a different initial geometry.

once methanol is located on the acid site, o-xylene tries to push it away again. This means that there is competitive adsorption. O-xylene holds almost 20 ps on the acid site in H-SAPO-5, whereas it holds for 15 ps in H-SSZ-24 as shown in Figure E.6. Thus, the switch from configuration (b) to (a) is slightly sooner in H-SSZ-24, probably due to more interaction between methanol and the acid site resulting from the higher acidity. However, this might also be a coincidence and only by running very long MD simulations one can truly know if the timescale for adsorption of o-xylene on the acid site is shorter in H-SSZ-24 than in H-SAPO-5. No competitive adsorption behavior was observed for DME and o-xylene in H-SAPO-5 and H-SSZ-24. Due to the lower acidity of H-SAPO-5, DME needs more time to adsorb on the acid site and replace toluene in configuration (b) than in H-SSZ-24. Nonetheless, DME remains on the site and o-xylene does not attempt to readsorb.

Table 6.2 summarizes the combinations of guest molecules and catalyst that give rise to competitive adsorption behavior. The co-adsorption of the aromatic with the largest proton affinity considered, o-xylene, and the methylating agent with the lowest proton affinity, methanol, is very prone to competitive adsorption and this in both H-SAPO-5 and H-SSZ-24. Figure 6.12 (a) and (b) show two observed co-adsorption complexes in which o-xylene is located at the acid site in H-SAPO-5 and H-SSZ-24 respectively. In both materials o-xylene lies preferentially flat while being adsorbed on the acid site.

Finally, some remarks must be made on the difference between the methanol and DME adsorption behavior in AFI. In both the MD run with methanol and toluene and with methanol and o-xylene (Figure E.3 and Figure E.7), there appears to be at some point a very stable interaction between methanol and the acid site of H-SSZ-24, which results in an almost constant distance of 1 Å from the oxygen atom of methanol to the proton of the acid site. This stable interaction corresponds to a protonated methanol species, whereas in all other cases methanol was only

Table 6.2: Summary of the competitive adsorption in AFI. ✓represents the cases were competitive adsorption is seen, whereas × stands for the absence of competitive adsorption

	Methanol		DME	
	H-SAPO-5	H-SSZ-24	H-SAPO-5	H-SSZ-24
Benzene	×	×	×	×
Toluene	×	×	×	×
O-xylene	✓	✓	×	×

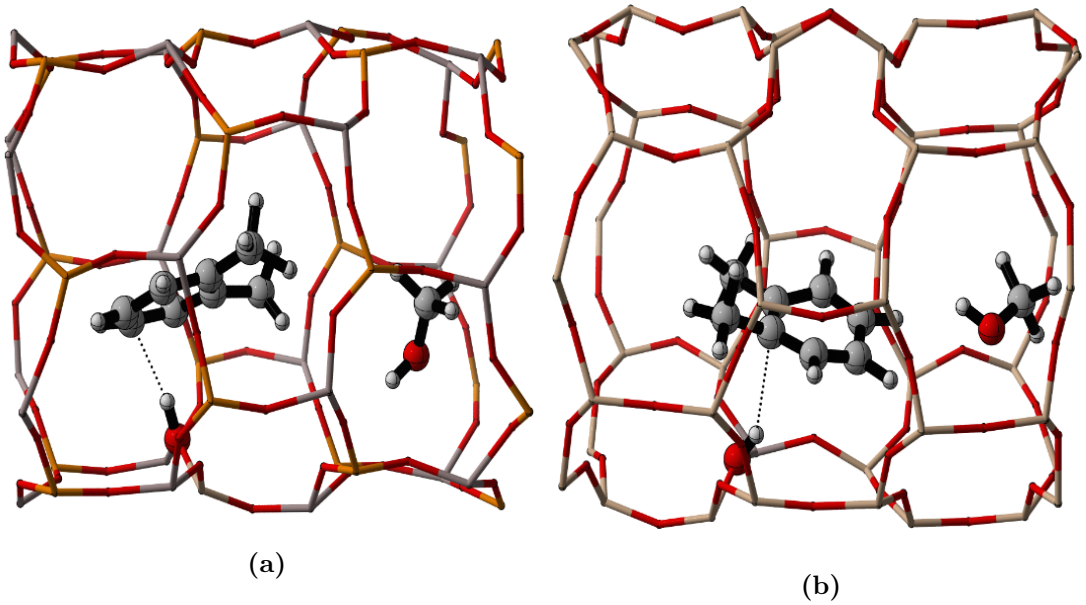

(a) **(b)**

Figure 6.12: Co-adsorption complexes with o-xylene located on the acid site and methanol co-adsorbed in H-SAPO-5 (a) and H-SSZ-24 (b) at 623 K and 1 atm.

physisorbed on the acid site. Figure 6.13 shows the protonated methanol species on the left, while the figure on the right shows a physisorbed methanol species. For o-xylene, this protonated state is briefly observed after about 60 ps (see Figure E.7), while for toluene the stable interaction is already observed after 5 ps and again after 35 ps and 45 ps in Figure E.3. This form of high interaction with the acid site is not seen in H-SAPO-5, due to the lower acidity of the material.

Protonation of the methylating agent is also not detected for DME. Maybe DME is less prone to the difference in acid strength between the two AFI catalysts due to its higher proton affinity. This was already detected in static calculations on the adsorption energy of methanol and DME in both AFI materials. For methanol the adsorption on an acid site in H-SSZ-24 was approximately 15 kJ mol^{-1} more stable than in H-SAPO-5, whereas the adsorption energy of DME only differed by approximately 1 kJ mol^{-1} in both materials [186]. In the next subsection, the difference between the studied methylating agents and aromatic compounds is assessed by

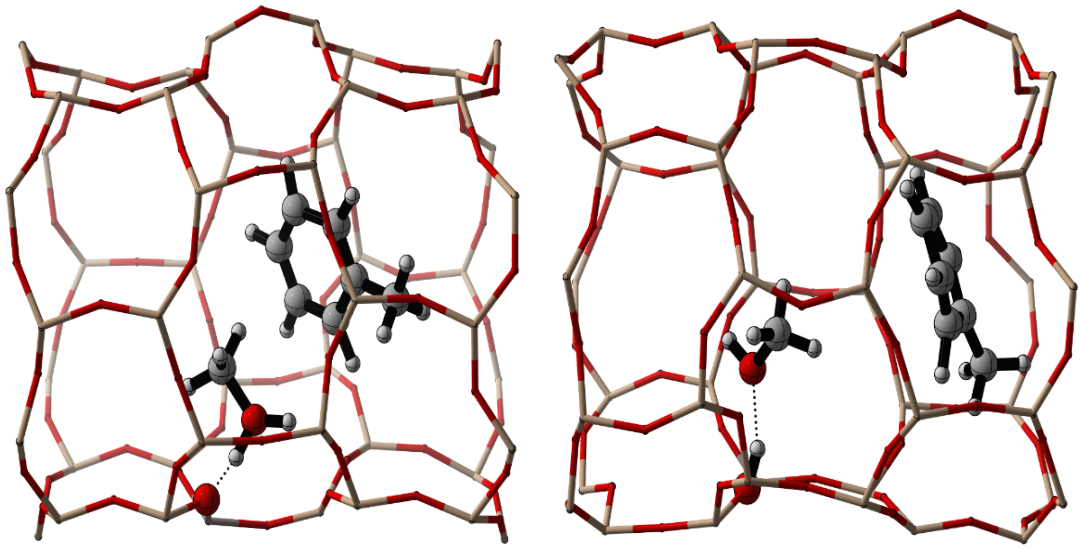

(a) **(b)**

Figure 6.13: Methanol chemisorbed (a) and physisorbed (b) in H-SSZ-24 with toluene coadsorbed at 623 K and 1 atm. The chemisorbed state of methanol corresponds to protonated methanol.

tracking pre-reactive complexes during the MD simulations.

6.3 Formation of pre-reactive complexes

As mentioned in section 4.3, MD is not suited to sample rare events, such as methylation reactions. The probability of sampling the required TS for a methylation reaction is very low during MD, especially when only simulating for 50 ps. However, pre-reactive complexes for the considered methylation reactions can be seen in these type of MD runs. The probability to form a favorable pre-reactive complexes is a measure for the reactivity towards methylation, as earlier shown by Westgård Erichsen et al. [106].

Upon the formation of a pre-reactive complex for methylation by methanol or DME its carbon atom must point towards the aromatic ring and not its oxygen atom. For this pre-reactive complex to react, the methylating agent must also be protonated. These two criteria are however not applicable to the case in which a framework-bound methoxide acts as the methylating agent. In this case, the distance between the aromatic ring and the methoxide must lie below a certain threshold value to obtain a pre-reactive complex. Below, the criteria for these pre-reactive complexes are discussed in more detail.

6.3.1 Methanol and DME as methylating agents

As described above, methanol and DME must be protonated prior to reaction. At high temperature, it was observed in the performed MD simulations that there spontaneously occurs a (partial) protonation of methanol and DME. The probability to observe this is directly linked

with the acid strength of the material and the proton affinity of the methylating agent. During the analysis of the performed MD simulations, the methylating agent is considered protonated when the distance from its O atom to the acidic proton, d1 on Figure 6.14, is shorter than 1.2 Å. Additionally for methanol, the bond length of its hydroxyl group, d2, must also be closer than 1.2 Å. As criterion for the pre-reactive complex the difference between the shortest distance from the C atoms of the aromatic ring to the O atom of the methylating agent (methanol, dimethyl ether), d3 and to the C atom(s) of the methylating agent, d4, was used. When this difference, d3-d4, during the MD runs is larger than 0.5 Å a pre-reactive complex is found and the methylating agents points with (one of) its C atom (s) towards the aromatic. Both criteria are schematically represented in Figure 6.14 for methanol, DME. Both criteria are applicable in H-SAPO-5 as well as in H-SSZ-24. The aforementioned criteria were already used by Westgård Erichsen et al. [106].

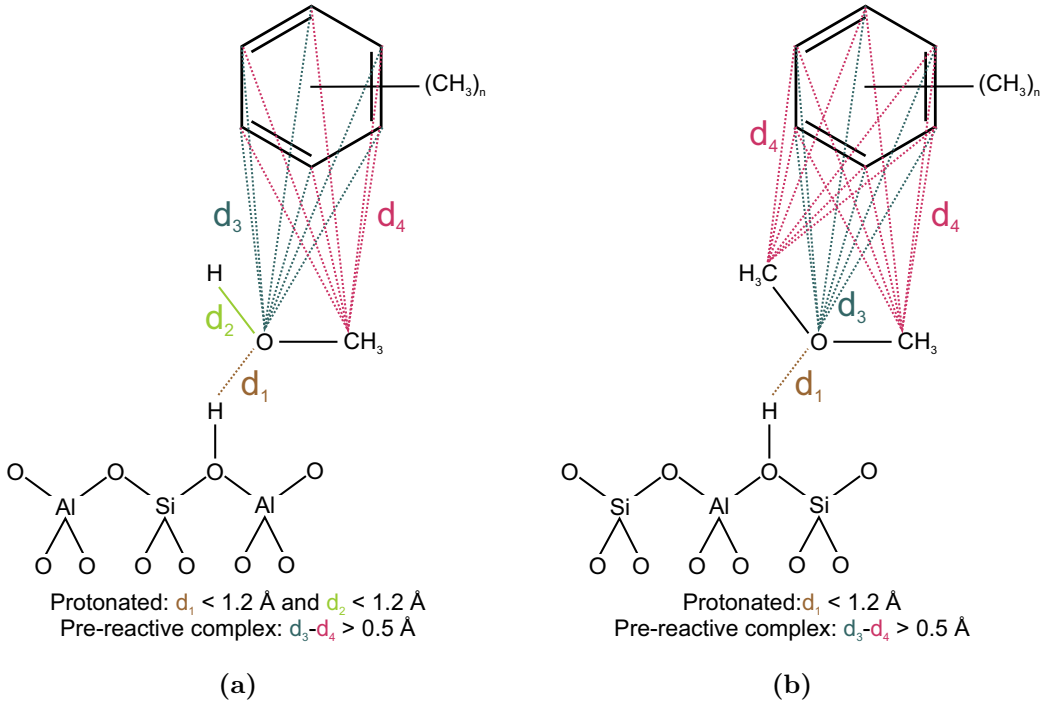

Figure 6.14: Schematic representation of the criterion for a pre-reactive complex and a protonated methylating agent for methanol in H-SAPO-5 (a) and for DME in H-SSZ-24 (b). Note that the criteria are independent of the used AFI catalyst.

Figure 6.15, Figure 6.16 and Figure 6.17 show a number of observed pre-reactive complexes in H-SAPO-5 and H-SSZ-24 for methanol and DME with benzene, toluene and o-xylene respectively. This is only a small grip out of the vast range of pre-reactive complexes observed during the MD runs. Again the orientation of the aromatic in the pre-reactive complexes for benzene is substantially different from the orientation of toluene and o-xylene due to the presence of the methyl substituents creating steric hindrance in the upright orientation corresponding to case (3) in Figure 6.6.

The probabilities for finding a desired orientation of the methylating agent towards the aromatic and for finding a protonated methylating agent during the 50 ps MD simulation at 623 K are

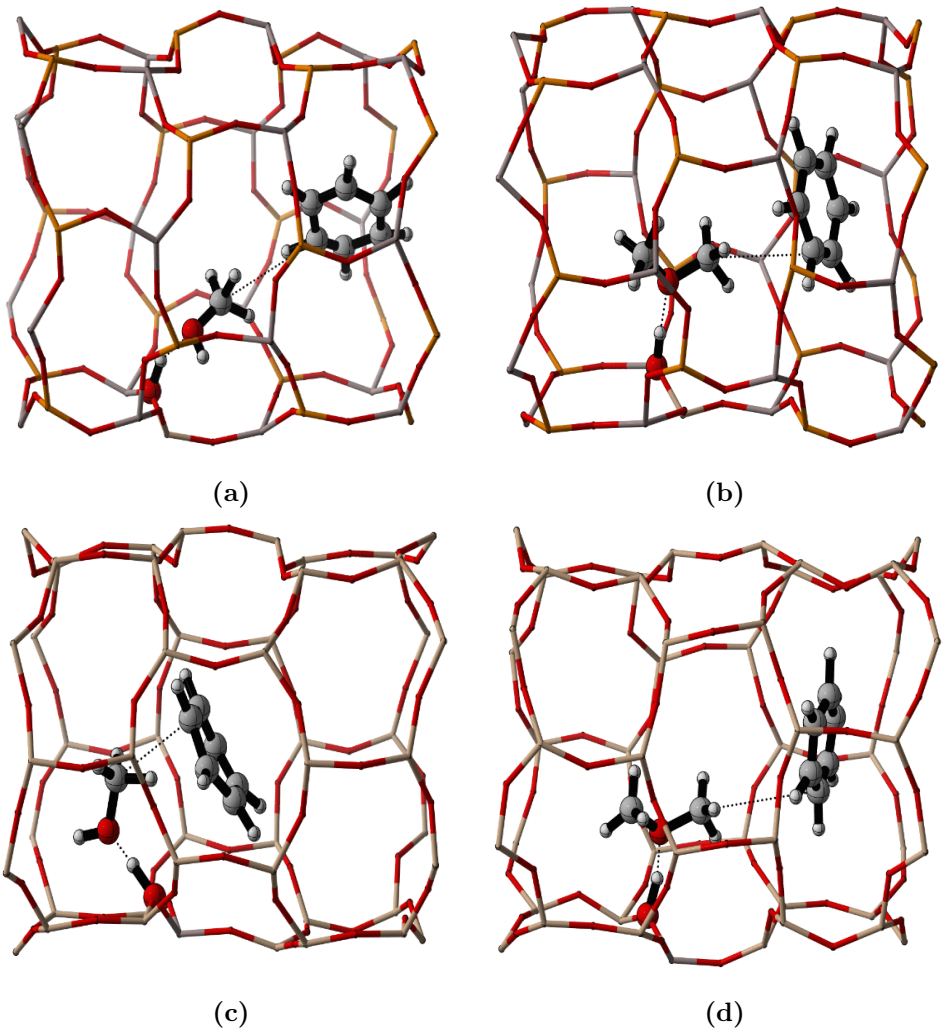

Figure 6.15: Pre-reactive complexes for benzene with methanol (a) and DME (b) in H-SAPO-5 and with methanol (c) and DME (d) in H-SSZ-24 at 623 K and 1 atm.

given in Figure 6.18 for H-SAPO-5 and H-SSZ-24. Overall, the probability of pre-reactive complex formation is higher for DME than for methanol. This is as expected, since statistically the probability of DME should be twice as high as for methanol due to the presence of 2 C atoms in DME, which are able to perform the methylation. However the probability of methanol and DME differ by more than a factor of 2, meaning that there is an additional stabilizing interaction between DME and the aromatics. This could be induced by the wall of the zeolite: due to a bulkier methylating agent such as DME, the mobility of the aromatics is reduced and the chance to "meet" DME is therefore higher than for methanol.

The influence of the acid strength is clearly visible in the protonation of the methylating agent. For the higher acidic material, the probability is higher as expected. The influence of the degree of methylation of the aromatics is not clear on the protonation probability and on the probability of a pre-reactive complex.

Further investigation in the differences towards methylation of benzene, toluene and o-xylene is required. These three compounds are different in terms of bulkiness and proton affinity. In

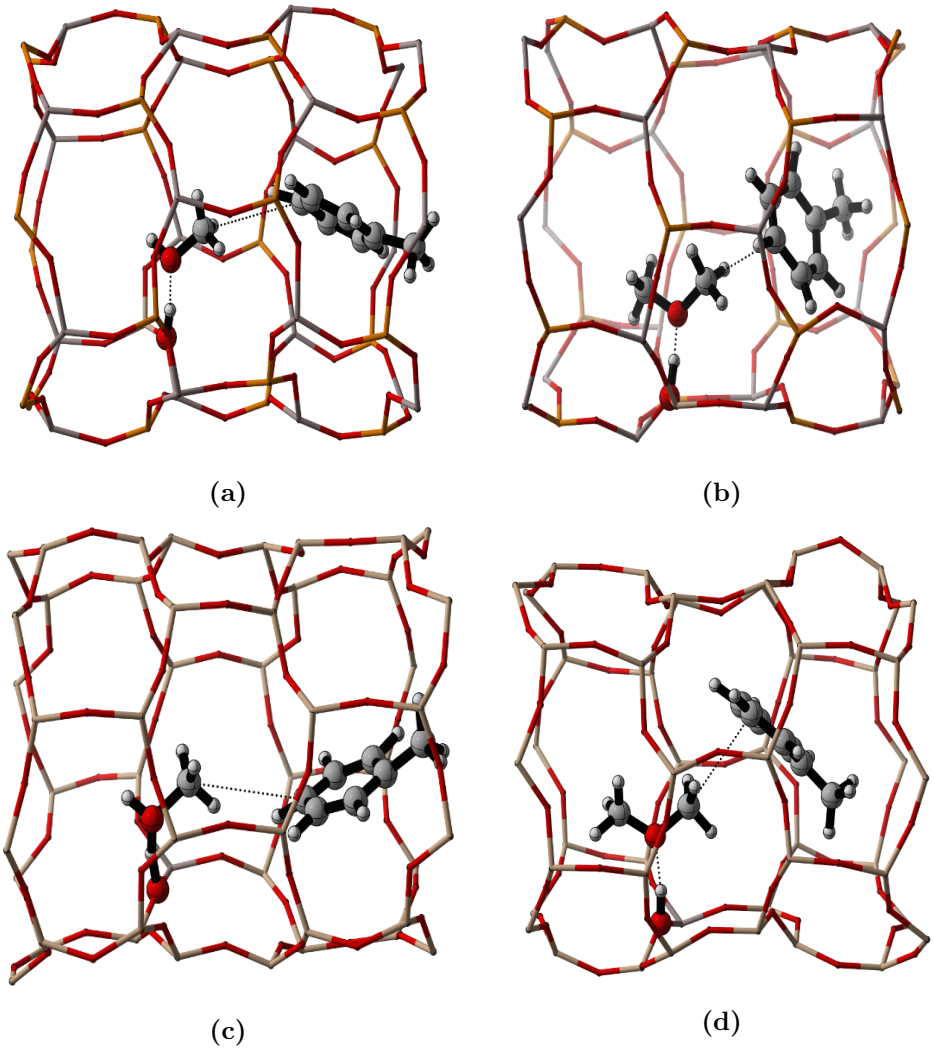

Figure 6.16: Pre-reactive complexes for toluene with methanol (a) and DME (b) in H-SAPO-5 and with methanol (c) and DME (d) in H-SSZ-24 at 623 K and 1 atm.

subsection 6.1.2 it was mentioned that toluene and o-xylene suffer from steric hinderance inside the AFI channels. However, this does not come forward in the probabilities of pre-reactive complex formation. Moreover, the effect of their proton affinity is also not clear in Figure 6.18. The employed criteria for a pre-reactive complex are, hence, not able to retrieve the steric and proton affinity influence on the pre-reactive complexes. Another explanation might be that the MD simulations are too short. With the use of MTD simulations, these influences might become clear in the sampled transition states.

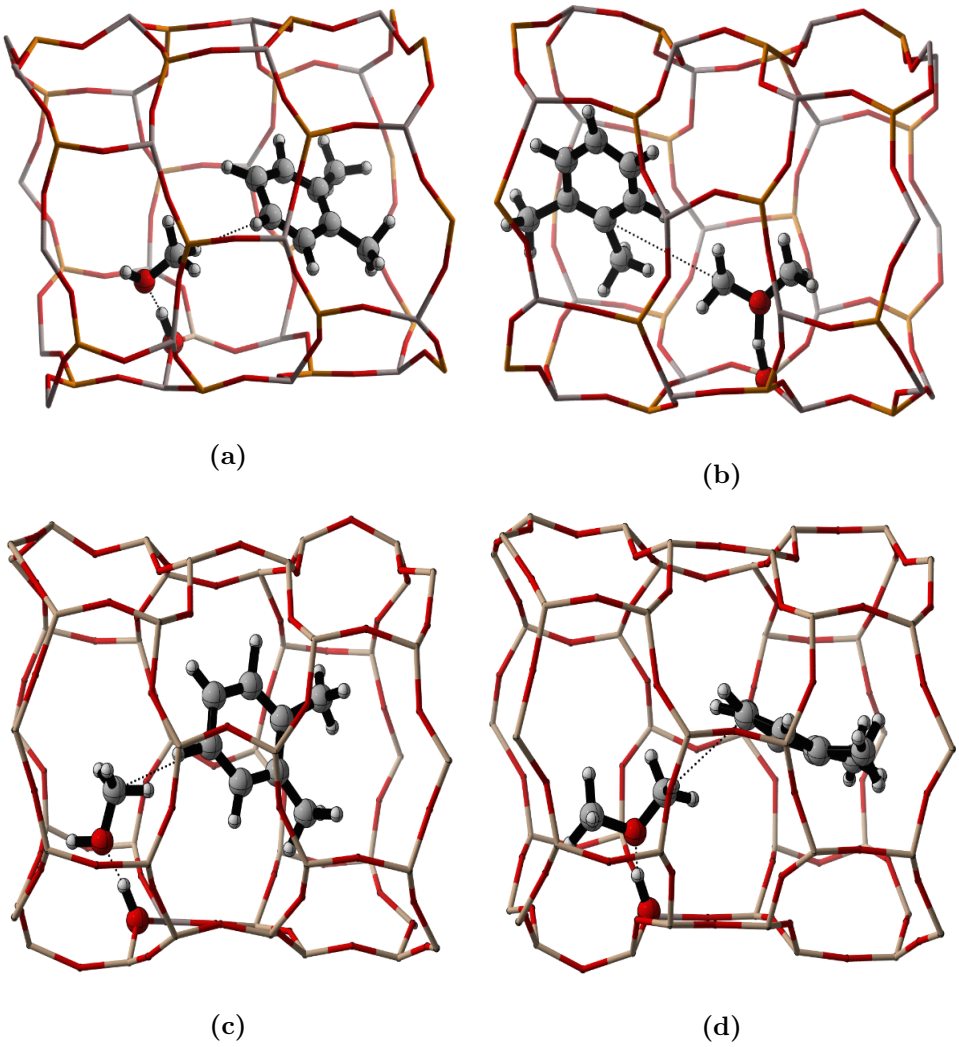

Figure 6.17: Pre-reactive complexes for o-xylene with methanol (a) and DME (b) in H-SAPO-5 and with methanol (c) and DME (d) in H-SSZ-24 at 623 K and 1 atm.

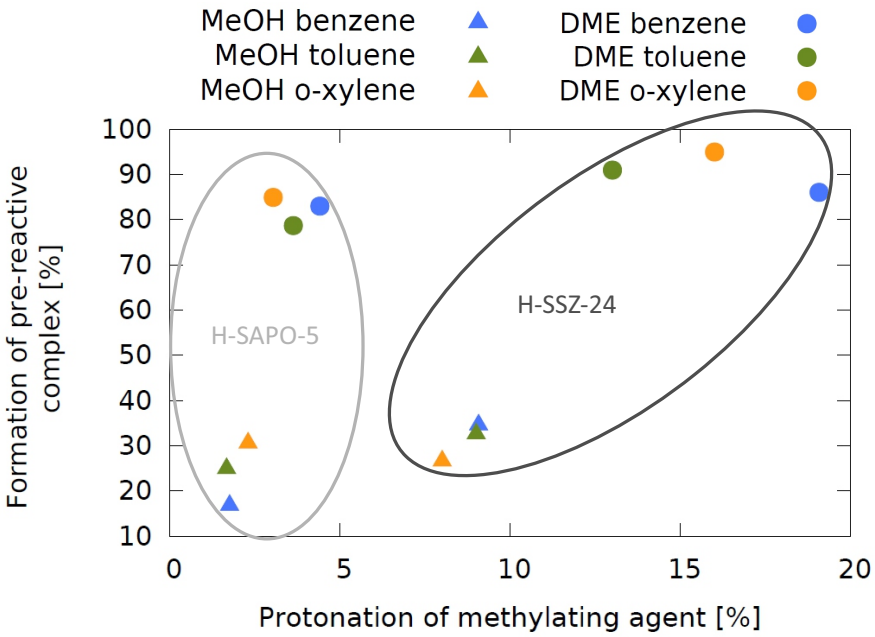

Figure 6.18: Probability of the formation of a pre-reactive complex as function of the protonation probability of the methylating agent in H-SAPO-5 and H-SSZ-24 at 623 K and 1 atm.

6.3.2 Framework-bound methoxide as methylating agent

Finally, the adsorption behavior of benzene, toluene and o-xylene is studied in the presence of a framework-bound methoxide. Such a species is also capable of performing a methylation reaction as mentioned in section 2.5.

Some examples of pre-reactive complexes for the methylation of benzene by a framework-bound methoxide can be found in Figure 6.5. For toluene and o-xylene some configurations are given below in Figure 6.19.

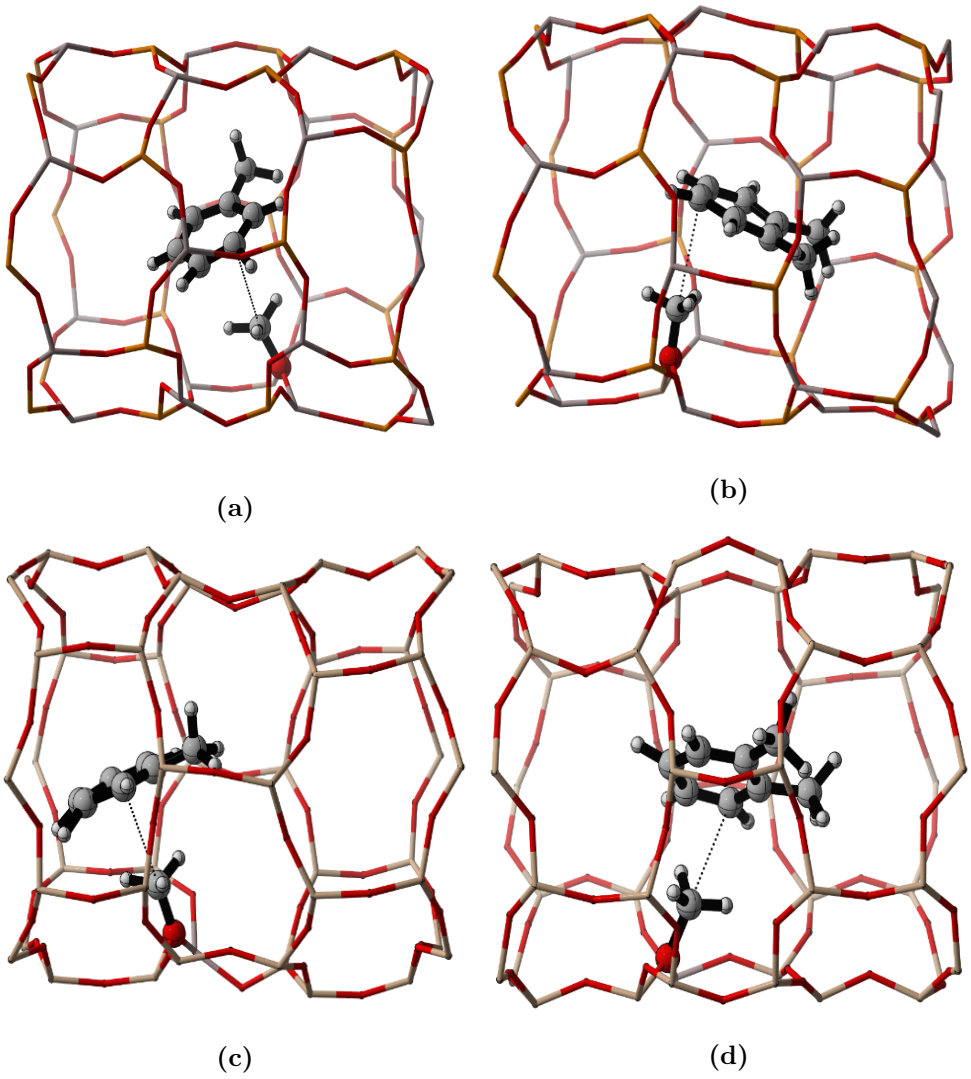

Figure 6.19: Pre-reactive complexes for toluene with a framework-bound methoxide in H-SAPO-5 (a) and H-SSZ-24 (c) and for o-xylene in H-SAPO-5 (b) and H-SSZ-24 (d) at 623 K and 1 atm.

In this case the definition for a pre-reactive complex was chosen differently than for the discussing of methanol and DME as methylating agents. It is assumed that the aromatic interacts with the methoxide when one or multiple ring carbon atoms approach the methoxide carbon atom within a distance closer than 3.5 Å, as shown in Figure 6.20 for both H-SAPO-5 and H-SSZ-24. The

shown pre-reactive complexes in Figure 6.19 all fulfill the above criterion. The cut-off distance was not picked randomly. In the TS of the methylation reaction with methanol and benzene, the CC distance is 2.19 Å in H-ZSM-5 [81]. This is statically calculated at 0 K using the B3LYP functional and DFT-D3 corrections. At higher temperature and in AFI, a larger distance is expected in the TS (assume 2.5 Å). For pre-reactive complexes it can be assumed that there is an interaction between the methylating agent and the aromatic ring starting from a CC distance of 1.0 Å bigger than the CC distance in the TS.

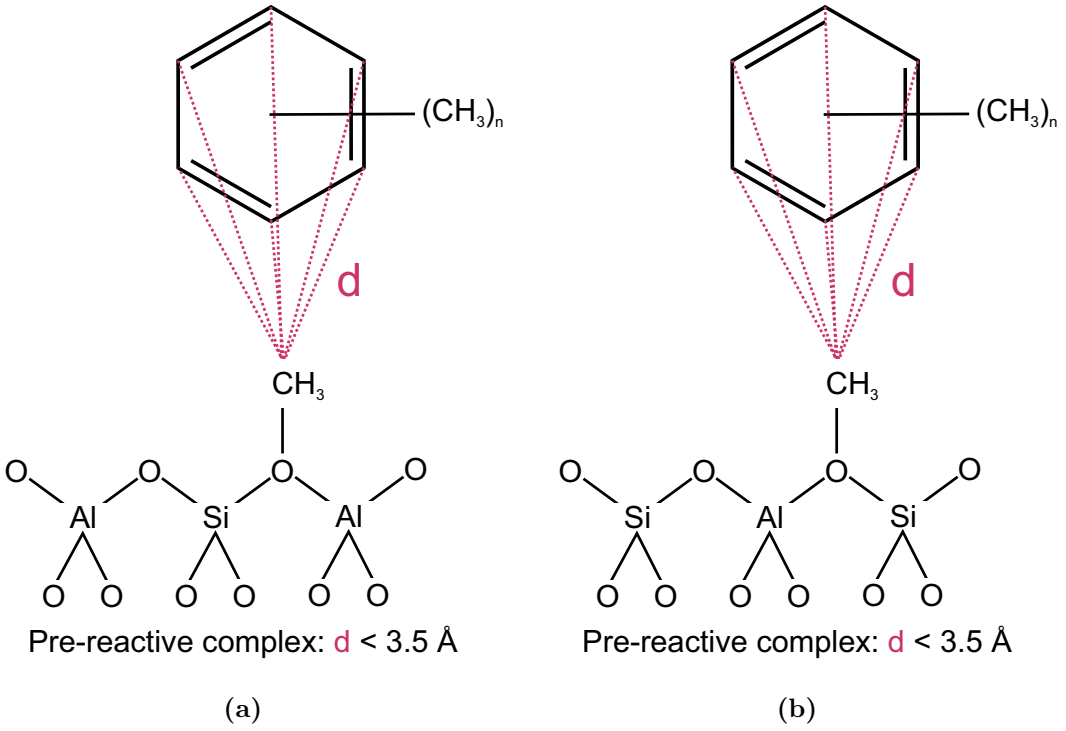

Figure 6.20: Schematic representation of the criterion for a pre-reactive complex and a protonated methylating agent for methanol in H-SAPO-5 (a) and for DME in H-SSZ-24 (b). Note that the criteria are independent of the used AFI catalyst.

In Figure 6.21 the probability of interaction between a methoxide and an aromatic is given for all three considered aromatics. This probability of forming a pre-reactive complex is based on the percentage of time one of the aromatic ring carbon atoms is located within a range of 3.5 Å from the methoxide carbon atom. It is known that adsorption enthalpy of aromatics increases with approximately 10 kJ mol^{-1} per extra C atom due to dispersion interactions. Therefore the probability of interaction with a framework-bound methoxide should increase from benzene to o-xylene. This trend is observed in H-SAPO-5. However in H-SSZ-24 no such trend is found. Although, DFT-D3 corrections are applied to the energy from the DFT functional, the dispersion energy is not correctly described by these corrections. Therefore the expected increasing trend is not observed in H-SSZ-24.

To ensure that all MD simulations have converged, the data needed for Figure 6.21 are calculated over different time intervals, as shown in Table 6.3 for H-SSZ-24. The same data is also available for H-SAPO-5 in Appendix F. It appears that in the more acidic material, o-xylene interacts less

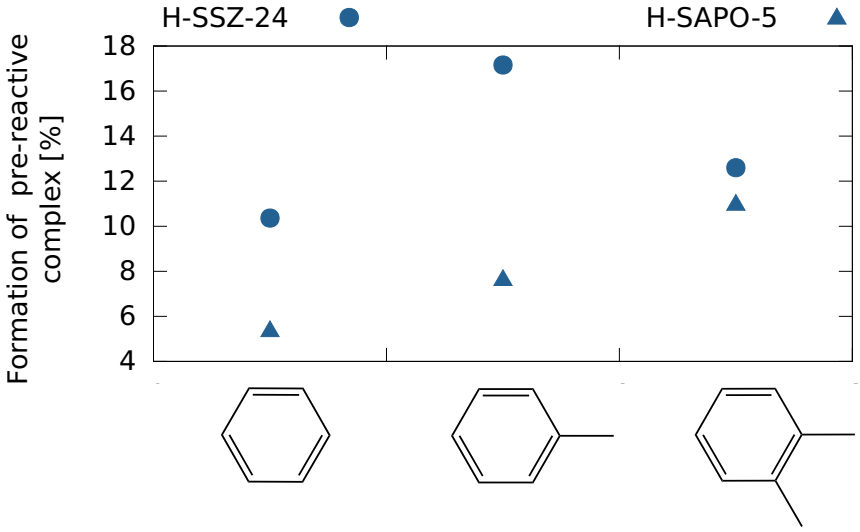

Figure 6.21: Probability in H-SAPO-5 (triangles) and in H-SSZ-24 (circles) at 623 K and 1 atm of finding geometries where the shortest distance from the carbon atoms of the aromat (benzene, toluene, o-xylene) to the C atom of the framework bounded methoxide is lower than 3.5 Å.

with the methoxide than toluene. However, after a simulation of 50 ps, the toluene and o-xylene run in H-SSZ-24 were not converged yet and thus ergodicity of the ensemble was not fulfilled as seen in Table 6.3. The longer the simulation with o-xylene ran, the lower the probability of interaction and the more distorted the increasing trend from Figure 6.21 became. When looking at the geometries at the end of the MD simulation is it seen that o-xylene found a quite stable state in which it is located almost in the middle of two methoxides. This explains why the probability for a pre-reactive complex formation with o-xylene tends to decrease at the end of the simulation. It would be interesting to consider also other aromatics with even larger proton affinities, to see if they obey the increasing trend in both H-SAPO-5 and H-SSZ-24.

6.4 Conclusion

In this chapter the effect of co-adsorption on the behavior of the adsorbates was studied in the AFI topology. First, this is achieved by comparing the average distance to the acid site for methanol, DME, benzene, toluene and o-xylene when being single adsorbed and co-adsorbed. In all cases, the average distance for the methylating agents to the acid site was approximately equal in H-SSZ-24. However, in H-SAPO-5 the average distance of the methylating agents to the acid site was much higher during single adsorption and would decrease upon adding the aromatics to the channel. Generally, the distance of the aromatics to the acid site increased upon adding the methylating agent, since the methylating agent would preferentially be located at the acid site.

Second, the co-adsorption behavior was analyzed by tracking the orientation of the aromatics after adding the considered methylating agents (methanol, DME and a framework-bound

Table 6.3: Probability of pre-reactive complex between the methoxide and benzene, toluene and o-xylene for different lengths of the MD simulation in H-SSZ-24 at 623 K and 1 atm.

time [ps]	Benzene	Toluene	O-xylene
40.0	8.91 %	14.14 %	17.58 %
45.0	9.98 %	16.56 %	18.43 %
47.5	10.36 %	17.39 %	17.59 %
50.0		16.52 %	16.71 %
52.5		17.48 %	15.91 %
55.0		17.94 %	15.19 %
57.5		17.96 %	14.53 %
60.0		17.64 %	13.93 %
62.5			13.37 %
65.0			12.85 %
67.5			12.58 %
entire simulation	10.36 %	17.16 %	12.60 %

methoxide). The acid strength was not found to have a substantial effect on the orientation of the aromatics. Due to steric hindrance there were differences in the orientation for the considered aromatics, namely benzene preferred the upright position in the channel while faced to the channel end and toluene and o-xylene favored the flat orientation.

The co-adsorption study also revealed the presence of a competitive adsorption between o-xylene and methanol in both AFI materials, resulting in less favorable pre-reactive complexes for the methylation reaction of o-xylene.

Lastly, plotting the probabilities of the formation of a pre-reactive complex against the protonation probability of methanol and DME for all three aromatics showed a clear clustering of the results of H-SAPO-5 and H-SSZ-24. The study indicates that the acid strength affects the protonation probabilities and that DME seems more reactive than methanol. Finally, a stronger interaction between the methoxide and the aromatic HP species with increasing degree of methylation was observed in both H-SAPO-5 and H-SSZ-24.

This chapter provided in a more qualitative, rather than quantitative description of the methylation reaction in the AFI topology. To truly quantify the difference in reactivity between all three methylating agents and between H-SAPO-5 and H-SSZ-24, the next chapter will focus on MTD simulations of the toluene methylation reaction as a case study.

Chapter 7

Reactivity towards methylation of aromatics in H-SAPO-5 and H-SSZ-24

In the previous chapter the reactivity towards methylation was assessed by means of a detailed study of the co-adsorption complexes formed by the reactants. Here, the reactivity will be measured by calculating the free energy barrier for the methylation of toluene. This property can be obtained from MTD simulations, since the MD simulation is biased making rare events such as a methylation reaction possible to sample in feasible run times. A simulation is performed for toluene and methanol in both H-SAPO-5 and H-SSZ-24 and also for toluene and DME in H-SSZ-24 at 623 K using the equilibrated volume from the NPT simulations from the previous chapter as constant volume.

Van Speybroeck et al. reported a difference of approximately 20 kJ mol^{-1} in the deprotonation energies of H-SAPO-34 and H-SSZ-13 due to a difference in acid strength [59]. This chapter will examine whether the acidity of a material also influences the barrier of a methylating reaction during MTO and to which extent. Questions such as "does the stepwise path involving a framework-bound methoxide occur more frequently for the more acidic material?" and "Is this path dominant over the concerted path" will be answered. The final part of this chapter will address the difference in reactivity between methanol and DME as a methylating agent.

7.1 Influence of the acid strength

In both H-SSZ-24 and H-SAPO-5, the methylation barriers have been (re)crossed multiple times during the MTD simulations. The MTD simulation in H-SAPO-5 is just under 120 ps long and the one in H-SSZ-24 is just over 110 ps long.

The first methylation reaction was found to be occuring in H-SAPO-5 after 23.5 ps and in H-SSZ-24 already after 17.5 ps. This is a first indication that H-SSZ-24 is more reactive towards methylation reactions of aromatics, since every 25 fs a Gaussian hill of 5 kJ mol^{-1} was placed until the first recrossing. Thus, fewer of these hills were needed in H-SSZ-24 to cross the methylation barrier.

As mentioned in section 4.3, the free energy surface (FES) of zeolitic systems is very complex due to the framework flexibility, the number of guest molecules and especially in AFI materials due to the wide pore channels which allow a lot of movement of these guest molecules. As result of this complex surface, the observed transition state during the MTD run are not always the same. The complexity of the FES is reflected in the path followed by the collective variables during the simulations. This path is given in Appendix G for all three MTD simulations. The collective variables followed many different routes to connect the reactant and product valley and often these routes lie quite far from one another. This suggests that the transition states on those paths are indeed substantially different. This was also observed for the transition states of the methylation of benzene in H-SSZ-24 [176].

Figure 7.1 shows a number of transition states observed during the MTD simulation of methanol and toluene in H-SAPO-5. It must be stressed that the term transition state might be slightly incorrect for these configurations, since these might not exactly correspond to the first order saddle point in the PES. Therefore, it is better to say that these configurations lay close to a transition state. The first couple of crossings of the methylation barrier always involved an attack of methanol at the ortho position of the aromatic ring. During the complete simulation in H-SAPO-5 only ortho methylated products were observed. Even in case only one type of product is observed, such as the ortho product in H-SAPO-5, the corresponding transition states were different. A methylation at the ipso position was not observed. Figure 7.1 (a) and (b) represent the same configuration for an ortho transition state but viewed from a different angle, whereas Figure 7.1 (c) represents a configuration leading to another ortho transition state. In case of Figure 7.1 (a) and (b), the aromatic lies flat inside the channel during the transition state, while in case of Figure 7.1 (c) toluene stands upright in the channel and there seems to be some sort of stabilizing interaction with the zeolite walls.

However, this upright position is also detected in H-SAPO-5 in a (failed) attempt to perform a methylation on the meta position of toluene, as shown in Figure 7.1 (d). This type of attack is unexpected, since toluene is an ortho/para director. Therefore, the meta attack will bring along a higher free energy barrier. This higher energy state may be partially stabilized by the interaction with the wall during an upright position in the channel. Since this meta attack on toluene was not successful, additional hills need to be added before the free energy barrier of this type of attack can be overcome. Note that these transition states in Figure 7.1 all resemble the S_N2-type transition state in which the methyl group undergoes an umbrella inversion.

Considering the transition states in H-SSZ-24, not only ortho attacks are observed but also para and even meta methylations. Again no ipso methylation was observed. The configuration around the ortho transition state, shown in Figure 7.2 (a) depicts an upright configuration. Probably, all the ortho transition states in H-SSZ-24 will stand upright as in case (3) of Figure 6.6, since this

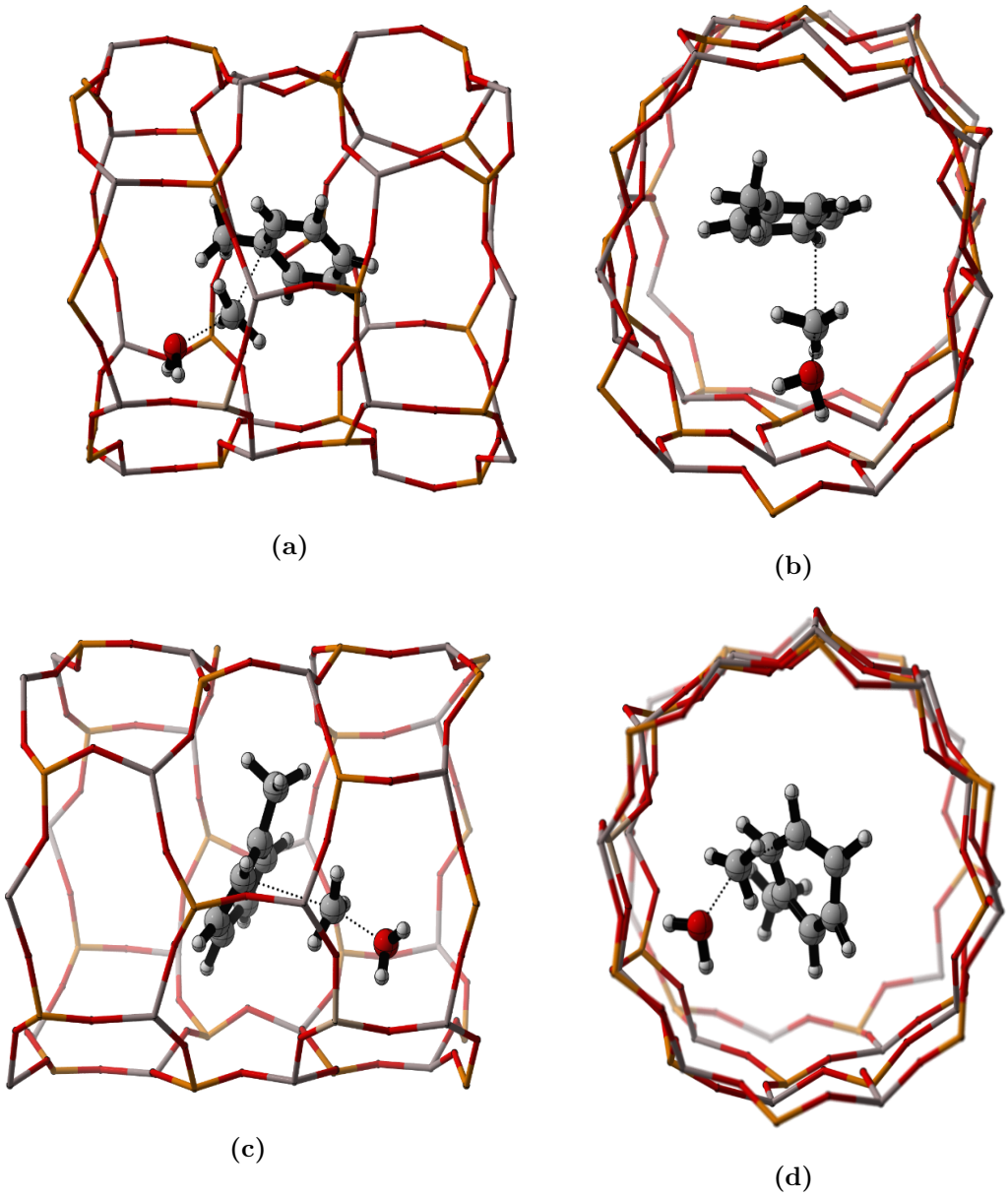

Figure 7.1: A vast variety of transition states is observed during MTD of toluene and methanol in H-SAPO-5 at 623 K: a configurations close to an ortho transition state is given from two perspectives (a) and (b), a configuration close to another ortho transition state is given in (c) and a configuration close almost forming a meta transition state is shown in (c).

position benefits from the stabilizing interaction with the walls. During the transition state, the aromatic ring becomes partially positively charged, while the framework is already negatively charged. This results in an electrostatic interaction of the aromatic with the channel walls. Due to the higher acidity of H-SSZ-24, the interaction of the aromatic with the wall is greater than in H-SAPO-5 and therefore only the upright position of the aromatic is observed during the ortho transition state in H-SSZ-24, whereas in H-SAPO-5 the aromatics orientation during transition state is less stringent.

This upright position for a para transition state is however subject to steric hindrance. There-

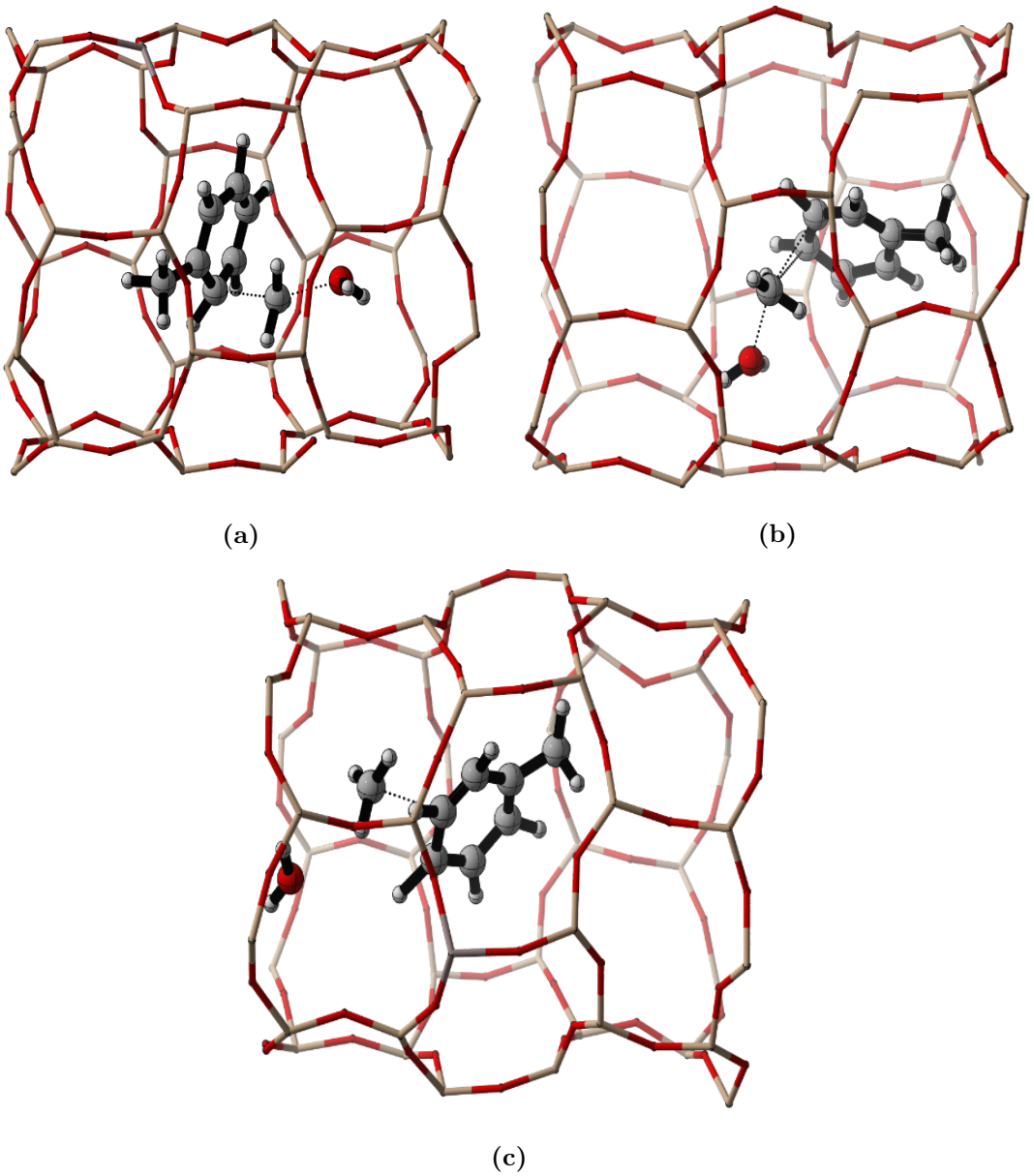

Figure 7.2: A vast variety of transition states is observed during MTD of toluene and methanol in H-SSZ-24 at 623 K: a configurations close to the ortho transition state is given in (a), a configuration close to the para transition state is given in (b) and a configuration close to the meta transition state is given in (c).

fore in that case no upright orientation was observed, as shown in Figure 7.2 (b). This para methylation is observed after 30 ps in the MTD run. This is shortly after the barrier for the ortho methylation had been recrossed suggesting that the barrier of the para methylation lies in the range of the one for an ortho methylation.

The meta attack, however, was only observed after adding a substantial number of Gaussian hills (after 102 ps) and the risk exists that the valley might have been overfilled, since several unexpected phenomena are occurring at the last part of the MTD simulation. Firstly, the methyl group has already broken free of the methanol molecule before it starts forming the transition

state and approaching the aromatic ring as shown in Figure 7.2 (c). Secondly, at the end of the MTD simulation the methyl group has subtracted an H atom from the aromatic ring, hereby creating methane and an unstable carbocation of toluene. To stabilize itself this carbocation will form a covalent bond with the negatively charged zeolite cage and a framework-bound methylphenoxide is formed, as seen on Figure 7.3. This type of framework-bound aromatic could act as a deactivator for the MTO conversion as it occupies the active site. The simulations was stopped here, since the used CVs could not describe this type of reaction and hence the simulation could not escape from this alternative product valley.

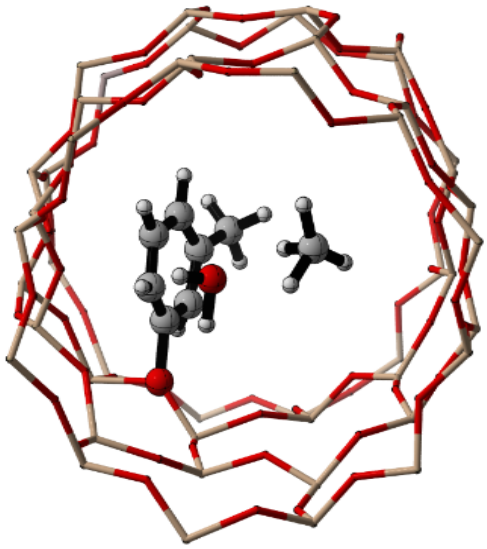

Figure 7.3: Formation of methane and framework-bound toluene observed in H-SSZ-24 at 623 K and 1 atm.

In terms of transition states and the position of the deposited methyl group on the aromatic ring, H-SAPO-5 and H-SSZ-24 clearly differ from each other. This difference will be reflected in the free energy barrier $\Delta G^{\ddagger}$ for the methylation reactions during MTO conversion. To obtain this barrier, first the lowest free energy path (LFEP) must be selected. This is done with the lowest free energy search algorithm proposed by Ensing et al. [163] which is implemented in the trace-irc program, as mentioned in section 4.3. A 2D representation of this path is given for both H-SAPO-5 and H-SSZ-24 as function of CV1 and CV2 in Figure 7.4 (a) and Figure 7.5 (a) respectively. The coordinates along this path are represented by s and the corresponding free energy by $G(s)$. The free energy profile along the LFEP is given in Figure 7.4 (b) and Figure 7.5 (b) respectively.

Considering the condition of the MTD simulation, it should be possible to accurately describe the free energy of the reactant valley and transition states. In this master thesis, the transition state is identified as the point in which the free energy is the highest along the LFEP. Nevertheless, this might not be the true transition state, because one needs to check if this is a first order saddle point on the PES to be sure. Furthermore, one must keep in mind that the products formed during the simulation are not the lowest in energy, since a wall was placed on the second

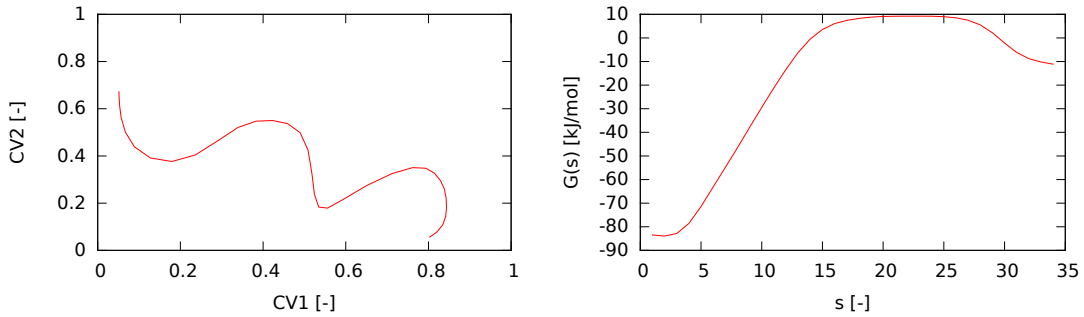

(a) **(b)**

Figure 7.4: Representation of the 2D minimum energy path from the reactant valley to the methylation product valley (a) and the corresponded free energy $G(s)$ (b) at each point s along the path in (a) for H-SAPO-5 with methanol as methylating agent at 623 K and 1 atm.

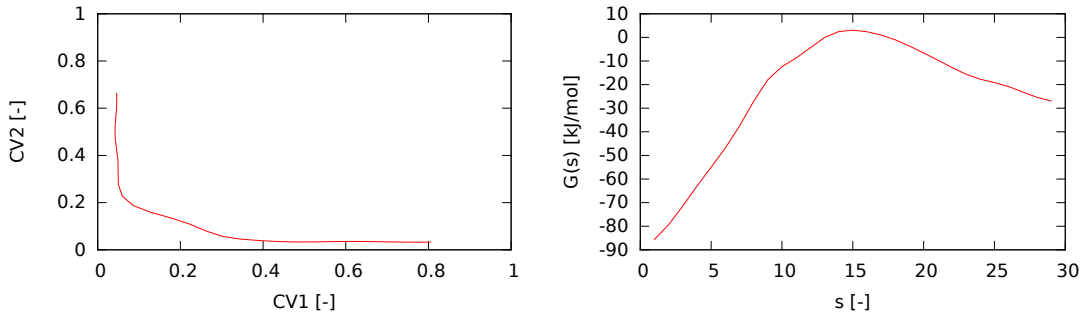

(a) **(b)**

Figure 7.5: Representation of the 2D minimum energy path from the reactant valley to the methylation product valley (a) and the corresponded free energy $G(s)$ (b) at each point s along the path in (a) for H-SSZ-24 with methanol as methylating agent at 623 K and 1 atm.

CV to prevent the formation of a more stable xylenium ion via a hydride shift. This means that the product valley is not completely sampled. Thus, only the forward reaction barrier can be calculated from the simulations.

As expected, the more acidic material, H-SSZ-24, results in the lowest free energy barrier towards methylation during MTO conversion, namely 90 kJ mol^{-1}. In H-SAPO-5, a barrier of 99 kJ mol^{-1} was found. This shows that the acid strength only influences the barrier with 9 kJ mol^{-1}. This is substantially lower than the 20 kJ mol^{-1} reported by Van Speybroeck et al. [59]. The barriers from this thesis must be handled with caution, since they might not have converged yet due to the low amount of recrossings of the methylation barrier. In all simulations the barriers were recrossed less then 10 times. Furthermore, the effect of adding extra hills to the barrier is represented in Appendix G for each simulation. This shows that a deviation of approximately 1 kJ mol^{-1} for H-SAPO-5 and 2 kJ mol^{-1} for H-SAPO-5 on the free energy barriers of the methylation reaction by methanol is still present when adding 100 hills or thus simulating an extra 2.5 ps. Due to the use of three CVs, the simulation will not easily (re)cross the barrier and long run times are computationally very demanding. Therefore, it is not straightforward

to obtain a converged free energy barrier. Moreover, the smaller influence of the acid strength on the free energy barrier can also be the result of a smaller difference in acid strength between H-SAPO-5 and H-SSZ-24 compared to the acid strength difference in H-SAPO-34 and H-SSZ-13. However, the shift upon CO adsorption show that the acid strength of H-SAPO-34 is similar to the one of H-SAPO-5 and the acid strength in H-SSZ-13 and H-SSZ-24 are similar as well [71], [103]. Therefore, this cannot explain the difference influence of the acid strength on the barriers considered.

In both H-SAPO-5 and H-SSZ-24 the stepwise methylation mechanism, involving formation of a methoxide species, is not observed during the MTD simulation. This suggests that the free energy barrier for this reaction is higher than the one for the methylation via the concerted pathway in which methanol is the methylating agent. However DME must also be considered as a methylating agent, since it will be formed during the begin stages of the MTO process, as was explained in chapter 2. The next section will focus on the differences between DME and methanol as the methylating agent during MTO conversion.

7.2 Influence of the methylating agent

The MTD simulation for DME and toluene co-adsorbed in H-SSZ-24 was executed under the same process condition as the MTD simulation with methanol in H-SAPO-5 and H-SSZ-24.

After approximately 9.5 ps the first methylation reaction performed by DME is observed in H-SSZ-24. The fast occurrence of this reaction already suggest that DME is more reactive towards a methylation reaction and hence, the methylation barrier for the concerted pathway should be lower than in case of methanol. This is based on the fact that the settings for the Gaussian hills are equal before the first recrossing of the methylation barrier in all simulations.

Figure 7.6 shows a configuration around the transition state and product that are formed during the first crossing of the methylation barrier. It concerns an attack of DME at the meta position of the aromatic ring. This is unexpected, since toluene is an ortho/para director and is thus not preferentially methylated at the meta position. A second crossing of the methylation barrier is seen after 17.3 ps. This time a para methylation reaction is executed, as shown in Figure 7.6.

Throughout the 60 ps MTD simulation, only these two transition states were sampled and each only once. The lack of an ortho methylation product might be explained by steric hindrance. DME consists of two methyl groups instead of one as in methanol, this second group might be the reason why DME will not approach the ortho position of toluene.

Again the LFEP was determined. The path is shown in Figure 7.7 along with the free energy of each point on the path. A methylation barrier of 91 $\mathrm{kJ\,mol^{-1}}$ was found. Although, it was expected that DME should have a lower barrier and should thus be more reactive towards methylation, this is not observed. The same explanation as in the previous chapter applies: since the catalyst is a strong acid the difference in proton affinity of the methylating agents, methanol and DME, will not highly affect the methylation reactions. Due to the high acidity of H-SSZ-24, methanol and DME are both very effective methylating agents and their free energy

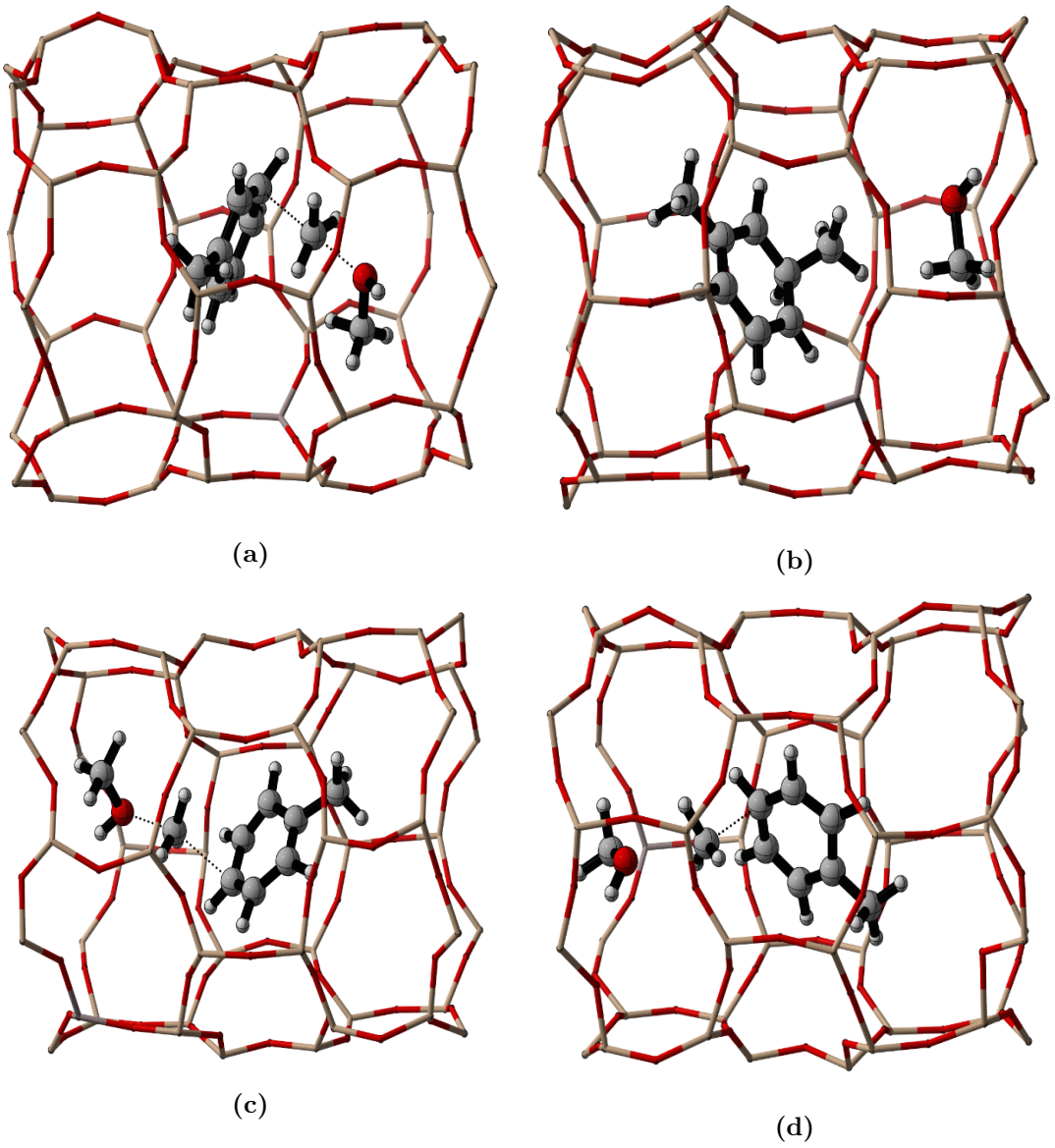

Figure 7.6: Configurations close to the transition state for the meta methylation (a) and para methylation (c) and meta (b) and para (d) methylation product in H-SSZ-24 with DME as methylating agent at 623 K and 1 atm.

barrier for methylation is, thus, similar. In future studies, the simulation in H-SAPO-5 should be included for DME. In this mildly acidic material, DME might be a better methylating agent than methanol, since during the adsorption study in the previous chapter it was also seen that the difference in proton affinities between methanol and DME will prevail more in H-SAPO-5 due to its lower acidity.

As mentioned in section 7.1, during the MTD simulation with methanol the stepwise methylation pathway had not taken place. In contrast, the simulations of DME shows the formation of a framework-bond methoxide already after 15.25 ps. A configuration close to the transition state and the methoxy product are shown in Figure 7.8.

DME is clearly more prone to the stepwise mechanism and it is expected that the barrier

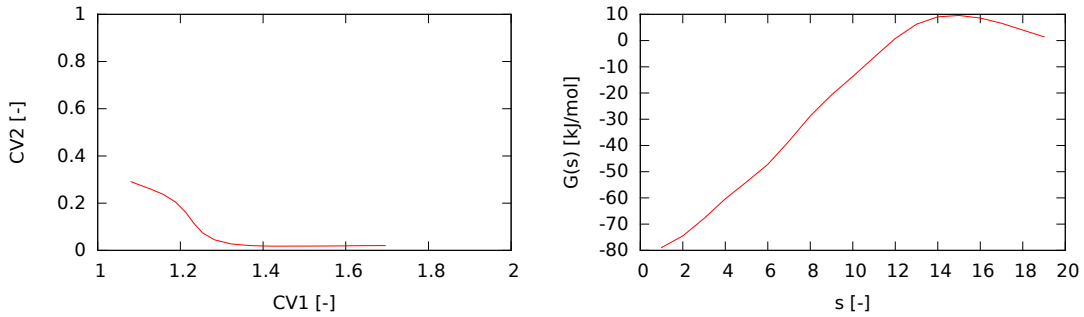

(a) **(b)**

Figure 7.7: Representation of the 2D LFEP from the reactant valley to the methylation product valley (a) and the corresponded free energy $G(s)$ (b) at each point s along the path in (a) for H-SSZ-24 with DME as methylating agent at 623 K and 1 atm.

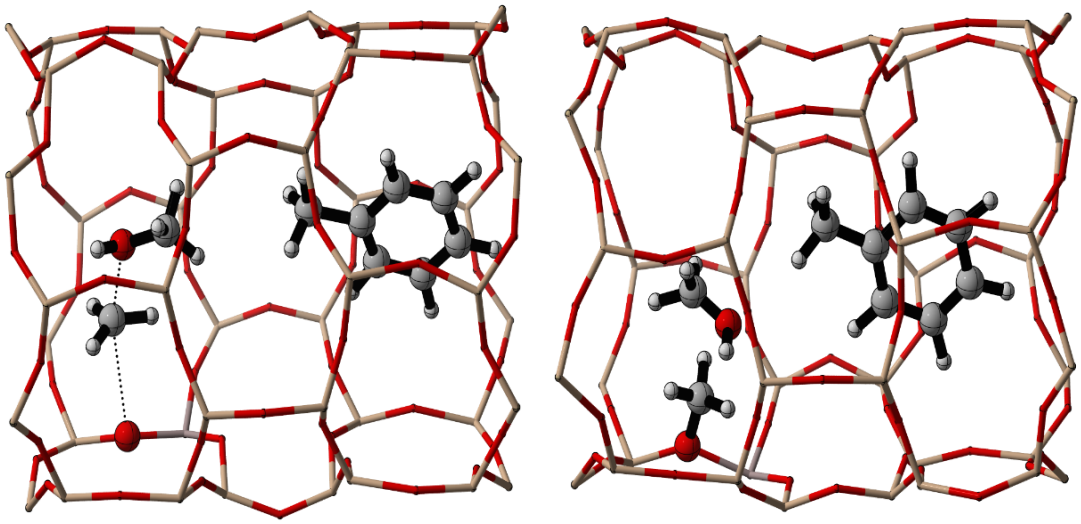

(a) **(b)**

Figure 7.8: Transition state for the formation of a framework-bound methoxide and the final methoxide in H-SSZ-24 with DME as methylating agent at 623 K and 1 atm.

for concerted and stepwise mechanism are very similar. Indeed, again the LFEP was calculated along with its free energy, which is shown in Figure 7.9, and a barrier of 92 kJ mol^{-1} was retrieved for the formation of a framework-bound methoxide in this case. The subsequent methylation reaction was unfortunately not observed. The formation of the framework-bound methoxide is believed to be the rate determining step of the stepwise methylation mechanism [76]. Thus, the free energy barrier of this step may be directly compared to the free energy barrier of the concerted mechanism. For DME in H-SSZ-24, the stepwise and concerted mechanism appear to be competitive at the studied MTO conditions [75]. In H-ZSM-22 it was observed that the stepwise mechanism was dominant at typical MTO conditions for methylation reaction of alkenes. However, H-ZSM-22 in comparison to H-SSZ-24 is a small pore catalyst and hence the dominant stepwise mechanism might be the result of the smaller transition state involved.

Furthermore, the stepwise mechanism was not observed for the simulation in which methanol is the methylating agent. It can be assumed that the barrier for the stepwise mechanism is higher for methanol than for DME. This was already confirmed for H-ZSM-5 [77]. In H-ZSM-5, free energy barriers for the methoxide formation were found to be 160 kJ mol^{-1} for methanol and 143 kJ mol^{-1} for DME. According to Van der Mynsbrugge et al. this higher barrier for methanol could be caused by a larger enthalpy penalty upon reaction due to a higher number of possible binding modes for methanol at the acid site.

The barriers in H-ZSM-5 seem higher than in H-SSZ-24, however the barriers reported here for the simulation of DME in H-SSZ-24 are not converged. The addition of 100 hills still leads to an average increase of 12 kJ mol^{-1} for the formation of a framework-bound methoxide and 10 kJ mol^{-1} for the concerted methylation barrier.

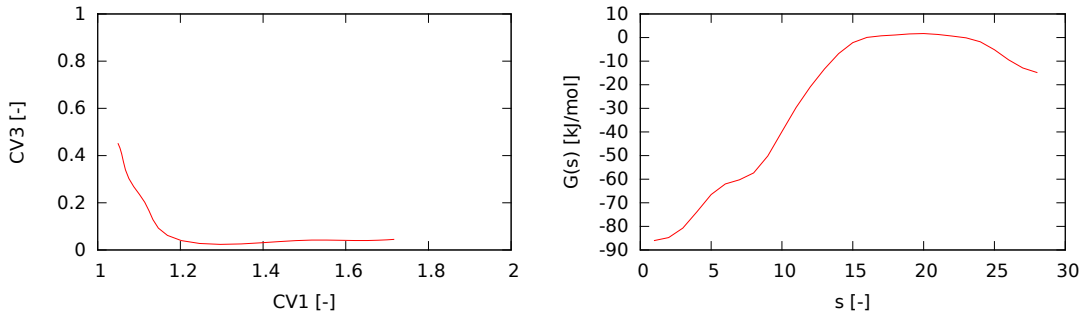

Figure 7.9: Representation of the 2D minimum energy path from the reactant valley to the framework-bound methoxide product valley (a) and the corresponded free energy $G(s)$ (b) at each point s along the path in (a) for H-SSZ-24 with DME as methylating agent at 623 K and 1 atm.

7.3 Conclusion

In this chapter, the difference in reactivity towards methylation reactions in H-SAPO-5 and H-SSZ-24 was investigated by means of MTD simulations. These simulations confirm the predictions made in previous chapters: the more acidic zeolite, H-SSZ-24, will show a higher reactivity towards methylation reactions during MTO conversion. This was proven by calculating the free energy barriers that need to be overcome during methylation of toluene by methanol or DME. Table 7.1 sums up all calculated barriers.

The use of MTD was preferred over static calculations, since this method can take into account a vast range of different reaction paths between the same reactant and product valley and thus account for the complexity of the free energy profiles. The use of MTD is certainly justified in case of the methylation reactions investigated, because during the simulations multiple transition and product states were observed. Although toluene is an ortho/para director, transition states for the meta methylation were observed in both catalyst. The meta product was even seen in

Table 7.1: Free energy barrier ΔG for a methylation reaction via the converted pathway and for the formation of a framework-bound methoxide in H-SAPO-5 and H-SSZ-24 with methanol and DME as methylating agent for toluene at 623 K and 1 atm.

Methylating agent	Catalyst	$\Delta G_{\text{concerted}}$ [kJ/mol]	$\Delta G_{\text{methoxide}}$ [kJ/mol]
Methanol	H-SAPO-5	99	-
Methanol	H-SSZ-24	90	-
DME	H-SSZ-24	91	92

H-SSZ-24 before any ortho or para product when the attack is performed by DME is involved.

Another interesting observation is that DME appears to form methoxide species more easily than methanol and thus the stepwise methylation mechanism is less activated for DME as methylating agent than for methanol. It was suggested that DME would also be more reactive towards methylation via the concerted pathway. However based on the free energy barriers, methanol and DME seem to require almost the same amount of energy to methylate toluene in H-SSZ-24, as seen in Table 7.1.

As a last remark, these simulations should also be performed for other types of aromatics and also for alkenes. For bulkier aromatic species, the difference in free energy barrier between H-SAPO-5 and H-SSZ-24 should be even higher than for toluene. Only then the mechanistic difference between H-SAPO-5 and H-SSZ-24 can be fully understood.

Chapter 8

Conclusion

The methanol-to-olefin (MTO) process provides a promising alternative for the traditional olefin production from crude oil. Reserves of crude oil are depleting and in the future these will no longer suffice to meet the increasing olefin demand.

In chapter 2, the various proposals for the very complex MTO mechanism were explored. After the direct mechanism of coupling intermediate C_1 species was ruled out, the hydrocarbon pool (HP) mechanism became generally accepted. These HP species, which co-catalyze the MTO reactions, can either be alkenes or aromatics. The interaction between these HP species is described by the dual cycle mechanism containing an arene and alkene catalytic cycle.

The nature of the HP species and their reactivity strongly depends on the type of catalyst and the process conditions. By comparing two isostructural catalysts with a different acid strength, namely H-SAPO-5 and H-SSZ-24, it was seen that the acid strength can control the reactivity of the HP species inside a solid acid catalyst. In H-SAPO-5 the alkene species are the most active, while in H-SSZ-24 the aromatic HP species are found to be dominant. Due to higher acid strength in H-SSZ-24, the product also contains much more paraffinic and aromatic compounds than the product from the MTO conversion in H-SAPO-5. Hence, literature has shown that the acid strength also directly affects the product selectivities.

Methylation reactions are of particular importance in both the arene and alkene cycle. The Brønsted acid sites play a crucial role during these methylation reactions. Two mechanisms have been proposed in literature for the methylation reaction: a concerted and a stepwise mechanism. During the concerted mechanism methanol or DME is protonated by the acid site and the methyl group is simultaneously transferred to the HP species through an S_N2 like transition state. The stepwise mechanism requires the intermediate formation of a framework-bound methoxy species. This methoxy species can then methylate the HP species. In H-ZSM-22, literature claims that the stepwise route is the dominant mechanism in case of high temperatures and low pressures, while for low temperatures and high pressures the concerted mechanism is the most active. However, this has not yet been assessed for the large pore AFI catalysts. Furthermore, the effect of the acid strength on the dominant methylation mechanism is not yet known.

This master thesis has attempted to get insight into the effect of the zeolitic acid strength by comparing H-SAPO-5 and H-SSZ-24 during MTO conversion. Since the MTO mechanism is governed by several methylation reactions, this thesis focuses on the methylation by methanol, DME and framework-bound methoxides of several aromatic species with different degree of methylation.

First, the adsorption of these methylating agents (methanol and DME) and of the aromatics (benzene, toluene and o-xylene) was studied inside both catalysts with molecular dynamics (MD) simulations at 623 K and 1 atm. Afterwards, the reactivity of the methylating agents was compared in terms of free energy barriers and also the influence of the acid strength on these barriers was investigated. This was done by executing metadynamics (MTD) simulations also at 623 K. During the first principles MD and MTD, the DFT method was used and the catalysts were periodically modeled with the CP2K program.

Several parameters obtained from the static calculations on the frameworks at 0 K were used to assess the zeolitic acid strength. Based on the average length of the OH bond of the acid site, no differences in acid strength could be discerned. Also, the OH stretching frequency did not give a conclusive answer. Finally, the shift in the OH stretching frequency as result of CO adsorption on the acid site confirmed that H-SSZ-24 was indeed more acidic than H-SAPO-5. Unfortunately, the frequencies and frequency shifts of the CO molecule could not quantitatively describe the difference in acid strength of the two AFI materials. A reliable scale for the zeolitic acid strength of the modeled materials remains therefore unavailable. In future work, the enthalpy change upon CO adsorption might be calculated as well.

To get insight in the reactivity of the species involved in a methylation reaction, an analysis was done on the average distance to the acid site for the adsorption and co-adsorption complexes in the MD simulations. For the methylating agent, the addition of an aromatic to the channel, barely influenced the average distance to the acid site in the most acidic material, H-SSZ-24. However in H-SAPO-5, the methylating agent was pushed closer to the acid site by the aromatics. In general, the average distance of the aromatics to the acid site increased upon adding the methylating agent, since the methylating agent would preferentially be located at the acid site with the aromatics co-adsorbed. Although, for o-xylene and methanol a competitive adsorption was observed, since o-xylene was able to remain on the acid site in the presence of methanol.

Three different orientations of the aromatics inside the AFI channel were distinguished during the MD simulations: a flat orientation of the aromatic with respect to the acid site, an upright orientation in which the aromatic ring faces the channel wall and an upright orientation in which the aromatic ring faces the channel end. Two effects of co-adsorption on the orientation of the aromatics were observed in the MD simulations. Firstly, the probability of the flat orientation of toluene and o-xylene would decrease by adding methanol or DME to the channel. Secondly, a similar probability of the flat orientation of toluene and o-xylene was obtained for a framework-bound methoxide as for a Brønsted acid site. These trends were observed for all aromatics in both catalysts except for toluene in H-SAPO-5. This results from the low attraction between the acid site and toluene in H-SAPO-5. In all other cases, the acid strength had no substantial effect

on the orientation of the aromatics. Furthermore, benzene seems to prefer the upright position in which it is faced to the channel end in both materials, while toluene and o-xylene favor the flat orientation, because toluene and o-xylene experience steric hindrance in the upright position.

The reactivity towards methylation in the two catalysts was also quantified by calculating the probabilities of protonation of methanol and DME and the probabilities of the formation of pre-reactive complexes. The criteria used to obtain these probabilities already resulted in probabilities that are in agreement with experiments during earlier work. The influence of the acid strength was the largest on the protonation probabilities of DME and methanol. These were clearly higher for the more acidic H-SSZ-24 material.For a framework-bound methoxide, the influence of the acid strength was also visible in the probabilities of the pre-reactive complex formation. Furthermore, the formation of favorably oriented pre-reactive complexes was more than twice as high with DME than with methanol in both H-SAPO-5 and H-SSZ-24, suggesting that DME is more reactive towards methylation reactions than methanol. For the framework-bound methoxide, an increasing probability of pre-reactive complex formation was obtained with an increasing number of methyl groups on the aromatics in both H-SAPO-5 and H-SSZ-24. For methanol and DME, the effect of the degree of methylation was much more subtle and the chosen reactivity criteria were not able to properly describe the effect.

The last chapter of this master thesis investigated multiple routes for the methylation of toluene by methanol in both AFI materials and by DME in H-SSZ-24 with MTD simulations. This showed that the interaction of the aromatics with the walls of the catalyst plays a role in their orientation during the transition state. In H-SAPO-5, ortho and para methylation reactions were detected, while in H-SSZ-24 also the meta attack on the aromatic ring was possible during the MTD simulation. In H-SAPO-5 and H-SSZ-24, the transition state for the formation of a framework-bound methoxide was not observed when methanol was used as the methylating agent, but its formation was detected for DME in H-SSZ-24. For every recrossing of the methylation barrier, a different transition state was observed. This justifies the use of an MTD simulation, since it can take multiple reaction paths into account for the calculation of the free energy barrier.

Finally, the free energy barriers for the methylation of toluene were calculated. Several trends were observed. As mentioned in the literature toluene is more easily methylated than benzene, since the energy barriers were lower. The effect of acid strength was also investigated: the methylation barrier for methanol was almost $10\,\mathrm{kJ\,mol^{-1}}$ lower in H-SSZ-24 than in H-SAPO-5. The free energy barrier for methanol and DME are very similar in H-SSZ-24 as well as the free energy barrier for the first step of the stepwise mechanism and the concerted mechanism with DME. Nevertheless, it has been suggested that at typical MTO conditions (above $600\,\mathrm{K}$ and 1 atm) the stepwise mechanism should be dominant (in a TON material). However, the topology also highly influences the equilibrium between the stepwise and concerted mechanism. Alternatively, the free energy barriers might not have converged yet due to a too low number of recrossings.

In conclusion, this master thesis demonstrates that MD and MTD are both valuable techniques to obtain insights into the MTO conversion and the role of zeolitic acid strength. Based on the

OH frequency shift upon CO adsorption, the model used for H-SSZ-24 is indeed more acidic. The influence of the acid strength was especially seen on the difference in protonation probabilities in the two AFI materials, as well as in the increased probability for pre-reactive complex formation in H-SSZ-24 with a framework-bound methoxide as the methylating agent. There was only a subtle effect of the acid strength on the aromatics orientation and the probability for pre-reactive complex formation with methanol and DME. Finally, the higher acid strength of H-SSZ-24 lowered the free energy barriers for the methylation of toluene. Therefore, catalysts with higher acid strength appear to be more active for methylation of aromatics during MTO conversion.

In the future, investigation of methylation reactions for more HP species is advised, ranging from bulkier aromatics to aliphatic HP species. It might also be useful to perform MTD simulations of other type of reactions, such as reactions from the paring and side-chain mechanism and the alkene cracking reactions. This will result in a more complete understanding of the influence of zeolitic acid strength on the MTO conversion.

Bibliography

[1] B. Plumer, "Why oil prices keep falling - and throwing the world into turmoil, url:http://www.vox.com/2014/12/16/7401705/oil-prices-falling", 2015.

[2] Q. Wang, X. Chen, A. N. Jha, and H. Rogers, "Natural gas from shale formation - The evolution, evidences and challenges of shale gas revolution in United States", *Renewable Sustainable Energy Rev.*, vol. 30, pp. 1–28, Feb. 2014.

[3] A. Chowdhurry, "Must-know: Why crude oil prices have been falling lately, url:http://finance.yahoo.com/news/must-know-why-crude-oil-161309435.html", 2014.

[4] L. Lorenzetti, "What's behind the drop in oil prices? Here's what analysts have to say, url:http://fortune.com/2014/10/15/whats-behind-the-drop-in-oil-prices-heres-what-analysts-have-to-say/", 2014.

[5] G. A. Olah, "Towards Oil Independence Through Renewable Methanol Chemistry", *Angew. Chem. Int. Ed.*, vol. 52, no. 1, pp. 104–107, 2013.

[6] J. Q. Chen, A. Bozzano, B. Glover, T. Fuglerud, and S. Kvisle, "Recent advancements in ethylene and propylene production using the UOP/Hydro MTO process", *Catal. Today*, International Conference on Gas-Fuel 05 International Conference on Gas-Fuel 05 International Conference on Gas-Fuel 05, vol. 106, no. 1–4, pp. 103–107, Oct. 2005.

[7] S. Kioes and W. Liebner, "Methane - the Promising Career of a Humble Molecule", *J. Nat. Gas Chem.*, no. 13, pp. 71–78, 2004.

[8] C. Dean, "Naphta catalytic cracking for propylene production, url:http://www.digit al-refining.com/article/1000787,naphthacatalyticcrackingforpropyleneproduction .html.vni-5i7n03i", 2013.

[9] D. Liederman, S. Yurchak, J. C. Kuo, and W. Lee, "Mobil Methanol-to-Gasoline Process", *Journal of Energy*, vol. 6, no. 5, pp. 340–341, 1982.

[10] S. Gimre, "Doing it differently: Methanol-to-Olefins technology opens new, economic routes to light olefins from low cost feedstocks, url:http://issuu.com/cewindia/docs/cewsep temberissue.com", *Chemical Engineering World*, Sep. 2014.

[11] I. I. Rahmim, "Gas-to-Liquid Technologies: Recent Advances, Economics, Prospects", Prague, Jun. 2003, pp. 1–36.

[12] D. A. Wood, C. Nwaoha, and B. F. Towler, "Gas-to-liquids (GTL): A review of an industry offering several routes for monetizing natural gas", *Journal of Natural Gas Science and Engineering*, vol. 9, pp. 196–208, Nov. 2012.

[13] J. R. Rostrup-Nielsen, "Production of synthesis gas", *Catal. Today*, vol. 18, no. 4, pp. 305–324, Dec. 1993.

[14] A. P. E. York, T. Xiao, and M. L. H. Green, "Brief Overview of the Partial Oxidation of Methane to Synthesis Gas", *Top. Catal.*, vol. 22, no. 3-4, pp. 345–358, Apr. 2003.

[15] J. R. Rostrup-Nielsen, "Promotion by Poisoning", in *Studies in Surface Science and Catalysis*, ser. Catalyst Deactivation 1991 Proceedings of the 5th International Symposium, C. H. B. a. J. B. Butt, Ed., vol. 68, Elsevier, 1991, pp. 85–101.

[16] M. M. Halmann, "Carbon dioxide reforming", in *Chemical Fixation of Carbon DioxideMethods for Recycling CO2 into Useful Products*, CRC Press, Jun. 1993, pp. 34–36.

[17] L. K. Rath and J. R. Longanbach, "A Perspective on Syngas from Coal", *Energy Sources*, vol. 13, no. 4, pp. 443–459, Oct. 1991.

[18] S. inc., "Types of gasifiers, url:http://www.syngastechnology.com/gasification2.html",

[19] J. Ott, V. Gronemann, F. Pontzen, E. Fiedler, G. Grossmann, D. B. Kersebohm, G. Weiss, and C. Witte, "Methanol", in *Ullmann's Encyclopedia of Industrial Chemistry*, Wiley-VCH Verlag GmbH & Co. KGaA, 2000.

[20] M. Bowker, H. Houghton, and K. Waugh, "Mechanism and Kinetics of Methanol Synthesis on Zinc-Oxide", *J. Chem. Soc., Faraday Trans. I*, vol. 77, pp. 3023–3036, 1981.

[21] V. Kuznetsov, F. Shub, and M. Temkin, "Kinetics of Methanol Synthesis and Hydrolysis on a Copper-Containing Catalyst .1. Experimental Results", *Kinet. Catal.*, vol. 25, no. 3, pp. 510–517, 1984.

[22] G. Liu, D. Willcox, M. Garland, and H. Kung, "The Role of Co2 in Methanol Synthesis on Cu-Zn Oxide - an Isotope Labeling Study", *J. Catal.*, vol. 96, no. 1, pp. 251–260, 1985.

[23] K. Klier, V. Chatikavanij, R. Herman, and G. Simmons, "Catalytic Synthesis of Methanol from Co/H2 .4. the Effects of Carbon-Dioxide", *J. Catal.*, vol. 74, no. 2, pp. 343–360, 1982.

[24] J. Lee, K. Lee, S. Lee, and Y. Kim, "A Comparative-Study of Methanol Synthesis from Co2/H-2 and Co/H-2 Over a Cu/Zno/Al2o3 Catalyst", *J. Catal.*, vol. 144, no. 2, pp. 414–424, Dec. 1993.

[25] G. A. Olah, A. Goeppert, and G. K. S. Prakash, "Chemical Recycling of Carbon Dioxide to Methanol and Dimethyl Ether: From Greenhouse Gas to Renewable, Environmentally Carbon Neutral Fuels and Synthetic Hydrocarbons", *J. Org. Chem.*, vol. 74, no. 2, pp. 487–498, Jan. 2009.

[26] D. P. Summers, S. Leach, and K. W. Frese Jr., "The electrochemical reduction of aqueous carbon dioxide to methanol at molybdenum electrodes with low overpotentials", *J. Electroanal. Chem. Interfacial Electrochem.*, vol. 205, no. 1–2, pp. 219–232, Jun. 1986.

[27] G. Arai, T. Harashina, and I. Yasumori, "Selective Electrocatalytic Reduction of Carbon Dioxide to Methanol on Ru-modified Electrode", *Chem. Lett.*, vol. 18, no. 7, pp. 1215–1218, 1989.

[28] U. Olsbye, S. Svelle, M. Bjørgen, P. Beato, T. V. W. Janssens, F. Joensen, S. Bordiga, and K. P. Lillerud, "Conversion of Methanol to Hydrocarbons: How Zeolite Cavity and Pore Size Controls Product Selectivity", *Angew. Chem. Int. Ed.*, vol. 51, no. 24, pp. 5810–5831, Jun. 2012.

[29] ExxonMobil, "Methanol to Gasoline (MTG): Production of Clean Gasoline from Coal, url:http://www.exxonmobil.com/apps/refiningtechnologies/files/sellsheet 09mtgbrochure.pdf",

[30] C. J. Maiden, "The New Zealand Gas-to-Gasoline Project", in *Studies in Surface Science and Catalysis*, ser. Methane Conversion Proceedings of a Symposium on the Production of Fuels and Chemicals from Natural Gas, C. D. C. D.M. Bibby R. F. Howe and S. Yurchak, Ed., vol. 36, Elsevier, 1988, pp. 1–16.

[31] S. Yurchak, "Development of Mobil's Fixed-Bed Methanul-to-Gasoline (MTG) Process", in *Studies in Surface Science and Catalysis*, ser. Methane Conversion Proceedings of a Symposium on the Production of Fuels and Chemicals from Natural Gas, C. D. C. D.M. Bibby R. F. Howe and S. Yurchak, Ed., vol. 36, Elsevier, 1988, pp. 251–272.

[32] G. A. Funk, D. Myers, and B. Vora, "A different game plan, url:http://www.uop.com /wp-content/uploads/2013/12/methanol-to-olefins-technologyhydrocarbon-eng ineering-dec-2013.pdf", *Hydrocarbon engineering*, Dec. 2013.

[33] C. P. M. A. India, *Mto, url:http://cpmaindia.com/images/ethylenealtproduction process.jpg*, 2012.

[34] M. Rothaemel and H.-D. Holtmann, "Methanol to propylene MTP: Lurgi's way", in *Erdöl, Erdgas, Kohle*, vol. 118, Urban, 2002, pp. 234–237.

[35] C. D. Chang and A. J. Silvestri, "The conversion of methanol and other O-compounds to hydrocarbons over zeolite catalysts", *J. Catal.*, vol. 47, no. 2, pp. 249–259, May 1977.

[36] J. F. Haw and D. M. Marcus, "Well-defined (supra)molecular structures in zeolite methanol-to-olefin catalysis", *Top. Catal.*, vol. 34, no. 1-4, pp. 41–48, May 2005.

[37] M. Stöcker, "Methanol-to-hydrocarbons: Catalytic materials and their behavior", *Microporous Mesoporous Mater.*, vol. 29, no. 1–2, pp. 3–48, Jun. 1999.

[38] D. Lesthaeghe, V. Van Speybroeck, G. B. Marin, and M. Waroquier, "Understanding the Failure of Direct C-C Coupling in the Zeolite-Catalyzed Methanol-to-Olefin Process", *Angew. Chem. Int. Ed.*, vol. 45, no. 11, pp. 1714–1719, 2006.

[39] Y. Wei, D. Zhang, F. Chang, and Z. Liu, "Direct observation of induction period of MTO process with consecutive pulse reaction system", *Catal. Commun.*, vol. 8, no. 12, pp. 2248–2252, Dec. 2007.

[40] J. F. Haw, W. Song, D. M. Marcus, and J. B. Nicholas, "The Mechanism of Methanol to Hydrocarbon Catalysis", *Acc. Chem. Res.*, vol. 36, no. 5, pp. 317–326, May 2003.

[41] I. M. Dahl and S. Kolboe, "On the Reaction Mechanism for Hydrocarbon Formation from Methanol over SAPO-34: I. Isotopic Labeling Studies of the Co-Reaction of Ethene and Methanol", *J. Catal.*, vol. 149, no. 2, pp. 458–464, Oct. 1994.

[42] T. Mole, J. A. Whiteside, and D. Seddon, "Aromatic co-catalysis of methanol conversion over zeolite catalysts", *J. Catal.*, vol. 82, no. 2, pp. 261–266, Aug. 1983.

[43] R. M. Dessau, "On the H-ZSM-5 catalyzed formation of ethylene from methanol or higher olefins", *J. Catal.*, vol. 99, no. 1, pp. 111–116, May 1986.

[44] S. Svelle, F. Joensen, J. Nerlov, U. Olsbye, K.-P. Lillerud, S. Kolboe, and M. Bjørgen, "Conversion of Methanol into Hydrocarbons over Zeolite H-ZSM-5: Ethene Formation Is Mechanistically Separated from the Formation of Higher Alkenes", *J. Am. Chem. Soc.*, vol. 128, no. 46, pp. 14 770–14 771, 2006.

[45] I. Dahl and S. Kolboe, "On the Reaction-Mechanism for Propene Formation in the Mto Reaction Over Sapo-34", *Catal. Lett.*, vol. 20, no. 3-4, pp. 329–336, 1993.

[46] W. Song, H. Fu, and J. F. Haw, "Supramolecular Origins of Product Selectivity for Methanol-to-Olefin Catalysis on HSAPO-34", *J. Am. Chem. Soc.*, vol. 123, no. 20, pp. 4749–4754, May 2001.

[47] W. Song, D. M. Marcus, H. Fu, J. O. Ehresmann, and J. F. Haw, "An Oft-Studied Reaction That May Never Have Been: Direct Catalytic Conversion of Methanol or Dimethyl Ether to Hydrocarbons on the Solid Acids HZSM-5 or HSAPO-34", *J. Am. Chem. Soc.*, vol. 124, no. 15, pp. 3844–3845, Apr. 2002.

[48] Y. Jiang, W. Wang, V. R. Reddy Marthala, J. Huang, B. Sulikowski, and M. Hunger, "Effect of organic impurities on the hydrocarbon formation via the decomposition of surface methoxy groups on acidic zeolite catalysts", *J. Catal.*, vol. 238, no. 1, pp. 21–27, Feb. 2006.

[49] M. Vandichel, D. Lesthaeghe, J. V. d. Mynsbrugge, M. Waroquier, and V. Van Speybroeck, "Assembly of cyclic hydrocarbons from ethene and propene in acid zeolite catalysis to produce active catalytic sites for MTO conversion", *J. Catal.*, vol. 271, no. 1, pp. 67–78, Apr. 2010.

[50] W. Dai, C. Wang, M. Dyballa, G. Wu, N. Guan, L. Li, Z. Xie, and M. Hunger, "Understanding the Early Stages of the Methanol-to-Olefin Conversion on H-SAPO-34", *ACS Catal.*, vol. 5, no. 1, pp. 317–326, Jan. 2015.

[51] M. Westgård Erichsen, S. Svelle, and U. Olsbye, "H-SAPO-5 as methanol-to-olefins (MTO) model catalyst: Towards elucidating the effects of acid strength", *J. Catal.*, vol. 298, pp. 94–101, Feb. 2013.

[52] D. Lesthaeghe, B. De Sterck, V. Van Speybroeck, G. B. Marin, and M. Waroquier, "Zeolite Shape-Selectivity in the gem-Methylation of Aromatic Hydrocarbons", *Angew. Chem. Int. Ed.*, vol. 46, no. 8, pp. 1311–1314, Feb. 2007.

[53] R. Sullivan, R. Sieg, G. Langlois, and C. Egan, "A New Reaction That Occurs in Hydrocracking of Certain Aromatic Hydrocarbons", *J. Am. Chem. Soc.*, vol. 83, no. 5, pp. 1156–&, 1961.

[54] T. Mole, G. Bett, and D. Seddon, "Conversion of methanol to hydrocarbons over ZSM-5 zeolite: An examination of the role of aromatic hydrocarbons using 13carbon- and deuterium-labeled feeds", *J. Catal.*, vol. 84, no. 2, pp. 435–445, Dec. 1983.

[55] W. Song, H. Fu, and J. F. Haw, "Selective Synthesis of Methylnaphthalenes in HSAPO-34 Cages and Their Function as Reaction Centers in Methanol-to-Olefin Catalysis", *J. Phys. Chem. B*, vol. 105, no. 51, pp. 12 839–12 843, 2001.

[56] W. Song, J. F. Haw, J. B. Nicholas, and C. S. Heneghan, "Methylbenzenes Are the Organic Reaction Centers for Methanol-to-Olefin Catalysis on HSAPO-34", *J. Am. Chem. Soc.*, vol. 122, no. 43, pp. 10 726–10 727, Nov. 2000.

[57] B. Arstad and S. Kolboe, "The Reactivity of Molecules Trapped within the SAPO-34 Cavities in the Methanol-to-Hydrocarbons Reaction", *J. Am. Chem. Soc.*, vol. 123, no. 33, pp. 8137–8138, Aug. 2001.

[58] B. P. C. Hereijgers, F. Bleken, M. H. Nilsen, S. Svelle, K.-P. Lillerud, M. Bjorgen, B. M. Weckhuysen, and U. Olsbye, "Product shape selectivity dominates the Methanol-to-Olefins (MTO) reaction over H-SAPO-34 catalysts", *J. Catal.*, vol. 264, no. 1, pp. 77–87, May 2009.

[59] V. Van Speybroeck, K. Hemelsoet, K. De Wispelaere, Q. Qian, J. Van der Mynsbrugge, B. De Sterck, B. M. Weckhuysen, and M. Waroquier, "Mechanistic Studies on Chabazite-Type Methanol-to-Olefin Catalysts: Insights from Time-Resolved UV/Vis Microspectroscopy Combined with Theoretical Simulations", *ChemCatChem*, vol. 5, no. 1, pp. 173–184, Jan. 2013.

[60] K. De Wispelaere, K. Hemelsoet, M. Waroquier, and V. Van Speybroeck, "Complete low-barrier side-chain route for olefin formation during methanol conversion in H-SAPO-34", *J. Catal.*, vol. 305, pp. 76–80, Sep. 2013.

[61] K. Hemelsoet, A. Nollet, M. Vandichel, D. Lesthaeghe, V. Van Speybroeck, and M. Waroquier, "The Effect of Confined Space on the Growth of Naphthalenic Species in a Chabazite-Type Catalyst: A Molecular Modeling Study", *ChemCatChem*, vol. 1, no. 3, pp. 373–378, Nov. 2009.

[62] C.-M. Wang, Y.-D. Wang, H.-X. Liu, Z.-K. Xie, and Z.-P. Liu, "Theoretical insight into the minor role of paring mechanism in the methanol-to-olefins conversion within HSAPO-34 catalyst", *Microporous Mesoporous Mater.*, vol. 158, pp. 264–271, Aug. 2012.

[63] D. Lesthaeghe, V. V. Speybroeck, and M. Waroquier, "Theoretical evaluation of zeolite confinement effects on the reactivity of bulky intermediates", *Phys. Chem. Chem. Phys.*, vol. 11, no. 26, pp. 5222–5226, Jun. 2009.

[64] M. Bjorgen, F. Joensen, K.-P. Lillerud, U. Olsbye, and S. Svelle, "The mechanisms of ethene and propene formation from methanol over high silica H-ZSM-5 and H-beta", *Catal. Today*, vol. 142, no. 1-2, pp. 90–97, Apr. 2009.

[65] S. Svelle, P. O. Rønning, and S. Kolboe, "Kinetic studies of zeolite-catalyzed methylation reactions: 1. Coreaction of [12c]ethene and [13c]methanol", *J. Catal.*, vol. 224, no. 1, pp. 115–123, May 2004.

[66] S. Svelle, P. O. Rønning, U. Olsbye, and S. Kolboe, "Kinetic studies of zeolite-catalyzed methylation reactions. Part 2. Co-reaction of [12c]propene or [12c]n-butene and [13c]methanol", *J. Catal.*, vol. 234, no. 2, pp. 385–400, Sep. 2005.

[67] S. Svelle, U. Olsbye, F. Joensen, and M. Bjørgen, "Conversion of Methanol to Alkenes over Medium- and Large-Pore Acidic Zeolites: Steric Manipulation of the Reaction Intermediates Governs the Ethene/Propene Product Selectivity", *J. Phys. Chem. C*, vol. 111, no. 49, pp. 17 981–17 984, 2007.

[68] M. Bjørgen, S. Svelle, F. Joensen, J. Nerlov, S. Kolboe, F. Bonino, L. Palumbo, S. Bordiga, and U. Olsbye, "Conversion of methanol to hydrocarbons over zeolite H-ZSM-5: On the origin of the olefinic species", *J. Catal.*, vol. 249, no. 2, pp. 195–207, Jul. 2007.

[69] D. Lesthaeghe, J. Van der Mynsbrugge, M. Vandichel, M. Waroquier, and V. Van Speybroeck, "Full Theoretical Cycle for both Ethene and Propene Formation during Methanol-to-Olefin Conversion in H-ZSM-5", *ChemCatChem*, vol. 3, no. 1, pp. 208–212, Jan. 2011.

[70] S. Teketel, U. Olsbye, K.-P. Lillerud, P. Beato, and S. Svelle, "Selectivity control through fundamental mechanistic insight in the conversion of methanol to hydrocarbons over zeolites", *Microporous Mesoporous Mater.*, vol. 136, no. 1–3, pp. 33–41, Dec. 2010.

[71] M. Westgård Erichsen, S. Svelle, and U. Olsbye, "The influence of catalyst acid strength on the methanol to hydrocarbons (MTH) reaction", *Catal. Today*, Catalysis and synthetic fuels: state of the art and outlook, vol. 215, pp. 216–223, Oct. 2013.

[72] S. Svelle, M. Visur, U. Olsbye, Saepurahman, and M. Bjørgen, "Mechanistic Aspects of the Zeolite Catalyzed Methylation of Alkenes and Aromatics with Methanol: A Review", *Top. Catal.*, vol. 54, no. 13-15, pp. 897–906, Sep. 2011.

[73] I. M. Hill, S. A. Hashimi, and A. Bhan, "Kinetics and mechanism of olefin methylation reactions on zeolites", *J. Catal.*, vol. 285, no. 1, pp. 115–123, Jan. 2012.

[74] Saepurahman, M. Visur, U. Olsbye, M. Bjørgen, and S. Svelle, "In Situ FT-IR Mechanistic Investigations of the Zeolite Catalyzed Methylation of Benzene with Methanol: H-ZSM-5 versus H-beta", *Top. Catal.*, vol. 54, no. 16-18, pp. 1293–1301, Sep. 2011.

[75] R. Y. Brogaard, R. Henry, Y. Schuurman, A. J. Medford, P. G. Moses, P. Beato, S. Svelle, J. K. Nørskov, and U. Olsbye, "Methanol-to-hydrocarbons conversion: The alkene methylation pathway", *J. Catal.*, vol. 314, pp. 159–169, May 2014.

[76] A. M. Vos, K. H. L. Nulens, F. De Proft, R. A. Schoonheydt, and P. Geerlings, "Reactivity Descriptors and Rate Constants for Electrophilic Aromatic Substitution: Acid Zeolite Catalyzed Methylation of Benzene and Toluene", *J. Phys. Chem. B*, vol. 106, no. 8, pp. 2026–2034, 2002.

[77] J. Van der Mynsbrugge, S. L. C. Moors, K. De Wispelaere, and V. Van Speybroeck, "Insight into the Formation and Reactivity of Framework-Bound Methoxide Species in H-ZSM-5 from Static and Dynamic Molecular Simulations", *ChemCatChem*, vol. 6, no. 7, pp. 1906–1918, Jul. 2014.

[78] V. V. Speybroeck, K. D. Wispelaere, J. V. d. Mynsbrugge, M. Vandichel, K. Hemelsoet, and M. Waroquier, "First principle chemical kinetics in zeolites: The methanol-to-olefin process as a case study", *Chem. Soc. Rev.*, vol. 43, no. 21, pp. 7326–7357, Oct. 2014.

[79] S. Svelle, C. Tuma, X. Rozanska, T. Kerber, and J. Sauer, "Quantum Chemical Modeling of Zeolite-Catalyzed Methylation Reactions:Toward Chemical Accuracy for Barriers", *J. Am. Chem. Soc.*, vol. 131, no. 2, pp. 816–825, 2008.

[80] I. Hill, A. Malek, and A. Bhan, "Kinetics and Mechanism of Benzene, Toluene, and Xylene Methylation over H-MFI", *ACS Catal.*, vol. 3, no. 9, pp. 1992–2001, Sep. 2013.

[81] J. Van der Mynsbrugge, M. Visur, U. Olsbye, P. Beato, M. Bjørgen, V. Van Speybroeck, and S. Svelle, "Methylation of benzene by methanol: Single-site kinetics over H-ZSM-5 and H-beta zeolite catalysts", *J. Catal.*, vol. 292, pp. 201–212, Aug. 2012.

[82] P. Dejaifve, A. Auroux, P. C. Gravelle, J. C. Védrine, Z. Gabelica, and E. G. Derouane, "Methanol conversion on acidic ZSM-5, offretite, and mordenite zeolites: A comparative study of the formation and stability of coke deposits", *J. Catal.*, vol. 70, no. 1, pp. 123–136, Jul. 1981.

[83] D. C. Martindale, J. A. Kocal, and T.-H. Chao, "Patent: Burning deactivating coke in the presence of an oxygen containing gas, url:http://www.google.com/pat ents/us4795845".

[84] M. Bjørgen, S. Svelle, F. Joensen, J. Nerlov, S. Kolboe, F. Bonino, L. Palumbo, S. Bordiga, and U. Olsbye, "Conversion of methanol to hydrocarbons over zeolite H-ZSM-5: On the origin of the olefinic species", *J. Catal.*, vol. 249, no. 2, pp. 195–207, Jul. 2007.

[85] D. Chen, H. P. Rebo, K. Moljord, and A. Holmen, "The role of coke deposition in the conversion of methanol to olefins over SAPO-34", in *Catalyst Deactivation 1997*, C. H. Bartholomew and G. A. Fuentes, Eds., vol. 111, Amsterdam: Elsevier Science Publ B V, 1997, pp. 159–166.

[86] D. Chen, K. Moljord, T. Fuglerud, and A. Holmen, "The effect of crystal size of SAPO-34 on the selectivity and deactivation of the MTO reaction", *Microporous Mesoporous Mater.*, vol. 29, no. 1-2, pp. 191–203, Jun. 1999.

[87] F. Bleken, M. Bjørgen, L. Palumbo, S. Bordiga, S. Svelle, K.-P. Lillerud, and U. Olsbye, "The Effect of Acid Strength on the Conversion of Methanol to Olefins Over Acidic Microporous Catalysts with the CHA Topology", *Top. Catal.*, vol. 52, no. 3, pp. 218–228, Apr. 2009.

[88] Z. Zhu, M. Hartmann, and L. Kevan, "Catalytic Conversion of Methanol to Olefins on SAPO-n (n = 11, 34, and 35), CrAPSO-n, and Cr-SAPO-n Molecular Sieves", *Chem. Mater.*, vol. 12, no. 9, pp. 2781–2787, Sep. 2000.

[89] A. M. Prakash, M. Hartmann, Z. Zhu, and L. Kevan, "Incorporation of Transition Metal Ions into MeAPO/MeAPSO Molecular Sieves", *J. Phys. Chem. B*, vol. 104, no. 7, pp. 1610–1616, Feb. 2000.

[90] Y. Kumita, J. Gascon, E. Stavitski, J. A. Moulijn, and F. Kapteijn, "Shape selective methanol to olefins over highly thermostable DDR catalysts", *Appl. Catal., A: General*, Recent Developments in Model Catalysis - Closing the Gap to Technical Applications Dedicated to Helmut Knözinger on the occasion of his 75th Birthday, vol. 391, no. 1–2, pp. 234–243, Jan. 2011.

[91] S. M. Auerbach, K. A. Carrado, and P. K. Dutta, *Handbook of Zeolite Science and Technology*. CRC Press, Jul. 2003.

[92] C. Baerlocher, W. H. Meier, and D. H. Olson, "Atlas of zeolite framework types, url:http:// www.iza-structure.org/databases/books/atlas$_6$*ed.pdf*", no. 6, 2007.

[93] T. Fjermestad, S. Svelle, and O. Swang, "Mechanism of Si Island Formation in SAPO-34", *J. Phys. Chem. C*, vol. 119, no. 4, pp. 2086–2095, Jan. 2015.

[94] C. Baerlocher and L. McCusker, "Database of zeolite structures, url:http:// www.iza-structure.org/databases/",

[95] L.-T. Yuen, S. I. Zones, T. V. Harris, E. J. Gallegos, and A. Auroux, "Product selectivity in methanol to hydrocarbon conversion for isostructural compositions of AFI and CHA molecular sieves", *Microporous Mater.*, vol. 2, no. 2, pp. 105–117, Feb. 1994.

[96] I. M. Dahl, H. Mostad, D. Akporiaye, and R. Wendelbo, "Structural and chemical influences on the MTO reaction: A comparison of chabazite and SAPO-34 as MTO catalysts", *Microporous Mesoporous Mater.*, vol. 29, no. 1–2, pp. 185–190, Jun. 1999.

[97] F. Bleken, *Master thesis: The effect of acid strength on the MTO reaction - conversion of methanol to hydrocarbons over H-SAPO-34 and high silica chabazite (H-SSZ-13)*, University of Oslo, 2007.

[98] Q. Qian, J. Ruiz-Martínez, M. Mokhtar, A. M. Asiri, S. A. Al-Thabaiti, S. N. Basahel, and B. M. Weckhuysen, "Single-catalyst particle spectroscopy of alcohol-to-olefins conversions: Comparison between SAPO-34 and SSZ-13", *Catal. Today*, Acid-Base Catalysis Advanced Sciences and Spreading Applications to Solutions of Environmental, Resources and Energy Issues: ABC-7, 7th International Symposium on Acid-Base Catalysis, Tokyo, May 12-15, 2013, vol. 226, pp. 14–24, May 2014.

[99] L. Wu and E. J. M. Hensen, "Comparison of mesoporous SSZ-13 and SAPO-34 zeolite catalysts for the methanol-to-olefins reaction", *Catal. Today*, vol. 235, pp. 160–168, 2014, Recent developments in catalyst design and activation.

[100] K.-Y. Lee, S.-W. Lee, and S.-K. Ihm, "Acid Strength Control in MFI Zeolite for the Methanol-to-Hydrocarbons (MTH) Reaction", *Ind. Eng. Chem. Res.*, vol. 53, no. 24, pp. 10 072–10 079, Jun. 2014.

[101] B. Valle, A. Alonso, A. Atutxa, A. G. Gayubo, and J. Bilbao, "Effect of nickel incorporation on the acidity and stability of HZSM-5 zeolite in the MTO process", *Catal. Today*, International Conference on Gas-Fuel 05 International Conference on Gas-Fuel 05 International Conference on Gas-Fuel 05, vol. 106, no. 1–4, pp. 118–122, Oct. 2005.

[102] K.-Y. Lee, H.-K. Lee, and S.-K. Ihm, "Influence of Catalyst Binders on the Acidity and Catalytic Performance of HZSM-5 Zeolites for Methanol-to-Propylene (MTP) Process: Single and Binary Binder System", *Top. Catal.*, vol. 53, no. 3-4, pp. 247–253, Dec. 2009.

[103] S. Bordiga, L. Regli, D. Cocina, C. Lamberti, M. Bjørgen, and K. P. Lillerud, "Assessing the Acidity of High Silica Chabazite H-SSZ-13 by FTIR Using CO as Molecular Probe: Comparison with H-SAPO-34", *J. Phys. Chem. B*, vol. 109, no. 7, pp. 2779–2784, Feb. 2005.

[104] K. Chakarova and K. Hadjiivanov, "H-Bonding of Zeolite Hydroxyls with Weak Bases: FTIR Study of CO and N2 Adsorption on H-D-ZSM-5", *J. Phys. Chem. C*, vol. 115, no. 11, pp. 4806–4817, Mar. 2011.

[105] M. Westgård Erichsen, *Master thesis: The methanol-to-hydrocarbons reaction : Influence of acid strength on the mechanism of olefin formation*, University of Oslo, 2010.

[106] M. Westgård Erichsen, K. De Wispelaere, K. Hemelsoet, S. L. C. Moors, T. Deconinck, M. Waroquier, S. Svelle, V. Van Speybroeck, and U. Olsbye, "How zeolitic acid strength and composition alter the reactivity of alkenes and aromatics towards methanol", *J. Catal.*, Special Issue: The Impact of Haldor Topsøe on Catalysis, vol. 328, pp. 186–196, Aug. 2015.

[107] M. Bjørgen, U. Olsbye, and S. Kolboe, "Coke precursor formation and zeolite deactivation: Mechanistic insights from hexamethylbenzene conversion", *J. Catal.*, vol. 215, no. 1, pp. 30–44, Apr. 2003.

[108] A. T. Aguayo, A. G. Gayubo, R. Vivanco, M. Olazar, and J. Bilbao, "Role of acidity and microporous structure in alternative catalysts for the transformation of methanol into olefins", *Appl. Catal., A: General*, vol. 283, no. 1–2, pp. 197–207, Apr. 2005.

[109] W. Dai, X. Wang, G. Wu, N. Guan, M. Hunger, and L. Li, "Methanol-to-Olefin Conversion on Silicoaluminophosphate Catalysts: Effect of Brønsted Acid Sites and Framework Structures", *ACS Catal.*, vol. 1, no. 4, pp. 292–299, Apr. 2011.

[110] O. Bortnovsky, P. Sazama, and B. Wichterlova, "Cracking of pentenes to C2–C4 light olefins over zeolites and zeotypes: Role of topology and acid site strength and concentration", *Appl. Catal., A: General*, vol. 287, no. 2, pp. 203–213, Jun. 2005.

[111] S. Teketel, S. Svelle, K.-P. Lillerud, and U. Olsbye, "Shape-Selective Conversion of Methanol to Hydrocarbons Over 10-Ring Unidirectional-Channel Acidic H-ZSM-22", *ChemCatChem*, vol. 1, 2009.

[112] R. B. Borade, A. Adnot, and S. Kaliaguine, "Acid sites in Al-ZSM-22 and Fe-ZSM-22", *Zeolites*, vol. 11, no. 7, pp. 710–719, Sep. 1991.

[113] P. G. Moses and J. K. Nørskov, "Methanol to Dimethyl Ether over ZSM-22: A Periodic Density Functional Theory Study", *ACS Catal.*, vol. 3, no. 4, pp. 735–745, Apr. 2013.

[114] S. R. Blaszkowski and R. A. van Santen, "Theoretical Study of C-C Bond Formation in the Methanol-to-Gasoline Process", *J. Am. Chem. Soc.*, vol. 119, no. 21, pp. 5020–5027, May 1997.

[115] ——, "Theoretical Study of the Mechanism of Surface Methoxy and Dimethyl Ether Formation from Methanol Catalyzed by Zeolitic Protons", *J. Phys. Chem. B*, vol. 101, no. 13, pp. 2292–2305, Mar. 1997.

[116] M. Svensson, S. Humbel, R. D. J. Froese, T. Matsubara, S. Sieber, and K. Morokuma, "Oniom: A Multilayered Integrated MO + MM Method for Geometry Optimizations and Single Point Energy Predictions. A Test for Diels-Alder Reactions and Pt(P(t-Bu)3)2 + H2 Oxidative Addition", *J. Phys. Chem.*, vol. 100, no. 50, pp. 19 357–19 363, 1996.

[117] S. Dapprich, I. Komáromi, K. S. Byun, K. Morokuma, and M. J. Frisch, "A new ONIOM implementation in Gaussian98. Part I. The calculation of energies, gradients, vibrational frequencies and electric field derivatives1", *J. Mol. Struct.: THEOCHEM*, vol. 461–462, pp. 1–21, Apr. 1999.

[118] J. W. Ponder and D. A. Case, "Force fields for protein simulations", *Adv. Protein Chem.*, vol. 66, pp. 27–85, 2003.

[119] B. R. Brooks, R. E. Bruccoleri, B. D. Olafson, D. J. States, S. Swaminathan, and M. Karplus, "Charmm: A program for macromolecular energy, minimization, and dynamics calculations", *J. Comput. Chem.*, vol. 4, no. 2, pp. 187–217, Jun. 1983.

[120] J. Hermans, H. J. C. Berendsen, W. F. Van Gunsteren, and J. P. M. Postma, "A consistent empirical potential for water–protein interactions", *Biopolymers*, vol. 23, no. 8, pp. 1513–1518, Aug. 1984.

[121] L. D. Schuler, X. Daura, and W. F. van Gunsteren, "An improved GROMOS96 force field for aliphatic hydrocarbons in the condensed phase", *J. Comput. Chem.*, vol. 22, no. 11, pp. 1205–1218, Aug. 2001.

[122] K. Hemelsoet, J. Van der Mynsbrugge, K. De Wispelaere, M. Waroquier, and V. Van Speybroeck, "Unraveling the Reaction Mechanisms Governing Methanol-to-Olefins Catalysis by Theory and Experiment", *ChemPhysChem*, vol. 14, no. 8, pp. 1526–1545, Jun. 2013.

[123] *Cp2k open source molecular dynamics, url:http://www.cp2k.org/.*

[124] B. M. Weckhuysen, "Chemical Imaging of Spatial Heterogeneities in Catalytic Solids at Different Length and Time Scales", *Angew. Chem.-Int. Edit.*, vol. 48, no. 27, pp. 4910–4943, 2009.

[125] K. Hammond, "Quantifying Defects in Zeolites and Zeolite Membranes, url:http: //scholarworks.umass.edu/openaccessdissertations/158", Feb. 2010.

[126] M. Born and R. Oppenheimer, "Zur Quantentheorie der Molekeln", *Ann. Phys.*, vol. 389, no. 20, pp. 457–484, Jan. 1927.

[127] M. Tuckerman, *The Born-Oppenheimer Approximation, url:http://www.nyu.edu/classes/tuckerman/quant.mech/lectures/lecture*$_1$0/*node*1.*html*.

[128] D. A. McQuarrie and J. D. Simon, *Physical Chemistry: A Molecular Approach*, 1 edition. Sausalito, Calif: University Science Books, 1997.

[129] J. P. Perdew, A. Ruzsinszky, J. M. Tao, V. N. Staroverov, G. E. Scuseria, and G. I. Csonka, "Prescription for the design and selection of density functional approximations: More constraint satisfaction with fewer fits", *J. Chem. Phys.*, vol. 123, no. 6, p. 062 201, Aug. 2005.

[130] J. P. Perdew and A. Zunger, "Self-interaction correction to density-functional approximations for many-electron systems", *Phys. Rev. B*, vol. 23, no. 10, pp. 5048–5079, May 1981.

[131] A. Becke, "Density-Functional Exchange-Energy Approximation with Correct Asymptotic-Behavior", *Phys. Rev. A*, vol. 38, no. 6, pp. 3098–3100, Sep. 1988.

[132] J. Perdew and W. Yue, "Accurate and Simple Density Functional for the Electronic Exchange Energy - Generalized Gradient Approximation", *Phys. Rev. B*, vol. 33, no. 12, pp. 8800–8802, Jun. 1986.

[133] J. Perdew, "Density-Functional Approximation for the Correlation-Energy of the Inhomogeneous Electron-Gas", *Phys. Rev. B*, vol. 33, no. 12, pp. 8822–8824, Jun. 1986.

[134] Y. Wang and J. Perdew, "Spin Scaling of the Electron-Gas Correlation-Energy in the High-Density Limit", *Phys. Rev. B*, vol. 43, no. 11, pp. 8911–8916, Apr. 1991.

[135] J. P. Perdew, K. Burke, and Y. Wang, "Generalized gradient approximation for the exchange-correlation hole of a many-electron system", *Phys. Rev. B*, vol. 54, no. 23, pp. 16 533–16 539, Dec. 1996.

[136] Y. Zhang and W. Yang, "Comment on "Generalized Gradient Approximation Made Simple"", *Phys. Rev. Lett.*, vol. 80, no. 4, pp. 890–890, Jan. 1998.

[137] M. Elstner, P. Hobza, T. Frauenheim, S. Suhai, and E. Kaxiras, "Hydrogen bonding and stacking interactions of nucleic acid base pairs: A density-functional-theory based treatment", *J. Chem. Phys.*, vol. 114, no. 12, p. 5149, 2001.

[138] S. Grimme, "Accurate description of van der Waals complexes by density functional theory including empirical corrections", *J. Comp. Chem.*, vol. 25, no. 12, pp. 1463–1473, Sep. 2004.

[139] P. Jurečka, J. Černý, P. Hobza, and D. R. Salahub, "Density functional theory augmented with an empirical dispersion term. Interaction energies and geometries of 80 noncovalent complexes compared with ab initio quantum mechanics calculations", *J. Comp. Chem.*, vol. 28, no. 2, pp. 555–569, Jan. 2007.

[140] O. von Lilienfeld, I. Tavernelli, U. Rothlisberger, and D. Sebastiani, "Optimization of Effective Atom Centered Potentials for London Dispersion Forces in Density Functional Theory", *Phys. Rev. Lett.*, vol. 93, no. 15, Oct. 2004.

[141] Y. Y. Sun, Y.-H. Kim, K. Lee, and S. B. Zhang, "Accurate and efficient calculation of van der Waals interactions within density functional theory by local atomic potential approach", *J. Chem. Phys.*, vol. 129, no. 15, p. 154 102, 2008.

[142] Y. Andersson, D. Langreth, and B. Lundqvist, "Van der Waals Interactions in Density-Functional Theory", *Phys. Rev. Lett.*, vol. 76, no. 1, pp. 102–105, Jan. 1996.

[143] D. C. Langreth, M. Dion, H. Rydberg, E. Schröder, P. Hyldgaard, and B. I. Lundqvist, "Van der Waals density functional theory with applications", *Int. J. Quantum Chem.*, vol. 101, no. 5, pp. 599–610, 2005.

[144] T. Sato, T. Tsuneda, and K. Hirao, "Van der Waals interactions studied by density functional theory", *Mol. Phys.*, vol. 103, no. 6-8, pp. 1151–1164, Mar. 2005.

[145] Y. Zhao and D. G. Truhlar, "Density Functionals with Broad Applicability in Chemistry", *Acc. Chem. Res.*, vol. 41, no. 2, pp. 157–167, 2008.

[146] J. Wellendorff, K. T. Lundgaard, A. Møgelhøj, V. Petzold, D. D. Landis, J. K. Nørskov, T. Bligaard, and K. W. Jacobsen, "Density functionals for surface science: Exchange-correlation model development with Bayesian error estimation", *Phys. Rev. B*, vol. 85, no. 23, p. 235 149, Jun. 2012.

[147] S. Grimme, J. Antony, S. Ehrlich, and H. Krieg, "A consistent and accurate ab initio parametrization of density functional dispersion correction (DFT-D) for the 94 elements H-Pu", *J. Chem. Phys.*, vol. 132, no. 15, p. 154 104, Apr. 2010.

[148] G. Lippert, J. Hutter, and M. Parrinello, "A hybrid Gaussian and plane wave density functional scheme", *Mol. Phys.*, vol. 92, no. 3, pp. 477–487, Oct. 1997.

[149] G. Lippert, J. Hutter, and M. Parrinello, "The Gaussian and augmented-plane-wave density functional method for ab initio molecular dynamics simulations", *Theor. Chem. Acc.*, vol. 103, no. 2, pp. 124–140, Dec. 1999.

[150] *Potential energy surfaces, url:http://www.chem.wayne.edu/ hbs/chm6440/PES. html.*

[151] G. Bussi, D. Donadio, and M. Parrinello, "Canonical sampling through velocity rescaling", *J. Chem. Phys.*, vol. 126, no. 1, p. 014 101, Jan. 2007.

[152] D. J. Evans and B. L. Holian, "The Nose–Hoover thermostat", *J. Chem. Phys.*, vol. 83, no. 8, pp. 4069–4074, Oct. 1985.

[153] P. Demontis and G. B. Suffritti, "Structure and Dynamics of Zeolites Investigated by Molecular Dynamics", *Chem. Rev.*, vol. 97, no. 8, pp. 2845–2878, Dec. 1997.

[154] A. I. Skoulidas and D. S. Sholl, "Self-Diffusion and Transport Diffusion of Light Gases in Metal-Organic Framework Materials Assessed Using Molecular Dynamics Simulations", *J. Phys. Chem. B*, vol. 109, no. 33, pp. 15 760–15 768, Aug. 2005.

[155] P. M. Zimmerman, D. C. Tranca, J. Gomes, D. S. Lambrecht, M. Head-Gordon, and A. T. Bell, "Ab Initio Simulations Reveal that Reaction Dynamics Strongly Affect Product Selectivity for the Cracking of Alkanes over H-MFI", *J. Am. Chem. Soc.*, vol. 134, no. 47, pp. 19 468–19 476, Nov. 2012.

[156] V. Van Speybroeck, K. Hemelsoet, L. Joos, M. Waroquier, R. G. Bell, and C. R. A. Catlow, "Advances in theory and their application within the field of zeolite chemistry", *Chem. Soc. Rev.*, 2015.

[157] K. De Wispelaere, *Master thesis: Molecular dynamics applied to zeolite-catalyzed reactions*, UGent, 2014.

[158] B. J. Palmer, "Direct Application of Shake to the Velocity Verlet Algorithm", *J. Comp. Phys.*, vol. 104, no. 2, pp. 470–472, Feb. 1993.

[159] M. Tuckerman and M. Parrinello, "Integrating the Car-Parrinello Equations .1. Basic Integration Techniques", *J. Chem. Phys.*, vol. 101, no. 2, pp. 1302–1315, Jul. 1994.

[160] D. Humphreys, R. Friesner, and B. Berne, "A Multiple-Time-Step Molecular-Dynamics Algorithm for Macromolecules", *J. Phys. Chem.*, vol. 98, no. 27, pp. 6885–6892, Jul. 1994.

[161] W. F. Van Gunsteren and H. J. C. Berendsen, "A Leap-Frog Algorithm for Stochastic Dynamics", *Mol. Simul.*, vol. 1, no. 3, pp. 173–185, 1988.

[162] A. Laio and F. L. Gervasio, "Metadynamics: A method to simulate rare events and reconstruct the free energy in biophysics, chemistry and material science", *Rep. Prog. Phys.*, vol. 71, no. 12, p. 126 601, Dec. 2008.

[163] B. Ensing, A. Laio, M. Parrinello, and M. L. Klein, "A Recipe for the Computation of the Free Energy Barrier and the Lowest Free Energy Path of Concerted Reactions†", *J. Phys. Chem. B*, vol. 109, no. 14, pp. 6676–6687, Apr. 2005.

[164] D. Branduardi, F. L. Gervasio, A. Cavalli, M. Recanatini, and M. Parrinello, "The Role of the Peripheral Anionic Site and Cation-π Interactions in the Ligand Penetration of the Human AChE Gorge", *J. Am. Chem. Soc.*, vol. 127, no. 25, pp. 9147–9155, Jun. 2005.

[165] A. Barducci, G. Bussi, and M. Parrinello, "Well-Tempered Metadynamics: A Smoothly Converging and Tunable Free-Energy Method", *Phys. Rev. Lett.*, vol. 100, no. 2, p. 020 603, Jan. 2008.

[166] G. Bussi, F. L. Gervasio, A. Laio, and M. Parrinello, "Free-Energy Landscape for β Hairpin Folding from Combined Parallel Tempering and Metadynamics", *J. Am. Chem. Soc.*, vol. 128, no. 41, pp. 13 435–13 441, Oct. 2006.

[167] S. Piana and A. Laio, "A Bias-Exchange Approach to Protein Folding", *J. Phys. Chem. B*, vol. 111, no. 17, pp. 4553–4559, May 2007.

[168] G. A. Tribello, M. Ceriotti, and M. Parrinello, "A self-learning algorithm for biased molecular dynamics", *PNAS*, vol. 107, no. 41, pp. 17 509–17 514, Oct. 2010.

[169] Y. Jeanvoine, J. G. Ángyán, G. Kresse, and J. Hafner, "On the Nature of Water Interacting with Brønsted Acidic Sites. Ab Initio Molecular Dynamics Study of Hydrated HSAPO-34", *J. Phys. Chem. B*, vol. 102, no. 38, pp. 7307–7310, Sep. 1998.

[170] T. Jiang, F. Goeltl, R. E. Bulo, and P. Sautet, "Effect of Temperature on the Adsorption of Short Alkanes in the Zeolite SSZ-13-Adapting Adsorption Isotherms to Microporous Materials", *ACS Catal.*, vol. 4, no. 7, pp. 2351–2358, Jul. 2014.

[171] P. Vansteenkiste, V. Van Speybroeck, G. B. Marin, and M. Waroquier, "Ab Initio Calculation of Entropy and Heat Capacity of Gas-Phase n-Alkanes Using Internal Rotations", *J. Phys. Chem. A*, vol. 107, no. 17, pp. 3139–3145, May 2003.

[172] A. Ghysels, T. Verstraelen, K. Hemelsoet, M. Waroquier, and V. Van Speybroeck, "Tamkin: A Versatile Package for Vibrational Analysis and Chemical Kinetics", *J. Chem. Inf. Model.*, vol. 50, no. 9, pp. 1736–1750, Sep. 2010.

[173] J. VandeVondele, M. Krack, F. Mohamed, M. Parrinello, T. Chassaing, and J. Hutter, "Quickstep: Fast and accurate density functional calculations using a mixed Gaussian and plane waves approach", *Comp. Phys. Commun.*, vol. 167, no. 2, pp. 103–128, Apr. 2005.

[174] S. Goedecker, M. Teter, and J. Hutter, "Separable dual-space Gaussian pseudopotentials", *Phys. Rev. B*, vol. 54, no. 3, pp. 1703–1710, Jul. 1996.

[175] S. L. C. Moors, K. De Wispelaere, J. Van der Mynsbrugge, M. Waroquier, and V. Van Speybroeck, "Molecular Dynamics Kinetic Study on the Zeolite-Catalyzed Benzene Methylation in ZSM-5", *ACS Catal.*, vol. 3, no. 11, pp. 2556–2567, Nov. 2013.

[176] K. De Wispelaere, B. Ensing, A. Ghysels, E. J. Meijer, and V. Van Speybroeck, "Complex Reaction Environments and Competing Reaction Mechanisms in Zeolite Catalysis: Insights from Advanced Molecular Dynamics", *Chem. - Eur. J.*, n/a–n/a, May 2015.

[177] A. Corma, "Inorganic Solid Acids and Their Use in Acid-Catalyzed Hydrocarbon Reactions", *Chem. Rev.*, vol. 95, no. 3, pp. 559–614, May 1995.

[178] J. F. Haw, "Zeolite acid strength and reaction mechanisms in catalysis", *Phys. Chem. Chem. Phys.*, vol. 4, no. 22, pp. 5431–5441, Nov. 2002.

[179] G. Sastre, D. W. Lewis, and A. Corma, "The role of the electrostatic potential, electric field and electric field gradient on the acidity of AFI and CHA zeotypes", *Phys. Chem. Chem. Phys.*, vol. 2, no. 1, pp. 177–185, 2000.

[180] H. Soscún, O. Castellano, J. Hernández, and A. Hinchliffe, "Acidity of the Brönsted acid sites of zeolites", *Int. J. Quantum Chem.*, vol. 82, no. 3, pp. 143–150, Jan. 2001.

[181] R. R. Pinto, P. Borges, M. A. N. D. A. Lemos, F. Lemos, J. C. Védrine, E. G. Derouane, and F. R. Ribeiro, "Correlating NH3-TPD and 1h MAS NMR measurements of zeolite acidity: Proposal of an acidity scale", *Appl. Catal., A: General*, vol. 284, no. 1–2, pp. 39–46, Apr. 2005.

[182] O. Bludský, M. Šilhan, D. Nachtigallová, and P. Nachtigall, "Calculations of Site-Specific CO Stretching Frequencies for Copper Carbonyls with the "Near Spectroscopic Accuracy": CO Interaction with Cu+/MFI", *J. Phys. Chem. A*, vol. 107, no. 48, pp. 10 381–10 388, Dec. 2003.

[183] C. O. Arean, M. R. Delgado, P. Nachtigall, H. V. Thang, M. Rubeš, R. Bulánek, and P. Chlubná-Eliášová, "Measuring the Brønsted acid strength of zeolites–does it correlate with the O-H frequency shift probed by a weak base?", *Phys. Chem. Chem. Phys.*, vol. 16, no. 21, pp. 10 129–10 141, Jun. 2014.

[184] E. P. L. Hunter and S. G. Lias, "Evaluated Gas Phase Basicities and Proton Affinities of Molecules: An Update", *J. Phys. Chem. Reference Data*, vol. 27, no. 3, pp. 413–656, May 1998.

[185] K. De Wispelaere, *Master thesis: Ab Initio Studie naar de deactivering van Zeoliet-en Zeotypekatalysatoren in het MTO-proces*, UGent, 2011.

[186] T. Deconinck, *Master thesis: Dynamic ab initio study towards new hydrocarbon pool cycles for MTO-conversion in H-SAPO-5*, UGent, 2014.

[187] S. Svelle and M. Bjørgen, "Mechanistic Proposal for the Zeolite Catalyzed Methylation of Aromatic Compounds", *J. Phys. Chem. A*, vol. 114, no. 47, pp. 12 548–12 554, Dec. 2010.

Appendix A

Quadratic walls used during the MTD simulations

The walls are determined by the following function: $K(CN - position)^2$. The used walls are as follows:

- $0.04 \leq$ CN1 for methanol and $1.04 \leq$ CN1 for DME with K= 50.0 hartree
- $0.03 \leq$ CN2 ≤ 0.72 for methanol and $0.015 \leq$ CN2 ≤ 0.36 for DME with K= 15.0 hartree
- No walls on CN3
- $0.03 \leq$ CN4 for both methanol and DME with K=100.0 hartree
- $0.03 \leq$ CN5 for methanol only with K=100.0 hartree

The wall for the first CN is positioned at 0.04 for methanol and at 1.04 for DME with a steepness K of 50 Hartree. This wall avoids that CN of the C-O bond in methanol or DME becomes smaller than 0.04. It ensures that once the methyl group has left the previous methanol or DME molecule, the O atom will still remain close to the methyl group hereby enhancing the change of recrossing after the methylation reaction occurred.

The second CN is restricted to the region between 0.03 and 0.72 for methanol and between 0.015 and 0.36 for DME by placing two walls at these positions each with a K of 15 Hartree. These bottom wall is applied to keep the two C-atoms near each other, while the upper wall will avoid the occurrence of a fast hydride shift in the product state. Once toluene is methylated and a carbocation is formed, a hydride shift almost immediately takes place. If the MD walker would land in this minimum, recrossing would become very unlikely.

Finally, two passive CN are introduced, meaning that no hills will be placed during the MTD simulation. A fourth CN is used for the bond between the O atom of the methylating agent and the H atom of the acid site and a fifth CN is only needed with methanol for the bond between the O atom and the H atom of methanol. These two CN cannot be smaller than 0.03

and therefore a quadratic wall is placed with a K of 100 Hartree. These walls must enhance the probability that the methylating agent remains protonated.

Appendix B

Cell parameters obtained from the NPT ensemble MD simulations

To perform an MD or MTD simulation within an NVT ensemble, the cell parameters must be known a priori. The cell parameters are dependent on the conditions during the MD simulation such as temperature, but also on the level of theory. The presence of guest molecules will also influence the cell parameters. Therefore the cell parameters used during an NVT MD simulation are based on the cell parameters averaged out over a NPT MD simulation of approximately 50 ps at the same temperature and level of theory as for the NVT ensemble. To ensure that the angles of the unit cell are still equal to 90° for α and β and equal to 120° for γ, the cell length are adjusted with a correction factor. This factor is equal to the ratio of the average volume from the NPT simulation and the volume calculated with the average cell lengths from the NPT simulation. All three average cell lengths are then multiplied by one third of the correction factor to obtain the corrected cell lengths.

Table B.1 shows the applied correction factor and the averaged cell parameters of each NPT MD simulation in H-SAPO-5. Analogously, the cell parameters in H-SSZ-24 are represented in Table B.2. As seen from both tables, the applied correction factor is quite small. Overall, the calculated volumes only deviates from the real average volumes by approximately 0.15 %.

Table B.1: Correction factor together with the cell lengths after corrections for the H-SAPO-5 supercell when guest molecules are present at 623 K and 1 atm.

On acid site	Extra molecule	Correction factor	a	b	c
Methanol	Toluene	0.9985	13.9810	14.0609	16.9672
Methanol	O-xylene	0.9986	13.9870	14.0592	16.9632
Toluene	Methanol	0.9989	13.9952	14.0466	16.9683
O-xylene	Methanol	0.9988	13.9988	14.0469	16.9746
DME	Toluene	0.9983	13.9733	14.0565	16.9602
DME	O-xylene	0.9984	13.9866	14.0555	16.9665
Toluene	DME	0.9985	13.9792	14.0421	16.9648
O-xylene	DME	0.9984	13.9831	14.0682	16.9651
Methoxide	Toluene	0.9983	13.9320	14.0876	16.9662
Methoxide	O-xylene	0.9980	13.9391	14.0911	16.9611

Table B.2: Correction factor together with the cell lengths after corrections for the H-SSZ-24 supercell when guest molecules are present at 623 K and 1 atm.

On acid site	Extra molecule	Correction factor	a	b	c
Methanol	Toluene	0.9989	13.8706	13.8704	16.8241
Methanol	O-xylene	0.9987	13.8712	13.8799	16.8141
Toluene	Methanol	0.9987	13.8615	13.8827	16.8155
O-xylene	Methanol	0.9984	13.8613	13.8900	16.8116
DME	Toluene	0.9984	13.8686	13.8791	16.8111
DME	O-xylene	0.9982	13.8667	13.8966	16.8048
Toluene	DME	0.9985	13.8548	13.8893	16.8148
O-xylene	DME	0.9987	13.8660	13.8815	16.8174
Methoxide	Toluene	0.9981	13.8729	13.8771	16.8039
Methoxide	O-xylene	0.9979	13.8722	13.8874	16.8035

Appendix C

Average distance to the acid site in AFI topology

Table C.1: Average distance and the correspondent standard deviation from the 6 C atoms of an aromatic ring or from the O atom of a methylating agent to the acid site or to a framework-bound methoxide in H-SAPO-5.

Molecule A	molecule B	Distance from A to the acid in presence of B [Å]
Benzene	Methanol	5.26 ± 1.30
Benzene	DME	6.40 ± 1.10
Benzene	Methoxide	5.23 ± 1.43
Toluene	-	5.34 ± 1.53
Toluene	Methanol	5.90 ± 1.19
Toluene	DME	6.44 ± 0.93
Toluene	Methoxide	5.12 ± 1.37
O-xylene	-	3.37 ± 0.97
O-xylene	Methanol	5.81 ± 1.30
O-xylene	DME	6.93 ± 1.06
O-xylene	Methoxide	5.04 ± 1.39
Methanol	-	4.44 ± 3.54
Methanol	Benzene	1.67 ± 0.38
Methanol	Toluene	1.66 ± 0.35
Methanol	O-xylene	1.84 ± 0.89
DME	Benzene	1.71 ± 0.69
DME	Toluene	1.61 ± 0.31
DME	O-xylene	1.70 ± 0.58

Table C.2: Average distance and the correspondent standard deviation from the 6 C atoms of an aromatic ring or from the O atom of a methylating agent to the acid site or to a framework-bound methoxide in H-SSZ-24.

Molecule A	molecule B	Distance from A to the acid in presence of B [Å]
Benzene	Methanol	5.26 ± 1.30
Benzene	DME	6.40 ± 1.10
Benzene	Methoxide	5.23 ± 1.43
Toluene	-	3.03 ± 0.81
Toluene	Methanol	5.80 ± 1.29
Toluene	DME	6.63 ± 0.88
Toluene	Methoxide	4.67 ± 1.27
O-xylene	-	3.54 ± 1.46
O-xylene	Methanol	5.80 ± 1.20
O-xylene	DME	6.40 ± 0.94
O-xylene	Methoxide	5.24 ± 1.49
Methanol	-	1.47 ± 0.80
Methanol	Benzene	1.48 ± 0.30
Methanol	Toluene	1.41 ± 0.37
Methanol	O-xylene	1.52 ± 0.34
DME	Benzene	1.49 ± 0.60
DME	Toluene	1.52 ± 0.33
DME	O-xylene	1.48 ± 0.30

Appendix D

Effect of range of angles on orientation of aromatics

As mentioned in subsection 6.1.2, their are three main types of alignment for the aromatics inside the AFI channel. In subsection 6.1.2, a deviation of 30° from the ideal cases was allowed. In this appendix the effect of the maximum deviation from the three idealized cases is considered for toluene and o-xylene in H-SAPO-5 and H-SSZ-24. These idealized cases are: the aromatic lays flat with respect to the acid site (1), the aromatic stands upright with respect to the acid site while faced to the channel wall (2) and the aromatic stands upright with respect to the acid site while faced to the channel end (3). They are represented in Figure 6.6.

Table D.1: Angles for the three idealized cases with $\vec{n}$ the normal to the aromatic plane, $\vec{c}$ the vector aligned with the channel axis and $\vec{p}$ the vector perpendicular to the channel axis and perpendicular to the OH bond of the channel.

	$\angle(\vec{c},\vec{n})$	$\angle(\vec{p},\vec{n})$
Case (1)	90°	90°
Case (2)	90°	0°
Case (3)	0°	90°

D.1 Toluene

D.1.1 H-SAPO-5

Table D.2: The percentage of each case for toluene in H-SAPO-5 as function of the deviation from the perfect cases (10°,15°,20°,25° and 30°).

	10°	15°	20°	25°	30°
Case (1)	9.59 %	13.44 %	18.79 %	27.34 %	35.13 %
Case (2)	4.59 %	8.52 %	13.48 %	18.84 %	22.08 %
Case (3)	0.27 %	0.43 %	0.57 %	0.97 %	1.56 %

Table D.3: The percentage of each case for toluene with methanol on the acid site in H-SAPO-5 as function of the deviation from the perfect cases (10°,15°,20°,25° and 30°).

	10°	15°	20°	25°	30°
Case (1)	9.21 %	19.22 %	27.12 %	33.59 %	38.36 %
Case (2)	5.77 %	10.45 %	14.20 %	16.35 %	20.04 %
Case (3)	0.00 %	0.00 %	0.11 %	0.85 %	3.15 %

Table D.4: The percentage of each case for toluene with DME on the acid site in H-SAPO-5 as function of the deviation from the perfect cases (10°,15°,20°,25° and 30°).

	10°	15°	20°	25°	30°
Case (1)	9.01 %	11.75 %	19.24 %	25.96 %	31.91 %
Case (2)	5.71 %	10.20 %	14.33 %	16.78 %	20.21 %
Case (3)	0.96 %	1.81 %	3.56 %	5.93 %	9.92 %

Table D.5: The percentage of each case for toluene with a framework-bound methoxy species in H-SAPO-5 as function of the deviation from the perfect cases (10°,15°,20°,25° and 30°).

	10°	15°	20°	25°	30°
Case (1)	19.80 %	33.17 %	42.63 %	51.61 %	56.94 %
Case (2)	4.07 %	7.77 %	11.10 %	13.36 %	15.85 %
Case (3)	0.00 %	0.12 %	0.72 %	1.74 %	3.55 %

D.1.2 H-SSZ-24

Table D.6: The percentage of each case for toluene in H-SSZ-24 as function of the deviation from the perfect cases (10°,15°,20°,25° and 30°).

	10°	15°	20°	25°	30°
Case (1)	24.34 %	36.47 %	41.88 %	51.83 %	60.96 %
Case (2)	0.00 %	0.00 %	0.00 %	0.00 %	1.44 %
Case (3)	0.00 %	0.00 %	0.00 %	0.00 %	0.00 %

Table D.7: The percentage of each case for toluene with methanol on the acid site in H-SSZ-24 as function of the deviation from the perfect cases (10°,15°,20°,25° and 30°).

	10°	15°	20°	25°	30°
Case (1)	12.63 %	18.27 %	27.70 %	33.62 %	38.23 %
Case (2)	5.66 %	8.99 %	12.12 %	14.17 %	18.02 %
Case (3)	1.37 %	1.82 %	3.51 %	4.85 %	6.11 %

Table D.8: The percentage of each case for toluene with DME on the acid site in H-SSZ-24 as function of the deviation from the perfect cases (10°,15°,20°,25° and 30°).

	10°	15°	20°	25°	30°
Case (1)	12.29 %	16.21 %	21.33 %	25.96 %	31.62 %
Case (2)	4.25 %	9.85 %	13.97 %	18.87 %	23.95 %
Case (3)	1.01 %	1.72 %	1.77 %	2.45 %	3.79 %

Table D.9: The percentage of each case for toluene with a framework-bound methoxy species in H-SSZ-24 as function of the deviation from the perfect cases (10°,15°,20°,25° and 30°).

	10°	15°	20°	25°	30°
Case (1)	22.81 %	34.49 %	43.65 %	53.15 %	60.66 %
Case (2)	3.45 %	4.06 %	5.24 %	8.42 %	11.83 %
Case (3)	0.00 %	0.00 %	0.00 %	0.00 %	0.15 %

D.2 O-xylene

D.2.1 H-SAPO-5

Table D.10: The percentage of each case for o-xylene in H-SAPO-5 as function of the deviation from the perfect cases (10°,15°,20°,25° and 30°).

	10°	15°	20°	25°	30°
Case (1)	13.65 %	21.73 %	32.75 %	46.42 %	60.00 %
Case (2)	0.19 %	0.84 %	1.11 %	1.87 %	4.80 %
Case (3)	0.0 %	0.0 %	0.0 %	0.0 %	0.0 %

Table D.11: The percentage of each case for o-xylene with methanol on the acid site in H-SAPO-5 as function of the deviation from the perfect cases (10°,15°,20°,25° and 30°).

	10°	15°	20°	25°	30°
Case (1)	9.71 %	13.48 %	19.88 %	25.72 %	31.51 %
Case (2)	13.32 %	17.81 %	23.25 %	29.24 %	33.03 %
Case (3)	0.00 %	0.00 %	0.00 %	0.30 %	1.55 %

Table D.12: The percentage of each case for o-xylene with DME on the acid site in H-SAPO-5 as function of the deviation from the perfect cases (10°,15°,20°,25° and 30°).

	10°	15°	20°	25°	30°
Case (1)	15.36 %	21.68 %	30.31 %	35.51 %	39.79 %
Case (2)	2.54 %	5.94 %	9.35 %	14.72 %	18.89 %
Case (3)	0.00 %	0.00 %	0.49 %	0.77 %	1.49 %

Table D.13: The percentage of each case for o-xylene with a framework-bound methoxy species in H-SAPO-5 as function of the deviation from the perfect cases (10°,15°,20°,25° and 30°).

	10°	15°	20°	25°	30°
Case (1)	27.26 %	36.78 %	47.46 %	54.50 %	59.99 %
Case (2)	2.05 %	3.08 %	5.61 %	7.29 %	9.22 %
Case (3)	0.00 %	0.00 %	0.00 %	0.39 %	0.71 %

D.2.2 H-SSZ-24

Table D.14: The percentage of each case for o-xylene in H-SSZ-24 as function of the deviation from the perfect cases (10°,15°,20°,25° and 30°).

	10°	15°	20°	25°	30°
Case (1)	11.88 %	17.44 %	25.99 %	37.80 %	49.30 %
Case (2)	4.37 %	6.87 %	8.25 %	10.70 %	13.13 %
Case (3)	0.00 %	0.00 %	0.00 %	0.03 %	0.28 %

Table D.15: The percentage of each case for o-xylene with methanol on the acid site in H-SSZ-24 as function of the deviation from the perfect cases (10°,15°,20°,25° and 30°).

	10°	15°	20°	25°	30°
Case (1)	14.04 %	20.49 %	25.62 %	31.39 %	38.42 %
Case (2)	7.69 %	13.07 %	18.30 %	23.14 %	26.22 %
Case (3)	0.00 %	0.00 %	0.00 %	0.00 %	0.08 %

Table D.16: The percentage of each case for o-xylene with DME on the acid site in H-SSZ-24 as function of the deviation from the perfect cases (10°,15°,20°,25° and 30°).

	10°	15°	20°	25°	30°
Case (1)	14.69 %	21.44 %	28.19 %	36.29 %	42.46 %
Case (2)	4.52 %	9.56 %	12.84 %	16.81 %	20.43 %
Case (3)	0.00 %	0.00 %	0.26 %	0.78 %	1.39 %

Table D.17: The percentage of each case for o-xylene with a framework-bound methoxy species in H-SSZ-24 as function of the deviation from the perfect cases (10°,15°,20°,25° and 30°).

	10°	15°	20°	25°	30°
Case (1)	31.17 %	42.78 %	49.72 %	56.19 %	62.35 %
Case (2)	1.84 %	2.45 %	3.74 %	5.88 %	9.83 %
Case (3)	0.00 %	0.00 %	0.00 %	0.00 %	0.00 %

Appendix E

Competitive adsorption in the AFI topology

This appendix contains the figures used to determine whether competitive adsorption between the aromatic and the methylating agent on the acid site takes place or not. For the MD runs starting from configuration (a) and (b) the shortest distance of the six aromatic ring carbon atoms to the hydrogen atom of the acid site is plotted together with the distance of the oxygen atom of the methylating agent to the acid site. The interaction between the acid site and the compound which is located nearest to the site will be the highest. It is known that the methylating agent have a hight affinity for the acid site, however since larger aromatics posses increasing proton affinities, the aromatic can start to compete with the methylating agent. If the fraction of the MD run in which the aromatic sits nearest to the acid site is very short, than it can be assumed that no competitive adsorption takes place and that the methylating agent sit predominantly on the acid site. In the next sections all guest molecule pairs are discussed per catalyst.

E.1 Methanol and Toluene in H-SAPO-5

In both Figure E.1 and Figure E.2 methanol sits preferencially on the acid site. In Figure E.2 it appears that there are 2 distinct states for methanol. The state with the longer equilibrium distance corresponds to a configuration where the acid site is pointing away from the methanol and into the zeolite framework.

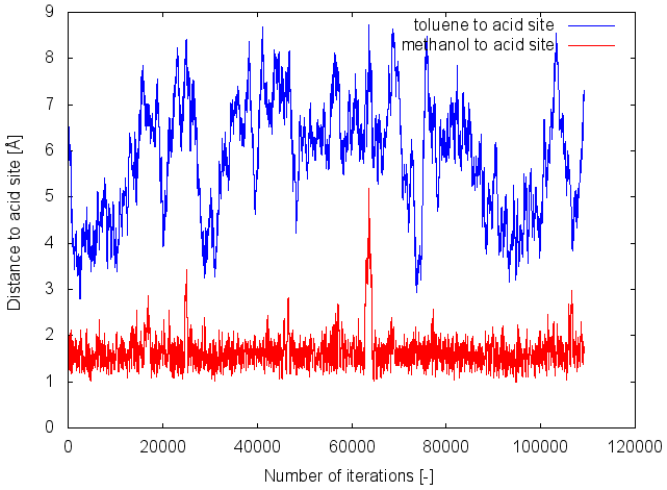

Figure E.1: The distance to the acid site for the closest C atom of the aromatic ring of toluene and for the O atom of methanol as function of the time step, when starting from a configuration where methanol is closest to the acid site in H-SAPO-5.

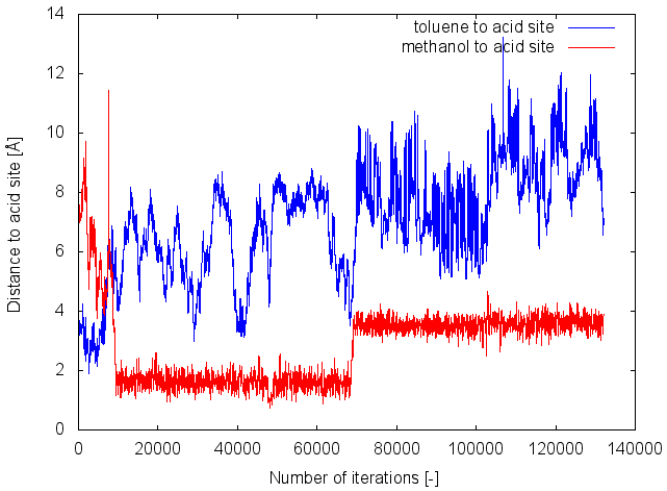

Figure E.2: The distance to the acid site for the closest C atom of the aromatic ring of toluene and for the O atom of methanol as function of the time step, when starting from a configuration where toluene is closest to the acid site in H-SAPO-5.

E.2 Methanol and Toluene in H-SSZ-24

As in H-SAPO-5, methanol is the most stable species to be adsorbed on the acid site when toluene is co-adsorbed in H-SSZ-24 as seen in Figure E.3 and Figure E.4. A stronger interaction with the acid site is observed at a distance of 1 Å to the acid site, explained by the fact that H-SSZ-24 is a more acidic catalyst.

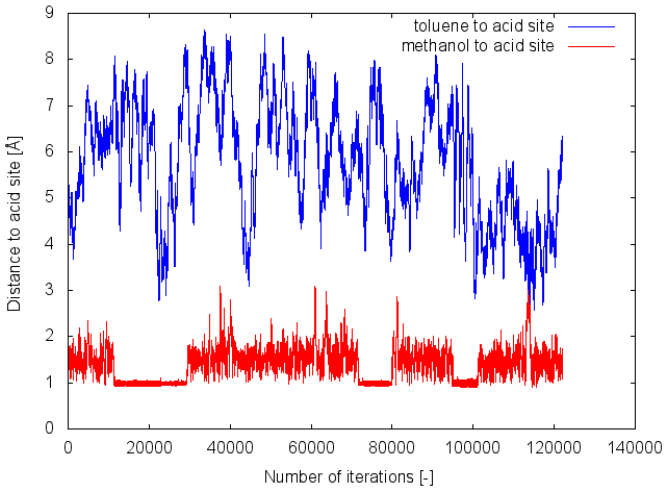

Figure E.3: The distance to the acid site for the closest C atom of the aromatic ring of toluene and for the O atom of methanol as function of the time step, when starting from a configuration where methanol is closest to the acid site in H-SSZ-24.

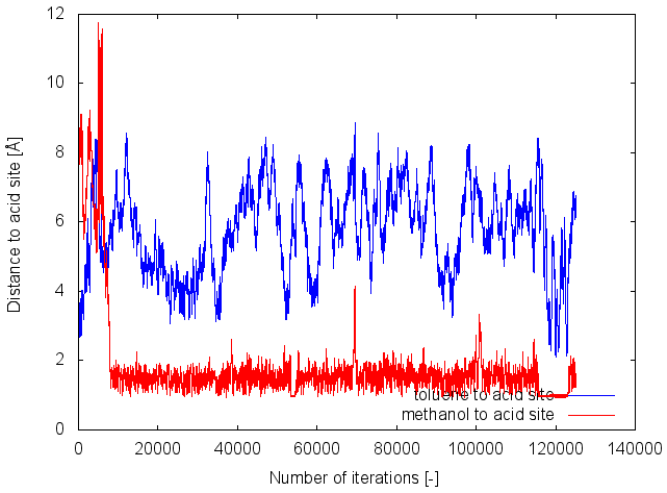

Figure E.4: The distance to the acid site for the closest C atom of the aromatic ring of toluene and for the O atom of methanol as function of the time step, when starting from a configuration where toluene is closest to the acid site in H-SSZ-24.

E.3 Methanol and O-xylene in H-SAPO-5

Also for methanol and o-xylene, methanol is the most stable adsorbate. However the switch from o-xylene to methanol on the acid site occurs much later in the simulation. O-xylene holds almost 20 ps on the acid site as shown in Figure E.6. This means that there is competitive adsorption.

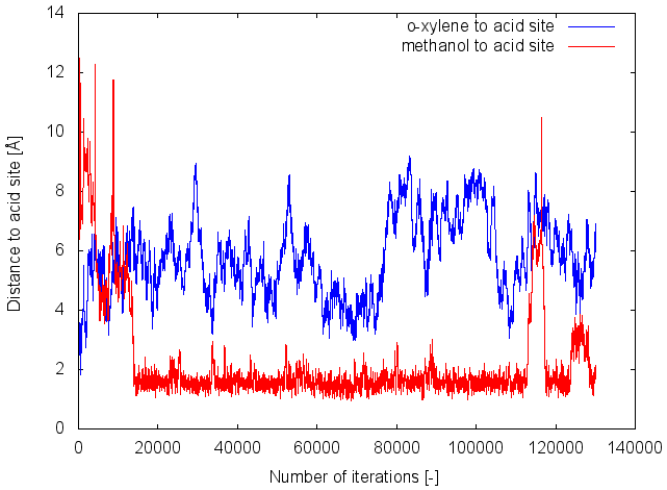

Figure E.5: The distance to the acid site for the closest C atom of the aromatic ring of o-xylene and for the O atom of methanol as function of the time step, when starting from a configuration where methanol is closest to the acid site in H-SAPO-5.

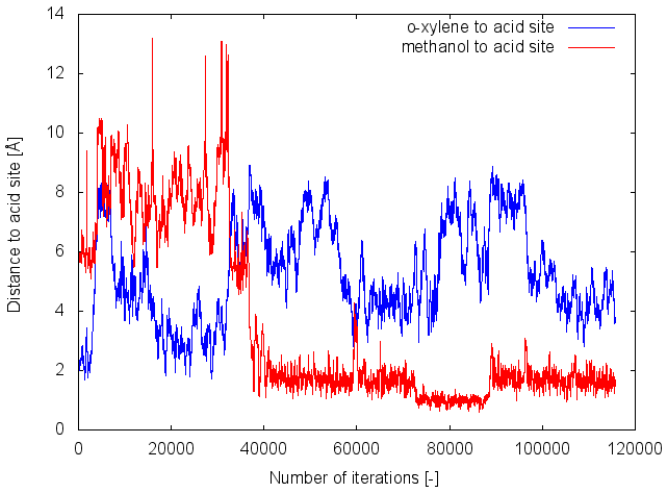

Figure E.6: The distance to the acid site for the closest C atom of the aromatic ring of o-xylene and for the O atom of methanol as function of the time step, when starting from a configuration where o-xylene is closest to the acid site in H-SAPO-5.

E.4 Methanol and O-xylene in H-SSZ-24

Like in H-SAPO-5, o-xylene isn't immediately pushed away from the acid site by methanol, as seen in Figure E.8. The switch is, however, slightly sooner than in H-SAPO-5, probably since the interaction with methanol and the acid site is greater due to the higher acidity.

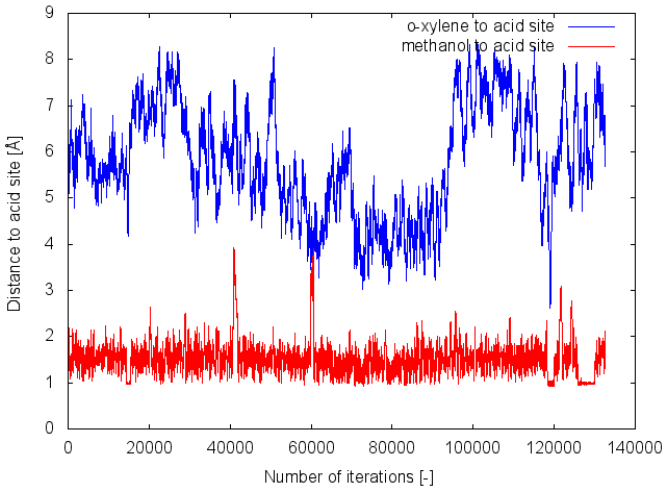

Figure E.7: The distance to the acid site for the closest C atom of the aromatic ring of o-xylene and for the O atom of methanol as function of the time step, when starting from a configuration where methanol is closest to the acid site in H-SSZ-24.

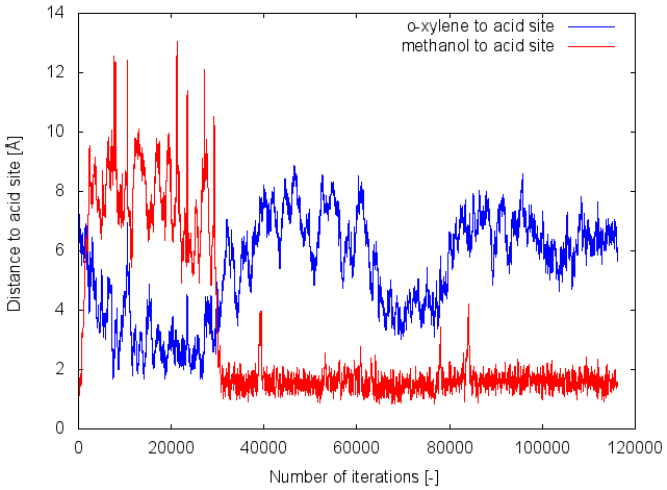

Figure E.8: The distance to the acid site for the closest C atom of the aromatic ring of o-xylene and for the O atom of methanol as function of the time step, when starting from a configuration where o-xylene is closest to the acid site in H-SSZ-24.

E.5 DME and Toluene in H-SAPO-5

In Figure E.9 DME is the most stable adsorbing species. However in the simulation corresponding to Figure E.10 DME cannot permanently settle on the acid site since toluene is blocking it.

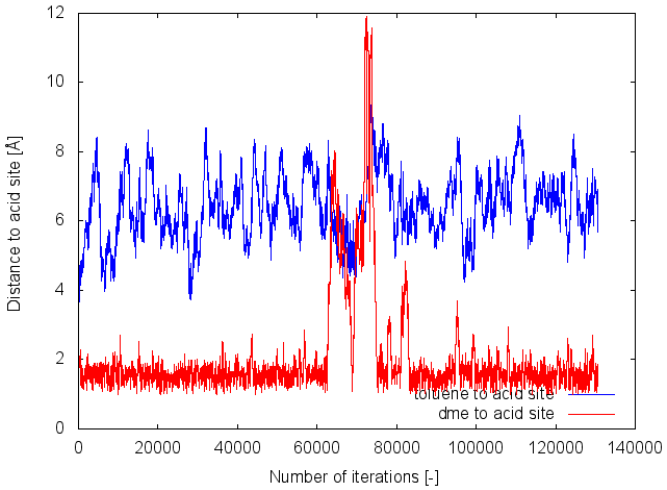

Figure E.9: The distance to the acid site for the closest C atom of the aromatic ring and for the O atom of DME as function of the time step, when starting from a configuration where DME is closest to the acid site in H-SAPO-5.

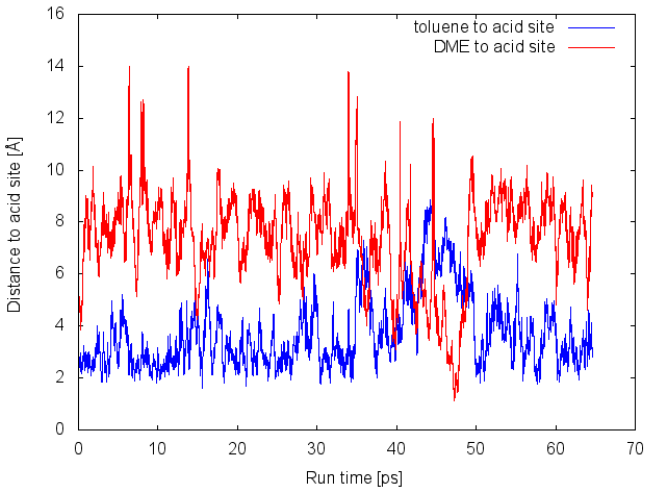

Figure E.10: The distance to the acid site for the closest C atom of the aromatic ring of toluene and for the O atom of DME as function of the time step, when starting from a configuration where toluene is closest to the acid site in H-SAPO-5.

E.6 DME and Toluene in H-SSZ-24

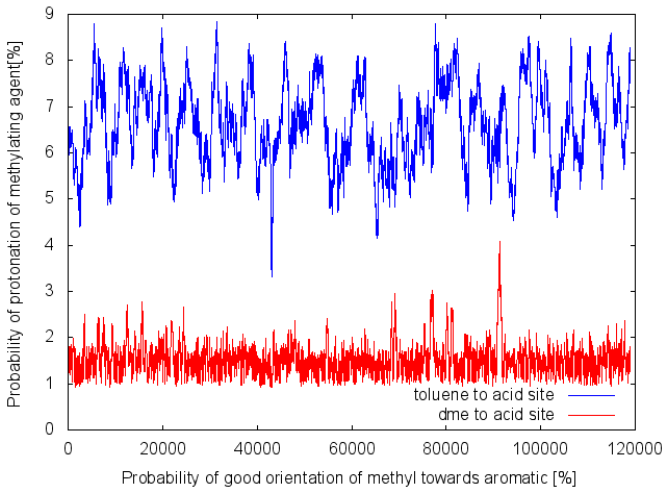

Figure E.11: The distance to the acid site for the closest C atom of the aromatic ring and for the O atom of DME as function of the time step, when starting from a configuration where DME is closest to the acid site in H-SSZ-24.

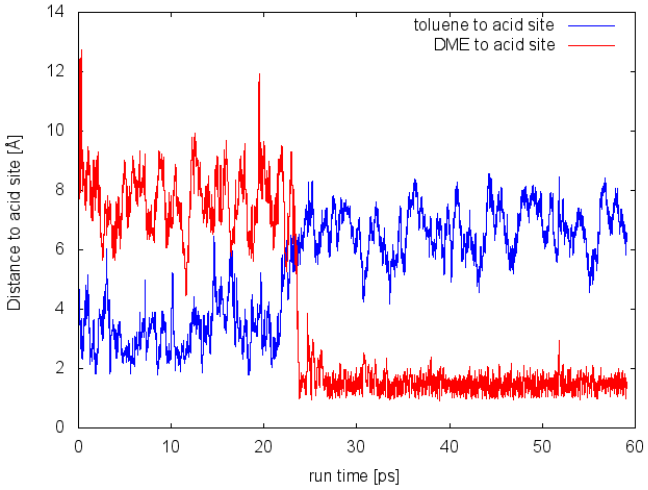

Figure E.12: The distance to the acid site for the closest C atom of the aromatic ring of toluene and for the O atom of DME as function of the time step, when starting from a configuration where toluene is closest to the acid site in H-SSZ-24.

A clear switch between toluene and DME is observed in Figure E.12. In H-SSZ-24, DME is the most stable adsorbate on the acid site. The situation in H-SAPO-5, shown in Figure E.10, might be a coincidence. Therefore a new MD simulation is started from a slightly different starting configuration to check whether the situation is reproducible.

E.7 DME and O-xylene in H-SAPO-5

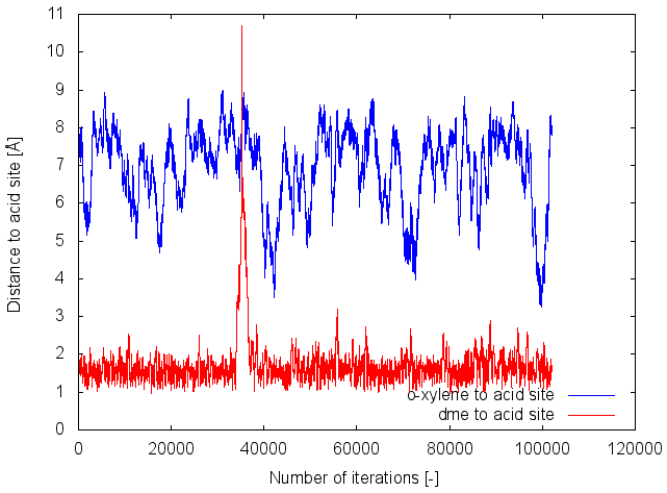

Figure E.13: The distance to the acid site for the closest C atom of the aromatic ring of o-xylene and for the O atom of DME as function of the time step, when starting from a configuration where DME is closest to the acid site in H-SAPO-5.

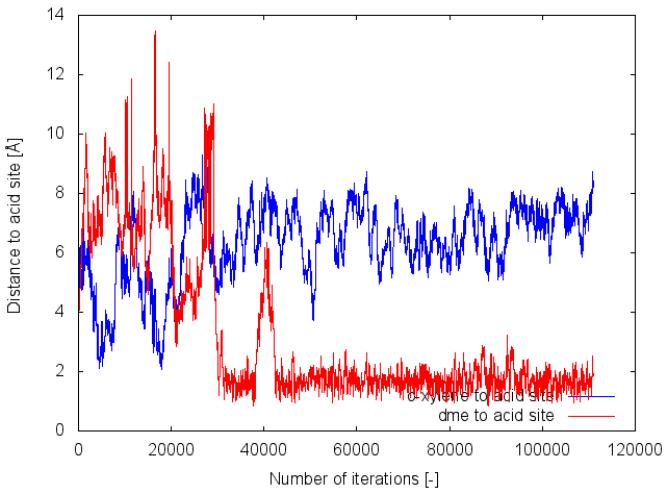

Figure E.14: The distance to the acid site for the closest C atom of the aromatic ring of o-xylene and for the O atom of DME as function of the time step, when starting from a configuration where o-xylene is closest to the acid site in H-SAPO-5.

Based on Figure E.13 and Figure E.14, it can safely be said that DME is the most stable adsorbate on the acid site in H-SAPO-5

E.8 DME and O-xylene in H-SSZ-24

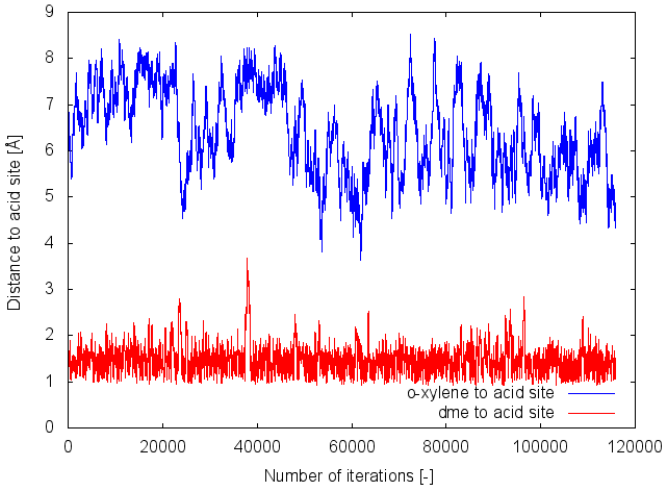

Figure E.15: The distance to the acid site for the closest C atom of the aromatic ring of o-xylene and for the O atom of DME as function of the time step, when starting from a configuration where DME is closest to the acid site in H-SSZ-24.

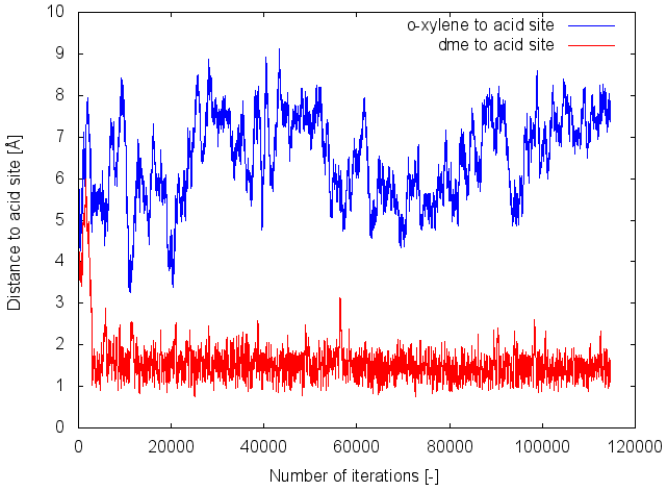

Figure E.16: The distance to the acid site for the closest C atom of the aromatic ring of o-xylene and for the O atom of DME as function of the time step, when starting from a configuration where o-xylene is closest to the acid site in H-SSZ-24.

Just like in H-SAPO-5, DME sits preferentially on the acid site in H-SSZ-24.

Appendix F

Convergence of the probabilities of pre-reactive complex formation

Table F.1: Probability of pre-reactive complex formation between the methoxide and benzene, toluene and o-xylene for different lengths of the MD simulation in H-SAPO-5 at 623 K and 1 atm.

time [ps]	Benzene	Toluene	O-xylene
40.0	4.52 %	9.77 %	13.92 %
45.0	5.36 %	8.73 %	12.37 %
47.5	5.39 %		11.72 %
50.0		8.42 %	11.13 %
52.5		8.02 %	11.00 %
55.0		7.65 %	
57.5		7.32 %	
60.0		7.26 %	
62.5		7.66 %	

Table F.2: Probability of pre-reactive complex formation of benzene, toluene and o-xylene with methanol or DME for different lengths of the MD simulation in H-SAPO-5 at 623 K and 1 atm.

	methanol on acid site			dme on acid site		
time [ps]	Benzene	Toluene	O-xylene	Benzene	Toluene	O-xylene
25.0	5.30%	21.90%	31.17%	92.36%	72.79%	88.94%
30.0		25.25%	29.10%		76.30%	88.24%
35.0		25.33%	25.44%		74.82%	85.27%
40.0	18.14%	26.56%	29.02%	86.85%	73.77%	85.90%
45.0		26.09%	29.97%		76.53%	85.11%
47.5		25.14%	31.91%		75.16%	85.88%
50.0	17.32%	25.67%	32.24%	84.06%	75.43%	84.94%
52.5			30.94%		76.23%	
55.0			31.09%		76.76%	
57.5					77.46%	
60.0					77.75%	
62.5					78.64%	
volledige run	17.19%	25.33%	30.96%	83.02%	78.73%	84.95%

Table F.3: Probability of pre-reactive complex formation of benzene, toluene and o-xylene with methanol or DME for different lengths of the MD simulation in H-SSZ-24 at 623 K and 1 atm.

	methanol on acid site			dme on acid site		
time [ps]	Benzene	Toluene	O-xylene	Benzene	Toluene	O-xylene
25.0	23.15%	40.47%	36.36%	77.83%	92.03%	98.85%
30.0		42.27%	31.51%		91.86%	98.93%
35.0		40.15%	27.93%		90.93%	97.72%
40.0	29.00%	37.41%	24.44%	82.73%	91.58%	96.45%
45.0		38.18%	21.96%		91.40%	94.59%
47.5		38.76%	21.61%		91.65%	94.87%
50.0	34.98%	39.04%	22.60%	85.61%	91.23%	95.13%
52.5		37.23%	24.16%		90.92%	95.36%
55.0		35.75%	25.82%		91.33%	95.57%
57.5		34.20%	25.94%		91.65%	95.77%
60.0		33.63%	27.13%			
62.5			27.46%			
65.0			27.31%			
volledige run	34.98%	33.72%	27.16%	86.08%	91.85%	95.80%

Appendix G

Metadynamics: extra results

Below the path followed by the three collective variables are represented in a 3D plot for each of the three MTD simulation (toluene and methanol in H-SAPO and H-SSZ-24 and toluene and DME in H-SSZ-24). The left valley on the graps represents the reactant valley of methanol adsorbed on acid site and toluene, while the valley on the right represents part of the product valley of water and a xylenium ion. The true product minimum is not sampled since this would involve a hydride shift in the xylenium atom, which is prevented by the placement of a wall on the second collective variable.

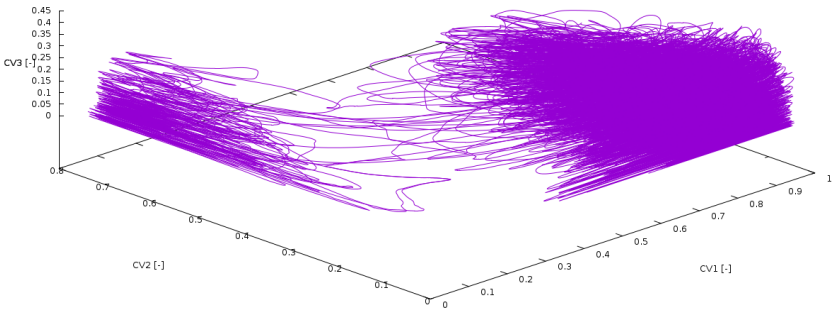

Figure G.1: 3D plot of the collective variables for the MTD simulation of methanol and toluene co-adsorbed in H-SAPO-5 at 623 K and 1 atm.

The evolution of the free energy profile by adding hills is also given below for all three MTD simulations.

The free energy barriers are recalculated by substracting 100 hills at a time from the end of each simulation. The difference in barrier between two simulations with 100 hills apart from oneanother gives an idea of the convergence of the MTD simulation. Results are shown below:

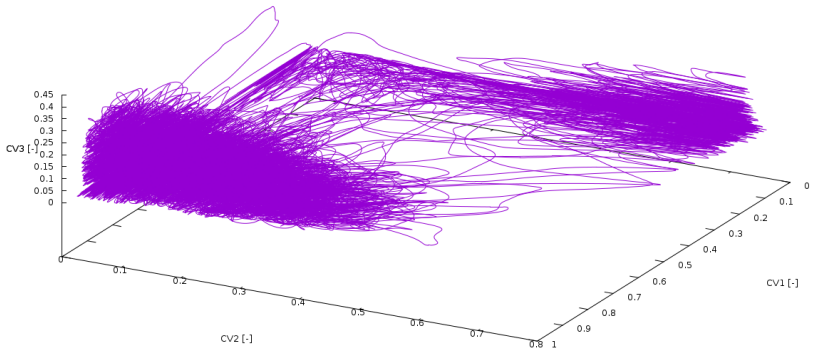

Figure G.2: 3D plot of the collective variables for the MTD simulation of methanol and toluene co-adsorbed in H-SSZ-24 at 623 K and 1 atm.

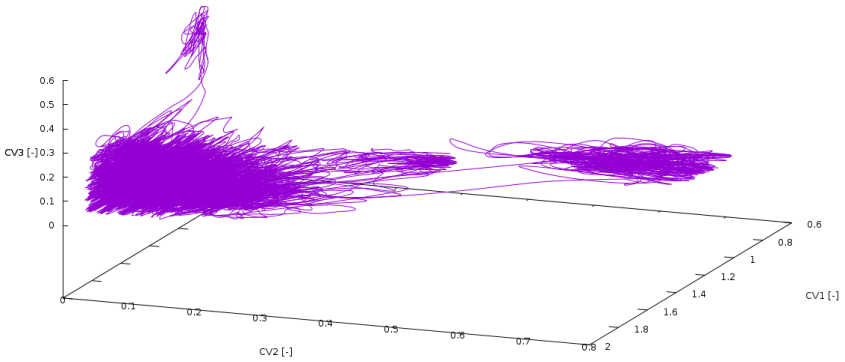

Figure G.3: 3D plot of the collective variables for the MTD simulation of DME and toluene co-adsorbed in H-SSZ-24 at 623 K and 1 atm.

Table G.1: The evolution of the free energy barrier as function of the number of hills, starting from the free energy barrier obtained from the simulation run 500 hills apart from the end. Here, no smoothening is applied to the LFEP.

Reaction	$\Delta(\Delta G^{\ddagger}_{400-500hills})$	$\Delta(\Delta G^{\ddagger}_{300-400hills})$	$\Delta(\Delta G^{\ddagger}_{200-300hills})$	$\Delta(\Delta G^{\ddagger}_{100-200hills})$
MeOH in H-SAPO-5	1.5 kJ mol^{-1}	4.6 kJ mol^{-1}	0.5 kJ mol^{-1}	0.2 kJ mol^{-1}
MeOH in H-SSZ-24	0.1 kJ mol^{-1}	0.1 kJ mol^{-1}	0.9 kJ mol^{-1}	2.3 kJ mol^{-1}
DME in H-SSZ-24	20.6 kJ mol^{-1}	9.5 kJ mol^{-1}	7.3 kJ mol^{-1}	10.3 kJ mol^{-1}
methoxide in H-SSZ-24	18.2 kJ mol^{-1}	19.7 kJ mol^{-1}	6.8 kJ mol^{-1}	9.8 kJ mol^{-1}

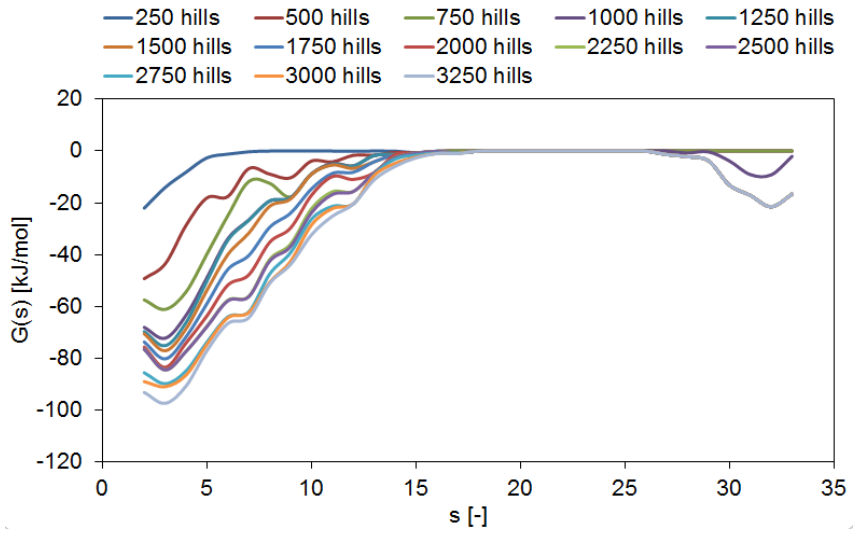

Figure G.4: The effect of adding Gaussian hills on the free energy profile $G(s)$ as function of the coordinates s along the minimum energy path for a methylation reaction given in chapter 7 for the MTD simulation of methanol and toluene co-adsorbed in H-SAPO-5 at 623 K and 1 atm.

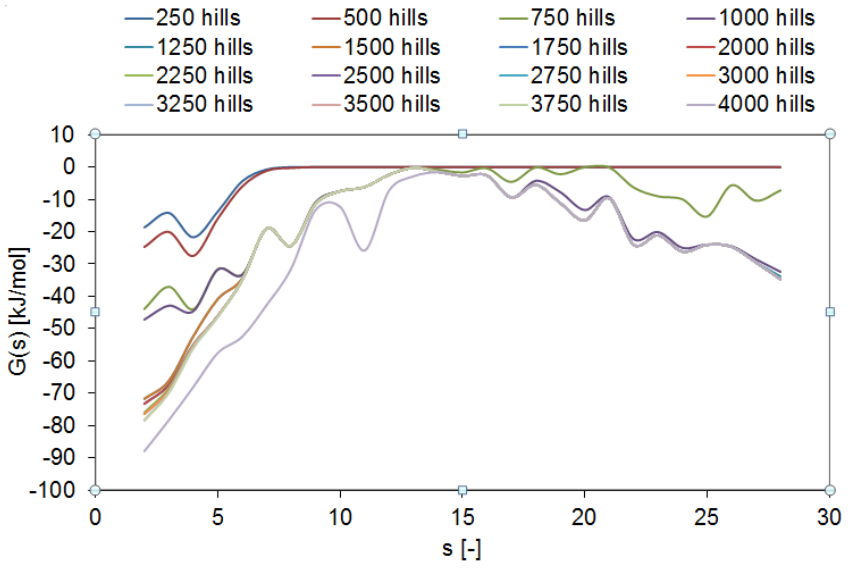

Figure G.5: The effect of adding Gaussian hills on the free energy profile $G(s)$ as function of the coordinates s along the minimum energy path for a methylation reaction given in chapter 7 for the MTD simulation of methanol and toluene co-adsorbed in H-SSZ-24 at 623 K and 1 atm.

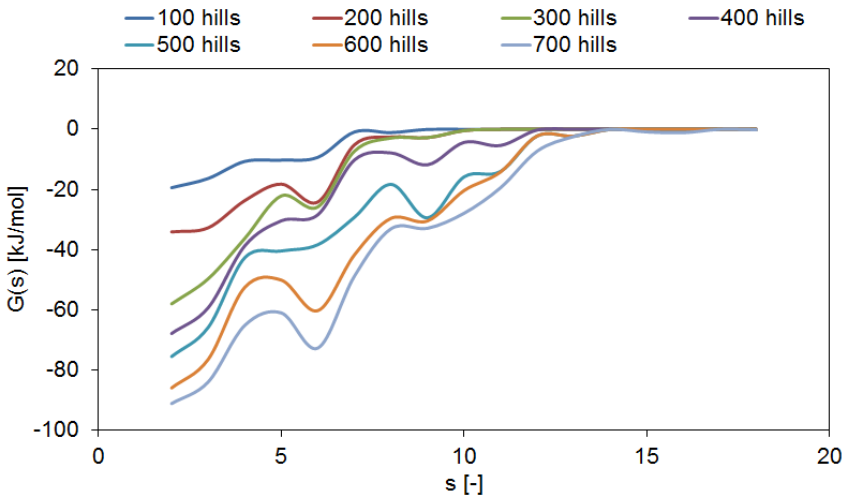

Figure G.6: The effect of adding Gaussian hills on the free energy profile $G(s)$ as function of the coordinates s along the minimum energy path for a methylation reaction given in chapter 7 for the MTD simulation of DME and toluene co-adsorbed in H-SSZ-24 at 623 K and 1 atm.

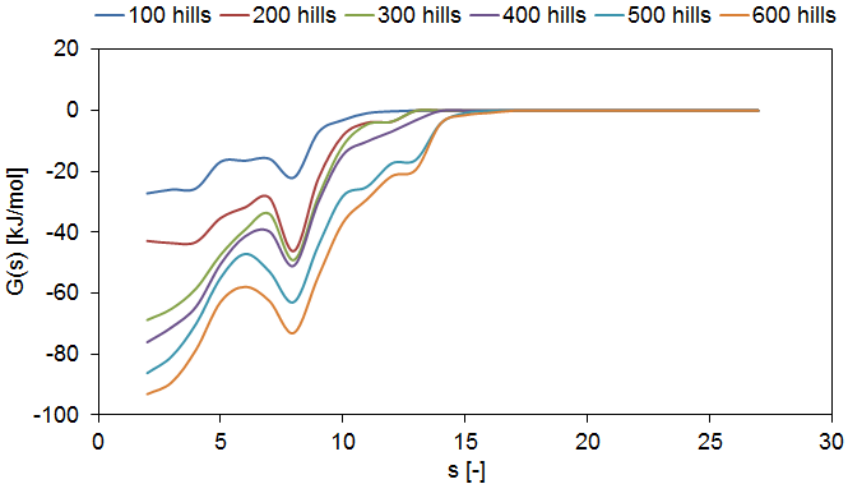

Figure G.7: The effect of adding Gaussian hills on the free energy profile $G(s)$ as function of the coordinates s along the minimum energy path for the formation of a framework-bound methoxide given in chapter 7 for the MTD simulation of DME and toluene co-adsorbed in H-SSZ-24 at 623 K and 1 atm.

Appendix H

NCCC poster

This appendix contains the poster which was presented on March 3 2015 at the 16th Netherlands' Catalysis and Chemistry Conference (NCCC), Noordwijkerhout (NL).

Dynamic ab initio study on the influence of acid strength on MTO conversion in H-SAPO-5 and H-SSZ-24

Margot Matton, Kristof De Wispelaere, Jeroen Van der Mynsbrugge, Karen Hemelsoet, Veronique Van Speybroeck

Center for Molecular Modeling, Ghent University, Technologiepark 903, 9052 Zwijnaarde, Belgium

Methanol To Olefins (MTO)

depleting crude oil reserves
increasing demand for olefins

➡ { syngas > methanol = alternative feedstock for olefins [1]
more flexibility on ethylene to propylene ratio
design of zeolite catalysts to optimize process

AFI Topology

large 1D channels (12 rings) allow feeding of large molecules
➡ AFI = ideal model for H-SAPO-34 (CHA)

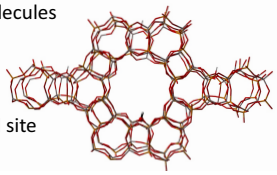

H-SAPO-5
per Si → one acid site
moderate acid strength

H-SSZ-24
per Al → one acid site
high acid strength

Goal and methodology

investigate effect of:
- acid strength
- methylating agent
- degree of methylation of HP species

on adsorption complexes in AFI via molecular dynamic (MD) simulations

ab initio MD [5] with **CP2K:**
periodic model
revPBE functional + D3 corrections
GPW basis set
NPT ensemble
Nosé Hoover thermostat: 623 K
MTK barostat: 1 atm

Why dynamic simulations?
large channel ➡ many possible configurations ➡ complex potential energy surface

Pre-reactive complexes in AFI

Methylating agents:
- methanol (MeOH)
- dimethyl ether (DME)
- framework-bound methoxide

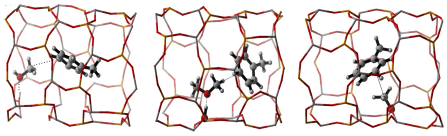

Reactivity towards methylation with MeOH and DME

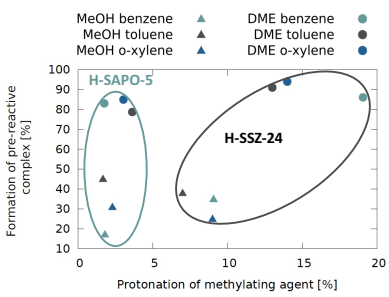

indicators:
1. methyl group points towards aromatic ring
2. methylating agent is protonated

- probability of protonation increases significantly in more acidic material
- formation of pre-reactive complex more favored when using DME as methylating agent

Reactivity towards methylation with framework-bound methoxide

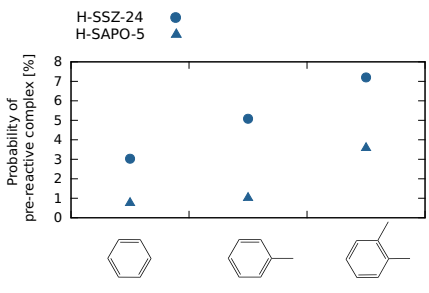

indicator:
shortest distance between ring-C and methoxide-C smaller than 3.5 Å

- probability higher in more acidic material
- probability increases with increasing degree of methylation

Mechanism

Hydrocarbon pool (HP) species [2]

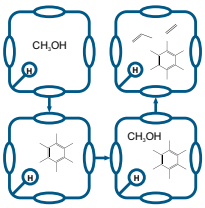

Dual cycle [2]

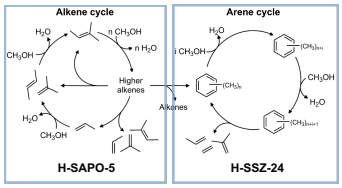

methylation reactions crucial in MTO mechanism

Experimental results

Experiments were conducted by the group of U. Olsbye at the University of Oslo, Norway

Methanol conversion [3]

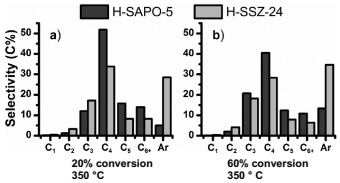

- production of aromatics significantly higher in H-SSZ-24
- more selective towards lower olefins (C_1-C_3) in H-SSZ-24
- more selective towards higher olefins (C_{4+}) in H-SAPO-5

Co-feeding of methanol and benzene [4]

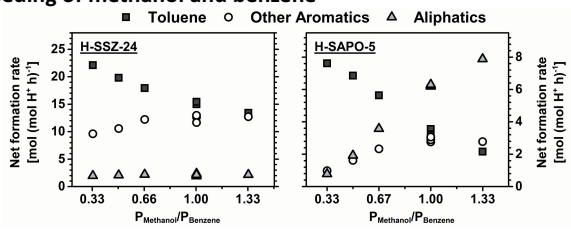

H-SSZ-24:
polyMB intermediates
low selectivity to aliphatics

H-SAPO-5
more methanol feed
→ aliphatics dominant

Competitive adsorption

Methylating agent (MA):
MeOH, DME

Degree of methylation (n):
0, 1, 2

more bulky aromatic
➡ higher proton affinity

always possible | undesired for methylation

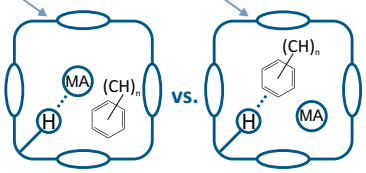

When do aromatics compete with MeOH or DME for adsorption on the acid site?

	H-SAPO-5			H-SSZ-24		
	Benzene	Toluene	O-xylene	Benzene	Toluene	O-xylene
MeOH	✗	✗	✓	✗	✗	✓
DME	✗	✓	✗	✗	✗	✗

Conclusion and Outlook

MD study on the influence of acid strength on the reactivity towards methylation shows :
- Protonation probabilities higher in the more acidic material H-SSZ-24
- Formation of properly oriented pre-reactive complexes higher with DME than with MeOH in both H-SAPO-5 and H-SSZ-24
- Increasing interaction between methoxide and aromatic HP with higher degree of methylation in both H-SAPO-5 and H-SSZ-24, but not for MeOH and DME.
- Competitive adsorption very likely for o-xylene + MeOH in both AFI materials

Future work: metadynamics study of methylation kinetics for aromatic HP in AFI

References

[1] U. Olsbye et al., Angew. Chem. Int. 51 (2012) 2-24.
[2] K. Hemelsoet et al., Chem. Phys. Chem. 14 (2013) 1526-1545.
[3] M. Westgård Erichsen et al., Catal. Today 215 (2013) 216-223.
[4] M. Westgård Erichsen et al., J. Catal. (2015), DOI: 10.1016/j.jcat.2015.01.013.
[5] V. Van Speybroeck et al., Chem. Soc. Rev. 43 (2014) 7326-7357.